

Dissertation zur Erlangung des Doktorgrades
der Fakultät für Chemie und Pharmazie
der Ludwig-Maximilians-Universität München

**Influence of Fullerene Additives on Stability and
Performance of Polymer-Nonfullerene Organic Solar Cells**

Marcella Maria Patricia Günther

aus

Weingarten, Deutschland

2022

Erklärung

Diese Dissertation wurde im Sinne von § 7 der Promotionsordnung vom 28. November 2011 von Frau Dr. habil. Tayebbeh Ameri betreut

Eidesstattliche Versicherung

Diese Dissertation wurde eigenständig und ohne unerlaubte Hilfe bearbeitet

München, den 26.03.2023

(Marcella Günther)

Dissertation eingereicht am:	23.11.2022
1. Gutachterin:	Dr. habil. Tayebbeh Ameri
2. Gutachter:	Prof. Dr. Thomas Bein
Mündliche Prüfung am:	22.12.2022

Danksagung

An dieser Stelle möchte ich als erstes meiner Doktormutter Tayebah Ameri danken für die Betreuung und ein spannendes Forschungsthema mit unendlich vielen Herausforderungen, das mich zwar manchmal gequält, aber immer auch sehr begeistert hat. Ein großer Dank gilt außerdem meinem Zweitgutachter Thomas Bein, für die Unterstützung und für die vielen Diskussionen und hilfreichen Fragen in den subgroup meetings.

Danken möchte ich außerdem meinen Kooperationspartnern für tolle Messungen und schnelle Antworten. Vielen Dank vor allem an meinen langandauerndsten und wichtigsten Kooperationspartner Domi, der auch nach seinem Themenwechsel immer als Diskussionspartner zur Verfügung stand, mich bei zähen Raman- und FTPS-Messungen unterstützt hat, und jetzt am Ende sogar noch die ausstehenden Revisions übernimmt.

Bedanken möchte ich mich zudem beim ‚alten‘ AK Bein, bei dem ich meine Promotion begonnen habe. Vielen Dank an Michi, dafür dass du von Anfang an als Kollege und ganz schnell auch als Freund immer für mich da warst. Danke an den harten Kern der Augustiner Crew, Michi, Joni, Julian und Stephan für so viele unterhaltsame Freitags-Mittagessen.

Danke auch an mein anfängliches Büro! Danke Derya für sehr viel Video-Wissen, das ich gar nie wollte, für unendlich viele Lacher, für Selbstverteidigungstipps, tiefgründige Gespräche, und natürlich für die gegenseitige Unterstützung in der Bewerbungsphase.

Danke Max für deine unermüdliche Hilfe und deinen ansteckenden Enthusiasmus und dafür, dass ich Punk Rock nicht mehr hören kann ohne dabei an das Labor zu denken. Danke Anderson für gemeinsames Leiden und Jammern und für deine unendliche Hilfsbereitschaft.

Danke auch an den neuen AK Bein, mit dem ich die zweite Hälfte meines Doktors verbringen durfte. Bedanken möchte ich mich bei der PV-subgroup, Rik, Flo, Andi, Shizhe und Ali B. für eine angenehme Arbeitsatmosphäre, gute Diskussionen und große Hilfsbereitschaft.

Ein besonderer Dank geht an meinen Bürokollegen Andi und meinen fast-Bürokollegen Peter! Danke für sowohl fachliche als auch musikalische und kulinarische Inspiration und die Film- und Buchtipps. Danke für die Aufmunterungen, die vielen Gespräche, und die manchmal dringend benötigte Erdung bei meiner Doktorarbeit.

Danke an die 90er Party-Crew – Meli, Laura², Kathi, Peter, Derya, Julian – für viele eskalative Abende und tolle Erinnerungen! Ich kann mir feiern ohne Team Weinschorle und McDonald's Hocke gar nicht mehr vorstellen.

Danke Kathi für gute Unterhaltungen und ungeplante Eskalationen.

Danke Meli, für lange Gespräche und gemeinsame Partys, für Aperol Spritz auf dem Balkon und dafür, dass du eine tolle Kollegin bist, die ich inzwischen Freundin nenne.

Vielen Dank an Laura F. dafür, dass wir die heiße Phase gemeinsam durchstehen konnten. Ohne all unsere Gespräche und gegenseitigen Erinnerungen hätte ich garantiert irgendwas Wichtiges vergessen.

Die Promotion spielt sich zwar innerhalb der Universität ab, aber auch außerhalb gibt es einige Menschen, ohne deren Unterstützung ein Abschluss nicht möglich gewesen wäre:

Deshalb geht ein großer Dank an Anna: danke für die Freundschaft, für die Unterstützung, für offene Ohren und die Bereitschaft für Notfall-Gespräche, ganz viel Gejammer, und wenn gar nichts mehr half Notfall-Shots. Ohne dich hätten Studium und Doktor nur halb so viel Spaß gemacht! Danke auch an die anderen beiden Swags Steffi und Maike, für so viele Skype-Parties, tolle gemeinsame Wochenenden und noch viel schönere gemeinsame Urlaube. Das Beste am Chemie-Studium war, dass ich euch drei dort kennenlernen durfte!

Ein ganz besonderer Dank außerdem für Julian: Danke, dass du immer für mich da bist und dass du meine Forschungsprobleme zur Not auch im Urlaub am Strand mit mir diskutiert hast. Du hast mich in all dem Auf und Ab immer wieder aufgemuntert und daran erinnert, dass es neben dem Doktor noch andere schöne Dinge im Leben gibt. Besonders in der letzten anstrengenden Phase hast du mir so viel abgenommen und warst (und bist) mein Ruhepol in dem ganzen Stress.

Der größte Dank geht an meine Familie, meine Eltern, meine Schwester und meine Oma, die nach wie vor fest davon überzeugt sind, dass ich den Nobelpreis kriegen kann. Die Professoren-Wette werde ich wohl auch nicht gewinnen, aber vielleicht schafft es ja die nächste Generation :)

Abstract

Over the past decade, organic solar cells (OSCs) have evolved from a niche topic to a serious technology that will enable completely new areas of application for solar cells in just a few years. This is primarily due to the fact that OSCs – in contrast to conventional silicon-based solar cells – can be manufactured at extremely low cost and energy consumption and furthermore provide the option of lightweight, flexible substrates. For actual commercialization, however, their efficiency and, above all, their long-term stability must be further improved. One promising approach is to build up the absorber layer from three components instead of the usual two, thus producing so-called ternary solar cells. The third component offers additional possibilities to tailor the properties of the absorbing layer and simultaneously increase efficiency and stability. However, it also makes the solar cells more complex and the mechanisms taking place in ternary OSCs are still not fully understood.

This thesis therefore focuses on a sub-class of organic solar cells consisting of a polymer donor (D) and a nonfullerene acceptor (NFA) and aims to understand how the use of fullerenes (FA) as a third component affects stability and performance.

In the introduction, the current state of understanding the working principles of ternary organic solar cells (TOSCs) in general is critically reviewed (chapter 1.3). Although TOSCs have been researched for more than ten years, there is still no universal model to define the mechanisms involved. Instead, various models exist, which we present in detail with a special focus on their inconsistencies, contradictions, and limitations. Furthermore, it is illustrated that the existing models are outdated and do not reflect more recent findings. We therefore provide an overview of the latest research on TOSCs with respect to their electronic and morphological properties. Finally, the conventional models for TOSCs are revisited in the light of new insights with the aim to point out existing gaps and to provide the stimulus for challenging old concepts.

In the first part (chapter 3), we study the photostability of polymer:NFA organic solar cells under ultraviolet (UV) illumination and how different fullerene derivatives serving as third components influence the lifetime. For the binary systems, the lifetime under UV illumination is found to be in the range of only several hours which is attributed to a photocatalytic decomposition of the vulnerable vinyl-bonds of the NFA caused by the used zinc oxide (ZnO) electron transport layer (ETL), resulting in the formation of trap states and a reduced fill factor. Since the photocatalytic decomposition occurs via the formation of radicals from oxygen

species adsorbed on the ZnO surface, we add different fullerene derivatives as third components to act as radical scavengers.

We find that already an addition of 5 % fullerene derivative not only increases the efficiency of the binary systems but also significantly enhances the photostability. We explain this positive effect with the fullerenes trapping the radicals and acting as sacrificial agents since their large conjugated system is able to delocalize the excess charge and does not form a trap state. We thus establish a straightforward and transferable way to increase the photostability of polymer:NFA OSCs by a ternary approach.

Building on this first project, the second part (chapter 4) takes a look from a more general perspective at how the use of ZnO as an electron transport layer affects stability studies of organic solar cells. Although ZnO is one of the most widely used ETL materials, it also has a pronounced defect chemistry with properties that are highly dependent on processing method and environment. One problem is the so-called light-soaking issue, which means that pristine ZnO-containing solar cells have a low performance due to an energy level mismatch at the ZnO interface caused by adsorbed oxygen species which have to be desorbed by a short UV light exposure but can re-adsorb from the environment. It is usually assumed that this light-soaking effect does not re-occur in an oxygen-free atmosphere and for this reason, based on convenience, stability measurements are frequently performed with a white light LED which contains no UV part. However, we show that even in an oxygen-free environment in the absence of UV light a reversible degradation occurs in OSCs which is independent of the used absorber materials and accelerates at higher temperatures but can be undone with a short UV exposure. We attribute this reversible aging to the re-adsorption of oxygen, which is unavoidably trapped at the interface of ZnO during the cell manufacturing. With this work, we establish that stability measurements of ZnO-containing OSCs should be handled carefully and must be performed exclusively with a UV-including illumination, since otherwise erroneous results will be obtained.

The third part (chapter 5) of this thesis finally elucidates the working principles in polymer:NFA:FA ternary organic solar cells. For this, a concise study is performed, systematically comparing ternary D:NFA:FA systems with different components and varying compositions. For all of the investigated systems, the open-circuit voltage is found to increase with increasing ratio of the fullerene, whereby the extent of this increase is directly correlated to the fullerene's LUMO position, indicating an electronic involvement in the charge transfer (CT) state formation. By using a combination of different analytics we are able to prove that

the investigated group of D:NFA:FA systems behaves according to an alloy model and that the charge transfer state indeed is delocalized over both acceptors. Furthermore, the investigation of the voltage losses in dependence of the composition reveals that the nonradiative recombination decreases with increasing fullerene fraction, however this beneficial effect is found to be almost completely cancelled by increasing radiative recombination. Notably, the recombination behavior is independent of the third component's nature and only seems to be related to the CT state energy, proving that the power gap law established for binary OSCs also applies for ternary systems. Based on the behavior of the internal quantum efficiency, we therefore propose that the positive effect of fullerenes as third components does not come from reduced nonradiative recombination but from a more efficient exciton splitting.

Table of Contents

Erklärung.....	I
Danksagung.....	III
Abstract	V
Table of Contents	IX
1 Introduction.....	1
1.1 Why Organic Solar Cells?.....	1
1.2 Basics of Organic Solar Cells.....	2
1.2.1 Organic Semiconductors	2
1.2.2 Working Principles of Organic Solar Cells.....	4
1.2.3 Absorber Materials in Organic Solar Cells	7
1.3 Ternary Organic Solar Cells.....	9
1.3.1 Introduction	9
1.3.2 Models for Ternary Organic Solar Cells	10
1.3.3 Advances in Understanding Ternary Mechanisms.....	23
1.3.4 Outlook.....	33
1.4 Stability of Organic Solar Cells	35
1.5 Zinc Oxide as Electron Transport Layer	36
1.6 References	38
2 Characterization Methods	55
2.1 Ultraviolet-Visible Spectroscopy	55
2.2 Photoluminescence Spectroscopy	56
2.3 Raman Spectroscopy	58
2.4 X-ray Diffraction.....	58
2.5 X-Ray Photoelectron Spectroscopy	61
2.6 Contact Angle Measurements	61

2.7	Atomic Force Microscopy	63
2.8	Current-Voltage Characterization and Light Intensity Dependence	64
2.9	External Quantum Efficiency Measurements	67
2.10	Fourier-Transform Photocurrent Spectroscopy	68
2.11	Electroluminescence Spectroscopy	70
2.12	References	72
3	Increasing Photostability of Inverted Nonfullerene Organic Solar Cells by Using Fullerene Derivative Additives	75
3.1	Abstract	76
3.2	Introduction	76
3.3	Results and Discussion.....	79
3.3.1	Performance of Ternary OSCs	79
3.3.2	UV Stability of Binary and Ternary Cells.....	81
3.3.3	Characterization of Fresh and Aged Devices	82
3.3.4	Origin of UV Aging and Explanation for the Protective Effect of the Fullerenes.....	87
3.3.5	Transferability of the Protective Effect.....	92
3.4	Conclusions	93
3.5	Experimental Section	94
3.6	Supporting Information	97
3.7	References	108
4	The Neglected Influence of Zinc Oxide Light-Soaking on Stability Measurements of Inverted Organic Solar Cells	115
4.1	Abstract	115
4.2	Introduction	116
4.3	Results and Discussion.....	118
4.4	Conclusions	128
4.5	Experimental Section	129
4.6	Supporting Information	132

4.7	References	136
5	Elucidating the Origin of Open-Circuit Voltage in Ternary Organic Solar Cells Comprising a Nonfullerene and a Fullerene Acceptor	139
5.1	Introduction	139
5.2	Results and Discussion	142
5.2.1	Properties of the Employed Materials	142
5.2.2	Photovoltaic Performance of the Ternary Devices	144
5.2.3	CT Energies and Loss Analysis	146
5.2.4	Internal Quantum Efficiency	149
5.2.5	Assignment to a Model	150
5.3	Conclusion and Outlook	154
5.4	Experimental Section	155
5.5	Supporting Information	157
5.6	References	165
6	Conclusions and Outlook	169
7	List of Abbreviations	173
8	Publications	175

1 Introduction

1.1 Why Organic Solar Cells?

Since the industrial revolution, humanity's energy demand has been steadily increasing, so far up to 165 billion megawatt hours in 2021.¹ A large part of this energy demand is supplied and used in the form of electric energy, which is usually generated by burning a primary energy source, such as coal or gas, and using the resulting thermal energy to drive a turbine and a generator that ultimately produces the electricity. Renewable energy sources such as wind or hydroelectric power plants also use a mechanical intermediate step to generate electricity with the help of a generator. Until today, solar cells, fuel cells, and thermoelectric materials are the only possibility for mankind to generate electricity directly from a primary energy source without further intermediate steps. In the case of solar cells, this conversion happens with a relatively moderate efficiency – in the ideal case a maximum of 33 % can be reached with single junction cell according to the Shockley-Queisser limit - but since sunlight as a primary energy source is virtually unlimited and available for free, solar cells are nevertheless an attractive option, both in terms of economic efficiency and environmental sustainability.

Table 1.1: Comparison of several figures of merit for different solar cell technologies based on silicon, perovskites, and organic materials.²⁻⁶

		Crystalline Si	Perovskite	Organic
	Record Efficiency	26.7 %	25.8 %	19.0 %
	Commercial Efficiency	~ 20 %	~ 15 %	~ 10 %
	Power per weight	0.043 kW/g	9 kW/g	10 kW/g
	CO₂ per power	50 g/kWh	~ 10 g/kWh	< 10 g/kWh

Among the commercially available solar cell technologies, inorganic silicon-based cells are by far the most widespread since they are able to deliver consistently high efficiencies over several decades at comparably low production costs. They are therefore unbeaten in classic, large-scale electricity production, for example on roofs or in solar parks, and currently no competitive solar

1 Introduction

cell technology exists in these areas of application. However, silicon-based solar cells also have drawbacks, as they are relatively heavy and energy-intensive to manufacture. These downsides play only a minor role for current applications but can limit the silicon-based technology for future fields of applications. Our energy infrastructure currently is undergoing a fundamental transformation, moving away from centralized power generation in fossil-fueled plants. Instead, the goal is a decentralized structure in which a large number of smaller, green power producers work together to meet our demands. In this future energy infrastructure, new types of solutions will be required, such as energy generation from solar cells attached to building facades. For this type of application, record efficiencies will no longer be the decisive factor, but cost-effective, sustainable production from abundant materials and, above all, a high power per weight ratio. In terms of those factors, the Si-based technology is far outperformed by novel solar cell technologies based on perovskites or organic materials (see **Table 1.1**). In fact, perovskite-based solar cells seemed to be the most promising option for many years now, with tremendous research efforts and impressive progress in efficiency and stability. However, so far most promising perovskite materials contain toxic water-soluble lead compounds, which complicates their commercial application worldwide and very likely precludes it in the European Union. For this reason, organic-based solar cell technologies are now receiving more and more attention and the combined research efforts have resulted in their efficiencies increasing drastically in recent years, reaching up to date a remarkable 19 %.⁴

1.2 Basics of Organic Solar Cells

1.2.1 Organic Semiconductors

Organic semiconductors are molecules based on conjugated, molecular bonds between organic atoms, mostly sp^2 hybridized carbon atoms but also contain heteroatoms such as sulfur, oxygen or nitrogen. Their semiconducting properties arise from the π -electrons, which can move freely through the C atom network and can be excited to higher states with relatively small energies – i.e. photons in the visible range – due to the delocalization. The state from which the electrons are excited is called highest occupied molecular orbital (HOMO), while the state to which the electrons can be excited is named lowest unoccupied molecular orbital (LUMO). When not a single molecule but several electronically interacting molecules are considered, a splitting of the excited state occurs (Davydov splitting), similarly to inorganic semiconductors, resulting in a band-like character of the excited state in a bulk organic semiconductor.⁷

Upon excitation of an organic semiconductor by photons, an electron-hole pair is generated. Due to the low permittivity of organic materials, the Coulomb forces between electron and hole

are only weakly screened, resulting in a high binding energy of 0.1 eV – 1 eV. Such strongly bound electron-hole pairs are called Frenkel excitons. Since the thermal energy at room temperature (≈ 0.025 eV) is not sufficient to overcome the binding energy, the exciton cannot split into free charges spontaneously. Instead, it can diffuse through the semiconductor and move from one molecule to the other either by non-radiative energy transfer via the exchange of a virtual photon or by radiative energy transfer, where the exciton recombines, and the generated photon is absorbed by the next molecule. Since excitons in organic semiconductors normally have a short lifetime, the diffusion length is limited to about 5-20 nm depending on the energetic disorder of the respective material.⁸

In the case that the exciton binding energy can be overcome, and free charge carriers are generated, they move on by a so-called hopping mechanism. In contrast to inorganic semiconductors, which are often highly ordered and in which charges travel in bands as highly delocalized waves, organic semiconductors are usually strongly disordered, resulting in many scattering events and a stronger localization of the charge carriers. They therefore move by ‘hopping’ from one localized energetic state to the next one, resulting in charge carrier mobilities on the order of around 10^{-4} cm²/Vs. For a simplified description of the hopping charge transport, often a Gaussian disorder model is used (Miller-Abrahams hopping). In this model, the distribution of energetic states $\rho(E)$ in dependence of their energy E of a disordered system is approximated with a Gaussian distribution:⁹

$$\rho(E) = 1/\sqrt{2\pi\sigma^2} \exp\left(-\frac{E^2}{2\sigma^2}\right) \quad (1.1)$$

where the standard deviation σ is a measure for the energetic disorder of the system. As shown in **Figure 1.1**, the free charge carriers move in this distribution by hopping to states with lower energy (or slightly higher energy driven by the thermal energy). Due to the energetic loss during this hopping process, the average transport energy of free charge carriers occurs at an energy fraction of $\sigma/k_B T$ lower than the center of the density of states (DOS). The thermally relaxed charge carriers then are collected by the respective electrode.

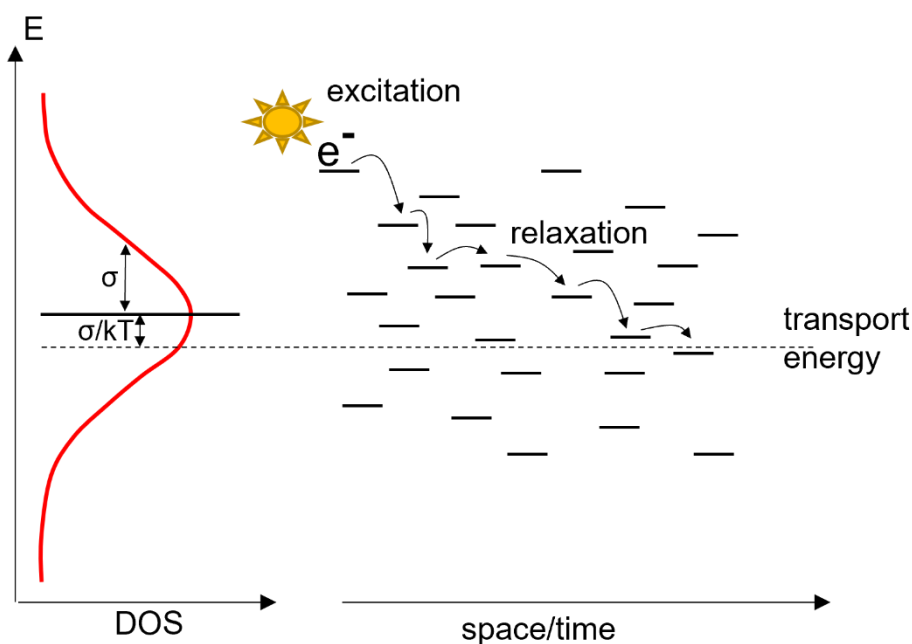


Figure 1.1: Schematic depiction of the hopping process in a disordered system with a gaussian density of states distribution, where the standard deviation σ is a measure for the disorder. After excitation, charges are thermally relaxing to the transport energy during hopping from one localized state to the other.⁸

1.2.2 Working Principles of Organic Solar Cells

The history of organic photovoltaics (OPV) began in 1986, with the work of Tang et al. who developed a bilayer organic solar cell consisting of copper phthalocyanine and a perylene tetracarboxylic derivative.¹⁰ These two compounds acted as electron rich (donor) and electron poor (acceptor) materials, respectively, thus mimicking the p-n junction of silicon solar cells. However, while silicon-based solar cells already exceeded 20 % efficiency at that time, the organic counterpart did not even quite reach 1 % efficiency.

The main problem was – and still is – related to an intrinsic material property of organic compounds: The low permittivity of $\epsilon \approx 2-5$ compared to silicon with $\epsilon \approx 12$ and the consequently high exciton binding energy.¹¹ In silicon-based solar cells the thermal energy at room temperature is already sufficient for the splitting of an electron-hole pair and the p-n junction is only necessary to provide a directed charge transport. However, in organic materials, to overcome the exciton binding energy and create free charge carriers, several steps are necessary (**Figure 1.2**): first, the exciton created in the donor-type material diffuses to an interface with the acceptor-type material. Since the donor-type material has a higher LUMO than the acceptor-type material, the exciton is provided with a driving force for building a charge transfer (CT) state, where the electron is transferred to the acceptor material while the hole stays at the donor material. This newly formed CT state still is coulombically bound, but

since the spatial separation between hole and electron is increased, the Coulomb forces and the CT state binding energy are reduced compared to the exciton binding energy. In the next step, the CT state binding energy has to be overcome to form the charge separated (CS) state.¹² Up to now, it has not been fully understood, how exactly the step from CT state to CS state takes place and how the necessary energy is provided. Possible explanations assume either that the Coulombic bonding of the CT state can be overcome by other energy gains, for example by entropic effects¹³ or local electric fields.¹⁴ Or so-called ‘hot’ CT states are assumed,¹⁵ where excess kinetic energy from the excitation can be used for the charge separation. Both explanation approaches are frequently found in the literature, but are just as often criticized and refuted, so that until today no unified explanation exists.

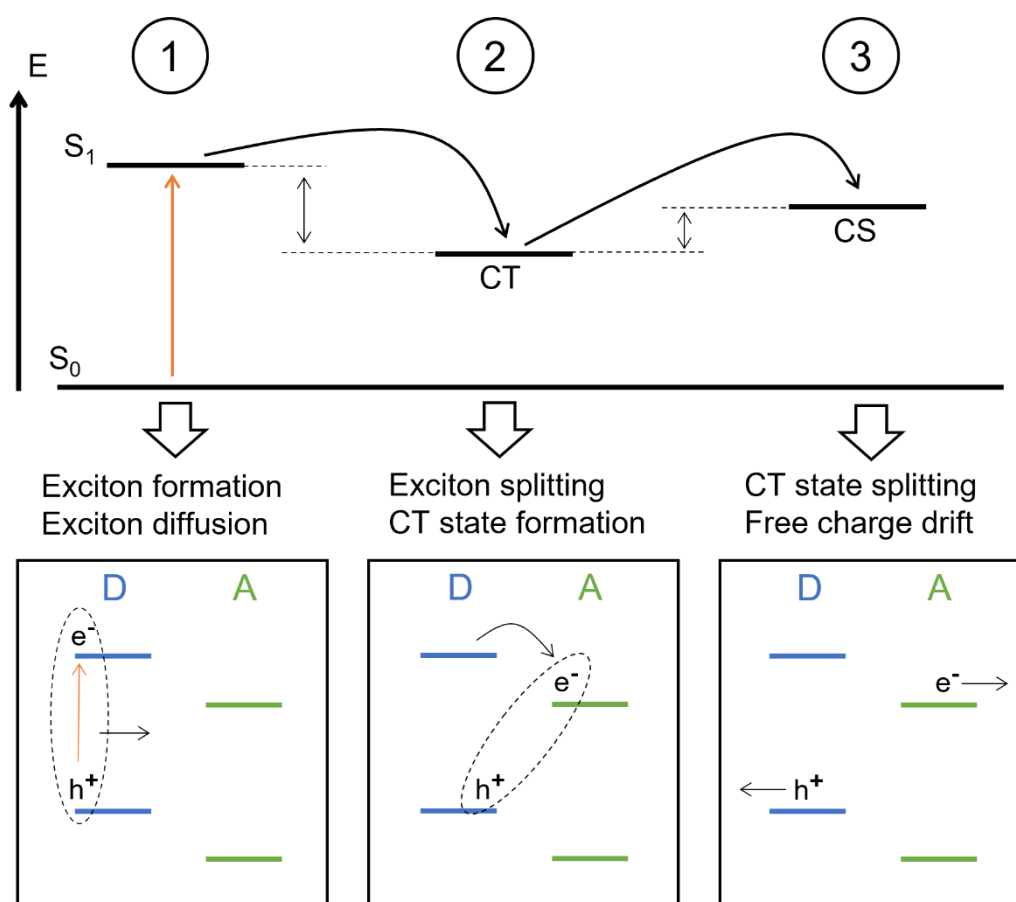


Figure 1.2: Simplified energetic picture of the charge generation process in an organic heterojunction, where the Jablonski-type diagram of the energetic states is shown in the upper part and the energy levels of donor and acceptor are shown in the bottom part. 1) When a donor molecule is excited from its ground state S_0 to the excited state S_1 , an exciton is formed, which then diffuses through the bulk until it reaches an acceptor molecule (or an acceptor domain). 2) Driven by the LUMO offset, the electron transfers to the acceptor molecule (or domain), forming a charge transfer state. 3) When the energy is provided to overcome its Coulomb binding energy, the CT state is split and the free charge carriers drift towards their respective electrodes.

1 Introduction

However, it is clear that it is critical for the efficiency of an organic solar cell that an exciton can diffuse rapidly to a donor-acceptor interface and form a CT state before geminately recombining again. It is therefore advantageous to have a large interface between the two materials so that diffusion paths are as short as possible. A decisive breakthrough for organic solar cells was therefore the introduction of the so-called bulk heterojunction (BHJ) by Heeger et al. in 1995.¹⁶ In a BHJ – in contrast to a bilayer architecture – donor and acceptor molecules are intimately mixed in one single layer, simultaneously providing a large interface and forming charge percolating pathways of each material. To date BHJ absorbing layers are state of the art for organic solar cells.

In BHJ organic solar cells, additional layers are necessary for a working cell, since the BHJ does not ensure a directional charge transport – unlike in silicon-based solar cells, where the p-n junction serves this purpose. For this reason, the active layer is sandwiched between a hole transport layer (HTL) and an electron transport layer (ETL) which at the same time serve as electron and hole blocking layers, respectively. Organic solar cells are processed on top of a transparent substrate, through which the cell is illuminated. Since the substrate also serves as an electrode, it is usually made of transparent, conductive metal oxides, such as indium doped tin oxide (ITO) or fluorine doped tin oxide (FTO). Thereby, two different architectures are possible: the transparent electrode can either serve as an anode and then has to be paired with a low work function top electrode (e.g. aluminum) as cathode, which for historical reason is called the ‘normal’ architecture. Or the transparent electrode serves as a cathode and is paired with a high work function top electrode (e.g. silver or gold) as anode, which correspondingly is called the inverted architecture.

With both architectures, the organic solar cell basically corresponds to a diode and its current density-voltage (J - V) characteristic is often described with an extended Shockley equation:⁸

$$J(V) = J_0 \left(\exp \left(\frac{q(V - JR_S)}{nk_B T} \right) - 1 \right) - \frac{V - JR_S}{R_P} - J_{Ph} \quad (1.2)$$

with the saturation current density J_0 , the photocurrent J_{Ph} , the diode ideality factor n , the Boltzmann constant k_B and the temperature T . In comparison to the basic Shockley equation, a series resistance R_S and a parallel resistance R_P are added to account for the behavior of a real solar cell with sheet resistances, injection barriers and local shunts. This equation, however, initially was developed for inorganic solar cells and consequently is not capable of completely describing organic solar cells, which, for example, have a stronger field-dependent photocurrent than their inorganic counterpart due to the charge generation via coulombically bound CT states.

1.2.3 Absorber Materials in Organic Solar Cells

As described above, the absorbing layer of OSCs must basically consist of two components, one having higher lying energy levels and acting as an electron donor, and one having lower energy levels and acting as an electron acceptor.

Acceptor materials can be divided into two large groups: the fullerene acceptors (FAs) and the nonfullerene acceptors (NFAs). FAs are derivatives or relatives of the C_{60} molecule and while they have very good electron accepting and transport properties, their absorption is usually low and in the near ultraviolet region, which is why their most popular representatives PC₆₁BM and PC₇₁BM (see **Figure 1.3**) in combination with various donor molecules were only able to reach maximum power conversion efficiencies (PCEs) of 11-12 %.

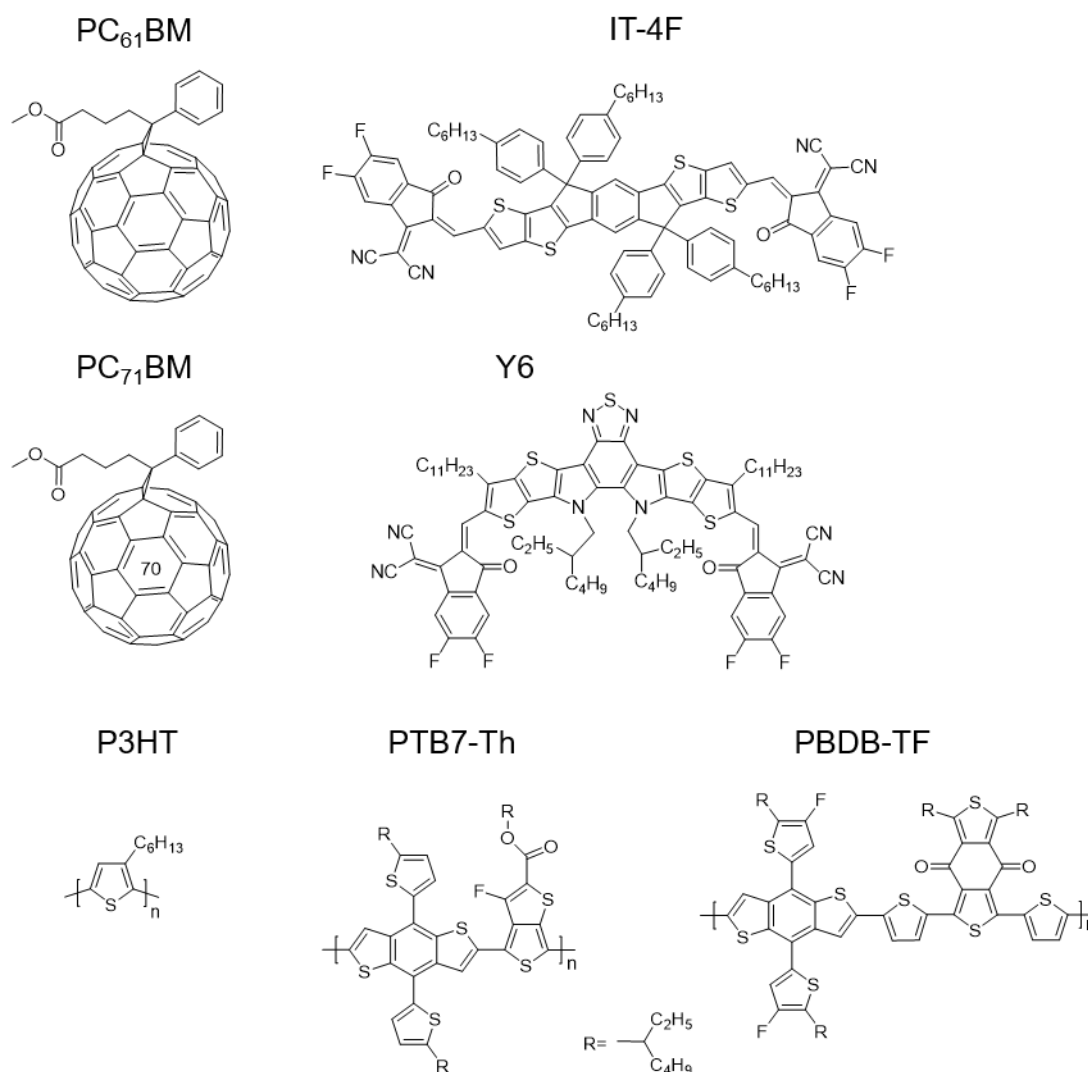


Figure 1.3: Chemical structures of exemplary acceptor and donor molecules.

NFAs, on the other hand, with their larger synthetic variability can reach higher absorption coefficients and their energy levels can be easily tuned to match a suitable donor molecule. In

1 Introduction

the group of NFAs, countless different molecules exist with a wide variety of structures, but the ones that are most frequently used and achieve the highest efficiencies are the ADA-type and A-DAD-A-type fused-ring electron acceptors. They are designed to have a strong intramolecular electron push-pull effect, which leads to a narrow band gap and thus a complementary absorption in combination with most high-performance donor molecules, which mostly have a larger band gap. Furthermore, they can be easily equipped with large alkyl side chains, which make the molecules more soluble and additionally prevents aggregation in the BHJ. Examples for this type of acceptor are the ITIC-family (ADA-type), molecules based on a core unit of indacenodithieno[3,2-b]thiophene with 1,1-dicyanomethylene-3-indanone (IC) end units, and the so-called Y-series (A-DAD-A-type), which possess a thienothienopyrrolo-thienothienoindole core with IC end units. The most frequently used representative of those two families – IT-4F and Y6 – are shown in **Figure 1.3**.¹²

Donor materials are usually polymers and are divided according to the size of their band gap into wide band gap donors ($E_g > 1.8$ eV), medium band gap donors (1.6 eV $< E_g < 1.8$ eV), and small band gap donors ($E_g < 1.6$ eV), since their band gap and the location of their frontier molecular orbitals decide with which type of acceptor they should be paired. Large band gap donors, such as the probably most famous poly(3-hexylthiophene-2,5-diyl) (P3HT, see **Figure 1.3**), were previously paired with the even larger band gap fullerenes, which resulted in the first successful OSCs, however, with only moderate absorption and currents. The development of polymers with smaller band gaps, such as the PTB-family which is based on thieno[3,4-b]thiophene and benzodithiophene units, increased the reachable photocurrents. With the advent of small-band gap NFAs, donors with large band gaps again were employed successfully, and newly developed polymers from the PBDB-family made today's record efficiencies possible. As representatives of the PTB-family and the PBDB-family, PTB7-Th and PBDB-TF are shown in **Figure 1.3**.¹⁷

1.3 Ternary Organic Solar Cells

This chapter is based on the following publication:

Marcella Günther, Negar Kazerouni, Dominic Blätte, Jose Dario Perea, Barry C. Thompson, Tayebbeh Ameri. Models and Mechanisms of Ternary Organic Solar Cells.

Manuscript under Revision

1.3.1 Introduction

Research on organic solar cells has been ongoing for more than 40 years now, but mainly due to the advances made in the last decade, they have evolved from being a niche topic to a promising commercial option, with power conversion efficiencies (PCE) that will exceed 20 % in the near future¹⁸⁻²⁰.

The fundamental principle of organic solar cells is based on the combination of two organic materials, one being an electron donor (D) and one being an electron acceptor (A), which allows the separation of the strongly bound Frenkel excitons via the transfer of an electron or hole to the other material and the formation of charge transfer (CT) states^{21,22}. Since the efficiency of this separation process correlates with the interface area present between the two materials, bulk heterojunction (BHJ) architectures are usually applied, where the intermixed materials allow for a larger interface area, while simultaneously providing transport pathways for the separated charges^{16,23}. With novel absorber molecules and ever improving architectures and processing methods, the efficiencies of such binary OSCs were progressively enhanced, however, this development is limited by the close correlation between voltage and current generation^{24,25}. By decreasing the energy differences between the highest occupied molecular orbital (HOMO) and lowest unoccupied molecular orbital (LUMO) of the absorbing materials, the absorption range can be broadened towards longer wavelengths and thereby more current will be generated, resulting in a higher short-circuit current density (J_{SC}). Nonetheless, the generated open-circuit voltage (V_{OC}), which is proportional to the energetic difference between the donor HOMO and the acceptor LUMO, would thereby decrease and thus offset this efficiency gain.

This constraint can be circumvented by a simple approach: the addition of a third component to the BHJ, which can either function as a second donor or as a second acceptor, resulting in a ternary organic solar cell (TOSC)²⁶. It has now been demonstrated numerous times that in TOSCs J_{SC} and V_{OC} can be improved simultaneously, in addition to many other positive effects,

1 Introduction

such as reduced energy losses, facilitated charge transport, and even significantly improved stability²⁷⁻³¹. The underlying complex working mechanisms of TOSCs are still not conclusively understood and different models are used to describe them. The most prominent models are the so-called cascade model, alloy model, and parallel-like model, which all provide a basic mechanism and establish a relationship between the ternary composition and the resulting V_{OC} . Many reviews have been devoted to the description of these models and their supporting experimental evidence²⁷⁻²⁹, however, there is still significant confusion as all models have theoretical gaps and often contradict each other. In addition, the development of all existing models now dates back several years, meaning that the state of knowledge at that time now is far outdated and the understanding of mechanisms in OSCs has fundamentally changed. Nevertheless, those models are still used unchanged and even completely new systems are assigned to them without challenging old concepts.

For this reason, this review will provide a critical analysis of all currently existing models for describing the mechanisms of operation in TOSCs. Five different concepts are identified and separately presented, with a particular focus on inconsistencies and gaps in scope, thereby emphasizing still open questions for ongoing research. The performance parameters for selected examples of each concept are shown in **Table 1.2**. Next, the new findings on general mechanisms in OSCs since the development of the conventional models are briefly summarized and recent results on TOSCs are discussed, divided by findings on CT states, recombination behavior, morphology, and the interplay of electronics and morphology. Finally, the models are discussed in the light of recent results, contradictions and shortcomings are highlighted and open questions are addressed, with the aim of setting the course for future research.

1.3.2 Models for Ternary Organic Solar Cells

The cascade model. The crucial aspect of the cascade model is that the third component in the ternary blend exclusively works as an absorption sensitizer by transferring charges or energy without participating in charge percolation, while the other two components (donor and acceptor) carry out the hole and the electron transport to the electrodes. This concept can be implemented under different energetic and morphological conditions. The most frequently described scenario is that the sensitizer introduces intermediate HOMO and LUMO levels resulting in an energy cascade through all three components (**Figure 1.4a**). In this case, the sensitizer molecules must be located at the interface of donor and acceptor domains to ensure trap-free charge transport (**Figure 1.4b**). Another possibility involves energy transfer from the sensitizer to the donor or to the acceptor. In this case, the sensitizer can also be embedded in

the donor (or acceptor) domains and its LUMO (or HOMO) does not necessarily have to be cascade aligned but also can be higher than the donor LUMO (or lower than the acceptor HOMO). The physically measurable consequence of the cascade model is that the V_{OC} should theoretically be a constant value, determined by the energetic difference of the hole and electron quasi-Fermi levels of donor and acceptor, and independent of the composition of the ternary blend (**Figure 1.4c**). At the same time, the additional absorption of the third component should translate into a correspondingly increased J_{SC} .

The idea of a cascade charge transfer mechanism was introduced in 2010 with the addition of a small-band gap polymer with intermediate HOMO and LUMO as sensitizer to a binary host system to broaden the absorption³². With photo-induced absorption it was proven that the sensitizer transfers a positive polaron to the host donor and an electron to the host acceptor, which carry out the charge transport. Analogous to these findings, the validity of the cascade model has been confirmed repeatedly by various groups^{33–38}.

It soon was realized that the third component – although having an appropriate energy level alignment for cascade charge transfer – instead can also be involved in energy transfer and that those two processes often compete in cascade-like systems^{39–42}. A summary of the details of energy transfer in TOSCs can be found elsewhere⁴³.

Ternary systems following the cascade model were demonstrated to be superior to their binary counterpart for several reasons. First, the sensitization with a third component, having either a smaller band gap^{34,44,45} or a larger band gap⁴⁶ than the binary host system, broadens the absorption range and improves light harvesting. Second, it has been found that the addition of a cascade sensitizer can improve the PCE even without broadening the absorption substantially by suppressing monomolecular and bimolecular recombination and increasing charge carrier mobility^{33,47–51}. The strategy of absorption extension has been used successfully, especially for fullerene-containing systems; however, with respect to the new class of non-fullerene acceptors (NFAs) with excellent absorption capability, it is questionable whether this approach still adds value. In fact, theoretical calculations have shown that for state-of-the-art absorbers, a ternary approach is only beneficial if it positively influences transport or recombination kinetics, thus increasing the fill factor⁵².

With respect to the exact mechanism in ternary cascade systems, the question arises between which components the charge transfers take place and which CT states are therefore occupied. Theoretically, three CT states are accessible, each corresponding to the charge transfer between two of the three components (**Figure 1.4d**). However, in a typical combination of two donors with one acceptor (or two acceptors with one donor), the CT state between the two donors (or

1 Introduction

the two acceptors) is energetically unfavorable and therefore usually only weakly occupied. In the meantime, though, it has been shown that under specific energetic and structural conditions this charge transfer may also take place and that therefore all three CT states may be occupied^{47,53}.

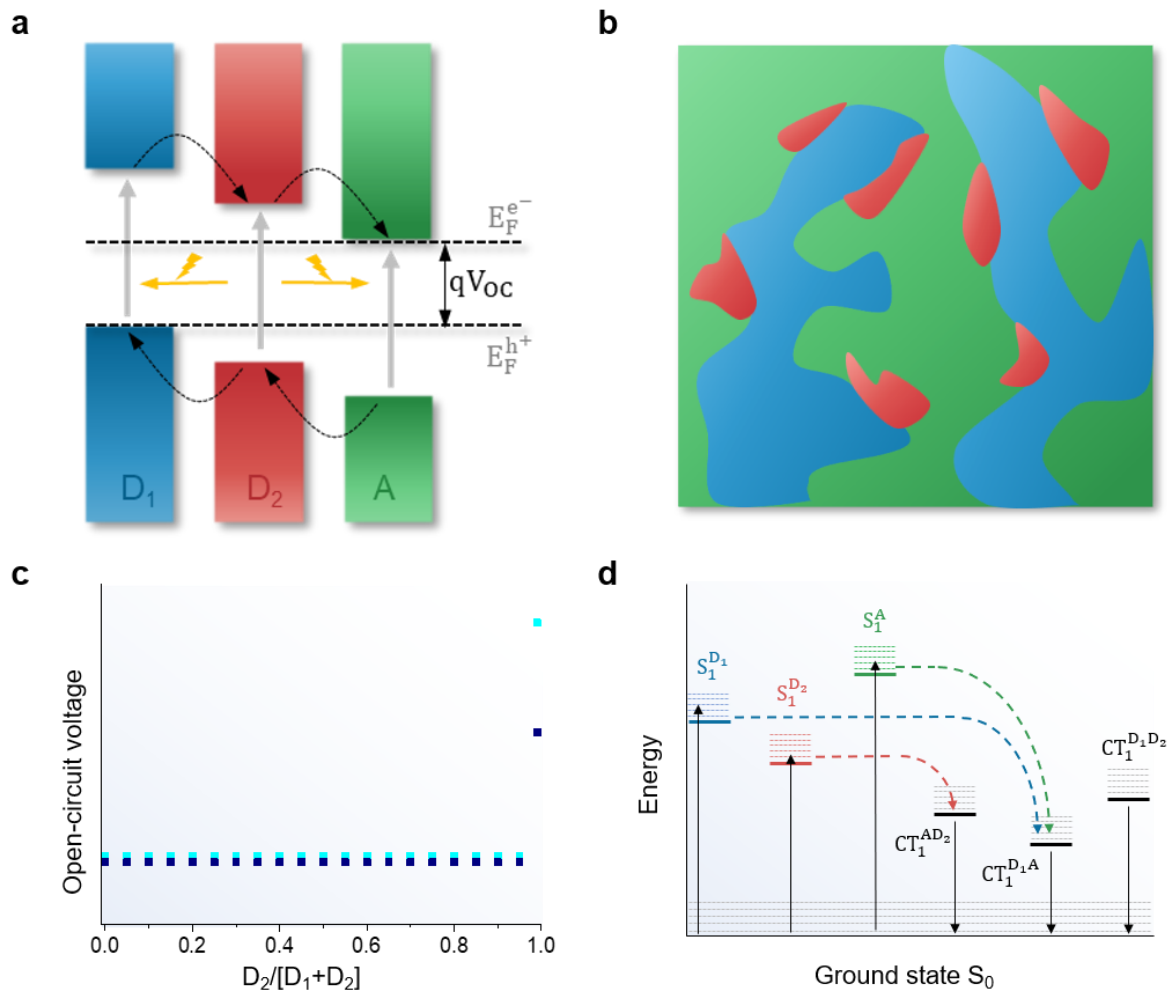


Figure 1.4: Energetic and morphological picture in the cascade model. a) Typical energy level alignment for a cascade-like ternary organic solar cell (TOSC), where the energy levels of the third component (D_2 , red) are located in between those of the donor (D_1 , blue) and the acceptor (A, green). Possible charge and energy transfers are displayed with black and yellow arrows, respectively. The quasi-Fermi levels for electrons and holes are indicated with black dotted lines, with the difference being the elementary charge q times the open-circuit voltage (V_{OC}). b) Corresponding morphology with the third component being located at the interface of donor and acceptor. c) Expected V_{OC} trend of a cascade-like ternary cell in dependence of the ratio of the two donors D_1 and D_2 , for the two donors having a large (light blue) or a small (dark blue) HOMO offset. d) Jablonski-type diagram for a cascade TOSC where for simplification one common ground state S_0 is assumed. From the excited states S_1 of all three components energetically different CT states (CT_1) are accessible, with the one between the two donors being the energetically least favorable.

In principle, the concept of cascade charge and energy transfer is a coherent and frequently used model to describe the operating principle of TOSCs, but there are limitations. The model

definition requires a very specific morphology, with the sensitizer being located at the donor:acceptor interface or being embedded in one host component, which is actually only achievable for low sensitizer ratios and very specific conditions of molecular miscibility. At the same time, however, the pinned V_{OC} for different sensitizer ratios is the simplest metric for assigning systems to the model. In fact, a pinned V_{OC} over the whole composition range is rather exceptional^{33,54,55} in literature, even for systems that are analytically shown to belong to the cascade model. Instead, a certain tunability of the V_{OC} with the sensitizer ratio is often observed^{34,40,44,46,48,56,57}. This can be partly attributed to the fact that the additional absorption of the sensitizer increases the photogenerated current of the cell, which in turn affects the V_{OC} . But just as importantly, the increasing sensitizer content prevents the required morphology and the cascade model therefore no longer applies⁵⁸⁻⁶¹. Notably, a recent work, which examines the cascade model with a more profound theoretical basis and uses kinetic Monte Carlo simulations for this purpose, has also shown that a tunable V_{OC} can indeed occur even with the cascade model, which is attributed to the stronger spatial separation of charge carriers in three different components and the consequently reduced CT recombination losses⁶².

In practice, however, the assignment to the cascade model is often based solely on the matching cascade-like energy level alignment of all three components^{55,56,63}. However, this should be avoided, since the accuracy of experimental HOMO and LUMO values is often debatable, due to their common determination by cyclic voltammetry (CV) in solution, which does not necessarily depict the energetic situation in a solid-state device⁶⁴.

The alloy model. In contrast to the more conceptually straightforward cascade processes, in which the V_{OC} would by necessity be pinned to the smallest HOMO_D-LUMO_A offset, the alloy model offers a framework to understand systems with a composition-dependent V_{OC} which has enabled organic solar cells approaching 19% efficiency.⁶⁵ The first important breakthrough was achieved, when a system consisting of a polymer donor and two fullerene acceptors was reported, whose V_{OC} could be tuned with the ratio of the two acceptors⁶⁶. To explain this unexpected tunability, the alloy model was introduced in 2013⁶⁷. The model proposes an intimate mixture of the synergistic components (either two donors or two acceptors) in which HOMO, LUMO and CT state energies take on values that are a weighted average of the synergistic components. Analogous to inorganic semiconductor alloys, where conduction and valence band energies vary with composition, the term organic alloy refers to the intimate blend of synergistic components, either two donors D₁ and D₂ or two acceptors A₁ and A₂, which possesses composition-dependent properties (**Figure 1.5a, b**). It is observed that the excitonic

1 Introduction

character (i.e. absorption spectra) of the synergistic components are distinctly preserved, likely due to the more localized nature of the exciton as compared to the CT state, allowing photons to be harvested across the full absorption range (enhancing J_{SC}), while the V_{OC} is a weighted average that usually is described as having a near-linear composition-dependence (**Figure 1.5c**)⁶⁸.

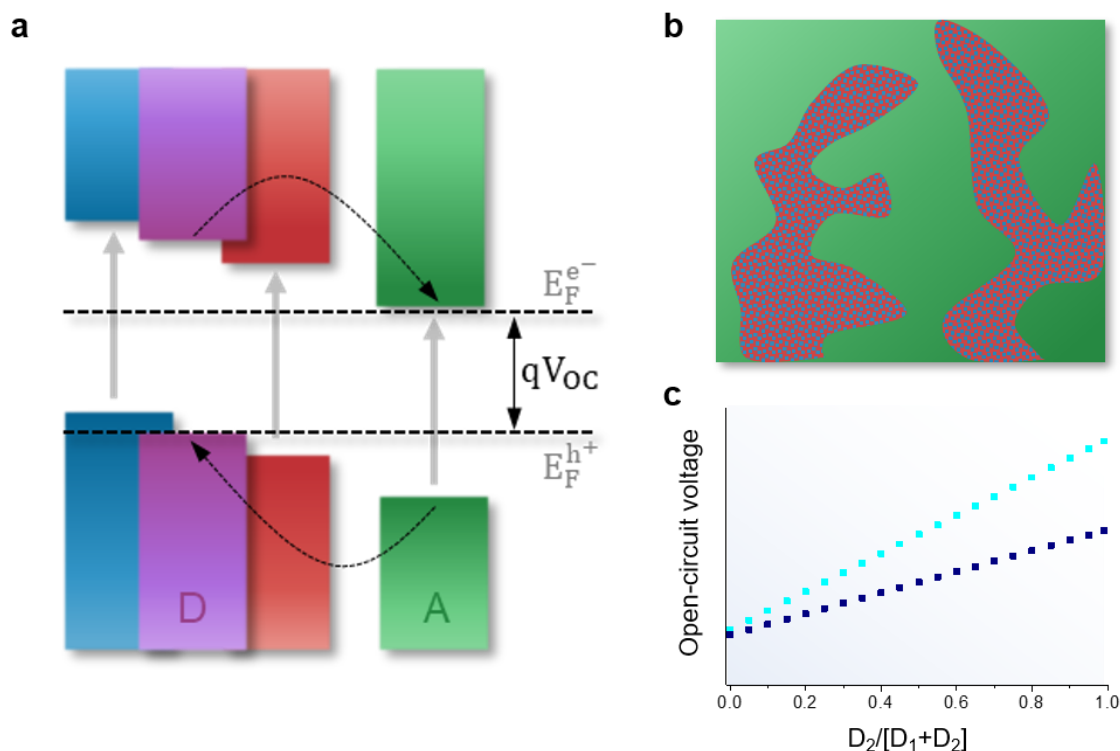


Figure 1.5: Electronic and morphological picture in the alloy model. a) Energy levels of a ternary system following the alloy model with the two donors forming an electronic alloy, thus resulting in a pseudo-binary cell consisting of a donor alloy (purple, with the pristine donors in blue and red) and the acceptor (green). Possible charge transfer pathways are indicated with black arrows. The difference of electron and hole quasi-Fermi levels (dotted black lines) corresponds to the elementary charge q times the open-circuit voltage (V_{OC}). b) Corresponding morphology of an alloy-like ternary blend, where the two donors are intimately mixed. c) The expected V_{OC} trend of an alloy-like system as a function of the two donors' ratio for a large (light blue) and a small (dark blue) HOMO offset of the two donors.

Significant evidence for the alloy model has been obtained through structural and electronic characterization. For example, utilizing solid-state nuclear magnetic resonance, it was found that blended fullerenes do form a solid solution (alloy)⁶⁹. However, most evidence in support of the alloy model has been collected using systems based on synergistic polymer donors or systems based on two non-fullerene acceptors. For example, it was demonstrated with two random analogs of poly(3-hexylthiophen-2,5-diyl) (P3HT), which showed compositional-dependence of the V_{OC} that the CT state energy also changes accordingly with the

composition^{67,70}. Based on the tuning of the V_{OC} and the CT state energy, it was proposed that there is a regular variation of the donor HOMO in the blend of the two polymers, and indeed it was found that the ionization potential (IP) changed linearly with composition⁷¹. Such composition dependence has been investigated via inverse photoemission spectroscopy (IPES) and ultraviolet photoelectron spectroscopy (UPS)⁷² where the measured ionization potential (IP) or electron affinity (EA) is correlated with the HOMO and LUMO energies⁷³. However, electrochemical measurements have also proven effective to observe the same composition trends and are far more accessible. Specifically, CV measurements on blend films of two synergistic NFAs showed a trend in both HOMO and LUMO energies with changing composition⁷⁴. For both D:A₁:A₂ and D₁:D₂:A systems, photocurrent spectral response (PSR)⁷⁵ enabled measurements of the CT state⁷⁶. PSR data clearly demonstrated that the CT state energy shifts continuously with composition, supporting the hypothesis that the LUMO of acceptor alloys and the HOMO of donor alloys varies with composition^{67,68}.

Ultimately, many groups have observed evidence of co-crystallization of synergistic components in ternary blend films through grazing incidence X-ray diffraction (GIXRD), resonant soft X-ray scattering (RSoXS), and differential scanning calorimetry (DSC) that show the hallmarks of alloy formation^{71,77-79}. However, while miscibility of synergistic components is necessary for alloy formation, reports suggest that co-crystallization is not^{71,80}.

While all ternary blends do not follow the alloy model, it is clear that there is a subset of TOSCs for which the alloy model provides the most accurate description of the morphology and the electronic properties. However, a detailed theoretical description is still lacking, especially investigation of the nature of newly formed delocalized CT states and free charge carriers. While there is evidence that new CT states have formed^{67,68}, others claim that they are mere superpositions^{81,82}. Furthermore, a detailed description of how HOMO/LUMO tuning occurs while optical properties of the components are invariant is missing.

The parallel-like model. The parallel-like model is based on the assumption that the ternary cell consists of two distinct binary sub-cells (D₁:A and D₂:A for a donor third component; D:A₁ and D:A₂ for an acceptor third component), which work independently and are not connected electronically (**Figure 1.6a**). The three components form three independent channels for charge transport and are morphologically separated (**Figure 1.6b**). The exciton splitting can happen at two different interfaces, resulting in two possible CT states, and in the idealized case no energy or charge transfer occurs between the two donors or two acceptors. The V_{OC} in the parallel-like

1 Introduction

model is the weighted average of the two sub-cells (**Figure 1.6c**), while the J_{SC} corresponds to the sum of the two sub-cells.

The concept of a parallel-like BHJ was introduced independently by two different groups in 2011 and 2012, when they observed that the photocurrent generation, V_{OC} , and external quantum efficiency (EQE) spectra of different ternary blends perfectly match a weighted average of the two corresponding binary blends, suggesting that the ternary blend actually was composed of two binary sub-cells^{83,84}. Those two sub-cells were assumed to be completely separated morphologically and therefore to not interact electronically.

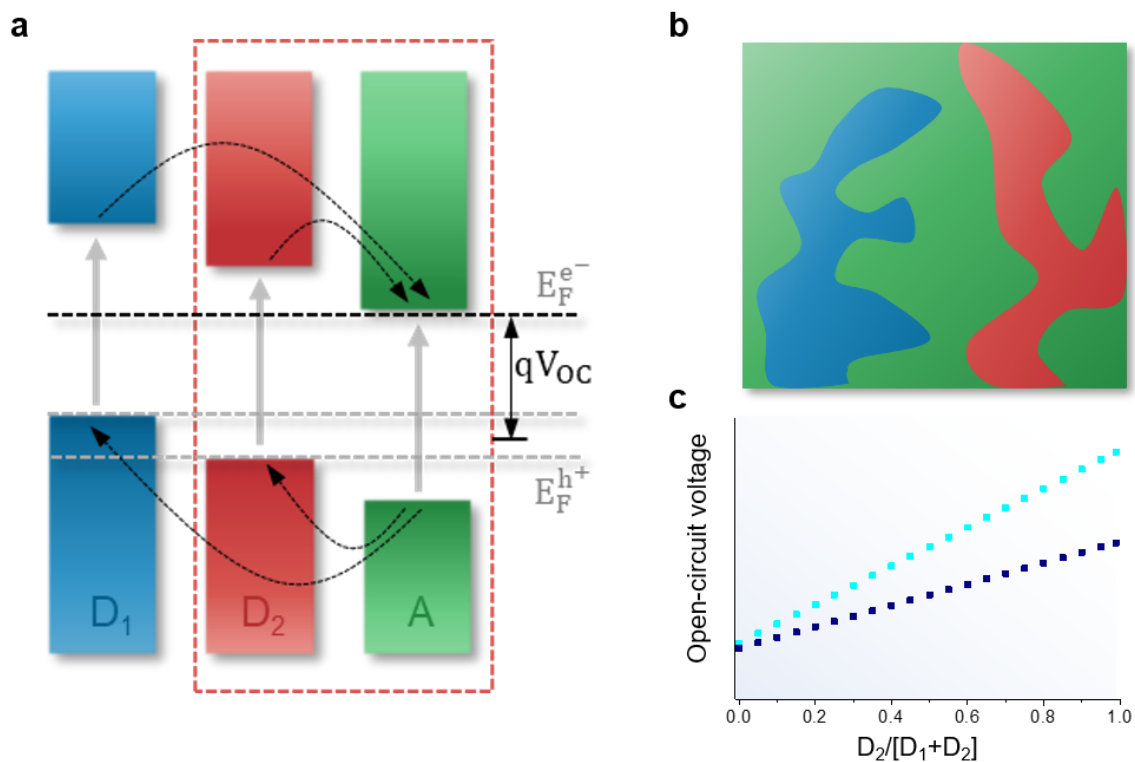


Figure 1.6: Electronic and morphological picture in the parallel-like model. a) Energy levels of a ternary system following the parallel-like model, where the donors (D_1 blue and D_2 red) each build a separate sub-cell with the acceptor (green), allowing no charge transfer between the two donors. The possible charge transfer pathways are indicated by black arrows. The two sub-cells result in one electron quasi-Fermi level (black dotted line) and two different hole quasi-Fermi levels (grey dotted lines). The elementary charge q times the open-circuit voltage (V_{OC}) corresponds to the difference of the electron quasi-Fermi level and the average of the hole quasi-Fermi levels. b) Related morphology of a parallel-like blend, with all three components forming separate domains. c) Expected V_{OC} trend of a parallel-like ternary cell as a function of the two donors' ratio for a large (light blue) and a small (dark blue) HOMO offset of the two donors.

While in the beginning the V_{OC} was predicted to be a mass weighted average of the two binary sub-cells, this idea was theoretically expanded in 2015 by considering the different absorption capability of the blend components, which results in differently occupied density of states

(DOS)⁸⁵. Additionally, the simplified idea of a complete electronic separation of the two sub-cells was waived. Instead, it was assumed that the DOS of the two donors (or two acceptors), indeed, equilibrate, but that this process is hindered and slowed down by the spatial separation. Consequently, the V_{OC} is not exclusively determined by the lower lying HOMO, as assumed for the cascade model, but if the equilibration of the two DOS is slower than the timescale of charge collection, the higher HOMO can also significantly contribute to the V_{OC} . In the ideal case of a parallel BHJ, where the equilibration is always slower, the V_{OC} of the ternary blend then is the average of the binary sub-cells, weighted by their current contribution.

Several other groups so far have attributed their TOSCs to the parallel-like model^{86–93}, supporting the operation mechanism with investigations of morphology and electronic behavior. However, reports about TOSCs following a parallel-like model are still scarce and therefore the generality and validity of the model is difficult to judge. A general criticism concerns the underlying physics of the model. When considering the equivalent circuit of a parallel-like system with two photodiodes being connected in parallel, it becomes evident that at a bias higher than the V_{OC} of the low- V_{OC} sub-cell, it is in fact biased in its forward direction and thus shorts the system. Even with the argument that such an equivalent circuit does not correspond to the microscopic reality of the parallel-like cell, the existence of two different quasi-Fermi levels in one blend is questionable since they should equalize immediately by the contact to the same metal electrode⁵².

Other approaches. In addition to the three popular models described above, two other approaches exist to explain the mechanisms in TOSCs which will be referred to as ‘state-filling model’ and ‘quadrupole concept’ below.

The state-filling model is based on the previously introduced concept of describing the electronic states of donor and acceptor molecules via a disorder broadened gaussian DOS where HOMO and LUMO are defined as the central energies of those distributions⁹. It should be noted that the energy levels defined in this way do not necessarily correspond to the valence and conduction band onsets that can be detected by measurement methods⁹⁴. The state-filling model⁵² was introduced in 2016 and transfers this concept to TOSCs by using one joint DOS for the two donors or two acceptors, respectively, which corresponds to a mass weighted average of the single components’ DOS (**Figure 1.7a, b**). This effective DOS then is filled according to a Fermi-Dirac distribution, resulting in a density of occupied states (DOOS) and a corresponding quasi-Fermi level for holes or electrons. The V_{OC} of the ternary blend results from the difference of the hole and electron quasi-Fermi level.

1 Introduction

As a consequence of this model, a composition-tunable V_{OC} is obtained, with a curvature that depends on the difference of the two donor HOMOs or the difference of the two acceptor LUMOs, respectively (**Figure 1.7c**). A small difference in energy levels results in a near-linear tunability, since both DOS contribute to the density of occupied states. On the other hand, a larger difference results in a more exponential curvature, since the lower lying HOMO (or the higher lying LUMO, respectively) only contributes significantly to the DOOS for a higher weight ratio.

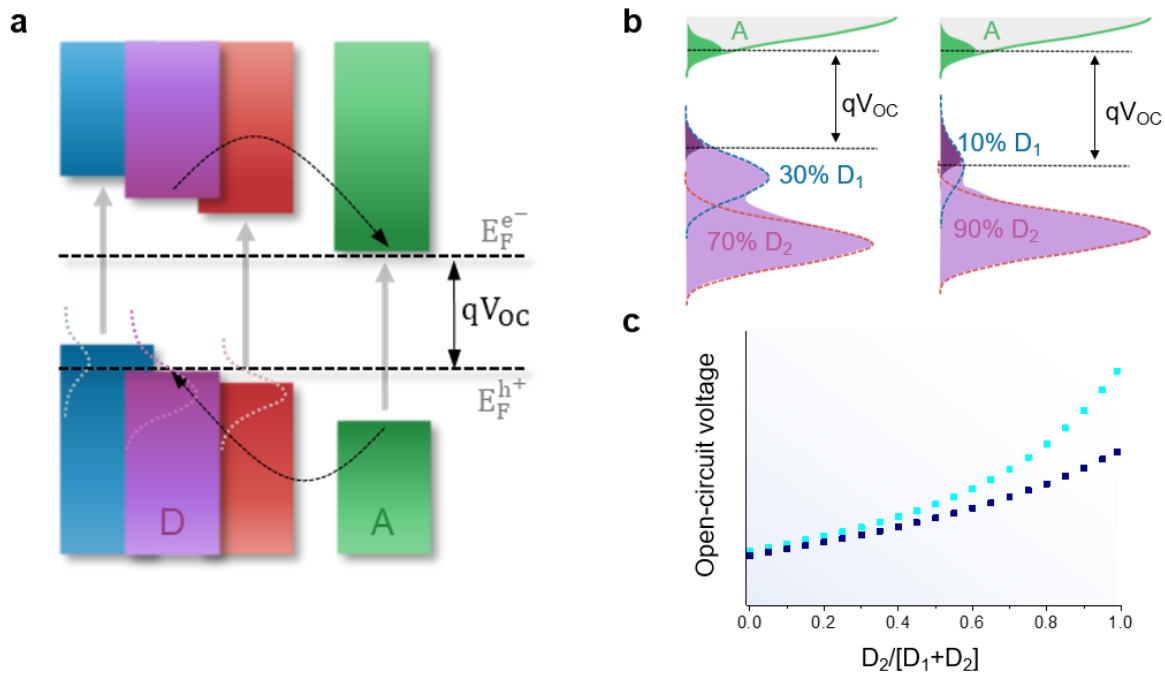


Figure 1.7: Electronic picture in the state-filling model. a) Energy levels of a ternary cell in the state-filling model. The two donors (blue and red) overlap, forming common energy levels (purple) with a new hole quasi-Fermi level, while the acceptor (green) remains unchanged. The difference of electron and hole quasi-Fermi levels corresponds to the elementary charge q times the open-circuit voltage (V_{OC}). b) Density of states (DOS) depiction of the energetic situation in a ternary blend with two different donor ratios. Shown are the DOS of the two donors (blue and red) and their superposition (purple) and the DOS of the acceptor (green) with the corresponding density of occupied states (DOOS). With decreasing amount of D_1 the donor DOOS is flattened and therefore down-shifted, resulting in a lower hole quasi-Fermi level and a higher V_{OC} . c) Expected V_{OC} trend of a ternary cell following the state-filling model as a function of the two donors' ratio for a large (light blue) and a small (dark blue) HOMO offset of the two donors.

The state-filling model was extended in the following year by considering a composition-dependent disorder for the gaussian DOS⁹⁵. From temperature-dependent hole and electron mobility measurements the energetic disorder of donor and acceptor was determined, respectively. It was found that the disorder of the materials changed upon adding the third component and can increase or decrease with the ratio, depending on the material. Since a

higher disorder leads to a broadened DOS, it also results in a down-shifted LUMO and an up-shifted HOMO and thus in a smaller V_{OC} . Considering the composition-dependent disorder values, the near linear tunability of the V_{OC} could be explained that is often observed in literature but was incorrectly predicted as exponential with the state-filling model that did not consider a composition-dependent disorder.

So far, not many groups have compared their experimental results with the state-filling model⁹⁶, since the simulation of the V_{OC} according to the model is not straight-forward but is based on equations that can only be solved numerically. In addition, the model neglects the existence of CT states, which makes it difficult to compare with other concepts, and it also ignores possible recombination losses.

Compared to the four models presented so far, the quadrupole concept is based on a different approach. While the other models assume constant molecular energy levels which are at most shifted by a varying degree of disorder, the quadrupole concept is based on the fact that the molecular energy levels are strongly dependent on the electrostatic environment, more precisely on the surrounding quadrupole moments⁹⁷⁻⁹⁹.

In general, to calculate HOMO and LUMO energies for molecules, an intramolecular part and an intermolecular part must be considered. The intramolecular part corresponds to the IP or EA of the single molecule in vacuum. The intermolecular part originates from permanent and induced electrostatic interactions of the molecule with the quadrupole moments of surrounding molecules and scales with the distance r^{-3} . In simulations of the HOMO and LUMO energy, this interaction is usually assumed to converge fast and therefore only a small surrounding volume is taken into account with a short cut-off of around $r = 4-8$ nm. However, it was found that the electrostatic interactions can have a much longer range, especially in aggregated thin-film structures (resembling a 2D-infinite film)⁹⁷. Thus, the energetic landscape changes drastically when $r = \infty$ is used instead as a cut-off. These results also have implications for the behavior of TOSCs, as demonstrated with a model system consisting of a blend of zinc phthalocyanine (ZnPc) and one of its fluorinated derivatives (F₄ZnPc, F₈ZnPc, F₁₆ZnPc) as donors and C₆₀ as an acceptor⁹⁸. The molecular structures, isopotential surfaces, and resulting quadrupole moments of ZnPc and F₁₆ZnPc are depicted in **Figure 1.8a**. Since the IP of the donor molecules is increasing with progressive fluorination, the V_{OC} of the ternary blends was found to increase with higher ratios of the fluorinated donor (**Figure 1.8b**) – a result that is to be expected based on models for TOSCs with tunable V_{OC} . However, the UPS measurements of blends of the donors revealed something unexpected: The UPS signal of the blend did not correspond to a weighted average of two fixed pristine signals, but the pristine peaks themselves

1 Introduction

were shifted in the blend (**Figure 1.8c**). Density functional theory (DFT) simulations of the HOMOs considering intermolecular interactions along the molecular stacking directions confirmed that each component's shift of energy levels in the blend observed with UPS can be attributed to the intermolecular charge-quadrupole interactions in molecular mixed stacks.

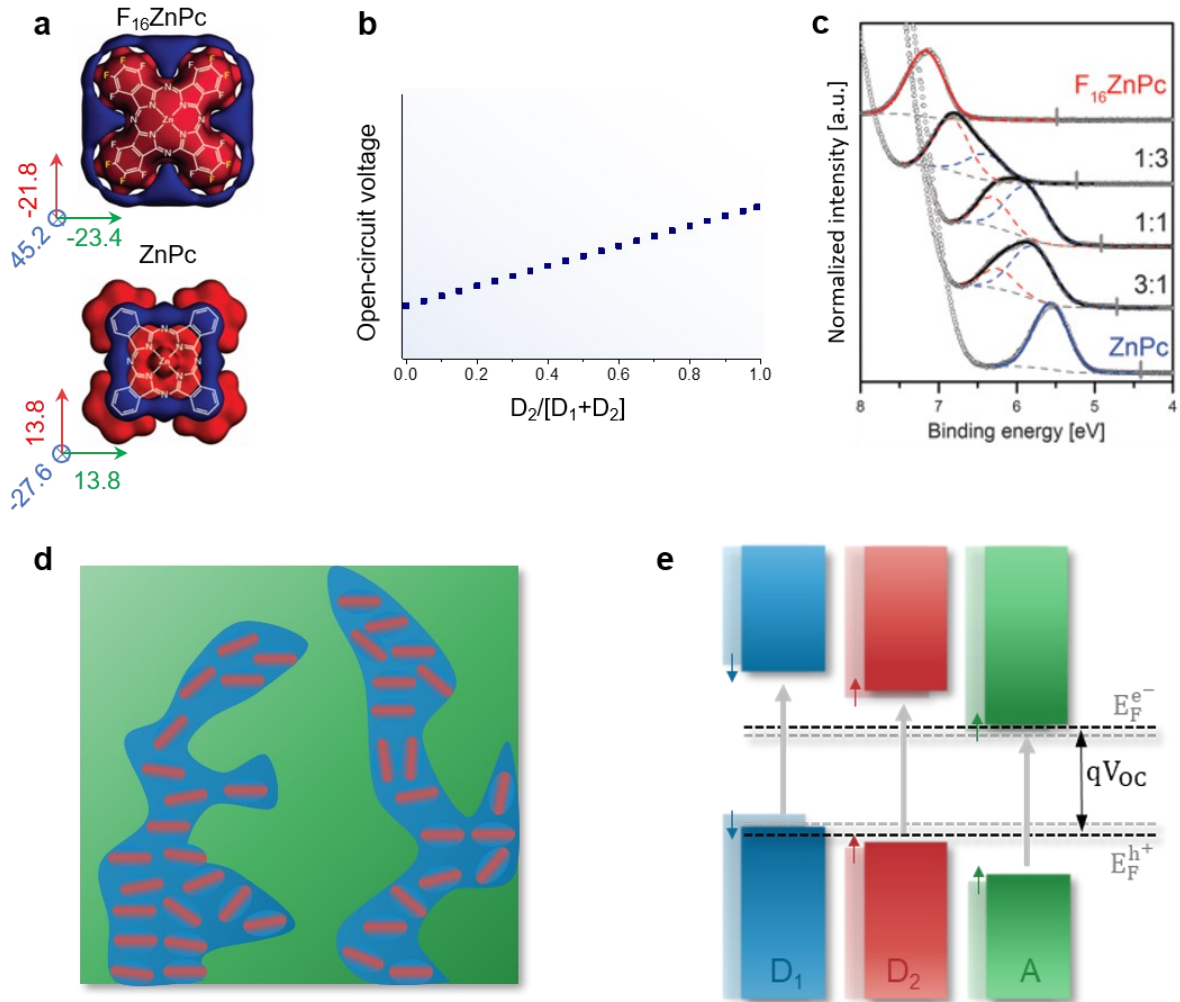


Figure 1.8: Electronic and morphological picture in the quadrupole model. a) Molecular structure of $ZnPc$ and $F_{16}ZnPc$, their isopotential surfaces at -0.3 V (blue) and $+0.3$ V (red) calculated via density functional theory, and the resulting three-dimensional quadrupole moments. b) Expected open-circuit voltage (V_{oc}) trend as a function of the two donors' ratio for ternary systems following the quadrupole model. c) Measured ultraviolet photoelectron spectra (gray circles) of $ZnPc:F_{16}ZnPc$ blends with varying compositions and the respective fits based on a superposition (black solid line) of the pristine materials' Gaussian fits (blue for $ZnPc$, red for $F_{16}ZnPc$). d) Schematic depiction of the morphology for a ternary blend in the quadrupole model, with the two donors (blue and red) being strongly intermixed while still forming stacks of several alike molecules and the acceptor (green) forming a phase separated domain. e) Energy level alignment for a ternary blend with two donors (blue and red) and one acceptor (green) in the quadrupole model. The respective lighter colors show the energy levels of the pristine components which are shifted (indicated by arrows) upon blending. Panels a and c are adapted from REF.⁹⁸.

Importantly, this effect does not need large aggregates, but simulations show that the IP is shifted already for five stacked molecules, allowing a quite large extent of miscibility in the ternary blend (**Figure 1.8d**). Additionally, the quadrupole moments of surrounding molecules also affect the acceptor and its EA, meaning that all energy levels in the ternary blend are shifted compared to the pristine components (**Figure 1.8e**). Subsequently, it was demonstrated that the observation of quadrupole moments influencing EA and IP in a model system is also transferable to several other molecules and that the electrostatic gradients at donor-acceptor interfaces induced by quadrupole moments could even increase the driving force for free charge generation⁹⁹.

The primary findings of the effects of quadrupole moments on energy levels and CT states have since been applied to homojunction OSCs¹⁰⁰ and to doping in organic semiconductors¹⁰¹, but not much further research exists on the effects on TOSCs. Therefore, the quadrupole concept for TOSCs is still subject to some limitations and leaves questions unanswered. So far, the causal relationship of quadrupole moments and V_{OC} in ternary blends has only been demonstrated for relatively small and planar molecules. Moreover, for a significant effect on the energetic landscape in the blend, the quadrupole moments of the blended species have to show a significant difference along the π - π stacking direction, and both species must be systematically oriented in the film. It is thus unclear whether this effect also applies to large, non-planar molecules or disordered polymers, and experimental data on this is lacking. Furthermore, in the previous work introducing the quadrupole concept for TOSCs, a single charge transfer state was assumed for the blend, without further discussion or justification, and it is not clear between which molecules this state occurs ($D_1:A$, $D_2:A$ or an alloyed $D_1/D_2:A$). Therefore, the exact description of the CT states in the quadrupole concept is still missing. In addition, the practical application of the model is limited by the need for advanced DFT calculations.

1 Introduction

Table 1.2: Selected performance parameters for TOSCs and their respective binary OSCs which were attributed to one of the described concepts. For the state-filling model no detailed performance data is available.

Blend	Type	Ratio	Performance				Attributed model	Ref
			PCE	J _{sc}	FF	V _{oc}		
PTB7:PID2:PC ₇₁ BM	D1:D2:A	0.9:0.1:1.5	8.2	16.8	68.7	0.72	Cascade	REF ³³
	D1:A	1:1.5	7.3	15.0	67.1	0.72		
	D2:A	1:1.5	2.0	5.3	44.4	0.86		
PBDB-T:ITCN:IT-M	D:A1:A2	1:1	2.2	5.0	36.7	1.17	Cascade	REF ⁵⁵
	D:A1	1:0.2:0.8	11.7	17.7	71.2	0.95		
	D:A2	1:1	10.8	17.1	68.1	0.94		
PTB7:PCDTBT:PC ₇₁ BM	D1:D2:A	0.7:0.3:2	8.8	17.0	65.3	0.79	Cascade	REF ⁴⁰
	D1:A	1:1.5	6.6	14.5	63.0	0.73		
	D2:A	1:4	6.1	10.9	63.0	0.89		
P3HTT-DPP-10%:P3HT ₇₅ -CO-EHT ₂₅ :PC ₆₁ BM	D1:D2:A	0.9:0.1:1:1	5.5	15.1	61.0	0.60	Alloy	REF ⁷⁰
	D1:A	1:1.3	5.1	14.4	62.0	0.57		
	D2:A	1:0.8	3.2	8.0	59.0	0.68		
PTB7-Th:TPE-4PDI:PC ₇₁ BM	D:A1:A2	66.7:3:97	10.1	17.4	73.9	0.78	Alloy	REF ¹⁰²
	D:A1	66.7:100	1.9	4.3	50.3	0.89		
	D:A2	66.7:100	9.2	16.5	71.2	0.77		
PM6:BTP-eC9:BTP-F	D:A1:A2	1:0.18:1.02	18.5	27.0	79.7	0.86	Alloy	REF ¹⁰³
	D:A1	1:1.2	17.6	26.8	77.5	0.85		
	A:A2	1:1.2	16.2	24.1	75.0	0.90		
DTffBT:DTPyT:PC ₆₁ BM	D1:D2:A	0.5:0.5:1	7.0	13.7	58.9	0.87	Parallel-like	REF ⁸⁴
	D1:A	1:1	6.3	12.2	56.5	0.91		
	D2:A	1:1	6.3	12.8	58.1	0.85		
PBDB-T:PC ₇₁ BM:ITIC-Th	D:A1:A2	1:0.5:0.5	10.2	15.5	70.5	0.93	Parallel-like	REF ⁸⁷
	D:A1	1:1	9.2	13.2	76.2	0.92		
	D:A2	1:1	7.1	12.6	59.0	0.95		
PBDTPD-HAT:ITIC:PC ₇₁ BM	D:A1:A2	1:0.9:0.6	12.1	17.4	74.0	0.95	Parallel-like	REF ⁸⁹
	D:A1	1:1.5	10.0	14.9	69.0	0.97		
	D:A2	1:1.5	7.8	12.1	75.0	0.86		
ZnPc:F ₄ ZnPc:C ₆₀	D1:D2:A	1.8:0.2:3	3.5	10.2	59.0	0.58	Quadrupole	REF ⁹⁸
	D1:A	2:3	3.3	10.2	59.0	0.55		
	D2:A	2:3	1.6	1.7	29.0	0.85		

1.3.3 Advances in Understanding Ternary Mechanisms

The development of the models described above took place mainly between 2011 and 2015, before the widespread use of non-fullerene acceptors, and the models are therefore focused on mechanisms in fullerene-containing OSCs. However, because NFAs differ from fullerenes in many crucial properties, the mechanistic understanding of binary OSCs has evolved since their emergence and also for TOSCs, recent discoveries have shed new light on the conventional models. For this reason, the following briefly summarizes the current understanding of binary mechanisms, with a particular focus on NFAs, and then explains the most important insights into TOSCs, their CT states, their recombination behavior, their morphology and its interplay with electronics. Finally, the conventional models are shortly reevaluated in light of the most recent findings.

New findings for binary mechanisms. The prevailing understanding of binary OSC mechanisms at the time of the ternary model development can be described in simplified terms as follows: Upon light absorption of the donor an exciton is generated which diffuses to an acceptor interface and by the transfer of an electron from the donor LUMO to the acceptor LUMO a CT state is formed. For this to happen, a driving force of around 0.3 eV is assumed to be necessary¹⁰⁴, provided by the LUMO offset. To split the CT state into free charges, the coulombic force between hole and electron has to be overcome, however, it is not fully understood how this energy is provided. In this picture, recombination occurs either geminately via the excited singlet state S_1 or the CT state, or it occurs non-geminately when free charges encounter each other (second order) or when a free charge encounters a trapped charge (first order) (**Figure 1.9**). In-depth explanations can be found in various other reviews^{8,105,106}.

With the emergence of NFAs this mechanistic understanding was reexamined, resulting in a revised understanding, which is briefly described below. More detailed accounts can be found in other recent reviews focusing on binary OPVs^{12,107,108}. First of all, in contrast to fullerene derivatives, NFAs have a strong absorption capability, whereby a CT state can additionally be formed by a hole transfer from the acceptor HOMO to the donor HOMO. Moreover, due to the usually red-shifted absorption of the NFA compared to the donor, energy transfer from the donor to the acceptor becomes an important possibility, which competes with electron transfer¹⁴. Another crucial difference is assumed to be that with involvement of NFAs the driving force for CT state formation (**Figure 1.9**, ΔG_{CT}) can be reduced up to a near-zero offset of the respective LUMOs^{109,110} or HOMOs^{111,112}, which is explained, among other things, by longer exciton lifetimes¹¹³ or the existence of quadrupole-induced local electrostatic fields¹¹⁴.

1 Introduction

However, the question of the extent to which the driving force can actually be dispensed is part of an ongoing debate¹¹⁵. In fact, very recent findings rather indicate that a near-zero offset is not possible and that previous results in this direction are based on an incorrect determination of the involved materials' energy levels¹¹⁶.

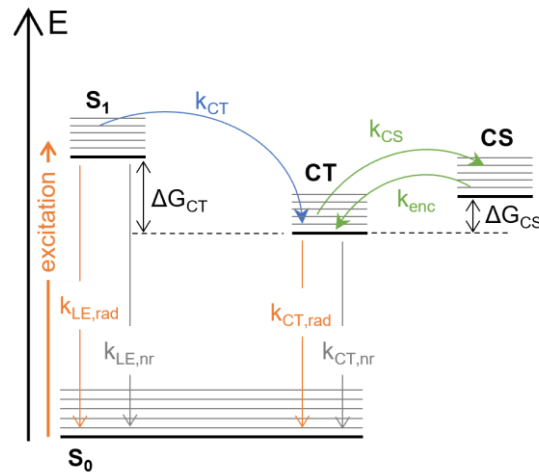


Figure 1.9: Schematic Jablonski-type diagram depicting the revised understanding of mechanisms in binary OSCs. Photoexcitation of the donor or acceptor results in an excited singlet state S_1 which can either recombine radiatively or non-radiatively (rate constants $k_{LE,rad}$ and $k_{LE,nr}$) or undergo a charge transfer (rate constant k_{CT}), driven by the energetic offset of S_1 and CT (ΔG_{CT}). The CT state can also either recombine or form a charge separated state CS if the necessary free energy ΔG_{CS} is provided. The CS state then results in a collection of the free charge carriers or the charge carriers encounter and reform a CT state before collection (rate constant k_{enc}).

The splitting of the CT states into free charges is still poorly understood. In general, there are two different approaches to explain how the coulombic force between hole and electron can be overcome (**Figure 1.9**, ΔG_{CS}). In one case it is assumed that the charge separated state is energetically favored by other effects, for example by a stronger delocalization of free charges¹¹⁷, by entropic effects¹³, or by local electric fields¹⁴. Alternatively, it is suspected that excess energy is available for charge separation due to ‘hot’ CT states¹⁵. The latter concept in particular, however, is increasingly being called into question, as evidence is accumulating that CT states and charge separated states (CS) are in a thermodynamic equilibrium. The existence of this equilibrium has several important consequences: The splitting of the CT state must occur from a thermally relaxed state, which excludes hot CT states, and the recombination of free charge carriers exclusively occurs via the reformation of a CT state^{118–122}. It thus has major implications on the understanding of recombination and energy loss in OSCs. Usually, the energy loss E_{loss} , meaning the difference between the band gap E_g of a solar cell and the cell's V_{OC} times the elementary charge q , is described in an energetic state picture according to equation (1.3)¹²³:

$$E_{loss} = E_g - qV_{OC} = (E_g - E_{CT}) + q\Delta V_{OC}^{rad,CT} + q\Delta V_{OC}^{nr} \quad (1.3)$$

With the first term being the energetic offset between the excited singlet state (also called local exciton, LE) and CT state, the second term being radiative losses, and the third term being non-radiative losses. Often also another definition for losses based on a detailed balance approach can be found, where the non-radiative losses are the same, but the radiative losses are defined differently¹²⁴.

Under the prerequisite of equilibrium between LE, CT and CS, the non-radiative recombination is mainly governed by the CT state and its coupling with skeletal molecular vibrations. Here, a high CT state energy is beneficial, since this weakens the coupling, resulting in smaller non-radiative losses (energy gap law)^{125,126}. Another influence on non-radiative recombination is the hybridization of local exciton and CT state, which has been demonstrated to occur for small offsets ΔE_{LE-CT} ^{109,127,128}. The hybridization is assumed to increase the oscillator strength of the CT to ground state transition, thus suppressing non-radiative losses^{129,130}. However, it is argued that this kind of suppression only results in more radiative recombination and does not reduce the total energy loss, if not also the LE lifetime is enhanced¹²¹.

There are also findings that contradict a full thermal equilibrium in OSCs. Measured charge carrier mobilities, for example, decrease with the time elapsed after photo-excitation, which suggests that excess thermal energy is essential for the charge transport¹³¹. Simulations furthermore indicate that the V_{OC} found in many OSCs is higher than what would be expected from a system being in thermal equilibrium, instead the excess energy could be explained by an incomplete relaxation of charge carriers in a global density of states, where the excess thermal energy of not fully relaxed charge carriers contributes to an increased V_{OC} ¹³².

CT states in TOSCs. The formation of the CT state is a crucial step in any organic solar cell and there is considerable evidence that its energy directly correlates with the V_{OC} for binary OSCs^{133–135}. For this reason, there has always been great interest in making it analytically accessible, however, this is complicated by the fact that CT states usually have weak absorption and emission. Nevertheless, a variety of methods exist to investigate CT states, which are described and discussed in other reviews^{22,124,136,137}. The most frequently used methods are highly sensitive EQE and EL measurements, from which the CT state energy is extracted by fitting to a model describing the transition between the ground state and the CT state. Already for binary OSCs, this is a highly controversial topic, as different models exist, such as the frequently used Marcus theory^{133,138}, the Marcus-Levich-Jortner theory^{139,140} or a three-state

1 Introduction

model^{127,130} and the measurements additionally are influenced by many parameters, such as the absorber layer thickness^{141,142}, the temperature¹⁴⁰ or the energetic disorder¹⁴³.

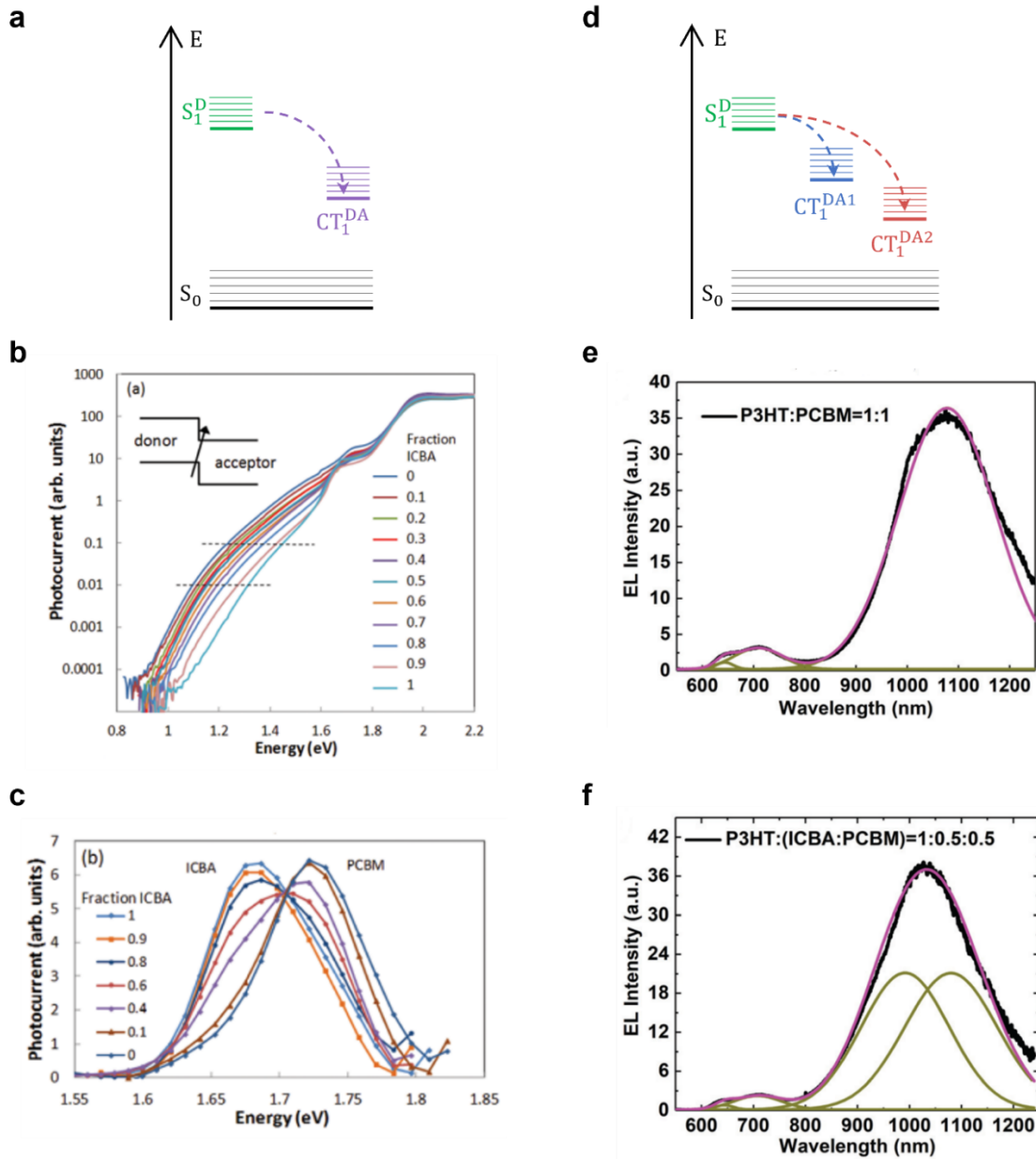


Figure 1.10: Comparison of different CT state perceptions of the same ternary system P3HT:PCBM:ICBA. a) Energetic situation in case of one alloyed CT state. b) Measured photocurrent spectral response (PSR) data for a P3HT:PCBM:ICBA ternary blend with varying PCBM:ICBA ratio, showing a shift of the interface band gap (indicated by the area between the dotted lines). c) Expansion of the PSR data in the region of the peak at 1.7 eV with subtracted background. The higher energy peak belongs to the PCBM absorption and is shifted continuously towards lower energies with increasing ICBA fraction, which here is taken as evidence for an alloyed CT state. d) Energetic situation in case of two distinct CT states. e) Measured electroluminescence spectra (black) and corresponding Gauss fits (pink) for binary P3HT:PCBM cells and f) ternary P3HT:ICBA:PCBM cells, where the Gauss fit corresponds to a linear superposition of the P3HT:PCBM and P3HT:ICBA blends' Gauss fits (green), which is here taken as evidence for two distinct CT states. Panel b, c adapted from REF⁶⁷. Panel e, f adapted from REF⁸².

Especially the three-state model is used more and more often for NFA-containing cells, since it describes the CT state absorption or emission not only as the coupling of the ground state and the CT excited state (two-state model), but additionally considers the coupling with the LE, whose contribution becomes more pronounced for smaller energetic offsets between CT and LE. Another problem occurs when the energetic offset between LE and CT state is small, which often is the case when NFAs are used, since the absorption of the CT state is then strongly overlapped by the absorption tail of the smallest band gap component and fitting is not reasonably possible anymore¹²².

For ternary systems it becomes even more complex, since theoretically not only one single CT state but even three distinct CT states can be accessible, one between every set of two components. However, the energetically highest CT state between the two like components (two donor-type components D_1 and D_2 or two acceptor-type components A_1 and A_2) is usually ignored or assumed to be negligibly occupied, even though there are a few reports indicating that a charge transfer can occur between two like components^{47,53}. The main discussion therefore revolves around the question of whether two simultaneously occupied CT states can exist ($D:A_1$ and $D:A_2$, or $D_1:A$ and $D_2:A$), analogous to the parallel-like concept, or whether only one CT state exists ($D:A_{1,2}$ or $D_{1,2}:A$), which results from long-range delocalization in a mixture of two components, analogous to the alloy concept. Answering this question with the help of CT state analytics is difficult, since the two potential CT states are energetically close and therefore distinguishing between a singular signal or the superposition of two signals is often not possible unambiguously, as contradictory results on similar systems demonstrate^{67,81,82} (**Figure 1.10**). This is further complicated by the fact that already in binary cells, energetically different CT states are sometimes detectable due to variations in crystallinity or molecular orientation throughout the blend^{144,145}.

The same ambiguity applies for a direct examination of the involved energy levels with photoelectron spectroscopy: theoretically, alloyed HOMOs (or LUMOs) should be distinguishable from a superposition of two separate energy levels, however, since the involved states are energetically close, the interpretation of the measurements is difficult and leads to contradictory results^{73,82,146}.

In principle, however, it is known for binary OSCs that large, homogeneous domains, especially in the case of crystalline NFAs, allow extensive delocalization of the CT state¹¹⁷. At the same time, in particular, structurally similar NFAs are known to form well-mixed, homogeneously crystalline phases^{103,147,148}. Therefore, it is reasonable to assume that in such systems the CT state is delocalized over both materials and exhibits an energetically averaged value. In fact, a

1 Introduction

recent study investigating ternary blends with two NFAs, one with a negative ionization energy offset to the donor and one with a positive offset, demonstrated that the quantum efficiency of the TOSC is determined by the average of both offsets, thus indirectly proving the delocalization of the CT state over two different materials¹⁴⁹.

Thus, while some evidence exists for the presence of an alloy-like CT state, the concept of two simultaneously occurring, energetically distinct CT states faces a fundamental problem: Under the now increasingly accepted assumption of the CT state being in equilibrium with the free charge carriers¹¹⁸⁻¹²¹, the occupation of two energetically different CT states should follow a Boltzmann distribution, which would result firstly in an exponential dependence of the V_{OC} on the composition and secondly in a strong temperature dependence of the V_{OC} . This is not compatible with the experimentally most often observed linear correlation of composition and V_{OC} in ternary blends that are attributed to work in a parallel-like model^{84,87,89} and a V_{OC} that tends to decrease with increasing temperature¹⁵⁰. One other possibility theoretically would be that the equilibrium between CT states and free charge carriers could be suppressed by morphological conditions, allowing the parallel existence of energetically different CT states, which are populated according to the absorption of the respective component and not according to a Boltzmann distribution, but so far, no systematic studies on this topic are available.

Recombination in TOSCs. For TOSCs, it is often assumed that E_{CT} and V_{OC} are linearly correlated, implicitly suggesting that all changes in V_{OC} with composition are caused by a change in E_{CT} , while recombination and transport behavior are composition independent. The models described above are also based on this assumption and therefore primarily focus their mechanistic description on the CT state. However, evidence is accumulating that the addition of a third component additionally affects recombination voltage loss, mobility, and energetic disorder in the blend, thus having a significant influence on the V_{OC} beyond the CT state energy. An increasing number of publications describe the reduction of charge carrier recombination via a ternary approach. For example, the power gap law already mentioned for binary OSCs can be beneficial for ternary blends¹²⁵: since energetically higher CT states couple less with molecular vibrations, an up-shifting of the CT state by the addition of a third component results automatically in less non-radiative recombination¹⁵¹. Similarly, the addition of a third component with an intrinsically lower non-radiative recombination can lead to an overall reduced voltage loss in the ternary blend¹⁵². Furthermore, the recombination behavior can be affected by morphological variations induced by a third component. For example, it has been demonstrated that suppressing the aggregation of NFAs, either by adding a fullerene

derivative¹⁵³ or another NFA with varied end-groups¹⁵⁴, reduces their self-quenching and increases the blend's electroluminescence, thus decreasing the non-radiative recombination. Analogously, the EL can be enhanced by using a third component with high photoluminescence quantum yield¹⁵⁵. Another promising approach is the combination of a symmetric and an asymmetric NFA in a ternary system, reducing both radiative and non-radiative recombination due to decreased energetic disorder and a lowered reorganization energy, which is attributed to a more ordered molecular packing between the two NFAs^{20,156}. In some cases, the voltage loss reduction by a ternary approach can even be large enough for the ternary cell's V_{OC} to exceed the V_{OC} of the respective binary references^{156,157}.

Morphology in TOSCs. Already the morphology of binary solar cells, which has been studied much more thoroughly than that of ternary ones^{158,159}, is rather complex. To simplify, the morphology of binary blends is therefore often described by a three-phase model^{160,161}, with a predominantly pure donor phase, a predominantly pure acceptor phase, and a mixed D:A phase, neglecting the possible existence of domains with variable mixing ratios or differences between crystalline and amorphous regions. Following this approach for ternary blends would result in a seven-phase model, with three predominantly pure phases as well as three binary and one ternary mixed phase. For this reason, a further simplification is usually employed for ternary blends, where mixed phases of donor and acceptor are ignored. In this heavily condensed view, two fundamentally different microstructures can occur: the third component (donor or acceptor) either forms a third, also pure phase, or it is compatible with the corresponding host component and forms a mixed donor or acceptor phase, building a pseudo-binary blend. These two morphologies are usually called parallel-like or alloy-like and describe the extreme cases of the range of possible morphologies in this simplified approach. It should be emphasized that the terms alloy-like and parallel-like here characterize a type of microstructure and should not be confused with the corresponding mechanistic models of analogous name.

The precise understanding of the ternary structure and the assignment to one of the two described types require elaborate analytics and the combination of many different methods, which will not be described here, but can be found in other reviews^{158,162,163}.

One widely used approach to make a simple prediction of a ternary blend's morphology type based on material properties is the miscibility^{71,164}, since two well-miscible components tend to form an alloy-like morphology, while poorly miscible components tend to be parallel-like. Miscibility of two components is widely expressed via the Flory-Huggins parameter χ ¹⁶⁵, which can be obtained either by a relation to the Hildebrandt or Hansen solubility parameters¹⁶⁶, via

1 Introduction

the melting point depression method^{167–169}, or from the components' surface tensions according to the Wu model¹⁷⁰. Several approaches also exist to calculate the miscibility of components theoretically^{171–174}.

Based on the predicted miscibility, two compatible donors or acceptors can be selected for the design of alloy-like morphologies; a strategy that has been demonstrated to result in high-performance TOSCs. However, the compatibility of two components is not only determined by the miscibility, but also by other factors. For two polymeric donors, it was demonstrated that, in addition to similar surface energies¹⁷⁵, structural compatibility is crucial, i.e., similar orientation and crystal sizes of the two polymers⁷⁸, strong lamellar interactions between them and additionally a similar phase separation with the acceptor¹⁷⁶. To achieve structural compatibility, a similar molecular structure or backbone of the polymers can be helpful¹⁷⁷, but is not mandatory^{176,178}. The same applies to the use of two non-fullerene acceptors: again, the molecules do not have to be structurally similar to be compatible for an alloy-like morphology¹⁷⁹, however, the strategy of employing similar NFAs is increasingly gaining popularity due to its simplicity^{147,180–183}. For example, the combination of two NFAs sharing the same central unit but one of them containing a single fluorinated end group has been shown to be a universal guideline for well-working TOSCs¹⁰³.

In contrast to an alloy-like morphology, a parallel-like morphology is less frequently reported in literature, mainly since it holds additional challenges. The combination of non-compatible components, especially in the case of polymers, usually leads to a severely disordered film, resulting in disrupted charge transport, decreased mobility, trap formation and increased recombination⁷⁸. Up to now, there are no repeatedly proven guidelines to design high-performance parallel-like TOSCs. However, one promising approach is based on the incorporation of a diblock copolymer as third component, which consists of one new acceptor homopolymer subunit and one host polymer subunit⁸⁶. Another strategy seems to be the combination of a fullerene acceptor with a non-fullerene acceptor, which appears to result in a parallel-like morphology in some cases^{87,89}. Yet, alloy-like TOSCs have also been reported for a diblock copolymer approach¹⁸⁴ or a fullerene:non-fullerene approach^{73,185}, proving once again that no universal guidelines for forming specific morphologies exist and that in general there is a disagreement about the interpretation of the results of morphological analyses.

Interplay of electronics and morphology. Morphology and electronic behavior cannot be considered separately in TOSCs since they are closely intertwined, and their interrelations affects all steps from charge generation to charge transport and extraction. Already the energy

levels of the individual molecules, although often assumed to be constant values, depend strongly on their chemical environment. Compared to a single molecule, the energy levels of solid films are shifted due to orientation, polarization or crystallinity effects^{186–188}. Furthermore, if several different molecules are mixed, as is the case with BHJ solar cells, the energy levels are additionally affected by the influence of neighbor molecules and long-range interactions from quadrupole moments^{97,189}.

With its impact on the energy levels, the morphology therefore naturally influences the CT state energy. For TOSCs it is therefore particularly difficult to understand the origin of composition-dependent CT state energies, since morphological effects such as changing chemical environments have to be distinguished from electronic effects such as alloying of two components. An elegant solution for this was demonstrated by comparing the CT state's composition dependence of binary and ternary blends with similar morphology¹⁹⁰. As a ternary blend, MEH-PPV:PC₆₁BM:ICBA was chosen, consisting of a strongly disordered polymer and two very similar acceptors, consequently having a comparable morphology with the binary MEH-PPV:PC₆₁BM blend. It was found that changing the acceptor ratio in the ternary blend has the same effect on CT state energies as changing the donor:acceptor ratio in the binary blend. The authors therefore concluded that the CT state energy simply depends on the aggregate size of PCBM, thus ruling out the possibility of an electronic alloy between the two acceptors, a conclusion that was recently confirmed for a different TOSC¹⁵¹. A similar effect also occurs for polymers, for which it has been shown that different CT state energies can be detected depending on the disorder at the interface with the acceptor¹⁹¹.

Morphologically induced disorder furthermore has an impact on the energy of free charge carriers¹⁹². The average energy of thermalized charge carriers lies by a value of $\sigma^2/k_B T$ below the center of the corresponding DOS¹⁹³, with σ being the standard deviation of the gaussian distribution and thus a measure for the energetic disorder broadening, the Boltzmann constant k_B and the temperature T . Therefore, an increased energetic disorder results in larger losses during thermalization and thus in a smaller V_{OC} . Ternary approaches have been shown to be particularly well suited for reducing energetic disorder, since the addition of a third component is a straight-forward strategy to tune the blend crystallinity and thus suppress disorder^{194,195}.

Adding a third component can furthermore improve the transport properties of a blend and promote charge extraction, which in turn enhances the fill factor. This is possible by increasing or balancing charge carrier mobility, for example, by adding components that have an intrinsically higher mobility, such as fullerene derivatives¹⁹⁶, or components with a high crystallinity⁴⁸. A particular advantage of ternary blends here could be that the high-mobility

1 Introduction

third component acts as a charge extraction ‘highway’, while the other two components are mainly involved in charge splitting^{48,57}. However, this potential advantage is controversially discussed, since simulations show that for a significantly increased mobility, the third component would have to form a continuous percolating phase, which would require a lot of material and is rather unrealistic with typical proportions of the third component of less than 20 % in the total blend⁶². An enhanced mobility and FF can additionally be achieved by changing the molecular orientation, where a face-on orientation often is assumed to be most beneficial for charge transport. For example, it has been shown that the addition of PC₇₁BM as a second acceptor can tune the orientation of the non-fullerene acceptor towards face-on stacking, resulting in an increased mobility and efficiency^{197,198}. However, it also has been demonstrated that a mixed face-on and edge-on orientation, achieved by adding a second donor, can be even more advantageous than the pure face-on orientation of the binary blend, which once again illustrates that nano-morphological design rules strongly depend on the employed molecules¹⁹⁹. One morphological feature that is often ignored but may have crucial implications on performance and working principles is the vertical inhomogeneity of ternary blends. This issue, for example, was systematically investigated by building pseudo-ternary blends from stacks of two separately manufactured P3HT:PC₆₁BM layers with different composition²⁰⁰. Since the energy levels of P3HT strongly depend on the mixing ratio with PC₆₁BM due to induced disorder, it was found that the V_{OC} depends on the stacking order of the two layers, with the layer being in contact with the hole transport layer governing the V_{OC} . Those findings thus are strong evidence that the assumption of constant Fermi levels throughout a blend possibly are not valid for morphologically inhomogeneous ternary mixtures.

The models in the light of recent findings. As described in the first part of the review, the presented models already have some inconsistencies and deficiencies within themselves in terms of a precise definition and differentiation from each other. Moreover, with the latest findings on mechanisms in binary and ternary OSCs, as presented in the second part, the ideas in the models have been overtaken or refuted in some points. One major issue is that apart from the quadrupole approach, all existing models assume the properties of the pristine materials to be preserved in the blend and thus ignore the strong influences due to electrostatic effects or disorder when mixed. Moreover, in all approaches except the state-filling model, the CT state energy is considered as a discrete value instead of being described by the varying occupation of a density of states. However, the biggest problem is the strong focus of the models on the CT state, especially in the case of cascade, alloy and parallel-like model. The CT state is considered

to be static and directly correlated with the V_{OC} , while all effects from charge separation, recombination, and transport are neglected. Newer findings, however, have shown that the CT state in fact is in a dynamic equilibrium with the free charge carriers, thus being virtually independent from the singlet excited state and determined by the kinetics of this equilibrium. This decisive aspect is consequently not represented in all existing descriptions of TOSC mechanisms.

1.3.4 Outlook

Ternary organic solar cells have been a hot research topic in recent years and the possibilities offered by the incorporation of three different components have provided impressive results in terms of both efficiencies and stability. And even though much progress has been made in understanding the mechanisms at work, a comprehensive picture of their operating principle is still missing. Instead, new systems are often carelessly assigned to old models that lack a precise definition and delineation. Therefore, to achieve a more profound understanding of TOSCs, research must move away from existing models and return to more in-depth mechanistic studies. One of the most challenging areas is the deciphering of the ternary blend morphology and its influence on the occurring mechanisms. For this, of course, the development of existing and new analytical methods must be advanced. In addition, more theoretical approaches to the representation of structural interactions must be developed. However, since a complete understanding of the morphological details will not be possible in the foreseeable future by either analytical or theoretical methods, mechanism research must detach itself from morphology to some extent. Instead, more studies should be conducted that systematically vary the components and composition of ternary blends and are able to establish relationships between molecular design and solar cell performance and properties. In addition to continued research on new systems, collecting data from already reported TOSCs and comparing them systematically in a meta-study could help answering many open questions.

Another fundamental aspect that needs more research, but is not exclusively related to solar cells, is charge transport in heterogeneous organic materials and how thermal relaxation and Fermi level position depend on the intermixing of two components. With respect to TOSCs, the community will likely need to move away from the ideal of a simple and comprehensive model for all compositions of a combination of three materials and instead face the possibility of different mechanisms and effects being present simultaneously or transitioning smoothly into each other.

1 Introduction

With this review, we want to stress that the currently used models for TOSCs are still works in progress and not yet finalized theories. Combined efforts and collaboration of the entire OSC community will be needed for a future with a comprehensive and in-depth understanding of the working principles of TOSCs.

1.4 Stability of Organic Solar Cells

For organic solar cells, research in recent years has been primarily focused on increasing efficiencies. So far, a record efficiency of 19 % has been achieved, which means that OSCs are slowly reaching the range they need to be a commercially competitive alternative. However, for a commercial application, stability is also crucial, and this issue has been rather neglected so far. Although there are individual publications that cite very impressive long-term stabilities for specific systems,^{201,202} detailed studies about degradation mechanisms and clear design rules for high stability are lacking.

In general, aging mechanisms of OSCs can be divided into four groups: extrinsic degradation, intrinsic degradation in the dark, photodegradation, and mechanical degradation. Extrinsic degradation occurs when molecules from the environment, mainly oxygen and water, are allowed to enter the device. They can chemically react with the absorbing materials or the interlayers and this results, for example, in a loss of absorption or increased series resistances in the device. However, this type of degradation is often ignored, since it could be addressed with a proper encapsulation, such that the research effort is more shifted towards developing those encapsulations. More critical problems are intrinsic degradation and photodegradation, since those aging processes may be unavoidable. Intrinsic degradation in the dark mostly occurs due to thermally induced rearrangements of molecules in the device. The diffusion of molecules in the photoactive layer can lead to a too fine intermixing or a phase separation, thus destroying the optimal BHJ morphology. Or molecules from the interlayers or electrodes can diffuse into the photoactive layer, creating shunts. Those processes are typically accelerated at higher temperatures and since a solar cell can easily heat up to over 60 °C during operation, these are problems that urgently need to be solved. Photodegradation can occur when the illumination itself causes the solar cell to lose efficiency, for example by photochemical reactions.²⁰³ Mechanical degradation is now gaining importance with the pursuit of producing OSCs on flexible substrates and mainly describes degradation due to bending of the solar cells, which can cause cracks, delamination or shunting in the different layers.²⁰⁴

The stability of solar cells is usually measured quantitatively by the so-called T_{80} time, which describes the time it takes for a solar cell to lose 20% of its initial efficiency under the respective aging conditions.

1.5 Zinc Oxide as Electron Transport Layer

Zinc oxide (ZnO) is by far the most commonly used electron transport material in inverted organic solar cells. The reason for this lies in its many advantageous properties - such as transparency, high conductivity, good processability, low-cost and non-toxicity – which make it an attractive material for both lab-scale and commercial applications.

ZnO has a direct band gap of around 3.3 eV and consequently an absorption onset below 375 nm, thus being highly transparent in most of the visible range. With a LUMO of ~ -4.3 eV (vs. vacuum), ZnO is able to accept electrons from most of the currently used high-performing organic acceptor materials, and the very low HOMO of ~ -7.6 eV makes it an excellent hole blocking material. The most stable structure of zinc oxide is the hexagonal wurtzite phase, while the other two polymorphs zinc blende and cubic ZnO are metastable.²⁰⁵

For organic solar cells, the ZnO electron transport layer (ETL) can be manufactured via two fundamentally different approaches: either the layer is produced directly via a sol-gel approach or ZnO nanoparticles are pre-synthesized and then processed as a dispersion to form a film. For the sol-gel synthesis, a zinc-precursor, normally zinc acetate, is dissolved in an alcoholic solvent and stirred for the hydrolysis reaction and the formation of zinc hydroxide acetate as an intermediate. The solution then is processed to form a thin film, for example by spin coating or doctor blading, and dried via a heating step which removes the remaining acetate.²⁰⁶ Since the sol-gel needs high temperatures in this last step which do not allow for flexible substrates, pre-synthesized ZnO nanoparticles are usually preferred. Those nanoparticles can be produced by different methods, such as sol-gel synthesis or a chemical precipitation, and then are dispersed in a solvent for the processing to form a thin film.

The n-type conductivity of ZnO is caused by defects in the crystal structure. While it was previously believed that the good conductivity is due to oxygen vacancies, recent results have shown that the conductivity mechanism is based on extrinsic impurities, mainly hydrogen but also other species.²⁰⁷ Since this type of impurity is very challenging to control, especially when the ZnO is produced and processed in a solution-based process, the conductivity of ZnO is difficult to adjust and often an additional doping is applied for better control.

Two of the most challenging aspects of ZnO as ETL are its surface chemistry and achieving a matching energy level alignment with the absorbing layer. This, for example, is expressed in the so-called light-soaking issue, which means that ZnO-containing OSCs reach their full performance only after illumination with light whose energy corresponds to the band gap of ZnO (UV region). The cause of the light-soaking issues is attributed to oxygen species being chemically adsorbed on the surface of zinc oxide, which trap negative charges at the surface of

the ZnO and thus at the interface to the photoactive layer of the solar cell. This leads to an upward band bending towards the surface of the ZnO layer and consequently a hindered electron extraction from the absorbing layer, resulting in enhanced interface recombination and a decreased fill factor (FF). UV irradiation generates electron-hole pairs in the ZnO, of which the holes can recombine with the trapped electrons, leading to a desorption of the oxygen and a reduced band bending. Consequently, the electron extraction issue at the interface of active layer and ZnO is resolved under continuous UV illumination.²⁰⁸⁻²¹⁰

On the other hand, however, this very process of UV illumination can also generate radical oxygen species, which in turn react with the active layer materials, reducing their absorption capability or generating traps, thus worsening the recombination behavior and the performance.^{211,212}

1.6 References

1. Statista. Weltweiter Primärenergieverbrauch in den Jahren von 1980 bis 2021. Available at <https://de.statista.com/statistik/daten/studie/42226/umfrage/welt-insgesamt-verbrauch-an-primaeerenergie-in-millionen-tonnen-oelaequivalent/> (2022).
2. Yoshikawa, K. *et al.* Silicon heterojunction solar cell with interdigitated back contacts for a photoconversion efficiency over 26%. *Nat Energy* **2** (2017).
3. Min, H. *et al.* Perovskite solar cells with atomically coherent interlayers on SnO₂ electrodes. *Nature* **598**, 444–450 (2021).
4. Wei, Y. *et al.* Binary Organic Solar Cells Breaking 19% via Manipulating the Vertical Component Distribution. *Adv. Mater.* **34**, e2204718 (2022).
5. Riede, M., Spoltore, D. & Leo, K. Organic Solar Cells—The Path to Commercial Success. *Advanced Energy Materials* **11**, 2002653 (2021).
6. Extance, A. The reality behind solar power's next star material. *Nature* **570**, 429–432 (2019).
7. Schmidt-Mende, L. & Weickert, J. *Organic and hybrid solar cells. An introduction* (De Gruyter, Berlin, Boston, 2016).
8. Deibel, C. & Dyakonov, V. Polymer-Fullerene Bulk Heterojunction Solar Cells. *Rep. Prog. Phys.* **73**, 96401 (2010).
9. Bäessler, H. Charge Transport in Disordered Organic Photoconductors a Monte Carlo Simulation Study. *phys. stat. sol. (b)* **175**, 15–56 (1993).
10. Tang, C. W. Two-layer organic photovoltaic cell. *Appl. Phys. Lett.* **48**, 183–185 (1986).
11. Hughes, M. P. *et al.* Determining the Dielectric Constants of Organic Photovoltaic Materials Using Impedance Spectroscopy. *Adv Funct Materials* **28**, 1801542 (2018).
12. Armin, A. *et al.* A History and Perspective of Non-Fullerene Electron Acceptors for Organic Solar Cells. *Adv. Energy Mater.* **11**, 2003570 (2021).
13. Hood, S. N. & Kassal, I. Entropy and Disorder Enable Charge Separation in Organic Solar Cells. *J. Phys. Chem. Letters* **7**, 4495–4500 (2016).
14. Karuthedath, S. *et al.* Intrinsic efficiency limits in low-bandgap non-fullerene acceptor organic solar cells. *Nat Mater* **20**, 378–384 (2021).

15. Few, S., Frost, J. M. & Nelson, J. Models of charge pair generation in organic solar cells. *Phys. Chem. Chem. Phys.* **17**, 2311–2325 (2015).
16. Yu, G., Gao, J., Hummelen, J. C., Wudl, F. & Heeger, A. J. Polymer Photovoltaic Cells: Enhanced Efficiencies via a Network of Internal Donor-Acceptor Heterojunctions. *Science* **270**, 1789–1791 (1995).
17. Li, Y. *et al.* Recent Progress in Organic Solar Cells: A Review on Materials from Acceptor to Donor. *Molecules* **27** (2022).
18. Wang, J. *et al.* A Tandem Organic Photovoltaic Cell with 19.6% Efficiency Enabled by Light Distribution Control. *Adv. Mater.* **33**, 2102787 (2021).
19. Cui, Y. *et al.* Single-Junction Organic Photovoltaic Cell with 19% Efficiency. *Adv. Mater.* **33**, 2102420 (2021).
20. Sun, R. *et al.* Single-Junction Organic Solar Cells with 19.17% Efficiency Enabled by Introducing One Asymmetric Guest Acceptor. *Adv. Mater.* **34**, e2110147 (2022).
21. Sariciftci, N. S., Smilowitz, L., Heeger, A. J. & Wudl, F. Photoinduced Electron Transfer from a Conducting Polymer to Buckminsterfullerene. *Science* **258**, 1474–1476 (1992).
22. Coropceanu, V., Chen, X.-K., Wang, T., Zheng, Z. & Brédas, J.-L. Charge-transfer electronic states in organic solar cells. *Nat Rev Mater* **4**, 689–707 (2019).
23. Halls, J. J. M. *et al.* Efficient photodiodes from interpenetrating polymer networks. *Nature* **376**, 498–500 (1995).
24. Elumalai, N. K. & Uddin, A. Open circuit voltage of organic solar cells: an in-depth review. *Energy Environ. Sci.* **9**, 391–410 (2016).
25. Xue, R., Zhang, J., Li, Y. & Li, Y. Organic Solar Cell Materials toward Commercialization. *Small* **14**, 1801793 (2018).
26. Brabec, C. J. *et al.* A Low-Bandgap Semiconducting Polymer for Photovoltaic Devices and Infrared Emitting Diodes. *Adv. Funct. Mater.* **12**, 709–712 (2002).
27. Ameri, T., Khoram, P., Min, J. & Brabec, C. J. Organic ternary solar cells: a review. *Adv. Mater.* **25**, 4245–4266 (2013).
28. An, Q. *et al.* Versatile ternary organic solar cells: a critical review. *Energy Environ. Sci.* **9**, 281–322 (2016).

1 Introduction

29. Gasparini, N., Salleo, A., McCulloch, I. & Baran, D. The role of the third component in ternary organic solar cells. *Nat Rev Mater* **9**, 145 (2019).
30. Yan, C. *et al.* Non-fullerene acceptors for organic solar cells. *Nat. Rev. Mater.* **3**, 18003 (2018).
31. Ameri, T. *et al.* Performance Enhancement of the P3HT/PCBM Solar Cells through NIR Sensitization Using a Small-Bandgap Polymer. *Adv. Energy Mater.* **2**, 1198–1202 (2012).
32. Koppe, M. *et al.* Near IR Sensitization of Organic Bulk Heterojunction Solar Cells: Towards Optimization of the Spectral Response of Organic Solar Cells. *Adv. Funct. Mater.* **20**, 338–346 (2010).
33. Lu, L., Xu, T., Chen, W., Landry, E. S. & Yu, L. Ternary blend polymer solar cells with enhanced power conversion efficiency. *Nature Photon* **8**, 716–722 (2014).
34. Ye, L. *et al.* Ternary Bulk Heterojunction Photovoltaic Cells Composed of Small Molecule Donor Additive as Cascade Material. *J. Phys. Chem. C* **118**, 20094–20099 (2014).
35. An, Q. *et al.* Simultaneous Improvement in Short Circuit Current, Open Circuit Voltage, and Fill Factor of Polymer Solar Cells through Ternary Strategy. *ACS Appl. Mater. Interfaces* **7**, 3691–3698 (2015).
36. Soltani, R. *et al.* Improved charge carrier dynamics in polymer/perovskite nanocrystal based hybrid ternary solar cells. *Phys. Chem. Chem. Phys.* **20**, 23674–23683 (2018).
37. Soltani, R. *et al.* Light harvesting enhancement upon incorporating alloy structured CdSe_xTe_{1-x} quantum dots in DPP:PC₆₁BM bulk heterojunction solar cells. *J. Mater. Chem. C* **5**, 654–662 (2017).
38. Koppe, M. *et al.* Charge Carrier Dynamics in a Ternary Bulk Heterojunction System Consisting of P3HT, Fullerene, and a Low Bandgap Polymer. *Adv. Energy Mater.* **3**, 949–958 (2013).
39. Huang, J.-S. *et al.* Polymer bulk heterojunction solar cells employing Förster resonance energy transfer. *Nature Photon* **7**, 479–485 (2013).
40. Gupta, V., Bharti, V., Kumar, M., Chand, S. & Heeger, A. J. Polymer-Polymer Förster Resonance Energy Transfer Significantly Boosts the Power Conversion Efficiency of Bulk-Heterojunction Solar Cells. *Adv. Mater.* **27**, 4398–4404 (2015).

41. Gasparini, N. *et al.* Favorable Mixing Thermodynamics in Ternary Polymer Blends for Realizing High Efficiency Plastic Solar Cells. *Adv. Energy Mater.* **9**, 1803394 (2019).
42. Karuthedath, S. *et al.* Impact of Fullerene on the Photophysics of Ternary Small Molecule Organic Solar Cells. *Adv. Energy Mater.* **9**, 1901443 (2019).
43. Mohapatra, A. A., Tiwari, V. & Patil, S. Energy transfer in ternary blend organic solar cells: recent insights and future directions. *Energy Environ. Sci.* **14**, 302–319 (2021).
44. Huang, J.-H., Velusamy, M., Ho, K.-C., Lin, J.-T. & Chu, C.-W. A ternary cascade structure enhances the efficiency of polymer solar cells. *J. Mater. Chem.* **20**, 2820 (2010).
45. An, Q. *et al.* Enhanced performance of polymer solar cells through sensitization by a narrow band gap polymer. *Solar Energy Materials and Solar Cells* **118**, 30–35 (2013).
46. Su, W. *et al.* Efficient ternary blend all-polymer solar cells with a polythiophene derivative as a hole-cascade material. *J. Mater. Chem. A* **4**, 14752–14760 (2016).
47. Yang, C. *et al.* Nonfullerene Ternary Organic Solar Cell with Effective Charge Transfer between Two Acceptors. *J. Phys. Chem. Letters* **11**, 927–934 (2020).
48. Gasparini, N. *et al.* Designing ternary blend bulk heterojunction solar cells with reduced carrier recombination and a fill factor of 77%. *Nat. Energy* **1**, 16118 (2016).
49. Groves, C. Suppression of geminate charge recombination in organic photovoltaic devices with a cascaded energy heterojunction. *Energy Environ. Sci.* **6**, 1546 (2013).
50. Gasparini, N. *et al.* High-performance ternary organic solar cells with thick active layer exceeding 11% efficiency. *Energy Environ. Sci.* **10**, 885–892 (2017).
51. Zhu, C. *et al.* Tuning the electron-deficient core of a non-fullerene acceptor to achieve over 17% efficiency in a single-junction organic solar cell. *Energy Environ. Sci.* **13**, 2459–2466 (2020).
52. Felekidis, N., Wang, E. & Kemerink, M. Open circuit voltage and efficiency in ternary organic photovoltaic blends. *Energy Environ. Sci.* **9**, 257–266 (2016).
53. Li, M.-Y., Pan, Y.-Q., Sun, G.-Y. & Geng, Y. Charge Transfer Mechanisms Regulated by the Third Component in Ternary Organic Solar Cells. *J. Phys. Chem. Letters* **12**, 8982–8990 (2021).

1 Introduction

54. Zhang, R. *et al.* Optimized domain size and enlarged D/A interface by tuning intermolecular interaction in all-polymer ternary solar cells. *J. Polym. Sci. Part B: Polym. Phys.* **54**, 1811–1819 (2016).
55. Jiang, W. *et al.* Ternary Nonfullerene Polymer Solar Cells with 12.16% Efficiency by Introducing One Acceptor with Cascading Energy Level and Complementary Absorption. *Adv. Mater.* **30** (2018).
56. Fan, B. *et al.* Improved Performance of Ternary Polymer Solar Cells Based on A Nonfullerene Electron Cascade Acceptor. *Adv. Energy Mater.* **7**, 1602127 (2017).
57. Zhou, Z. *et al.* High-efficiency small-molecule ternary solar cells with a hierarchical morphology enabled by synergizing fullerene and non-fullerene acceptors. *Nat Energy* **3**, 952–959 (2018).
58. Löslein, H. *et al.* Transient absorption spectroscopy studies on polythiophene-fullerene bulk heterojunction organic blend films sensitized with a low-bandgap polymer. *Macromolecular rapid communications* **34**, 1090–1097 (2013).
59. Honda, S., Nogami, T., Ohkita, H., Benten, H. & Ito, S. Improvement of the light-harvesting efficiency in polymer/fullerene bulk heterojunction solar cells by interfacial dye modification. *ACS Appl. Mater. Interfaces* **1**, 804–810 (2009).
60. Honda, S., Ohkita, H., Benten, H. & Ito, S. Selective Dye Loading at the Heterojunction in Polymer/Fullerene Solar Cells. *Adv. Energy Mater.* **1**, 588–598 (2011).
61. Honda, S., Yokoya, S., Ohkita, H., Benten, H. & Ito, S. Light-Harvesting Mechanism in Polymer/Fullerene/Dye Ternary Blends Studied by Transient Absorption Spectroscopy. *J. Phys. Chem. C* **115**, 11306–11317 (2011).
62. Upreti, T., Wang, Y., Gao, F. & Kemerink, M. On the Device Physics of High-Efficiency Ternary Solar Cells. *Sol. RRL*, 2200450 (2022).
63. Cheng, P., Li, Y. & Zhan, X. Efficient ternary blend polymer solar cells with indene-C₆₀ bisadduct as an electron-cascade acceptor. *Energy Environ. Sci.* **7**, 2005 (2014).
64. Davis, R. J. *et al.* Determination of energy level alignment at interfaces of hybrid and organic solar cells under ambient environment. *J. Mater. Chem.* **21**, 1721–1729 (2011).
65. Bi, P. *et al.* Reduced non-radiative charge recombination enables organic photovoltaic cell approaching 19% efficiency. *Joule* **5**, 2408–2419 (2021).

66. Khlyabich, P. P., Burkhart, B. & Thompson, B. C. Efficient ternary blend bulk heterojunction solar cells with tunable open-circuit voltage. *JACS* **133**, 14534–14537 (2011).
67. Street, R. A., Davies, D., Khlyabich, P. P., Burkhart, B. & Thompson, B. C. Origin of the tunable open-circuit voltage in ternary blend bulk heterojunction organic solar cells. *JACS* **135**, 986–989 (2013).
68. Street, R. A., Khlyabich, P. P., Rudenko, A. E. & Thompson, B. C. Electronic States in Dilute Ternary Blend Organic Bulk Heterojunction Solar Cells. *J. Phys. Chem. C* **118**, 26569–26576 (2014).
69. Angmo, D., Bjerring, M., Nielsen, N. C., Thompson, B. C. & Krebs, F. C. Fullerene alloy formation and the benefits for efficient printing of ternary blend organic solar cells. *J. Mater. Chem. C* **3**, 5541–5548 (2015).
70. Khlyabich, P. P., Burkhart, B. & Thompson, B. C. Compositional dependence of the open-circuit voltage in ternary blend bulk heterojunction solar cells based on two donor polymers. *JACS* **134**, 9074–9077 (2012).
71. Khlyabich, P. P., Rudenko, A. E., Thompson, B. C. & Loo, Y.-L. Structural Origins for Tunable Open-Circuit Voltage in Ternary-Blend Organic Solar Cells. *Adv. Funct. Mater.* **25**, 5557–5563 (2015).
72. Shen, W. *et al.* High-performance ternary polymer solar cells from a structurally similar polymer alloy. *J. Mater. Chem. A* **5**, 12400–12406 (2017).
73. Kim, M. *et al.* Nonfullerene/Fullerene Acceptor Blend with a Tunable Energy State for High-Performance Ternary Organic Solar Cells. *ACS Appl. Mater. Interfaces* **10**, 25570–25579 (2018).
74. Gao, J. *et al.* Over 14.5% efficiency and 71.6% fill factor of ternary organic solar cells with 300 nm thick active layers. *Energy Environ. Sci.* **13**, 958–967 (2020).
75. Street, R. A., Song, K. W., Northrup, J. E. & Cowan, S. Photoconductivity measurements of the electronic structure of organic solar cells. *Phys. Rev. B* **83**, 211 (2011).
76. Street, R. A. *et al.* Electronic Structure and Transition Energies in Polymer–Fullerene Bulk Heterojunctions. *J. Phys. Chem. C* **118**, 21873–21883 (2014).

1 Introduction

77. Gu, H. *et al.* Simultaneous Performance and Stability Improvement of Ternary Polymer Solar Cells Enabled by Modulating the Molecular Packing of Acceptors. *Sol. RRL* **4**, 2000374 (2020).
78. Yang, Y. *et al.* High-performance multiple-donor bulk heterojunction solar cells. *Nature Photon* **9**, 190–198 (2015).
79. Oh, S. *et al.* Enhanced efficiency and stability of PTB7-Th-based multi-non-fullerene solar cells enabled by the working mechanism of the coexisting alloy-like structure and energy transfer model. *J. Mater. Chem. A* **7**, 22044–22053 (2019).
80. Gobalasingham, N. S., Noh, S., Howard, J. B. & Thompson, B. C. Influence of Surface Energy on Organic Alloy Formation in Ternary Blend Solar Cells Based on Two Donor Polymers. *ACS Appl. Mater. Interfaces* **8**, 27931–27941 (2016).
81. Kouijzer, S., Li, W., Wienk, M. M. & Janssen, R. A. J. Charge transfer state energy in ternary bulk-heterojunction polymer–fullerene solar cells. *J. Photon. Energy* **5**, 57203 (2015).
82. Huang, X., Liu, X., Ding, K. & Forrest, S. R. Is there such a thing as a molecular organic alloy? *Mater. Horiz.* **7**, 244–251 (2020).
83. Ojala, A. *et al.* Parallel bulk-heterojunction solar cell by electrostatically driven phase separation. *Adv. Mater.* **23**, 5398–5403 (2011).
84. Yang, L., Zhou, H., Price, S. C. & You, W. Parallel-like bulk heterojunction polymer solar cells. *JACS* **134**, 5432–5435 (2012).
85. Savoie, B. M., Dunaisky, S., Marks, T. J. & Ratner, M. A. The Scope and Limitations of Ternary Blend Organic Photovoltaics. *Adv. Energy Mater.* **5**, 1400891 (2015).
86. Mok, J. W. *et al.* Parallel bulk heterojunction photovoltaics based on all-conjugated block copolymer additives. *J. Mater. Chem. A* **4**, 14804–14813 (2016).
87. Liu, T. *et al.* Highly Efficient Parallel-Like Ternary Organic Solar Cells. *Chem. Mater.* **29**, 2914–2920 (2017).
88. Kelly, M. A. *et al.* The finale of a trilogy: comparing terpolymers and ternary blends with structurally similar backbones for use in organic bulk heterojunction solar cells. *J. Mater. Chem. A* **6**, 19190–19200 (2018).

89. Hadmojo, W. T. *et al.* Performance Optimization of Parallel-Like Ternary Organic Solar Cells through Simultaneous Improvement in Charge Generation and Transport. *Adv. Funct. Mater.* **27**, 1808731 (2019).
90. Zhang, W. *et al.* Phthalimide Polymer Donor Guests Enable over 17% Efficient Organic Solar Cells via Parallel-Like Ternary and Quaternary Strategies. *Adv. Energy Mater.* **10**, 2001436 (2020).
91. Zhang, M., Zhang, F., Wang, J., An, Q. & Sun, Q. Efficient ternary polymer solar cells with a parallel-linkage structure. *J. Mater. Chem. C* **3**, 11930–11936 (2015).
92. Ke, L. *et al.* Panchromatic ternary/quaternary polymer/fullerene BHJ solar cells based on novel silicon naphthalocyanine and silicon phthalocyanine dye sensitizers. *J. Mater. Chem. A* **5**, 2550–2562 (2017).
93. Lee, T. H. *et al.* Investigation of Charge Carrier Behavior in High Performance Ternary Blend Polymer Solar Cells. *Adv. Energy Mater.* **6**, 1600637 (2016).
94. Blakesley, J. C. & Neher, D. Relationship between energetic disorder and open-circuit voltage in bulk heterojunction organic solar cells. *Phys. Rev. B* **84** (2011).
95. Felekidis, N., Melianas, A. & Kemerink, M. Design Rule for Improved Open-Circuit Voltage in Binary and Ternary Organic Solar Cells. *ACS Appl. Mater. Interfaces* **9**, 37070–37077 (2017).
96. Jain, N. *et al.* Light induced quasi-Fermi level splitting in molecular semiconductor alloys. *Mater. Adv.* **3**, 5344–5349 (2022).
97. Poelking, C. *et al.* Impact of mesoscale order on open-circuit voltage in organic solar cells. *Nat Mater* **14**, 434–439 (2015).
98. Schwarze, M. *et al.* Band structure engineering in organic semiconductors. *Science* **352**, 1446–1449 (2016).
99. Schwarze, M. *et al.* Impact of molecular quadrupole moments on the energy levels at organic heterojunctions. *Nat Commun* **10**, 2466 (2019).
100. Dong, Y. *et al.* Orientation dependent molecular electrostatics drives efficient charge generation in homojunction organic solar cells. *Nat Commun* **11**, 4617 (2020).
101. Warren, R. *et al.* Controlling energy levels and Fermi level en route to fully tailored energetics in organic semiconductors. *Nat Commun* **10**, 5538 (2019).

1 Introduction

102. Chen, Y. *et al.* Achieving High-Performance Ternary Organic Solar Cells through Tuning Acceptor Alloy. *Adv. Mater.* **29** (2017).
103. Li, Y. *et al.* A facile strategy for third-component selection in non-fullerene acceptor-based ternary organic solar cells. *Energy Environ. Sci.* **14**, 5009–5016 (2021).
104. Scharber, M. C. *et al.* Design Rules for Donors in Bulk-Heterojunction Solar Cells—Towards 10 % Energy-Conversion Efficiency. *Adv. Mater.* **18**, 789–794 (2006).
105. Brabec, C. J. *et al.* Polymer-fullerene bulk-heterojunction solar cells. *Adv. Mater.* **22**, 3839–3856 (2010).
106. Proctor, C. M., Kuik, M. & Nguyen, T.-Q. Charge carrier recombination in organic solar cells. *Progress in polymer science* **38**, 1941–1960 (2013).
107. Karki, A., Gillett, A. J., Friend, R. H. & Nguyen, T.-Q. The Path to 20% Power Conversion Efficiencies in Nonfullerene Acceptor Organic Solar Cells. *Adv. Energy Mater.* **11**, 2003441 (2021).
108. He, D., Zhao, F., Wang, C. & Lin, Y. Non-Radiative Recombination Energy Losses in Non-Fullerene Organic Solar Cells. *Adv Funct Materials* **32**, 2111855 (2022).
109. Liu, J. *et al.* Fast charge separation in a non-fullerene organic solar cell with a small driving force. *Nat. Energy* **1**, 16089 EP - (2016).
110. Chen, S. *et al.* Efficient Nonfullerene Organic Solar Cells with Small Driving Forces for Both Hole and Electron Transfer. *Adv. Mater.* **30**, e1804215 (2018).
111. Li, S. *et al.* Highly Efficient Fullerene-Free Organic Solar Cells Operate at Near Zero Highest Occupied Molecular Orbital Offsets. *JACS* (2019).
112. Zhang, J. *et al.* Accurate Determination of the Minimum HOMO Offset for Efficient Charge Generation using Organic Semiconducting Alloys. *Adv. Energy Mater.* **10**, 1903298 (2020).
113. Classen, A. *et al.* The role of exciton lifetime for charge generation in organic solar cells at negligible energy-level offsets. *Nat Energy* **5**, 711–719 (2020).
114. Perdigón-Toro, L. *et al.* Barrierless Free Charge Generation in the High-Performance PM6:Y6 Bulk Heterojunction Non-Fullerene Solar Cell. *Adv. Mater.* **32**, e1906763 (2020).
115. Allen, T. G. *et al.* Reconciling the Driving Force and the Barrier to Charge Separation in Donor–Nonfullerene Acceptor Films. *ACS Energy Lett.* **6**, 3572–3581 (2021).

116. Bertrandie, J. *et al.* The Energy Level Conundrum of Organic Semiconductors in Solar Cells. *Adv. Mater.*, e2202575 (2022).
117. Zhang, G. *et al.* Delocalization of exciton and electron wavefunction in non-fullerene acceptor molecules enables efficient organic solar cells. *Nat. Commun.* **11**, 3943 (2020).
118. Burke, T. M., Sweetnam, S., Vandewal, K. & McGehee, M. D. Beyond Langevin Recombination: How Equilibrium Between Free Carriers and Charge Transfer States Determines the Open-Circuit Voltage of Organic Solar Cells. *Adv. Energy Mater.* **5**, 1500123 (2015).
119. Armin, A., Durrant, J. R. & Shoaee, S. Interplay Between Triplet-, Singlet-Charge Transfer States and Free Charge Carriers Defining Bimolecular Recombination Rate Constant of Organic Solar Cells. *J. Phys. Chem. C* **121**, 13969–13976 (2017).
120. Hinrichsen, T. F. *et al.* Long-lived and disorder-free charge transfer states enable endothermic charge separation in efficient non-fullerene organic solar cells. *Nat. Commun.* **11**, 5617 (2020).
121. Shivhare, R. *et al.* Short Excited-State Lifetimes Mediate Charge-Recombination Losses in Organic Solar Cell Blends with Low Charge-Transfer Driving Force. *Adv. Mater.* **34**, e2101784 (2022).
122. Perdigón-Toro, L. *et al.* Excitons Dominate the Emission from PM6:Y6 Solar Cells, but This Does Not Help the Open-Circuit Voltage of the Device. *ACS Energy Lett.* **6**, 557–564 (2021).
123. Vandewal, K., Benduhn, J. & Nikolis, V. C. How to Determine Optical Gaps and Voltage Losses in Organic Photovoltaic Materials. *Sustainable Energy Fuels* **2**, 538–544 (2018).
124. Jungbluth, A., Kaienburg, P. & Riede, M. Charge transfer state characterization and voltage losses of organic solar cells. *J. Phys. Mater.* **5**, 24002 (2022).
125. Benduhn, J. *et al.* Intrinsic non-radiative voltage losses in fullerene-based organic solar cells. *Nat. Energy* **2**, 17053 (2017).
126. Azzouzi, M. *et al.* Nonradiative Energy Losses in Bulk-Heterojunction Organic Photovoltaics. *Phys. Rev. X* **8** (2018).
127. Chen, X.-K., Coropceanu, V. & Brédas, J.-L. Assessing the nature of the charge-transfer electronic states in organic solar cells. *Nat Commun* **9**, 5295 (2018).

1 Introduction

128. Deping Qian *et al.* Design rules for minimizing voltage losses in high-efficiency organic solar cells. *Nat Mater* **17**, 703–709 (2018).
129. Eisner, F. D. *et al.* Hybridization of Local Exciton and Charge-Transfer States Reduces Nonradiative Voltage Losses in Organic Solar Cells. *JACS* **141**, 6362–6374 (2019).
130. Chen, X.-K. *et al.* A unified description of non-radiative voltage losses in organic solar cells. *Nat Energy* **6**, 799–806 (2021).
131. Melianas, A. & Kemerink, M. Photogenerated Charge Transport in Organic Electronic Materials: Experiments Confirmed by Simulations. *Adv. Mater.* **31**, e1806004 (2019).
132. Upreti, T., Wilken, S., Zhang, H. & Kemerink, M. Slow Relaxation of Photogenerated Charge Carriers Boosts Open-Circuit Voltage of Organic Solar Cells. *J. Phys. Chem. Letters* **12**, 9874–9881 (2021).
133. Vandewal, K., Tvingstedt, K., Gadisa, A., Inganäs, O. & Manca, J. V. Relating the open-circuit voltage to interface molecular properties of donor:acceptor bulk heterojunction solar cells. *Phys. Rev. B* **81** (2010).
134. Graham, K. R. *et al.* Re-evaluating the role of sterics and electronic coupling in determining the open-circuit voltage of organic solar cells. *Adv. Mater.* **25**, 6076–6082 (2013).
135. Wang, Y. *et al.* Optical Gaps of Organic Solar Cells as a Reference for Comparing Voltage Losses. *Adv. Energy Mater.* **8**, 1801352 (2018).
136. Vandewal, K. Interfacial Charge Transfer States in Condensed Phase Systems. *Annual review of physical chemistry* **67**, 113–133 (2016).
137. Lin, Y. L., Fusella, M. A. & Rand, B. P. The Impact of Local Morphology on Organic Donor/Acceptor Charge Transfer States. *Adv. Energy Mater.* **8**, 1702816 (2018).
138. Marcus, R. A. Relation between charge transfer absorption and fluorescence spectra and the inverted region. *J. Phys. Chem. C* **93**, 3078–3086 (1989).
139. Jortner, J. Temperature dependent activation energy for electron transfer between biological molecules. *J. Chem. Phys.* **64**, 4860–4867 (1976).
140. Göhler, C. *et al.* Temperature-Dependent Charge-Transfer-State Absorption and Emission Reveal the Dominant Role of Dynamic Disorder in Organic Solar Cells. *Phys. Rev. Applied* **15** (2021).

141. List, M. *et al.* Correct determination of charge transfer state energy from luminescence spectra in organic solar cells. *Nat Commun* **9**, 3631 (2018).
142. Armin, A. *et al.* Limitations of Charge Transfer State Parameterization Using Photovoltaic External Quantum Efficiency. *Adv. Energy Mater.* **10**, 2001828 (2020).
143. Göhler, C. & Deibel, C. The Role of Dynamic and Static Disorder for Charge-Transfer States in Organic Bulk Heterojunction Solar Cells. *ACS Energy Lett.* **7**, 2156–2164 (2022).
144. Belova, V. *et al.* Evidence for Anisotropic Electronic Coupling of Charge Transfer States in Weakly Interacting Organic Semiconductor Mixtures. *JACS* **139**, 8474–8486 (2017).
145. Broch, K. *et al.* Time-resolved photoluminescence spectroscopy of charge transfer states in blends of pentacene and perfluoropentacene. *Phys. Status Solidi RRL* **11**, 1700064 (2017).
146. Lami, V., Hofstetter, Y. J., Butscher, J. F. & Vaynzof, Y. Energy Level Alignment in Ternary Organic Solar Cells. *Adv. Electron. Mater.* **6**, 2000213 (2020).
147. Liu, T. *et al.* Use of two structurally similar small molecular acceptors enabling ternary organic solar cells with high efficiencies and fill factors. *Energy Environ. Sci.* **11**, 3275–3282 (2018).
148. Cai, Y. *et al.* A Well-Mixed Phase Formed by Two Compatible Non-Fullerene Acceptors Enables Ternary Organic Solar Cells with Efficiency over 18.6%. *Adv. Mater.* **33**, 2101733 (2021).
149. Karuthedath, S. *et al.* Mixing of Non-Fullerene Acceptors Ionization Energies: An Additional Tool to Tune the Quantum Efficiency of Ternary Organic Solar Cells. *SSRN Journal* (2022).
150. Qi, B., Zhou, Q. & Wang, J. Exploring the open-circuit voltage of organic solar cells under low temperature. *Scientific reports* **5**, 11363 (2015).
151. Fritsch, T. *et al.* On the Interplay between CT and Singlet Exciton Emission in Organic Solar Cells with Small Driving Force and Its Impact on Voltage Loss. *Adv. Energy Mater.*, 2200641 (2022).
152. Xie, Y. *et al.* Ternary Organic Solar Cells with Small Nonradiative Recombination Loss. *ACS Energy Lett.* **4**, 1196–1203 (2019).

1 Introduction

153. Yu, R. *et al.* Improved Charge Transport and Reduced Nonradiative Energy Loss Enable Over 16% Efficiency in Ternary Polymer Solar Cells. *Adv. Mater.* **31** (2019).
154. Li, Y., Zhang, Y., Zuo, X. & Lin, Y. Organic photovoltaic electron acceptors showing aggregation-induced emission for reduced nonradiative recombination. *Chem. Comm.* **57**, 5135–5138 (2021).
155. Liu, X. *et al.* Reducing non-radiative recombination energy loss via a fluorescence intensifier for efficient and stable ternary organic solar cells. *Mater. Horiz.* **8**, 2335–2342 (2021).
156. Zhan, L. *et al.* Desired open-circuit voltage increase enables efficiencies approaching 19% in symmetric-asymmetric molecule ternary organic photovoltaics. *Joule* **6**, 662–675 (2022).
157. Wang, C. *et al.* Ternary organic solar cells with enhanced open circuit voltage. *Nano Energy* **37**, 24–31 (2017).
158. Zhao, F., Wang, C. & Zhan, X. Morphology Control in Organic Solar Cells. *Adv. Energy Mater.* **8**, 1703147 (2018).
159. Zhu, L. *et al.* Progress and prospects of the morphology of non-fullerene acceptor based high-efficiency organic solar cells. *Energy Environ. Sci.* **14**, 4341–4357 (2021).
160. Westacott, P. *et al.* On the role of intermixed phases in organic photovoltaic blends. *Energy Environ. Sci.* **6**, 2756 (2013).
161. Ma, W. *et al.* Quantification of nano- and mesoscale phase separation and relation to donor and acceptor quantum efficiency, J(sc), and FF in polymer:fullerene solar cells. *Adv. Mater.* **26**, 4234–4241 (2014).
162. Xu, X., Li, Y. & Peng, Q. Ternary Blend Organic Solar Cells: Understanding the Morphology from Recent Progress. *Adv. Mater.*, 2107476 (2021).
163. Müller-Buschbaum, P. The active layer morphology of organic solar cells probed with grazing incidence scattering techniques. *Adv. Mater.* **26**, 7692–7709 (2014).
164. Ameri, T. *et al.* Morphology analysis of near IR sensitized polymer/fullerene organic solar cells by implementing low bandgap heteroanalogue C-/Si-PCPDTBT. *J. Mater. Chem. A* **2**, 19461–19472 (2014).
165. Flory, P. J. *Principles of Polymer Chemistry* (Cornell University Press, 1953).

166. Yang, C. *et al.* Molecular design of a non-fullerene acceptor enables a P3HT-based organic solar cell with 9.46% efficiency. *Energy Environ. Sci.* **13**, 2864–2869 (2020).
167. Ai, Q. *et al.* Ternary organic solar cells: compatibility controls for morphology evolution of active layers. *J. Mater. Chem. C* **5**, 10801–10812 (2017).
168. Ghasemi, M. *et al.* Panchromatic Sequentially Cast Ternary Polymer Solar Cells. *Adv. Mater.* **29** (2017).
169. Pan, L. *et al.* Efficient Organic Ternary Solar Cells Employing Narrow Band Gap Diketopyrrolopyrrole Polymers and Nonfullerene Acceptors. *Chem. Mater.* **32**, 7309–7317 (2020).
170. Wu, S. Calculation of Interfacial Tension in Polymer Systems. *J. Polymer. Sci.* **34**, 19–30 (1971).
171. Du, X. *et al.* Crystallization of Sensitizers Controls Morphology and Performance in Si-/C-PCPDTBT-Sensitized P3HT:ICBA Ternary Blends. *Macromolecules* **50**, 2415–2423 (2017).
172. Perea, J. D. *et al.* Combined Computational Approach Based on Density Functional Theory and Artificial Neural Networks for Predicting The Solubility Parameters of Fullerenes. *J. Phys. Chem. B* **120**, 4431–4438 (2016).
173. Perea, J. D. *et al.* Introducing a New Potential Figure of Merit for Evaluating Microstructure Stability in Photovoltaic Polymer-Fullerene Blends. *J. Phys. Chem. C* **121**, 18153–18161 (2017).
174. Wang, Z. *et al.* From Alloy-Like to Cascade Blended Structure: Designing High-Performance All-Small-Molecule Ternary Solar Cells. *JACS* **140**, 1549–1556 (2018).
175. Khlyabich, P. P., Rudenko, A. E., Street, R. A. & Thompson, B. C. Influence of polymer compatibility on the open-circuit voltage in ternary blend bulk heterojunction solar cells. *ACS Appl. Mater. Interfaces* **6**, 9913–9919 (2014).
176. Mai, J. *et al.* Understanding Morphology Compatibility for High-Performance Ternary Organic Solar Cells. *Chem. Mater.* **28**, 6186–6195 (2016).
177. An, Q. *et al.* Two compatible polymer donors contribute synergistically for ternary organic solar cells with 17.53% efficiency. *Energy Environ. Sci.* **13**, 5039–5047 (2020).

1 Introduction

178. Xie, G., Zhang, Z., Su, Z., Zhang, X. & Zhang, J. 16.5% efficiency ternary organic photovoltaics with two polymer donors by optimizing molecular arrangement and phase separation. *Nano Energy* **69**, 104447 (2020).
179. Liu, T. *et al.* Ternary Organic Solar Cells Based on Two Compatible Nonfullerene Acceptors with Power Conversion Efficiency >10%. *Adv. Mater.* **28**, 10008–10015 (2016).
180. Ma, X. *et al.* Achieving 17.4% Efficiency of Ternary Organic Photovoltaics with Two Well-Compatible Nonfullerene Acceptors for Minimizing Energy Loss. *Adv. Energy Mater.* **10**, 2001404 (2020).
181. Liu, F. *et al.* Organic Solar Cells with 18% Efficiency Enabled by an Alloy Acceptor: A Two-in-One Strategy. *Adv. Mater.* **33**, 2100830 (2021).
182. Jiang, M. *et al.* Rational compatibility in a ternary matrix enables all-small-molecule organic solar cells with over 16% efficiency. *Energy Environ. Sci.* **14**, 3945–3953 (2021).
183. Zhan, L. *et al.* Over 17% efficiency ternary organic solar cells enabled by two non-fullerene acceptors working in an alloy-like model. *Energy Environ. Sci.* **13**, 635–645 (2020).
184. Luo, Y. *et al.* A large-bandgap copolymer donor for efficient ternary organic solar cells. *Mater. Chem. Front.* **5**, 6139–6144 (2021).
185. Privado, M. *et al.* Fullerene/Non-fullerene Alloy for High-Performance All-Small-Molecule Organic Solar Cells. *ACS Appl. Mater. Interfaces* **13**, 6461–6469 (2021).
186. Fukagawa, H. *et al.* Origin of the highest occupied band position in pentacene films from ultraviolet photoelectron spectroscopy: Hole stabilization versus band dispersion. *Phys. Rev. B* **73** (2006).
187. Chen, W. *et al.* Molecular Orientation-Dependent Ionization Potential of Organic Thin Films. *Chem. Mater.* **20**, 7017–7021 (2008).
188. Zhong, Y. *et al.* Crystallization-Induced Energy Level Change of [6,6]-Phenyl-C 61 -Butyric Acid Methyl Ester (PCBM) Film: Impact of Electronic Polarization Energy. *J. Phys. Chem. C* **119**, 23–28 (2015).
189. Tietze, M. L. *et al.* Correlation of open-circuit voltage and energy levels in zinc-phthalocyanine: C 60 bulk heterojunction solar cells with varied mixing ratio. *Phys. Rev. B* **88** (2013).

190. Mollinger, S. A., Vandewal, K. & Salleo, A. Microstructural and Electronic Origins of Open-Circuit Voltage Tuning in Organic Solar Cells Based on Ternary Blends. *Adv. Energy Mater.* **5**, 1501335 (2015).
191. Kästner, C., Vandewal, K., Egbe, D. A. M. & Hoppe, H. Revelation of Interfacial Energetics in Organic Multiheterojunctions. *Adv. Sci.* **4**, 1600331 (2017).
192. Yuan, J. *et al.* Effects of energetic disorder in bulk heterojunction organic solar cells. *Energy Environ. Sci.* **15**, 2806–2818 (2022).
193. Sharma, A. & Sheinman, M. Analytical approximation for chemical potential in organic materials with Gaussian density of states. *J. Phys. D: Appl. Phys.* **46**, 125106 (2013).
194. Lv, J. *et al.* Energetic Disorder and Activation Energy in Efficient Ternary Organic Solar Cells with Nonfullerene Acceptor Eh-IDTBR as the Third Component. *Sol. RRL* **4**, 1900403 (2020).
195. Zeng, Y. *et al.* Exploring the Charge Dynamics and Energy Loss in Ternary Organic Solar Cells with a Fill Factor Exceeding 80%. *Adv. Energy Mater.* **11**, 2101338 (2021).
196. Fu, H. *et al.* Efficient Ternary Organic Solar Cells Enabled by the Integration of Nonfullerene and Fullerene Acceptors with a Broad Composition Tolerance. *Adv. Funct. Mater.* **29**, 1807006 (2019).
197. Lu, H. *et al.* Ternary-Blend Polymer Solar Cells Combining Fullerene and Nonfullerene Acceptors to Synergistically Boost the Photovoltaic Performance. *Adv. Mater.* **28**, 9559–9566 (2016).
198. Dai, S. *et al.* Enhancing the Performance of Polymer Solar Cells via Core Engineering of NIR-Absorbing Electron Acceptors. *Adv. Mater.* **30**, e1706571 (2018).
199. Kumari, T., Lee, S. M., Kang, S.-H., Chen, S. & Yang, C. Ternary solar cells with a mixed face-on and edge-on orientation enable an unprecedented efficiency of 12.1%. *Energy Environ. Sci.* **10**, 258–265 (2017).
200. Lee, H., Mun, J., Nguyen, N. N., Rho, J. & Cho, K. Open-circuit voltage of organic solar cells: Effect of energetically and spatially nonuniform distribution of molecular energy levels in the photoactive layer. *Nano Energy* **78**, 105336 (2020).
201. Du, X. *et al.* Efficient Polymer Solar Cells Based on Non-fullerene Acceptors with Potential Device Lifetime Approaching 10 Years. *Joule* **3**, 215–226 (2019).

1 Introduction

202. Burlingame, Q. *et al.* Intrinsically stable organic solar cells under high-intensity illumination. *Nature* **573**, 394–397 (2019).
203. Mateker, W. R. & McGehee, M. D. Progress in Understanding Degradation Mechanisms and Improving Stability in Organic Photovoltaics. *Adv. Mater.* **29** (2017).
204. Duan, L. & Uddin, A. Progress in Stability of Organic Solar Cells. *Adv. Sci.* **7**, 1903259 (2020).
205. Hewlett, R. M. & McLachlan, M. A. Surface Structure Modification of ZnO and the Impact on Electronic Properties. *Adv. Mater.* **28**, 3893–3921 (2016).
206. Znaidi, L. Sol–gel-deposited ZnO thin films: A review. *Materials Science and Engineering: B* **174**, 18–30 (2010).
207. Janotti, A. & van de Walle, C. G. Fundamentals of zinc oxide as a semiconductor. *Rep. Prog. Phys.* **72**, 126501 (2009).
208. Melnick, D. A. Zinc Oxide Photoconduction, an Oxygen Adsorption Process. *The Journal of Chemical Physics* **26**, 1136–1146 (1957).
209. Manor, A., Katz, E. A., Tromholt, T. & Krebs, F. C. Electrical and Photo-Induced Degradation of ZnO Layers in Organic Photovoltaics. *Adv. Energy Mater.* **1**, 836–843 (2011).
210. Lilliedal, M. R., Medford, A. J., Madsen, M. V., Norrman, K. & Krebs, F. C. The effect of post-processing treatments on inflection points in current–voltage curves of roll-to-roll processed polymer photovoltaics. *Solar Energy Materials and Solar Cells* **94**, 2018–2031 (2010).
211. Jiang, Y. *et al.* Photocatalytic Effect of ZnO on the Stability of Nonfullerene Acceptors and its Mitigation by SnO₂ for Nonfullerene Organic Solar Cells. *Mater. Horiz.* **6**, 1438–1443 (2019).
212. Park, S. & Son, H. J. Intrinsic Photo-Degradation and Mechanism of Polymer Solar Cells: the Crucial Role of Non-Fullerene Acceptors. *J. Mater. Chem. A* **7**, 25830–25837 (2019).

2 Characterization Methods

2.1 Ultraviolet-Visible Spectroscopy

Since the efficiency of solar cells correlates with the cell's capability to absorb light from the sun, spectroscopy in the ultraviolet (UV) and visible (Vis) spectral range is an essential method. The parameters accessible with this method are the samples' transmittance (T), absorbance (A), and reflectance (R). The transmittance compares the intensity of light before it passes through a sample (I_0) with the intensity after passing through (I) and is usually expressed as a percentage:

$$T = \frac{I}{I_0} \quad (2.1)$$

The absorbance is derived from this as shown in equation (2.2) and is a dimensionless quantity, which is often also denoted as optical density.

$$A = -\log(T) = \log\left(\frac{I_0}{I}\right) \quad (2.2)$$

The reflectance R compares the intensity of the light reflected from a sample (I_R) with the intensity of light reflected from a reference material ($I_{R,0}$), usually a white standard.

$$R = \frac{I_R}{I_{R,0}} \quad (2.3)$$

Different types of samples are measured with different geometries and methods. Solutions are usually measured in transmission mode and evaluated according to the Lambert-Beer law that neglects any scattering losses and relates the absorbed light directly to the path length L through the sample, the concentration c and the extinction coefficient ε of the solution:

$$A = \varepsilon \cdot c \cdot L \quad (2.4)$$

UV-vis spectra of powders obtained in diffuse reflectance can be measured evaluated the Kubelka-Munk theory, which assumes that absorption and reflection of the powder surface is neglectable and instead the behavior is dominated by scattering/diffuse reflectance. The obtained diffuse reflectance R then can be used to approximate the absorption:

$$A = \frac{(1 - R)^2}{2R} \quad (2.5)$$

For solar cells, however, measurements of solid films on a transparent substrate are most commonly used. Films can be measured in transmission mode by measuring the transmittance

2 Characterization Methods

of the substrate separately and subtracting it. In this case the transmission/absorbance depends on the film thickness L , and therefore, usually the absorption coefficient α is used instead. Following the Lambert-Beer law, the intensity decays exponentially with the penetration depth L in the film:

$$I = I_0 \cdot e^{-\alpha \cdot L} \quad (2.6)$$

Inserting equation (2.2) in equation (2.6) and solving by the absorption coefficient results in equation (2.7), with the pre-factor 2.303 coming from the conversion of the logarithm to the natural logarithm.¹

$$\alpha = 2.303 \cdot \frac{A}{L} \quad (2.7)$$

However, two factors are neglected with this type of measurement, which is why the absorption measured in this way deviates significantly from the true absorption of the organic solar cell. The first factor involves reflective losses, which can be easily accounted for by measuring each film in transmission and reflection mode. The second, more complicated influence comes from the organic solar cells behaving as a non-linear optical cavity.² Due to reflections and interferences occurring at the interfaces of the multiple layers the electric field intensity distribution within the devices is complex and has to be assessed via a transfer-matrix approach which considers the thicknesses and optical constants of the different layers.³ Nevertheless, this influence usually is ignored for normal absorption measurements and only has to be considered for the calculation of internal quantum efficiencies.

UV-Vis spectra of thin films were recorded in transmission with a Perkin-Elmer Lambda 1050 spectrometer including an integrating sphere and an InGaAs-detector.

2.2 Photoluminescence Spectroscopy

Photoluminescence (PL) spectroscopy monitors the spontaneous emission of light in the visible range after the absorption of photons, and thus is the complementary method of UV-Vis spectroscopy. In principle, two different phenomena can be observed with PL spectroscopy, namely fluorescence and phosphorescence (see **Figure 2.1**). Fluorescence is the radiative transition from a molecule's excited state S_1 to the ground state S_0 and usually occurs with minimal time delays compared to the absorption. Phosphorescence occurs when the excited singlet state S_1 undergoes a non-radiative intersystem crossing to the triplet state T_1 (or its higher vibrational levels), which then decays radiatively to the ground state. Since transitions

with a change of multiplicity are formally forbidden, phosphorescence occurs on longer timescales than fluorescence and usually shows weaker intensities.⁴

For PL measurements, the sample is usually excited with a monochromatic light source and the photons emitted from the sample are spectrally dispersed and collected by a photodetector. The photodetector is often equipped with a cut-off filter in order to avoid detecting a strong signal from the excitation wavelength. Excitation wavelengths and recorded spectral range must be selected appropriately for each sample.

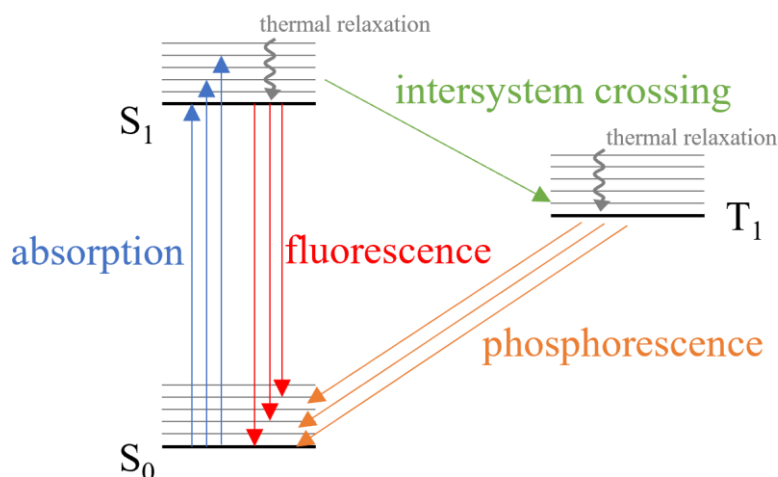


Figure 2.1: Simplified Jablonski diagram of a molecule. By the absorption of a photon, the molecule is excited from its ground state S_0 to its excited state S_1 . If it is excited to higher vibrational levels of S_1 a thermal relaxation to the vibrational ground state occurs. Then, the excited state can either decay radiatively (fluorescence) or it can undergo an intersystem crossing with a change of multiplicity, forming an excited triplet state T_1 . The radiative decay of the triplet state to the ground state is called phosphorescence.

Following the rule of thumb that a good solar cell also needs to be a light emitting diode, most solar cell materials exhibit a strong photoluminescence, with dominating radiative decay pathways, since non-radiative decay corresponds to loss mechanisms in the solar cell.⁵ This also applies to the separate materials in organic solar cells, however, when a donor and an acceptor are combined to a bulk heterojunction, the PL of the separate materials is quenched, since a charge transfer occurs between the two materials to form a CT state. Since CT states usually have small transition dipole moments, they show a negligible PL intensity. For this reason, the quenching of the pristine materials' PL in the BHJ can be used as a measure of effectiveness of the charge transfer.

PL spectra were obtained with a FluoTime 300 (PicoQuant), using an excitation wavelength of 378 nm provided by a diode laser (LDH-P-C-375, PicoQuant).

2.3 Raman Spectroscopy

Raman spectroscopy is a technique to study vibrational modes of molecules. In contrast to its complementary method infrared spectroscopy, it does not rely on absorption of light but on its inelastic scattering. A monochromatic light source, often a laser in the visible or near-infrared range, illuminates the sample and the photons interact with molecular vibrations, resulting in inelastic scattering processes. This interaction can either decrease (Stokes shift) or increase (anti-Stokes shift) the photon's energy. This so-called Raman effect arises from the interaction of the light's electric field with the electron cloud of the molecule and therefore its extent depends on the polarizability of the respective sample. Strongly polarized bonds such as C-O or C-F, which generate a strong absorption signal in IR-spectroscopy, often have a lower polarizability and thus show a low intensity in Raman spectroscopy. On the other hand, symmetrical bonds such as C=C, which are not visible with IR-spectroscopy, often have a high polarizability and are easy to detect with Raman. To predict if a vibrational transition is Raman or IR active, selection rules derived from group theory are applied. Those selection rules state that normal modes of vibration are IR active if they transform similar to the cartesian coordinates x, y, z . In contrast, normal modes are Raman active if they transform similar to the products of the cartesian coordinates ($xy, xz, yz, x^2, y^2, z^2$).⁶

Raman spectra are usually showing the difference in energy of the incoming photons and the detected photons by using wavenumbers as a unit, resulting in a symmetric spectrum with negative values for an anti-Stokes shift and positive values for a Stokes-shift. However, usually only the positive part is shown since the signal intensity for the Stokes-shift is larger.

Fourier-transform Raman spectra of powder samples were recorded with a RAM II extension of the Bruker Vertex 70 with a germanium detector at an excitation wavelength of 1064 nm and a laser power of 50 mW.

2.4 X-ray Diffraction

The absorbing layer of bulk heterojunction organic solar cells has a complex nanomorphology consisting of domains in the nanometer-range with varying size, composition, and crystallinity. This structure is decisive for the performance of the solar cells and therefore, there is a high interest in understanding it in detail. An interesting technique for characterization is X-ray diffraction (XRD), since it can provide information about domain sizes and crystallinity of the BHJ.

XRD is based on the elastic scattering of X-rays by the electron density in a material. Since the lattice planes in a crystal determine differences in electron density, X-rays are scattered by them. Most of the scattered X-ray waves cancel each other out but under certain conditions constructive interference is possible, which is described by Bragg's law:

$$n\lambda = 2d \cdot \sin\theta \quad (2.8)$$

Here, λ is the wavelength of the incident X-rays, n is an integer variable describing the order of scattering, d is the distance of the lattice planes and θ is the X-ray incident angle. In case of a powder sample, the orientation of the crystal lattice planes is equally distributed and the incident angles causing a constructive interference can be depicted as intensity maxima (reflexes) in the 1D diffraction pattern.⁷

The width of the reflexes is determined by the size of the scattering crystallites. An infinitely large crystallite would cause an infinitely narrow reflex, only broadened by the limits of instrumental resolution, but smaller crystallites cause a broadening of the reflexes. The correlation of the reflection broadening at half the maximum intensity (full width at half maximum = FWHM) and the mean crystallite size s is given by the Scherrer equation:

$$s = \frac{K\lambda}{\beta \cos\theta} \quad (2.9)$$

Here, K is a factor related to the shape of the crystallites (usually set at $K=0.9$), λ is the X-ray wavelength, β is the reflex broadening at FWHM and θ is the Bragg angle.

In case of organic solar cells, the samples usually are thin films with moderate crystallinity, which is why the scattering volume is very low in a transmission geometry measurement. For this reason, X-ray scattering experiments for such samples are commonly performed in a so-called grazing-incidence geometry, where the X-ray beam impinges onto the sample under a very small incident angle. This kind of geometry has two advantages: Firstly, a focused beam with small diameter under a small incident angle is projected into a long stripe on the sample surface, increasing the interaction volume. Secondly, when the incident angle is smaller than the critical angle of the material studied, the incident beam undergoes total external reflection. Under those conditions, the incident beam cannot propagate into the material, instead it is exponentially damped (evanescent wave), and therefore undesired scattering from the bulk is suppressed.⁸

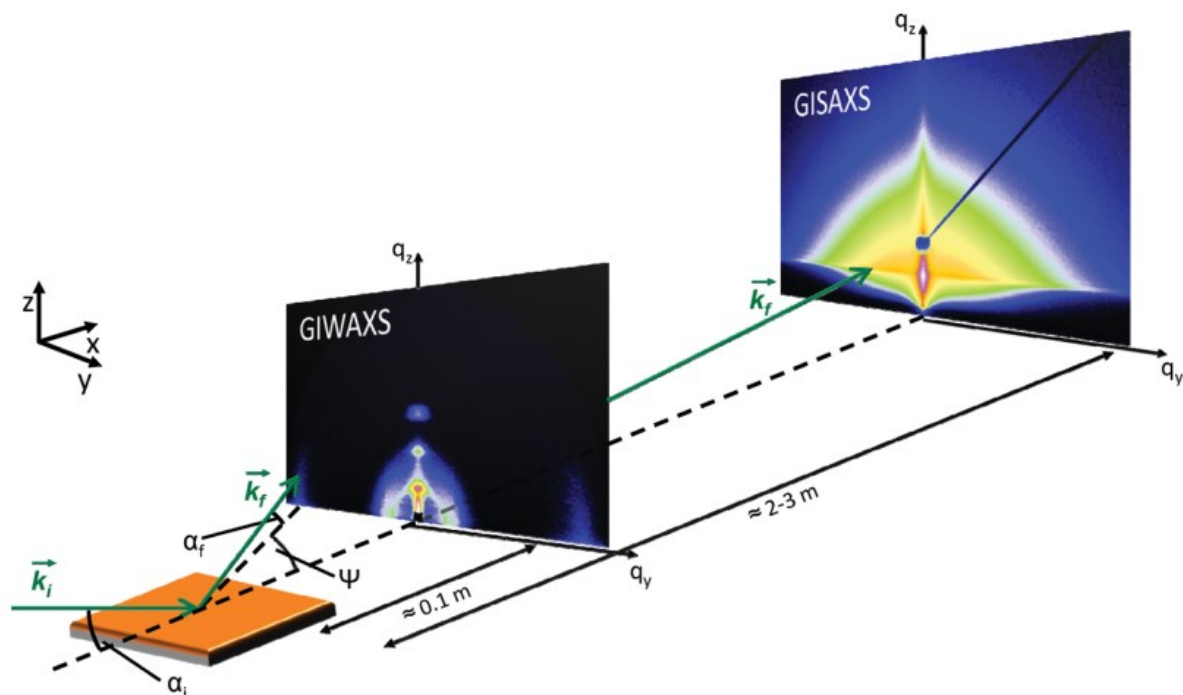


Figure 2.2: Schematic depiction of the measurement geometry for grazing-incidence X-ray scattering with a 2-dimensional detector. The sample surface lies in the x-y plane and the wave vector k_i comes in under the angle α_i . The scattered wave vector k_f is deflected by an angle ψ in y-direction and an angle α_f in z-direction. When the detector is placed near the sample, the larger scattering angles are monitored, for a detector being placed with a larger distance, smaller scattering angles can be examined.⁸

Grazing-incidence X-ray scattering is classified into two sub-groups based on the exit angle of the scattered signal. Grazing-incidence wide-angle X-ray scattering (GIWAXS) results from larger scattering angles and probes molecular length-scales. Grazing-incidence small-angle X-ray scattering (GISAXS) results from smaller scattering angles, and probes nanometer length-scales, such as domain sizes and distances. As shown in **Figure 2.2**, GIWAXS and GISAXS measurements of thin film samples are usually performed with a 2-D detector, to obtain additional information about the orientation of crystallites and domains in the sample.⁸

Wide angle XRD measurements of powder samples were performed in transmission with a STOE STADI P diffractometer (Cu $K_{\alpha 1}$, $\lambda = 1.5406 \text{ \AA}$) and a Ge(111) single crystal monochromator equipped with a DECTRIS solid state strip detector MYTHEN 1K.

GIWAXS and GISAXS measurements of thin films on glass substrates were done in collaboration with the group of Prof. Müller-Buschbaum (TU Munich) at the P03 beamline at DESY (Hamburg).

2.5 X-Ray Photoelectron Spectroscopy

The method X-ray photoelectron spectroscopy (XPS) makes use of the photoelectric effect to determine the elements and their chemical state in a sample. For the measurement, the sample is irradiated with X-rays of a specific wavelength, whereby electrons are emitted. The kinetic energy E_{kin} of the emitted electrons, which is measured by a detector, is given by the energy E_{Xray} of the incident X-rays minus the electron's binding energy $E_{binding}$ and a surface and setup dependent correction factor Φ :

$$E_{kin} = E_{Xray} - E_{binding} - \Phi \quad (2.10)$$

As a result of the measurement a plot of the number of electrons at each binding energy is obtained. Since every element has a unique set of binding energies coming from its orbitals, the peaks can often be clearly assigned to an element. The signal intensity directly correlates with the present number of atoms of one element, whereby the composition of a sample can be inferred. However, it must be noted that XPS is a surface-sensitive method and cannot provide information about the bulk of a sample.

A particularly interesting possibility arises from the fact that the electron binding energies of an atom are changed according to the oxidation state or the direct chemical environment of the atom. This can be used to identify different species of the same element and to deduce, for example, the chemical bonds present.⁹

XPS measurements of thin films on glass substrates were carried out in collaboration with the group of Prof. Hofmann (TU Darmstadt) in the cluster tool Darmstadt Integrated System for Solar Cell research (DAISY-SOL) using a Thermo Fisher Scientific Escalab 250 system equipped with a monochromatized Al K α X-ray source (1486.6 eV).

2.6 Contact Angle Measurements

Contact angle measurements are an interesting tool for solution-processed organic solar cells, since on the one hand the wetting of the active layer solution on the respective substrate can be analyzed and on the other hand surface energies of the active layer components can be calculated, from which, in turn, their miscibility with each other can be concluded.

The contact angle θ is defined as the angle at the three-phase boundary formed by a liquid droplet on a solid substrate, surrounded by a gaseous atmosphere, as depicted in **Figure 2.3**.

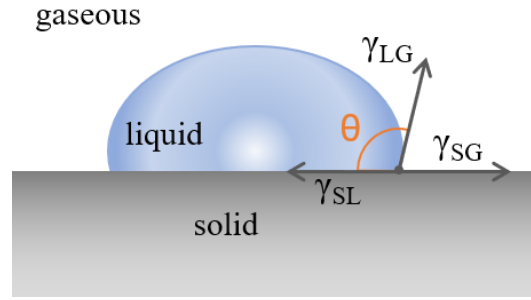


Figure 2.3: Schematic depiction of the contact angle θ formed between a liquid droplet and a solid substrate. The grey arrows indicate the interfacial energy vectors γ between the different phases.

To measure the contact angle, a drop of a liquid is dispensed onto a substrate surface and a photograph is taken of it, based on which the angle between the substrate and the drop surfaces is determined. The value of the contact angle is determined by the thermodynamic equilibrium of the solid-liquid interfacial energy (γ_{LS}), the solid-gas interfacial energy (γ_{SG}), and the liquid-gas interfacial energy (γ_{LG}), as described by the Young equation:¹⁰

$$\gamma_{SG} - \gamma_{SL} - \gamma_{LG} \cos\theta = 0 \quad (2.11)$$

The contact angle therefore is a direct measure for the wetting of a liquid on a solid, whereas a smaller contact angle accounts for a better wettability. This method, for example, can be used to select appropriate solvents for the coating process, which show good wettability on the respective substrate.

However, the more frequently used application is the determination of materials' surface energies (whereby surface energy is a different term for the solid-gas interfacial energy γ_{SG}). Interfacial energies can be split into the interactions of polar and dispersive components of the respective phases:

$$\gamma = \gamma^p + \gamma^d \quad (2.12)$$

Since the dominating interactions between two phases therefore is correlated with their polarities, different theories exist to describe surface energies. For the surface energy of polymers, where polar-polar interactions have a strong contribution, usually a model developed by Souheng Wu is employed,¹¹ which describes the correlation of the interfacial energy of a liquid (γ_{LG}) and of a solid planar film (γ_{SG}) with the contact angle between the solid and the liquid. Since the gaseous phase normally is air in all cases, those interfacial energies for simplicity are named γ_L and γ_S in the following:¹²

$$\gamma_L \cdot (1 + \cos\theta) = \frac{4 \cdot \gamma_L^d \cdot \gamma_S^d}{\gamma_L^d + \gamma_S^d} + \frac{4 \cdot \gamma_L^p \cdot \gamma_S^p}{\gamma_L^p + \gamma_S^p} \quad (2.13)$$

By measuring the contact angle of two different liquids with known polar and dispersive components, usually water and glycerol, a numerically solvable linear system of two equations

is obtained with the polar and dispersive components of the solid materials as variables, from which the total surface energy can be calculated with equation (2.12).

By determining the surface energy of different active layer materials, their miscibility in the bulk heterojunction can be inferred, since the closer the surface energies, the higher the miscibility. This can also be expressed quantitatively via the Flory-Huggins parameter χ :¹³

$$\chi_{12} = K(\sqrt{\gamma_1} - \sqrt{\gamma_2})^2 \quad (2.14)$$

with the surface energies of films of the two materials γ_1 and γ_2 (in units of mJ/m²) and the proportionality constant $K=116 \times 10^3 \text{ m}^{-1/2}$. A smaller Flory-Huggins parameter indicates a better miscibility of the two components.

Contact angle measurements were performed with an optical tensiometer (nanoScience instruments) and the photographs were evaluated with the One Attension software package in the Young-Laplace analysis method.

2.7 Atomic Force Microscopy

Atomic force microscopy (AFM) is a powerful microscopic method, since in contrast to classical optical microscopy methods it is not limited by the optical diffraction limit. The imaging is based on the physical contact of a measuring tip with the sample surface and can obtain a resolution in the order of several nanometers. In doing so, the tip can either actually touch the sample constantly (contact mode) or with a specific frequency (tapping mode), or the tip is held above the sample at a certain distance controlled by the interaction force between tip and the surface (force measurement), while the sample is moved under the tip, usually by a piezo-controlled stage, to obtain a 2-dimensional image. The movement of the tip is monitored via a laser spot that is reflected from the cantilever surface, to which the tip is attached, and detected by a photodetector, as schematically shown in **Figure 2.4**.

The most frequently used measurement method is the tapping mode, which has several advantages compared to the contact mode. Since in contact mode a static bending of the cantilever has to be monitored, the influences of noise and drift are difficult to distinguish from the measurement signal, especially since the interaction forces between tip and surface have to be kept small (and therefore also the bending of the cantilever) to not mechanically destroy the sample surface with the tip. In tapping mode, on the other hand, the tip is driven to oscillate up and down close to its resonance frequency, minimizing the actual contact between tip and surface and also reducing the impact of noise.¹⁴

2 Characterization Methods

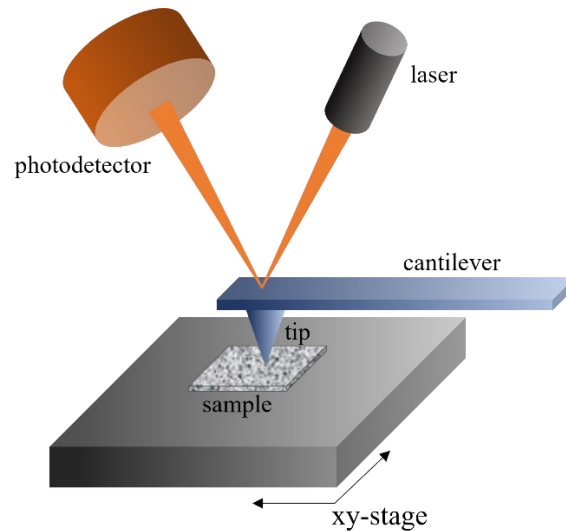


Figure 2.4: Typical configuration of an atomic force microscope. The tip is in contact with the sample (or in tapping mode) while the xy-stage is moving. The laser points onto the cantilever and the beam is reflected from the surface to the photodetector. From the displacement of the laser beam with respect to the detector, the deflection of the cantilever can be inferred while scanning over the sample surface.

AFM measurements were done with a NANOINK atomic force microscope in tapping mode.

2.8 Current-Voltage Characterization and Light Intensity Dependence

The most fundamental characterization of each solar cell is done with a current-voltage measurement which provides the basic parameters to describe the cell's performance. For this measurement, a voltage sweep is performed on the solar cell while being illuminated and the generated current is measured. For comparable results, the illumination must be done with a standardized spectrum, usually the AM 1.5 global spectrum (AM1.5 G), which corresponds to the solar spectrum as perceived on earth under a solar zenith angle of 48.2° with a power density of 1000 W/m^2 .¹⁵ Usually, such a spectrum is achieved by using a xenon arc lamp and correcting its output with optical filters. The intensity of the lamp is calibrated with a silicon diode whose current under AM1.5 G is known. The use of an unsuitable light source or an incorrect calibration diode can lead to a so-called spectral mismatch and thus to an erroneous determination of the cell efficiency.¹⁵

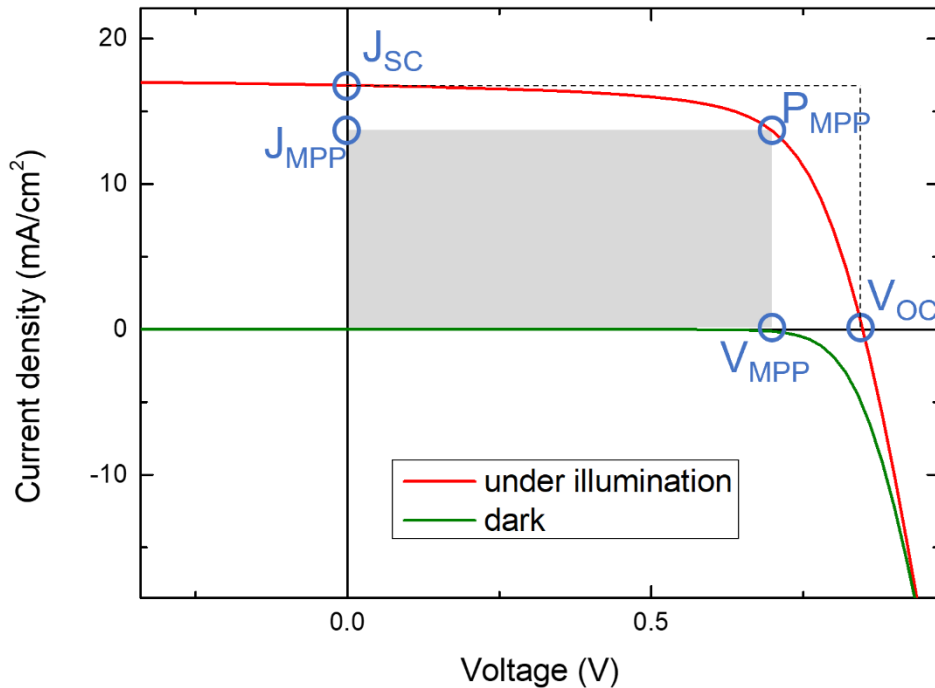


Figure 2.5: Schematic depiction of a current-voltage characteristic of an organic solar cell under illumination (red) and in the dark (green). The performance parameters short-circuit current (J_{SC}), open-circuit voltage (V_{OC}) and the maximum power point (P_{MPP}) that can be directly extracted from the curve are indicated in blue.

Since the generated current depends on the illuminated area of the solar cell, usually a shadow mask is applied on top of the cell to exactly define this area and the current per area (current density J) is used as parameter, resulting in JV -curves, with a typical measurement for illuminated and dark cells shown in **Figure 2.5**.

From the JV -measurements, several parameters can be extracted¹⁶: the open-circuit voltage (V_{OC}), which is the maximum achievable voltage of the cell when no current is flowing, the short-circuit current density (J_{SC}), which is the current density at zero voltage, and the maximum power point (P_{MPP}), which corresponds to the highest achievable power of the cell and is the maximum product of the cell's voltage V_{MPP} and current density J_{MPP} . From those values the fill factor (FF) of the cell can be calculated according to equation (2.15):

$$FF = \frac{P_{MPP}}{V_{OC} \cdot J_{SC}} = \frac{V_{MPP} \cdot J_{MPP}}{V_{OC} \cdot J_{SC}} \quad (2.15)$$

Finally, the power conversion efficiency (PCE) of the cell can be assessed by relating J_{SC} , V_{OC} and FF to the power of the incident light P_{in} , as shown in equation (2.16):

2 Characterization Methods

$$PCE = \frac{P_{MPP}}{P_{in}} = \frac{V_{OC} \cdot J_{SC} \cdot FF}{P_{in}} \quad (2.16)$$

When JV -measurements are performed with different illumination intensities, additionally the recombination behavior of the cells can be investigated.

The following expression for the V_{OC} of organic solar cells was derived by Koster et al.¹⁷:

$$V_{OC} = \frac{E_{gap}}{q} - \frac{k_B T}{q} \ln \left(\frac{(1-P)\gamma N_c^2}{PG} \right) \quad (2.17)$$

with E_{gap} being the difference of donor HOMO and acceptor LUMO, the elementary charge q , the temperature T , the Boltzmann constant k_B , the charge separation probability P , the Langevin coefficient γ , the effective density of states N_c , and the charge generation rate G .

From this equation it is apparent that only the charge generation rate G depends on the incident light intensity, since E_{gap} , P , N_c , and γ are inert properties of the used materials. Therefore, the dependence of the V_{OC} on the light intensity I can be simplified as follows:

$$V_{OC} = C + n \cdot \frac{k_B T}{q} \cdot \ln(I) \quad (2.18)$$

with C being a constant and the slope $n=1$. The equation of Koster et al. is based on the assumption of only bimolecular recombination (Langevin recombination) and cannot be solved for V_{OC} when additionally trap-assisted recombination (Shockley-Read-Hall recombination) is considered. Nevertheless, it is assumed that the V_{OC} in this case stills shows a natural logarithmic dependence on the light intensity but with a slope n larger than unity.^{18,19} In this way, n can be used as a measure for the occurrence of trap-assisted recombination, with larger n indicating more trap-assisted recombination. However, it must be taken into account that the absolute value of n has no physical meaning and only should be used for qualitative comparison.

JV measurements in air were performed using a Keithley 2401 source-measure unit and a Newport ABA solar simulator, which was calibrated to AM 1.5G with a Fraunhofer silicon diode. The cells were illuminated through a shadow mask with 8.31 mm² open area. For JV measurements under a protective atmosphere, the measurements were carried out in a nitrogen-filled glove box using a Keithley 2401 source-measure unit and a white light LED (Bridgelux), which was calibrated to 100 mW cm⁻² with a silicon diode (Hamamatsu S1227-66BQ). The cells were illuminated through a shadow mask with 6.25 mm² open area.

2.9 External Quantum Efficiency Measurements

While current-voltage characterization provides information about the behavior of a solar cell as a whole, external quantum efficiency (EQE) measurements can be used to take a closer look at the contribution of the individual materials, which is especially interesting for OSCs since they consist of at least two different absorbing components.

The term external quantum efficiency describes for each wavelength which ratio of incident photons is converted by the solar cell to electrons contributing to the generated photocurrent:

$$EQE(\lambda) = \frac{\text{number of photogenerated electrons}}{\text{number of incident photons}} \quad (2.19)$$

If every single incident photon is converted to an electron the EQE would be 100%. The external quantum efficiency, however, counts all incident photons and therefore does not consider losses due to reflection or scattering. This is taken into account by the so-called internal quantum efficiency (IQE), which describes the ratio of the number of generated electrons to actually absorbed photons, and which is obtained by dividing the EQE by the absorption per wavelength $A(\lambda)$:

$$IQE(\lambda) = \frac{EQE(\lambda)}{A(\lambda)} \quad (2.20)$$

For measuring the EQE, the sample solar cell is illuminated through a monochromator with spectrally selected light and the resulting photocurrent density J is measured. Since the number of incident photons is unknown in such a setup, a calibration is necessary. For this purpose, a silicon diode (Si1) with known EQE spectrum is measured before the sample solar cell. Usually, the setup also contains a permanently installed second silicon diode (Si2) which monitors any fluctuations of the light intensity between the calibration measurement (Si2-cal) and the sample measurements (Si2-sample):

$$EQE_{sample}(\lambda) = \frac{J_{sample}(\lambda)}{J_{Si1}(\lambda)} \cdot EQE_{Si1}(\lambda) \cdot \frac{J_{Si2-cal}(\lambda)}{J_{Si2-sample}(\lambda)} \quad (2.21)$$

In this way, the EQE of the sample solar cell can be determined by measuring only current densities and at the same time the measurement is also independent of the exact setup geometry or the absolute intensity of the light source.

Additionally, the J_{SC} of the solar cell can be predicted from the EQE measurement by integrating the measured photocurrent for each wavelength over the whole spectral range. The prior calibration ensures the correct result even if the intensity of the spectral slices used does not exactly match with the solar spectrum.

2 Characterization Methods

One problem of EQE measurements is that by using narrow spectral slices for illumination, the charge carrier density in the cell for each measurement point is much lower than it is under an illumination with 100 mW cm^{-2} . For this reason, the photocurrent predicted by EQE measurements is often overestimated, especially for devices with a nonlinear light intensity dependency.²⁰ If this is the case, EQE measurements should be performed with an additional white backlight, which ensures a realistic charge carrier density in the device.

EQE measurements were performed with a home-built setup using a 150 W Xe short arc lamp (LOT Oriel) combined with a monochromator (HORIBA microHR) and two Si-diodes to calibrate the photon flux and compensate for light intensity fluctuations. For voltage-dependent EQE measurements, a potentiostat (Metrohm Autolab) was used to apply voltage and simultaneously measure current.

2.10 Fourier-Transform Photocurrent Spectroscopy

In organic solar cells the working principles are governed by the sub-band gap charge transfer states. Since CT states have a low oscillator strength they are difficult to access directly by spectroscopic methods as for example UV-Vis spectroscopy. Instead, CT states are usually investigated with a special, highly-sensitive form of EQE measurements called Fourier-transform photocurrent spectroscopy (FTPS). For this method, the output light beam of an FTIR spectrometer is used to illuminate the sample solar cell and the generated photocurrent is measured. The intensity modulation of the light beam is used for a Fourier transformation of the photocurrent signal and results in a photocurrent spectrum.²¹

The absorption of the CT state is energetically below the materials' band gaps, but in the spectrum it is usually still superimposed by the band gap absorption and therefore only appears as a shoulder instead of a separate peak. The CT state energy E_{CT} can theoretically be determined by the intersection of the FTPS spectrum with the corresponding electroluminescence spectrum, but since this requires elaborate measurements with both methods, the CT state energy is usually determined by fitting the FTPS spectrum.

As derived by Vandewal et al,²² the EQE can be expressed as the total absorption multiplied by the absorbed-photon-to-electron internal-conversion efficiency η . Hereby, the total absorption is approximated by $\alpha 2d$ with the absorption coefficient α and the active layer thickness d , with the factor 2 considering reflection at the back electrode. The absorption coefficient, in turn, can be expressed by the product of the density of states in dependence of the energy $\sigma(E)$ and the number of charge transfer complexes N_{CTC} :

$$EQE(E) = \eta\sigma(E)N_{CTC}2d \quad (2.22)$$

The density of states can be expressed according to the Marcus theory,²³ which describes the absorption cross section for a transition from the CT ground state to the CT excited state:

$$\sigma(E)E = \frac{f_\sigma}{\sqrt{4\pi\lambda k_B T}} \exp\left(-\frac{(E_{CT} + \lambda - E)^2}{4\lambda k_B T}\right) \quad (2.23)$$

with the Boltzmann constant k_B , the absolute temperature T , the reorganization energy λ of the CT absorption process, and the energy independent factor f_σ that is proportional to the square of the electronic coupling matrix.

By using equation (2.23) for $\sigma(E)$ in equation (2.22) the following expression is obtained:

$$EQE(E) = \frac{f}{E\sqrt{4\pi\lambda k_B T}} \exp\left(-\frac{(E_{CT} + \lambda - E)^2}{4\lambda k_B T}\right) \quad (2.24)$$

The pre-factor f equals to $\eta N_{CTC} 2df_\sigma$ and is energy independent. The FTPS spectrum now can be fitted by this formula with the free parameters f , λ and E_{CT} . This is normally done in a semi-logarithmic graph, as shown schematically in **Figure 2.6**.

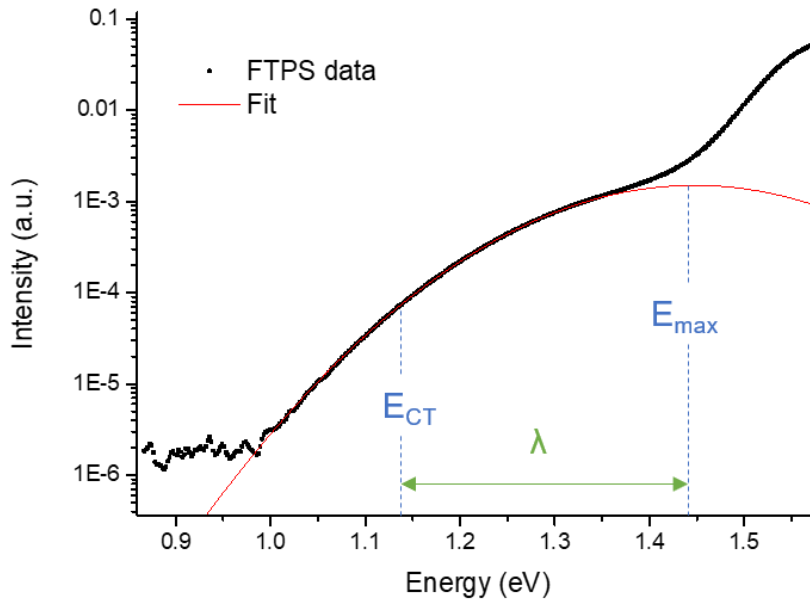


Figure 2.6: Schematic depiction of typical FTPS data (black dots) for an OSC with corresponding fit (red line) and indication of the charge transfer energy E_{CT} , the reorganization energy λ , and the maximum of CT absorption E_{max} .

FTPS measurements were performed with a modified Bruker Vertex 70 FTIR instrument by focusing light from a tungsten halogen lamp through a CaF₂ beam splitter with integrated gold mirrors to illuminate the devices under short-circuit conditions. The current from the devices was amplified with a FEMTO DHPA-100 current amplifier, passed through an analog-to-digital converter, and fed back to the FTIR instrument for Fourier transformation.

2.11 Electroluminescence Spectroscopy

Organic solar cells feature several emissive states: the emission of the excited state of the separate donor and acceptor and additionally the emission of the charge transfer state. Those states can be accessed via the above-mentioned PL spectroscopy or by applying a bias to the solar cells, thus injecting charges, and monitoring the resulting electroluminescence (EL).

Similar to the reciprocity between absorption and PL of a material, the external quantum efficiency of a solar cell (EQE_{PV}) and the quantum efficiency of its EL (EQE_{EL}) are directly related to each other, as shown by Rau's photoelectronic reciprocity theorem:^{24,25}

$$EQE_{EL}(E) = EQE_{PV}(E) \cdot \Phi_{BB}(E) \cdot \left(\exp\left(\frac{qV}{k_B T}\right) - 1 \right) \quad (2.25)$$

where Φ_{BB} is the black body spectrum at an energy E , q the elementary charge, V the applied voltage, k_B the Boltzmann constant, and T the temperature.

Therefore, analogously to FTPS, the CT state energy E_{CT} can be extracted by fitting the high-energy tail of the emission spectrum $I(E)$ with an expression derived from Marcus theory:²²

$$I(E) = E \frac{f_I}{\sqrt{4\pi\lambda kT}} \exp\left(-\frac{(E_{CT} - \lambda - E)^2}{4\lambda kT}\right) \quad (2.26)$$

With the factor f_I which is proportional to the electronic coupling matrix element and the reorganization energy λ . The analogy between FTPS and EL spectra and there corresponding fitting becomes evident in **Figure 2.7**, where an exemplary reduced (= divided by the energy) EQE and EL spectrum of the same solar cell are shown with the corresponding Marcus fits.

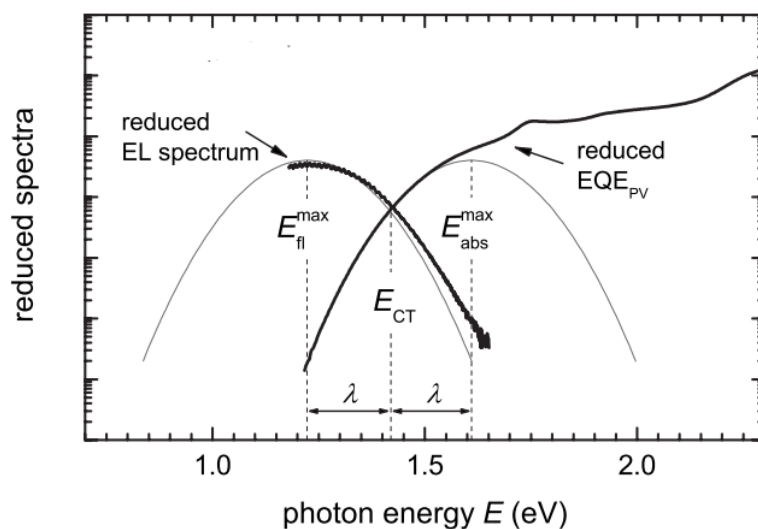


Figure 2.7: Exemplary reduced external quantum efficiency (EQE_{PV}) and EL spectrum of an organic solar cell with the corresponding Marcus fits. The fit maxima are shifted by two times the reorganization energy λ . The intersection of both spectra corresponds to the charge transfer state energy E_{CT} .²²

EL spectroscopy was performed in collaboration with the group of Dr. Wolfgang Tress (ZHAW Winterthur).

2.12 References

1. Schmidt-Mende, L. & Weickert, J. *Organic and hybrid solar cells. An introduction* (De Gruyter, Berlin, Boston, 2016).
2. Armin, A. *et al.* Quantum Efficiency of Organic Solar Cells: Electro-Optical Cavity Considerations. *ACS Photonics* **1**, 173–181 (2014).
3. Burkhard, G. F., Hoke, E. T. & McGehee, M. D. Accounting for interference, scattering, and electrode absorption to make accurate internal quantum efficiency measurements in organic and other thin solar cells. *Advanced materials (Deerfield Beach, Fla.)* **22**, 3293–3297 (2010).
4. Lakowicz, J. R. *Principles of Fluorescence Spectroscopy* (Springer US, Boston, MA, 2006).
5. Yablonovitch, E., Miller, O. D. & Kurtz, S. R. A great solar cell also needs to be a great LED: External fluorescence leads to new efficiency record (AIP2013), pp. 9–11.
6. Shipp, D. W., Sinjab, F. & Notingher, I. Raman spectroscopy: techniques and applications in the life sciences. *Adv. Opt. Photon.* **9**, 315 (2017).
7. Smart, L. E., Moore, L. E. & Moore, E. A. *Solid State Chemistry* (CRC Press, 2005).
8. Müller-Buschbaum, P. The active layer morphology of organic solar cells probed with grazing incidence scattering techniques. *Adv. Mater.* **26**, 7692–7709 (2014).
9. John F. Moulder. *Handbook of X-ray Photoelectron Spectroscopy. A Reference Book of Standard Spectra for Identification and Interpretation of XPS Data* (Physical Electronics Division, Perkin-Elmer, 1992).
10. Thomas Young. III. An essay on the cohesion of fluids. *Phil. Trans. R. Soc.* **95**, 65–87 (1805).
11. Wu, S. Calculation of Interfacial Tension in Polymer Systems. *J. Polymer. Sci.* **34**, 19–30 (1971).
12. Khlyabich, P. P., Rudenko, A. E., Street, R. A. & Thompson, B. C. Influence of polymer compatibility on the open-circuit voltage in ternary blend bulk heterojunction solar cells. *ACS Appl. Mater. Interfaces* **6**, 9913–9919 (2014).

13. Xu, X., Li, Y. & Peng, Q. Ternary Blend Organic Solar Cells: Understanding the Morphology from Recent Progress. *Adv. Mater.*, 2107476 (2021).
14. García, R. Dynamic atomic force microscopy methods. *Surface Science Reports* **47**, 197–301 (2002).
15. Shrotriya, V. *et al.* Accurate Measurement and Characterization of Organic Solar Cells. *Adv. Funct. Mater.* **16**, 2016–2023 (2006).
16. Deibel, C. & Dyakonov, V. Polymer-Fullerene Bulk Heterojunction Solar Cells. *Rep. Prog. Phys.* **73**, 96401 (2010).
17. Koster, L. J. A., Mihailetschi, V. D., Ramaker, R. & Blom, P. W. M. Light Intensity Dependence of Open-Circuit Voltage of Polymer:Fullerene Solar Cells. *Appl. Phys. Lett.* **86**, 123509 (2005).
18. Kuik, M., Koster, L. J. A., Wetzelaer, G. A. H. & Blom, P. W. M. Trap-assisted recombination in disordered organic semiconductors. *Proceedings of the National Academy of Sciences* **107**, 256805 (2011).
19. Ryu, S., Ha, N. Y., Ahn, Y. H., Park, J.-Y. & Lee, S. Light intensity dependence of organic solar cell operation and dominance switching between Shockley-Read-Hall and bimolecular recombination losses. *Scientific reports* **11**, 16781 (2021).
20. Zimmermann, E. *et al.* Erroneous efficiency reports harm organic solar cell research. *Nature Photon* **8**, 669–672 (2014).
21. Vandewal, K. *et al.* Fourier-Transform Photocurrent Spectroscopy for a fast and highly sensitive spectral characterization of organic and hybrid solar cells. *Thin Solid Films* **516**, 7135–7138 (2008).
22. Vandewal, K., Tvingstedt, K., Gadisa, A., Inganäs, O. & Manca, J. V. Relating the open-circuit voltage to interface molecular properties of donor:acceptor bulk heterojunction solar cells. *Phys. Rev. B* **81** (2010).
23. Marcus, R. A. Relation between charge transfer absorption and fluorescence spectra and the inverted region. *J. Phys. Chem. C* **93**, 3078–3086 (1989).
24. Rau, U. Reciprocity relation between photovoltaic quantum efficiency and electroluminescent emission of solar cells. *Phys. Rev. B* **76** (2007).

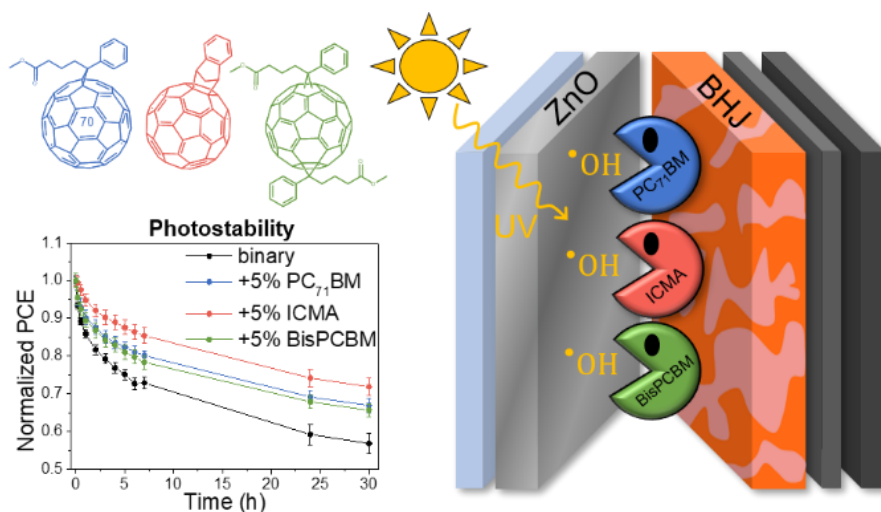
2 Characterization Methods

25. Rau, U., Blank, B., Müller, T. C. M. & Kirchartz, T. Efficiency Potential of Photovoltaic Materials and Devices Unveiled by Detailed-Balance Analysis. *Phys. Rev. Applied* **7** (2017).

3 Increasing Photostability of Inverted Nonfullerene Organic Solar Cells by Using Fullerene Derivative Additives

This chapter is based on the following publication:

Marcella Günther, Dominic Blätte, Anna Lena Oechsle, Sergio Sánchez Rivas, Amir Abbas Yousefi Amin, Peter Müller-Buschbaum, Thomas Bein, and Tayebbeh Ameri. Increasing Photostability of Inverted Nonfullerene Organic Solar Cells by Using Fullerene Derivative Additives. *ACS Appl. Mater. Interfaces* 13, 19072–19084; 10.1021/acsami.1c00700 (2021).



3 Increasing Photostability of Inverted Nonfullerene Organic Solar Cells by Using Fullerene Derivative Additives

3.1 Abstract

Organic solar cells recently achieved efficiencies of over 18 % and are well on their way to practical applications, but still considerable stability issues need to be overcome. One major problem emerges from the electron transport material zinc oxide (ZnO), which is mainly used in the inverted device architecture and decomposes many high performance nonfullerene acceptors due to its photocatalytic activity. In this work we add three different fullerene derivatives – PC₇₁BM, ICMA and BisPCBM – to an inverted binary PBDB-TF:IT-4F system in order to suppress the photocatalytic degradation of IT-4F on ZnO via the radical scavenging abilities of the fullerenes. We demonstrate that the addition of 5 % fullerene not only increases the performance of the binary PBDB-TF:IT-4F system, but also significantly improves the device lifetime under UV illumination in inert atmosphere. While the binary devices lose 20 % of their initial efficiency after only 3 hours, this time is increased fivefold for the most promising ternary devices with ICMA. We attribute this improvement to a reduced photocatalytic decomposition of IT-4F in the ternary system, which results in a decreased recombination. We propose that the added fullerenes protect the IT-4F by acting as a sacrificial reagent, and thereby suppress the trap state formation. Furthermore, we show that the protective effect of the most promising fullerene ICMA is transferable to two other binary systems PBDB-TF:BTP-4F and PTB7-Th:IT-4F. Importantly, this effect can also increase the air stability of PBDB-TF:IT-4F. This work demonstrates that the addition of fullerene derivatives is a transferable and straightforward strategy to improve the stability of organic solar cells.

3.2 Introduction

With efficiencies reaching over 18 %, ¹⁻³ organic solar cells (OSCs) have become serious competitors for state-of-the-art inorganic solar cells. This is especially true because their properties such as lightweight, low cost, sustainable materials and flexibility allow them to open entirely new markets. For commercial applications, however, not only the efficiency has to be convincing, but also the stability must be sufficiently high, which is not yet the case for many high-performance OSC systems. A major degradation influence, which of course cannot be avoided, is light. Nearly all organic solar cells show an initial fast degradation when being exposed to light the first time, which is referred to as a burn-in. ^{4,5}

This initial light-induced degradation can have two fundamentally different causes of either morphological or molecular nature. Morphological changes occur when the energy introduced into the OSC by light causes diffusion⁶ or recrystallization of components, thus resulting in a loss of the optimal interpenetrating network of the bulk heterojunction (BHJ).⁷⁻⁹ Molecular

3 Increasing Photostability of Inverted Nonfullerene Organic Solar Cells by Using Fullerene Derivative Additives

changes occur when the incident light breaks chemical bonds directly¹⁰ or activates reactions of the components with each other,^{11,12} with impurities,¹³ or with interlayers.¹⁴

An inverted architecture is normally considered being more stable for devices containing fullerene acceptors.^{15,16} However, for nonfullerene acceptors the inverted geometry brings up new stability issues. Especially, the electron transport layer (ETL) ZnO, which is commonly used in inverted devices, can cause stability problems.¹⁷ ZnO is known as photocatalyst for the degradation of organic compounds and, for example, is used for water purification.^{18–20} Upon irradiation with UV light, electron-hole pairs are created in the ZnO, which then can either react directly with adsorbed pollutants or form reactive oxygen species (e.g. $\bullet\text{OH}$, $\bullet\text{O}_2^-$) with the surrounding water, which act as mobile, potent oxidizing agents and decompose dissolved pollutants.²⁰

This photocatalytic reactivity of ZnO, which is very desirable for water purification, can have a detrimental effect in organic solar cells.^{14,21,22} The organic molecules, which are located adjacent to the ZnO layer, can be reduced or oxidized directly due to the photoinduced charge carriers in ZnO.²⁰ Furthermore, as a result of the manufacturing process, water and oxygen are adsorbed on the ZnO surface,^{23,24} which again can form mobile, reactive oxygen species that attack the active materials.²⁵

Nonfullerene acceptors have been shown to be particularly susceptible to the destructive influence of ZnO,^{14,21} since they usually contain end groups like indandione (e.g. ITIC, IT-4F, IEICO-4F) or rhodanine (e.g. IDFBR) that are connected to the core by a non-aromatic double bond, which is vulnerable to addition reactions. It has been demonstrated that IT-4F, ITIC and IEICO-4F films coated on a ZnO substrate undergo complete photobleaching in less than 100 hours when exposed to UV illumination.¹⁴ A more detailed investigation with ITIC revealed that the excitation of ZnO causes an addition reaction of radical oxygen species to the vinyl bond in ITIC and dimerization of ITIC was also detected.²¹ In a solar cell, this process causes a loss of absorption and more importantly, the degraded molecules can act as charge traps and thus as recombination centers.

The use of UV filters in front of the solar cells could solve the degradation problem by suppressing the photocatalytic activity of ZnO, however, this is not a reasonable option due to ZnO suffering from the so-called light-soaking issue.²⁶ Photovoltaics containing ZnO as ETL need UV illumination to passivate defect states on the surface of the ZnO and to reach their optimum performance. It is assumed that those defect states originate from the chemisorption of oxygen on the ZnO surface, which traps electrons from the ZnO conduction band by forming O_2^- species and thus creates a depletion layer and band bending next to the interface.²⁷ This

3 Increasing Photostability of Inverted Nonfullerene Organic Solar Cells by Using Fullerene Derivative Additives

results in a barrier for electron injection or extraction and consequently in an s-shaped current density-voltage curve (JV -curve), which causes a reduced fill factor. UV illumination generates electron-hole pairs in the ZnO which help desorbing the oxygen due to the holes recombining with O_2^- and forming O_2 again.²⁷ This results in a decrease of the injection/extraction barrier and the recovery of the performance of the solar cell.

A more promising way to suppress the detrimental influence of ZnO on the absorbing materials is to introduce a protective interlayer between ETL and absorbing layer.^{22,28,29} For example, a thin pyrene-bodipy based layer on top of ZnO was shown to significantly increase the device lifetime under illumination for both PBDB-TF:IT-4F and PTB7-Th:PC₇₁BM systems, respectively.²²

However, this method of using a protective layer increases the complexity in manufacturing the solar cells due to the additional layer and thereby would also increase the potential cost of the OSC manufacturing. A much simpler approach would be to suppress the UV aging due to ZnO by directly adding a protective third compound to the binary absorber mixture of the active layer. Promising candidates for this approach are fullerenes, since they are well known radical scavengers^{30,31} and already established materials for OSCs.

In this work, we use a ternary approach to investigate the influence of three different fullerene derivatives, namely PC₇₁BM, ICMA and BisPCBM, on the UV stability of inverted binary solar cells consisting of the donor PBDB-TF and the acceptor IT-4F (all systematic names can be found in the experimental part). The fullerene derivatives are found to significantly slow down the UV-induced aging of the binary system, mainly due to decreased losses of the fill factor. It is shown that the addition of fullerenes reduces the formation of defect states, which emerge due to the photocatalytic degradation of IT-4F on the electron transport layer ZnO. In the present work, a mechanism is proposed that explains the protective effect of the fullerenes with their radical scavenging abilities, suppressing the detrimental influence of ZnO.

3.3 Results and Discussion

3.3.1 Performance of Ternary OSCs

In **Figure 3.1a**, the molecular structures of the used materials are illustrated. The corresponding energy levels are provided in **Figure S 3.1**. Binary and ternary organic solar cells were built in an inverted architecture with ZnO as the ETL and MoO_x as the hole transport layer (HTL), as illustrated in **Figure 3.1b**. For the binary blend, the polymeric donor PBDB-TF and the small molecule acceptor IT-4F were used in a 1:1 weight ratio. For the ternary blends 5 wt% of PC₇₁BM, ICMA or BisPCBM were added, respectively. A weight ratio of 5% was found to achieve the highest power conversion efficiency (*PCE*) values for all three ternary blends, as illustrated in **Figure S 3.2**.

Inverted binary OSCs with PBDB-TF:IT-4F have been reported to yield champion efficiencies between 12% to 13%^{14,32} however, since the aim of this study was to compare the device stability of binary and ternary solar cells, the *PCE* was not extensively optimized, but all cells were built following a standardized procedure.

The *PCE* distribution of the binary and the three different ternary systems is shown in **Figure 3.1c**, the corresponding distributions of the open-circuit voltage (V_{OC}), short-circuit current density (J_{SC}) and fill factor (FF) can be found in **Figure S 3.3**. For each system, 30 individual cells fabricated in three different experimental batches are presented. The associated average and record photovoltaic performance parameters are summarized in **Table 3.1**. The binary reference system on average achieved an efficiency of 8.8%, with a V_{OC} of 0.83 V, a J_{SC} of 16.9 mAcm⁻² and a FF of 64%. The addition of 5% fullerene derivative had a positive effect for all three studied fullerenes and resulted in an average *PCE* improvement of 6%, 10%, and 7% for PC₇₁BM, ICMA and BisPCBM, respectively, compared to the binary system. This improvement originates mainly from an increased J_{SC} and FF , whereas the V_{OC} remains nearly unchanged with the addition of the third component. As can be seen from the absorption coefficients of the binary and ternary blends in **Figure S 3.4**, the fullerenes do not significantly improve the absorption of the different solar cells. However, in the external quantum efficiency (EQE) spectra, shown in **Figure 3.1d**, a difference becomes visible. In the wavelength region from 500 to 800nm, the EQE of all ternary cells is higher than that of the binary cell, with the ternary ICMA showing the strongest increase. This region corresponds to the absorption range of IT-4F (**Figure S 3.4**), and thus suggests that the fullerenes improve charge transport from the acceptor. This effect probably also accounts for the enhanced FF , since the addition of fullerenes is known to result in an increased and more balanced charge carrier mobility.^{33,34}

3 Increasing Photostability of Inverted Nonfullerene Organic Solar Cells by Using Fullerene Derivative Additives

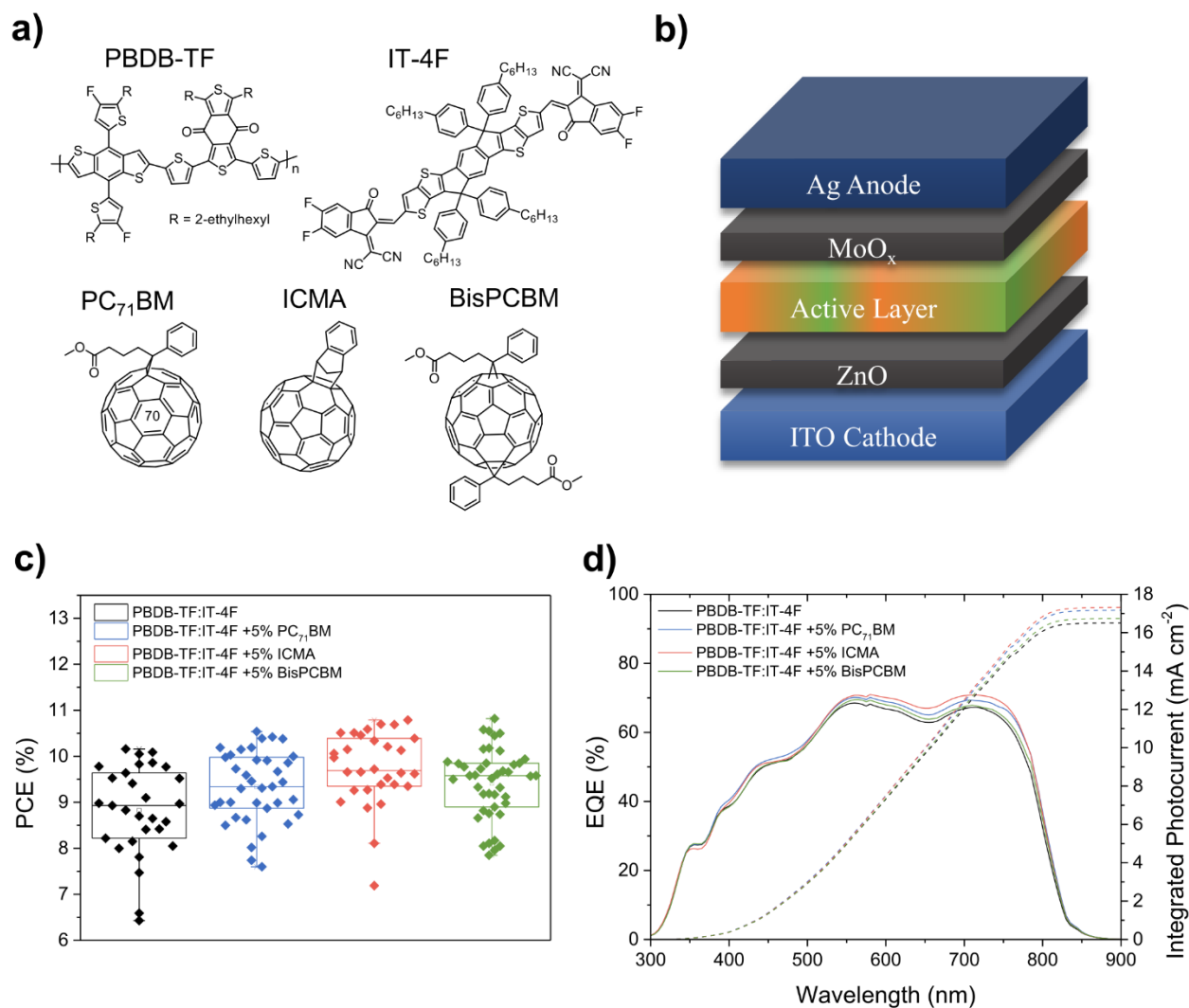


Figure 3.1: a) Chemical structures of all used active layer materials, b) inverted device architecture of all built OSCs, c) PCE distribution (from 30 individual solar cells each) of the binary and the three ternary systems with added fullerenes as indicated, and d) the respective external quantum efficiency spectra (EQE) of the best cells with corresponding integrated photocurrents.

Table 3.1: Maximum and average values (in brackets) of performance parameters for binary and ternary devices from 30 cells conducted in three different experimental rounds.

	<i>PCE</i> (%)	<i>V</i> _{oc} (V)	<i>J</i> _{sc} (mA cm ⁻²)	<i>FF</i> (%)
PBDB-TF:IT-4F	10.2 (8.8 ± 1.0)	0.85 (0.83 ± 0.02)	17.3 (16.9 ± 1.3)	69 (64 ± 4)
PBDB-TF:IT-4F + 5% PC ₇₁ BM	10.5 (9.3 ± 0.8)	0.83 (0.82 ± 0.01)	17.7 (17.4 ± 0.5)	71 (66 ± 4)
PBDB-TF:IT-4F + 5% ICMA	10.8 (9.7 ± 0.8)	0.83 (0.83 ± 0.01)	17.7 (17.4 ± 0.5)	73 (69 ± 4)
PBDB-TF:IT-4F + 5% BisPCBM	10.8 (9.4 ± 0.8)	0.84 (0.83 ± 0.01)	17.8 (17.0 ± 1.0)	72 (67 ± 4)

3 Increasing Photostability of Inverted Nonfullerene Organic Solar Cells by Using Fullerene Derivative Additives

3.3.2 UV Stability of Binary and Ternary Cells

The UV stability of binary and ternary cells was examined by exposing them to a continuous UV illumination in a nitrogen atmosphere. A UV LED emitting at 365 nm was used as the light source and its intensity was calibrated to match the intensity of the UV part (300-400 nm) of one sun radiation. At regular time intervals, a *JV*-curve was measured under a white light LED to determine the change in the performance of the solar cells. The spectra of all used light sources can be found in **Figure S 3.5**.

In **Figure 3.2a**, the aging of the four different systems during 30 hours of continuous UV illumination is presented. For every system three individual cells were averaged, and all data points were normalized to the performance of the respective fresh devices. The *PCE* curves for all devices show a typical burn-in behavior⁴ with an exponential decay of the efficiency in the first few hours. However, it is evident that the addition of the fullerenes significantly reduces the burn-in, and thus increases the device lifetime in all cases. The lifetime is usually defined as the time after which the device has lost 20 % of its initial efficiency (so called T_{80} lifetime).¹⁵ For the binary cells this time is only three hours, while it is more than doubled by the addition of PC₇₁BM (7 h) and BisPCBM (6h). For the cells with ICMA even a fivefold T_{80} lifetime (16 h) is achieved.

The degradation of the *PCE* for all four systems is mainly from *FF* losses, with rather small losses in V_{OC} and J_{SC} . The fill factor is also the parameter that experiences the strongest stability improvement through the addition of the fullerenes, with ICMA showing the most pronounced effect and PC₇₁BM and BisPCBM behaving very similar. Interestingly, the stability of the V_{OC} and J_{SC} values is also improved to the greatest extent by the addition of ICMA, followed by PC₇₁BM and BisPCBM with a similar effect.

To examine if the observed stabilization effect scales with the amount of added fullerene, ternary devices with different ratios of the most promising candidate ICMA were built and aged under the same conditions for 120 hours. The degradation over time for V_{OC} and *FF*, which are the two performance parameters with the most distinct aging effect, is shown in **Figure 3.2b**. The corresponding *PCE* and J_{SC} curves can be found in **Figure S 3.6**. It is obvious that the stabilizing effect of ICMA depends on the fullerene content, but already amounts as small as 1.25 wt% result in a significantly improved stability. Furthermore, the stabilizing effect seems to saturate with an increasing ratio of ICMA. Since the performance of fresh devices decreases when 10 % or more ICMA is added, 5 % ICMA was chosen as the best trade-off between reaching a high device efficiency and a long device stability.

3 Increasing Photostability of Inverted Nonfullerene Organic Solar Cells by Using Fullerene Derivative Additives

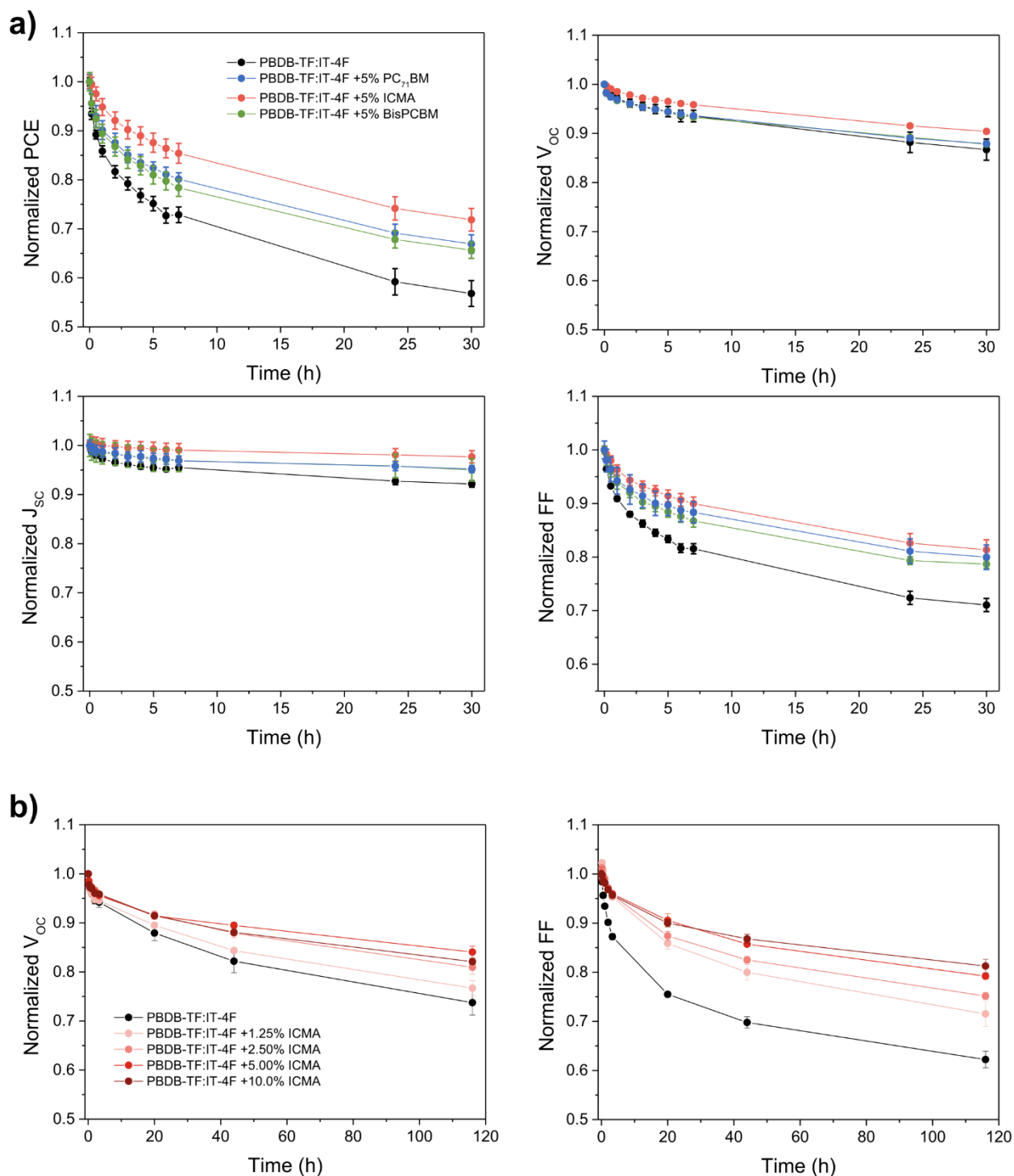


Figure 3.2: a) UV stability of the photovoltaic parameters of binary and ternary devices (averaged over 3 devices each) as a function of time. b) UV stability of V_{OC} and FF as a function of time for binary PBDB-TF:IT-4F cells and ternary cells with different ratios of ICMA.

3.3.3 Characterization of Fresh and Aged Devices

To investigate the origin of the UV instability of the binary system and to understand the stabilizing effect of the three added fullerenes, various characterization methods were

3 Increasing Photostability of Inverted Nonfullerene Organic Solar Cells by Using Fullerene Derivative Additives

performed to compare the fresh devices with the corresponding devices aged for 24 hours under UV illumination.

Already a first look at the JV -curves of fresh and aged devices shows a striking difference. As depicted in **Figure 3.3a**, the JV -curves of the three fresh ternary devices are very similar to the one of the fresh binary devices. However, the aged binary devices not only show a much higher fill factor loss (**Figure 3.2a**), but above all a strongly increased series resistance. On average, the fresh binary devices have a series resistance (R_S) of $6.7 \Omega \text{ cm}^2$, whereas aged devices show a series resistance of $19.6 \Omega \text{ cm}^2$, which corresponds to an increase of almost 200 %. Meanwhile, R_S only increased by about 60 % for the aged ternary devices compared to the fresh ones. The strong increase of R_S in binary devices indicates that the aging might be interface-related and that the fullerenes have a protective function in the ternary devices.

To learn more about the observed losses in J_{SC} , UV-vis spectroscopy and EQE measurements were performed for fresh and aged devices. As shown in **Figure S 3.7a**, all systems experience a small loss in absorption, which is most pronounced for the binary system, and which mainly seems to come from the absorption region of IT-4F (550-800 nm). Remarkably, the EQEs of the binary fresh and aged devices (**Figure S 3.7b**) do not reflect this loss. While the EQEs of the ternary systems remain nearly unchanged after the UV exposure, the aged binary system shows a small loss over the entire wavelength range, what is more clearly visible when the EQE difference is plotted, as in **Figure S 3.7c**. Since the main aging induced current losses in all systems occur at around maximum power point (see **Figure 3.3a**) and not for the J_{SC} , voltage-dependent EQE was performed additionally. By measuring the cells biased with 0.6 V, the changes in current density for fresh and aged cells become more obvious, as depicted in **Figure 3.3b** (see **Figure S 3.7d** for EQE differences). The EQEs of all fresh devices biased with 0.6 V are very similar, however, after 24 h of UV illumination the binary and ternary EQEs differ greatly from each other. They all show a loss over the whole wavelength region, but this loss is much larger for the binary system. This finding suggests that although during the aging the IT-4F is partly attacked, it is not the absorption loss but another dominant process that reduces the exciton harvesting all over the spectrum. This process apparently is slowed down by the addition of the fullerene derivatives.

Furthermore, since the main PCE losses for all systems originate from the fill factor, light intensity dependent JV -measurements and Fourier-transform photocurrent spectroscopy (FTPS) were carried out in order to study the recombination behavior of fresh and aged devices.³⁵

3 Increasing Photostability of Inverted Nonfullerene Organic Solar Cells by Using Fullerene Derivative Additives

In **Figure 3.3c**, the light intensity dependence of the V_{OC} is depicted for all four systems, fresh and after 24 hours of UV aging. According to $V_{OC} \sim nkT / e \cdot \ln(I)$ the V_{OC} is linearly dependent on the natural logarithm of the light intensity I and the slope corresponds to the product of the ideality factor n , the Boltzmann constant k and the temperature T .³⁶ An ideality factor of one hereby signifies a recombination mechanism that is exclusively bimolecular, while for only monomolecular recombination the ideality factor is two.³⁷ The fresh devices all have a rather similar ideality factor between 1.24 and 1.27, and all devices show an increased ideality factor after exposure to UV illumination. However, the extent of this increase is quite different. While the ideality factor of the binary system increases from 1.26 to 1.43, the ternary systems with ICMA and BisPCBM exhibit 40 % less increase of n compared to the binary one. The ideality factor of the ternary system with PC₇₁BM increases in a similar way as the binary one.

The FTPS results of the fresh and aged devices are depicted in **Figure 3.3d**. The spectral region from 900 to 1450 nm (sub-band gap) can be divided into two parts.^{38,39} The part between 900-1000 nm is attributed to the absorption of band tail states and is mainly related to the energetic disorder of the bulk. The part from 1000 nm upwards, which has a much lower slope, can be assigned to the absorption of defect states. The FTPS results of all fresh devices are quite similar, but for the aged devices differences emerge in both regions. In the absorption region of the band tail states, all aged systems show a small shift to lower energies, suggesting an increased energetic disorder. The more remarkable feature, however, is the change in the defect state region. Here, the aged binary system shows a strongly increased current from defect state absorption, while the aged ternary devices feature a substantially smaller increase. We note that the extent of this increase corresponds to the observed ranking in the stability of the systems with the ICMA device being the most stable device and showing the least increase.

These findings suggest that a large share of the binary system aging is caused by increased trap-assisted recombination and that the addition of the fullerenes, especially ICMA, partly suppresses this effect.

3 Increasing Photostability of Inverted Nonfullerene Organic Solar Cells by Using Fullerene Derivative Additives

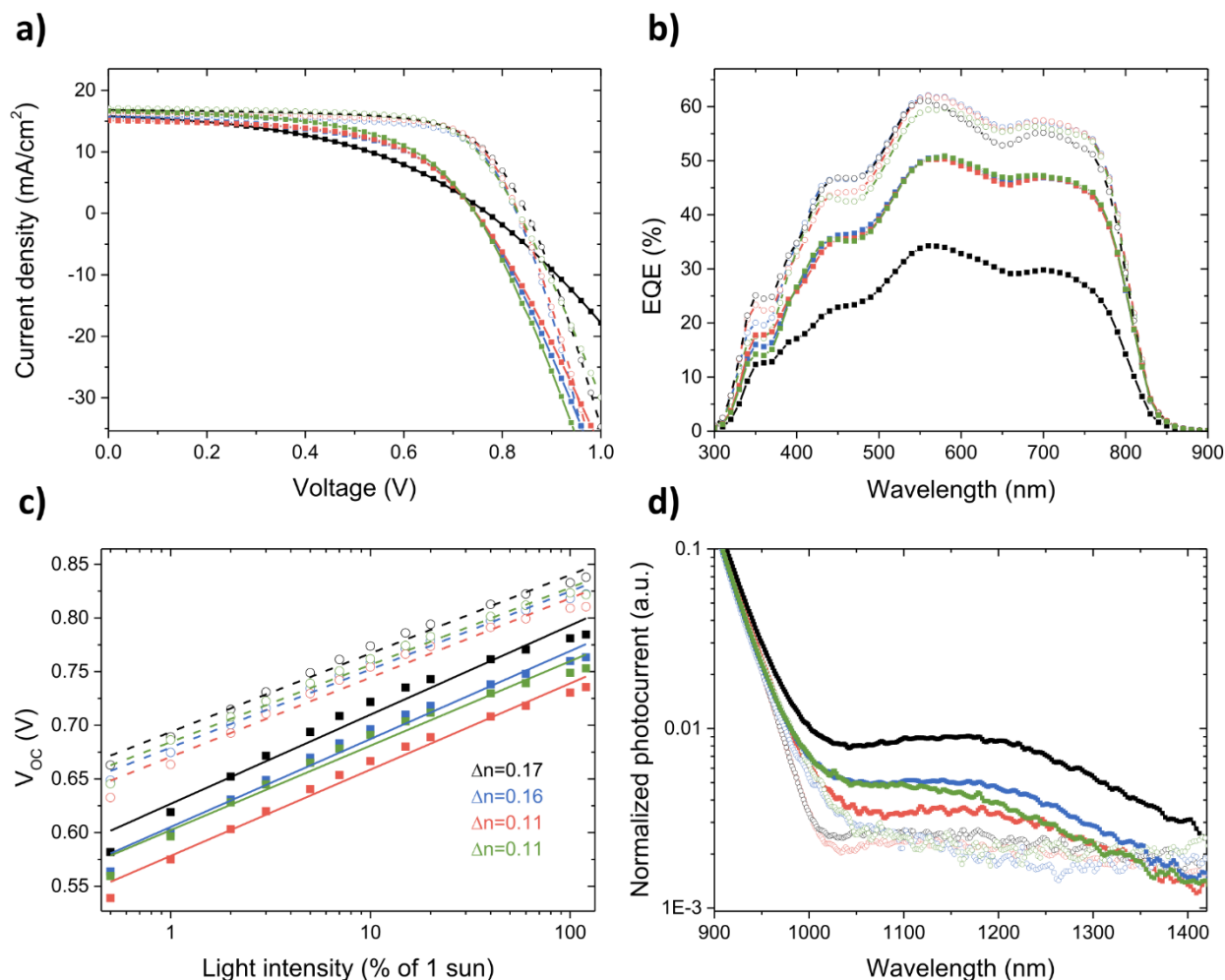


Figure 3.3: Characterization of the fresh binary/ternary devices and of the same devices aged for 24 hours under UV light. a) JV characteristics under illumination, b) voltage-dependent EQE-spectra at a bias of 0.6 V, c) light intensity dependence of V_{OC} , and d) FTPS measurements of binary PBDB-TF:IT-4F (black) and ternary devices with added PC₇₁BM (blue), ICMA (red), and BisPCBM (green). Fresh devices are shown with dashed lines/empty symbols and 24 h UV aged ones with solid lines/filled symbols.

To examine whether morphological changes are the reason for the emergence of traps, grazing-incidence wide-angle and small-angle X-ray scattering (GIWAXS and GISAXS) measurements were performed for the binary and ternary blends. The 2D GIWAXS data of the fresh and aged blends are shown in **Figure S 3.8**, the corresponding out-of-plane and in-plane cake cuts are presented in **Figure 3.4a** and **Figure 3.4b**. In all GIWAXS patterns, the (100) diffraction peak at $q \approx 3.2 \text{ nm}^{-1}$ is visible, indicating a high crystallinity of the polymer PBDB-TF.⁴⁰ Additionally, the in-plane cuts show a broad diffraction peak between $q \approx 12 \text{ nm}^{-1}$ and 18 nm^{-1} , which is attributed to the (010) Bragg peak of crystalline PBDB-TF.⁴⁰ No significant differences are visible in the line cuts, neither between the binary and ternary devices nor between the fresh and aged ones. To additionally investigate possible changes on larger length scales addressing

3 Increasing Photostability of Inverted Nonfullerene Organic Solar Cells by Using Fullerene Derivative Additives

domain sizes and distributions, an in-depth analysis of the 2D GISAXS data was performed by modeling the intensity curves resulting from horizontal line cuts in the Yoneda region. To account for the different length-scales of the domains, the data is modeled with three cylindrically-shaped substructures, according to the local monodisperse approximation (LMA) in the framework of the distorted wave Born approximation (DWBA).^{41–43} The 2D GISAXS data and all LMA-DWBA fit parameters can be found in **Figure S 3.9** and **Table S 3.1**.

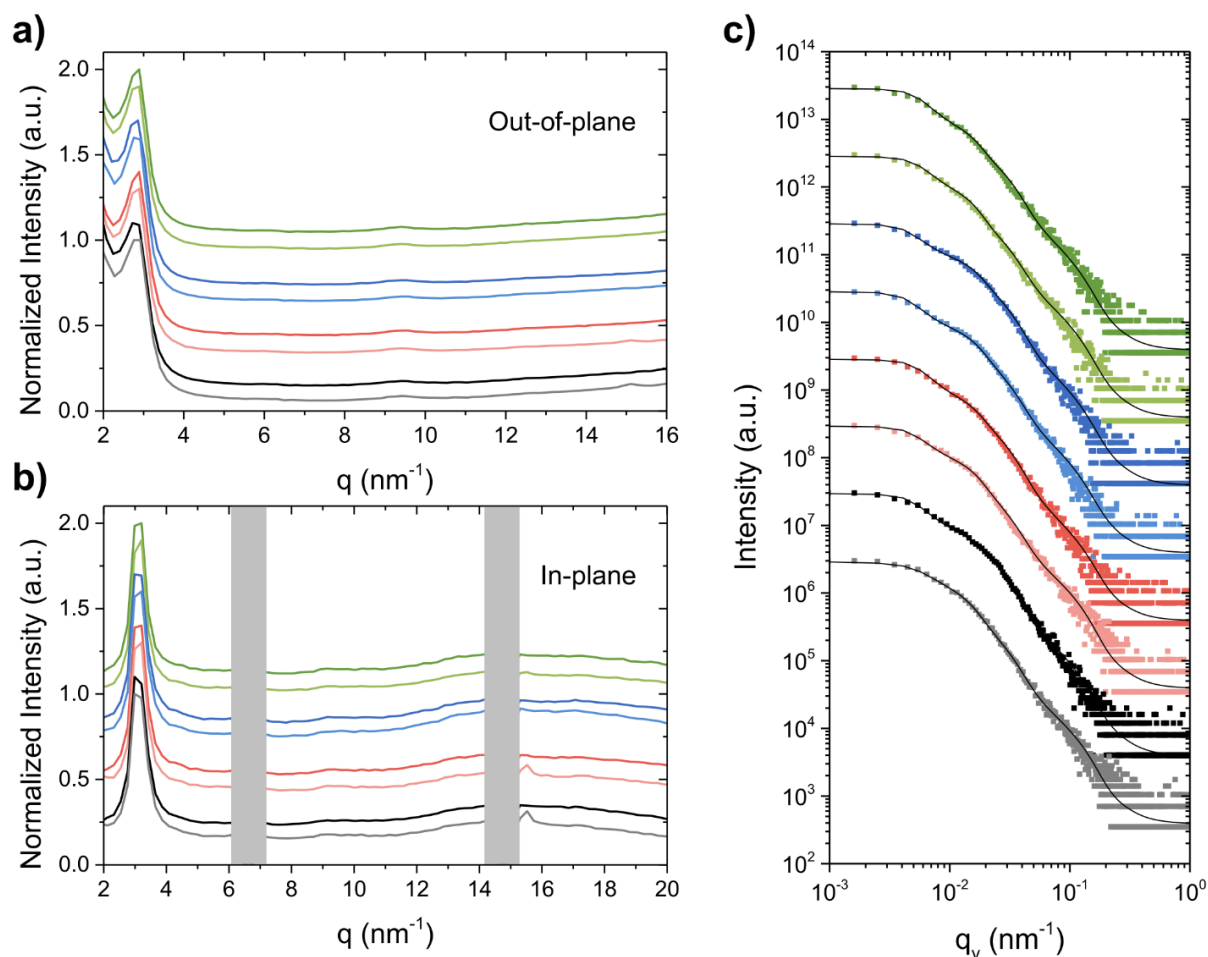


Figure 3.4: Normalized a) out-of-plane and b) in-plane cake cuts of the 2D GISAXS data and c) horizontal line cuts of 2D GISAXS data at the critical angle of 0.1° (symbols) and the corresponding fits of binary PBDB-TF:IT-4F (black lines) and ternary devices with added PC71BM (blue), ICMA (red), and BisPCBM (green). Fresh devices are shown with light colors and 24h UV aged ones with darker colors. The curves are shifted along the y-axis for clarity of the presentation.

The intensity cuts and their modeled fits, as shown in **Figure 3.4c**, are very similar for fresh and aged films of the binary and ternary blends. A closer look at the fit parameters (**Table S 3.1**) confirms that indeed radius and center-to-center domain distances for the three different length-scales are the same within the error bars. For the medium sized substructures, it is noticeable that the intensity-weighted proportion in the fit increases somewhat after the aging. However, since this is the case for all four systems, this increase cannot be the reason for the

3 Increasing Photostability of Inverted Nonfullerene Organic Solar Cells by Using Fullerene Derivative Additives

different aging behavior. Therefore, both GIWAXS and GISAXS measurements indicate that no morphological changes are responsible for the improved aging behavior of the fullerene containing devices. Interestingly, such stability of the PBDB-TF:IT-4F film morphology is in contrast to similar systems studied in operando experiments. For example, Wienhold et al. observed in PBDB-T-SF:IT-4F OSCs a J_{SC} driven aging, which was caused by a reduction of interfaces per cross section area.⁴⁴

3.3.4 Origin of UV Aging and Explanation for the Protective Effect of the Fullerenes

In this work, the GIWAXS and GISAXS results indicate that the different aging behavior of binary and ternary systems is not morphology related. However, there might be morphological changes that are not clearly visible in GIWAXS and GISAXS, for example on very small scales or in amorphous regions. Moreover, adding fullerenes as the third compound has been shown to stabilize the microstructure of binary blends against recrystallization and phase separation and thus increasing the stability.^{45,46}

Therefore, in order to further ensure that the origin of the aging process of the binary PBDB-TF:IT-4F system is not morphological, the UV aging was compared to two other aging conditions. On the one hand, the binary system under nitrogen was exposed to a white light LED, which has been calibrated to one sun ($\approx 100 \text{ mW cm}^{-2}$) and therefore emits a much higher overall intensity than the used UV LED ($\approx 4.6 \text{ mW cm}^{-2}$). The spectra of the used LEDs can be found in **Figure S 3.5**. On the other hand, the binary device was thermally aged at 85°C under nitrogen atmosphere. In contrast to chemical aging, degradation of the binary blend that is caused by morphological changes, such as recrystallization or diffusion, should mainly depend on the amount of energy absorbed. Consequently, if the aging resulted from morphological modifications, the aging due to the white LED or the elevated temperature would show a similar or worse behavior as the UV LED aging, since the overall absorbed energy is higher (see absorption spectra in **Figure S 3.4**).

However, such a similar behavior cannot be observed in the obtained time-dependent *PCE* curves, as shown in **Figure 3.5a**. The corresponding V_{OC} , J_{SC} and FF curves can be found in **Figure S 3.10**. The binary cells exposed to the white light LED and to the increased temperature both show a considerably slower loss of efficiency than the one exposed to the UV LED. This clearly demonstrates that the mechanism of the observed aging under UV illumination is dependent on the wavelength of the LED. In addition to the GIWAXS and GISAXS findings, it is taken as a strong indication for the UV aging being a molecular rather than a morphological

3 Increasing Photostability of Inverted Nonfullerene Organic Solar Cells by Using Fullerene Derivative Additives

degradation process, in contrast to other findings about white light aging of PBDB-TF:IT-4F devices.⁸

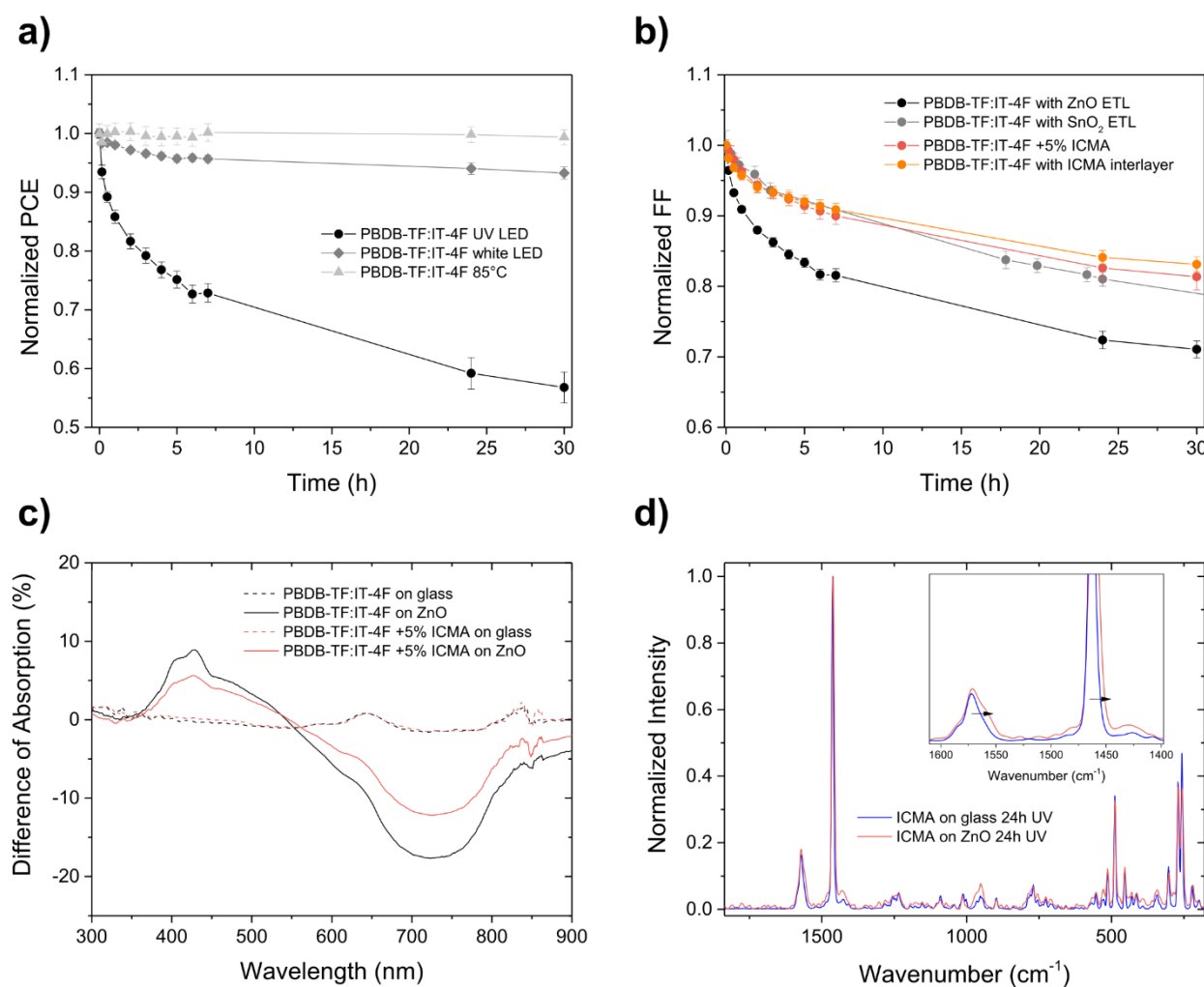


Figure 3.5: a) PCE as a function of time for binary PBDB-TF:IT-4F devices aged for 30 hours under different conditions. Devices were aged in nitrogen atmosphere either under a UV LED calibrated to the UV part of one sun radiation (black), under a white light LED calibrated to one sun radiation (grey) or in the dark on a hotplate at 85°C (light grey). For each condition the average of three individual devices is shown. b) FF as a function of time during continuous UV illumination for binary devices with a ZnO ETL (black), binary devices with a SnO₂ ETL (grey), ternary ICMA devices (red), and binary devices with an ICMA interlayer between ZnO and BHJ (orange). c) Difference of UV-vis spectra of fresh blends and blends aged for 24 hours under UV illumination for a binary blend on glass (dotted black) and on ZnO (solid black) and for a ternary ICMA blend on glass (dotted red) and on ZnO (solid red). d) Raman spectra of ICMA that was aged on glass (blue) and on ZnO (red) as a film, scraped off and measured as powder.

One possible molecular degradation pathway of active layer materials, already shown by several groups,^{47–49} arises from the presence of the additive DIO, which was also used for the manufacturing of the cells in this work. In particular, it was demonstrated that residual DIO

3 Increasing Photostability of Inverted Nonfullerene Organic Solar Cells by Using Fullerene Derivative Additives

under the influence of UV illumination can form radicals, that attack and decompose the acceptor material ITIC.⁴⁹ This mechanism could also be transferable to the ITIC derivative IT-4F used here. To investigate whether the observed aging trends of binary and ternary cells are related to the additive used, binary PBDB-TF:IT-4F cells and ternary PBDB-TF:IT-4F:ICMA cells were prepared without DIO (see **Table S 3.2** for performance parameters) and aged under the same conditions. As visible in **Figure S 3.11**, the aging trends for binary and ternary cells with and without DIO are quite comparable. The binary cells without DIO age slightly slower than with DIO and this difference could well be due to a detrimental influence of the additive. However, more importantly, the fullerene ICMA has the same stabilizing effect with and without DIO, which proves that ICMA slows down an aging process that is clearly not related to the additive DIO.

Other possible causes of chemical and non-morphological aging processes are linked to the interfaces with the transport layers. To investigate this, binary devices were built with SnO₂ instead of ZnO as an ETL. SnO₂ has a larger band gap than ZnO and does not absorb at the wavelength used for the UV aging, as shown in the UV-vis spectra in **Figure S 3.12**. Therefore, UV-induced aging processes, which originate from the ETL, can be excluded when using SnO₂. The performance parameters of these cells can be found in **Table S 3.3**. The SnO₂-based cells were built using the same recipe as for the ZnO-based cells, although the efficiency is worse, mainly due to a smaller J_{SC} and FF . Afterward, they were aged under the same conditions as those used for the ZnO-based cells. Remarkably, their aging behavior is different from that of the ZnO-based binary cells, as shown in **Figure 3.5b** and **Figure S 3.13**. Especially, the aging of the FF is significantly slowed down and resembles more the curve of the ternary cell with ICMA. However, there seems to be another process, that causes the V_{OC} to age faster and therefore decrease the stability of the system. Nevertheless, this slower aging of the binary system on SnO₂ is a strong indication that the ZnO interlayer is the reason for a photocatalytic degradation process in the binary devices.

To prove that the fullerene implemented in the bulk photoactive layer really suppresses this proposed degradation at the interface, binary cells were built with a thin interlayer of ICMA in between ZnO and photoactive layer (for details see experimental section). The device performance after UV aging is also shown in **Figure 3.5b** and **Figure S 3.13**. It is evident that the aging behavior of the ternary ICMA devices and the devices with ICMA interlayer is very similar and that in both cases the stability compared to the binary devices is improved in the same way. This finding proves that ICMA suppresses an interface related degradation process, which even works when ICMA is mixed into the active layer.

3 Increasing Photostability of Inverted Nonfullerene Organic Solar Cells by Using Fullerene Derivative Additives

In order to understand what this UV-induced molecular degradation process at the interface looks like and what causes it, the UV-vis spectra of the fresh and aged thin films of the binary and ternary ICMA blend were more closely examined. In **Figure 3.5c** we present the difference in absorption of the fresh and aged films, normalized to the intensities of the fresh films. Interestingly, the respective films on glass (dotted lines) show no change in absorption after aging, indicating a good UV stability of the pristine molecules. However, if a ZnO layer is present underneath the films, the absorption is changed after UV illumination. Both the binary and the ternary blend show an absorption loss between 550-850nm (the absorption range of IT-4F), that is more pronounced for the binary blend, and an absorption increase between 350-550nm. Such an absorption loss of IT-4F or ITIC containing blends on top of ZnO has also been observed by other groups and has been attributed to photocatalytic degradation of the nonfullerene acceptor on the ZnO.^{14,50} The absorption increase between 350nm and 550nm is assumed to be caused by the degradation products.¹⁴ Obviously, the addition of ICMA, respectively the other fullerenes, suppresses the ZnO-induced photocatalytic degradation of IT-4F.

To get an indication of how the fullerenes protect the other active layer materials and whether they themselves are altered in the process, thin layers of ICMA on glass and on ZnO were aged under UV, scraped off and the obtained powder was analyzed with Raman spectroscopy. The two spectra, shown in **Figure 3.5d**, are very similar and show the same peaks as pristine ICMA, namely several small peaks between 700cm^{-1} and 1480cm^{-1} , which can be attributed to various vibrations of C-H groups and two larger features from vibrations of C_{60} at 1462cm^{-1} and 1572cm^{-1} , where the former comes from the symmetric C=C stretching.⁵¹ A closer look at this region reveals that for the ICMA aged on ZnO those two peaks experience a broadening towards smaller wave numbers, indicating the slight expansion of some bonds in the C_{60} , which could for example happen due to an addition reaction of an electronegative functional group to a C=C bond. Thus, these results are a clear evidence that ZnO can cause UV-induced molecular changes to a fullerene.

Combining these observations with the finding that the main difference in UV stability of binary and ternary cells comes from a different trap density, the following explanation for the stabilizing effect of the fullerenes is proposed and schematically depicted in **Figure 3.6**: Upon UV illumination, an electron-hole pair is excited in the ZnO, which can interact with species that are adsorbed on the surface of ZnO.²³ This results in the generation of reactive oxygen species,²⁰ symbolized here as an OH-radical, which can then attack the vulnerable vinyl bonds of the IT-4F (**Figure 3.6a**), and thus destroy the conjugation in the small molecule acceptor.¹⁴

3 Increasing Photostability of Inverted Nonfullerene Organic Solar Cells by Using Fullerene Derivative Additives

The degraded IT-4F firstly absorbs less, which leads to a small decrease in J_{SC} of the binary cell. Secondly, and more importantly, the degraded IT-4F acts as a recombination center and therefore strongly reduces the fill factor of the binary devices. The added fullerene, depicted here as ICMA, acts as a radical scavenger and can catch several of those reactive oxygen species,^{30,31} and thus, protects the IT-4F molecule from chemical degradation (**Figure 3.6b**). The fullerenes with their large delocalized systems and good electron accepting properties can stabilize radicals and, therefore, do not act as recombination center.

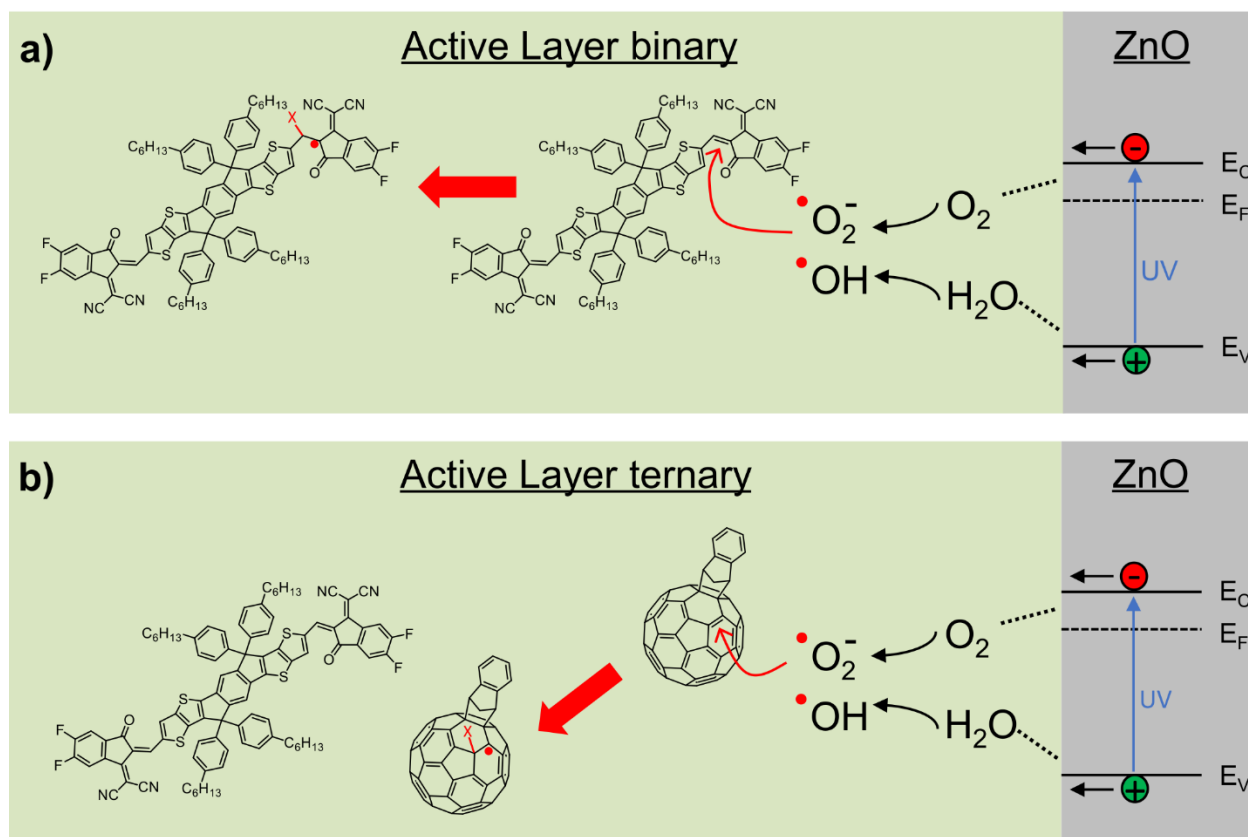


Figure 3.6: Scheme of the proposed mechanism for the ZnO-induced aging process in binary and ternary devices. UV light generates an electron-hole-pair in the ZnO, which reacts with species adsorbed on the ZnO surface. Reactive oxygen species, as for example OH-radicals, are created, which then can attack the vulnerable vinyl bonds of IT-4F (a). The deteriorated IT-4F acts as recombination center. ICMA protects IT-4F as sacrificial reagent and radical scavenger (b). Due to the large delocalized system, it can stabilize radicals, thus not acting as recombination center.

To understand the different effects of the three used fullerenes on the UV stability of the binary blend (ICMA>PC₇₁BM>BisPCBM), the location of the fullerenes in the ternary blend must be considered. For this reason, contact angle measurements of all pristine components were performed with water and glycerol and the surface energy was calculated according to the Wu model.⁵² The results are summarized in **Table S 3.4**. The surface energy of ICMA (40.3 mN m⁻¹

3 Increasing Photostability of Inverted Nonfullerene Organic Solar Cells by Using Fullerene Derivative Additives

¹) is much higher than the values of PBDB-TF (18.0 mN m⁻¹) and IT-4F (24.5 mN m⁻¹), and therefore it is expected to demix from the host system during film preparation and accumulate at the ZnO interface, while the lower surface energy components accumulate at the air surface to reduce the total energy.⁵³ Consequently, ICMA can trap the reactive oxygen species on the ZnO surface more efficiently and the protective effect is high. On the other hand, the surface energies of BisPCBM (27.8 mN m⁻¹) and PC₇₁BM (30.6 mN m⁻¹) are only somewhat higher than those of the binary host, which means that they do not demix to the same extent and thus show a smaller protective effect than ICMA.

3.3.5 Transferability of the Protective Effect

In order to examine whether the protective effect of the fullerenes is transferable, two other binary systems were chosen. On the one hand, PBDB-TF was combined with another nonfullerene acceptor BTP-4F and on the other hand IT-4F was combined with another polymer PTB7-Th. In both cases, corresponding ternary devices containing additionally 5% ICMA were also built. The average performance parameters of all devices can be found in **Table S 3.5**. Next, binary and ternary devices then were exposed to the same UV aging conditions as described above for the PBDB-TF:IT-4F system.

As visible from **Figure 3.7a**, the PBDB-TF:BTP-4F binary cells show the exact same aging behavior as the PBDB-TF:IT-4F system and, most importantly, the addition of ICMA has the same stabilizing effect, which mainly comes from reduced losses in FF and V_{OC} (**Figure S 3.14**). The UV stability of the PTB7-Th:IT-4F binary devices, shown in **Figure 3.7b**, demonstrate also a burn-in behavior which is comparable to the PBDB-TF:IT-4F system and furthermore, the added ICMA in the ternary cells slows down the aging. However, in this system the protective effect of the fullerene is not as strong as for PBDB-TF:IT-4F and PBDB-TF:BTP-4F, which could be related to a different miscibility of the PTB7-Th polymer with the acceptors IT-4F and ICMA.

Remarkably, this protective effect can not only be transferred to other materials systems, but even to other aging conditions. Binary devices based on PBDB-TF:IT-4F and the corresponding ternary devices with additional 5% ICMA were exposed to air for 24 hours in the dark. The PCE as a function of time, presented in **Figure 3.7c**, clearly reveals that the addition of ICMA significantly slows down the PCE loss, which likewise mainly originates from smaller losses in FF and V_{OC} , while the J_{SC} remains nearly unchanged in both devices (**Figure S 3.14**). In agreement with our photostability results, the better air-stability of the ternary device also suggest that ICMA acts as a radical scavenger for oxygen radicals diffusing into the active layer

3 Increasing Photostability of Inverted Nonfullerene Organic Solar Cells by Using Fullerene Derivative Additives

and consequently suppresses the oxidation of the ZnO surface.⁵⁴ However, further investigations, which are beyond the scope of this work, will be necessary to elucidate the detailed mechanism of this effect.

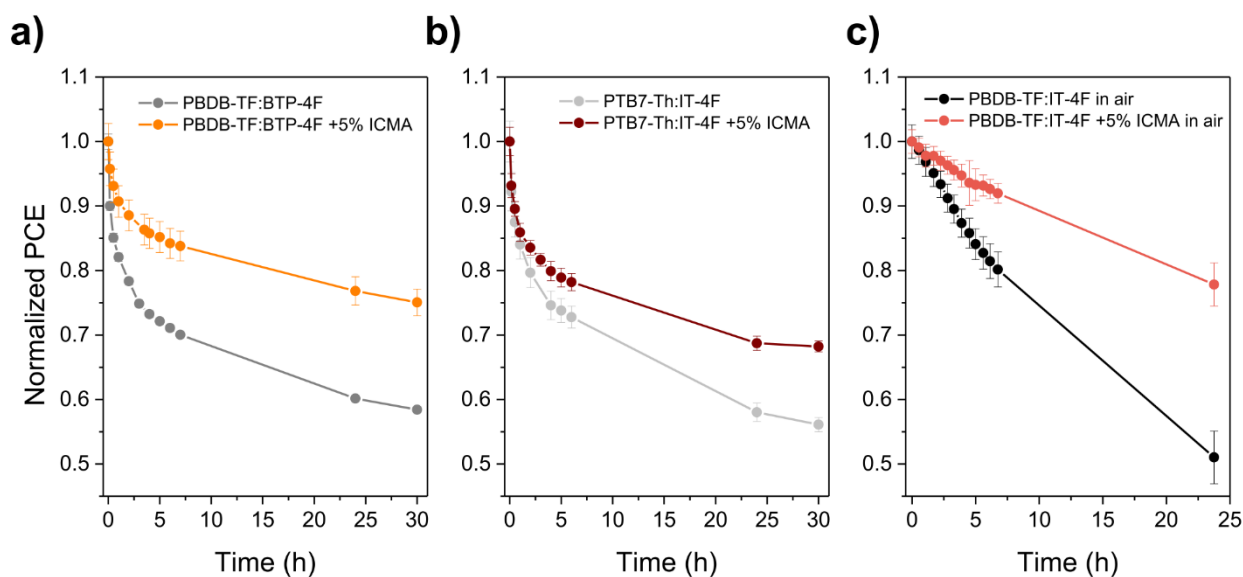


Figure 3.7: a,b) UV stability of the PCE as a function of time for binary PBDB-TF:BTP-4F devices and PTB7-Th:IT-4F devices and the corresponding ternary devices containing additionally 5% ICMA. c) Air stability of the PCE as a function of time for binary PBDB-TF:IT-4F devices and the corresponding ternary device with 5% ICMA. For all systems four individual devices were averaged and normalized to the respective fresh device.

3.4 Conclusions

In conclusion, we successfully demonstrated that the efficiency and UV photostability of a PBDB-TF:IT-4F based OSC can be improved by simply incorporating different fullerene derivatives into the bulk heterojunction, resulting in an up to fivefold increased lifetime without affecting the active layer morphology or negatively impacting on the *PCE*. Upon UV illumination, devices without fullerenes showed a rapidly decreasing fill factor due to increasing monomolecular recombination, which is attributed to the photocatalytic degradation of IT-4F at the ZnO interface. Based on the light intensity-dependent V_{OC} and FTPS results, the fullerenes protect IT-4F from the detrimental influence of ZnO by acting as radical scavengers and, thus, suppressing the emergence of trap states. Furthermore, we showed that the protective effect of fullerenes is transferable to OSCs based on different polymers and nonfullerene acceptors and even significantly increases the air stability. This work illustrates that a ternary approach – compared to additional protective interlayers – provides a simple and versatile method to protect nonfullerene acceptors from the photocatalytic activity of ZnO and increase the photostability of inverted organic solar cells.

3.5 Experimental Section

Materials. ITO substrates with $15 \Omega\text{cm}^2$ were purchased from Kintec. The ZnO nanoparticle dispersion (Avantama-N10) was purchased from Avantama AG. Poly[(2,6-(4,8-bis(5-(2-ethylhexyl)thiophen-2-yl)-benzo[1,2-b:4,5-b']dithiophene))-alt-(5,5-(1',3'-di-2-thienyl-5',7'-bis(2-ethylhexyl)benzo[1',2'-c:4',5'-c']dithiophene-4,8-dione))] (denoted PBDB-TF, sometimes called PBDB-T-2FF or PM6), 3,9-bis(2-methylene-((3-(1,1-dicyanomethylene)-6,7-difluoro)-indanone))-5,5,11,11-tetrakis(4-hexylphenyl)-dithieno[2,3-d:2',3'-d']-s-indaceno[1,2-b:5,6-b']dithiophene (IT-4F) and 2,2'-((2Z,2'Z)-((12,13-bis(2-ethylhexyl)-3,9-diundecyl-12,13-dihydro-[1,2,5]thiadiazolo[3,4-e]thieno[2'',3''':4',5']thieno[2',3':4,5]pyrrolo[3,2-g]thieno[2',3':4,5]thieno [3,2-b]indole-2,10-diyl)bis(methanylylidene))bis(5,6-difluoro-3-oxo-2,3-dihydro-1H-indene-2,1-diylylidene))dimalononitrile (denoted BTP-4F, sometimes called Y6) were provided by Solarmer. Poly[4,8-bis(5-(2-ethylhexyl)thiophen-2-yl)benzo[1,2-b:4,5-b']dithiophene-2,6-diyl-alt-(4-(2-ethylhexyl)-3-fluorothieno[3,4-b]thiophene)-2-carboxylate-2-6-diyl] (denoted PTB7-Th, sometimes called PCE10) was purchased from 1-Material. [6,6]-Phenyl-C71-butyric acid methyl ester (PC₇₁BM), indene-C₆₀ monoadduct (ICMA) and bis(1-[3-(methoxycarbonyl)propyl]-1-phenyl)-[6,6]C₆₂ (BisPCBM) with a purity of >99% were obtained from Solenne BV. Chlorobenzene, 1,8-diiodooctane (DIO), and 1-chloronaphthalene were purchased from Sigma Aldrich.

Device Fabrication. ITO substrates were cleaned with detergent and ultrasonicated in water, acetone and isopropanol for 10 min. The substrates were then dried under a nitrogen flow and plasma cleaned for 20 min. A 40nm ZnO layer was spin coated (1400rpm for 60s) and annealed for 10min at 120°C in air. Subsequently, the substrates were moved to a nitrogen glovebox. For the active layer solutions, all compounds were dissolved separately, then mixed and stirred overnight. For the PBDB-TF:IT-4F binary active layer a 1:1 weight ratio with a total concentration of 20 mg ml⁻¹ in chlorobenzene was prepared. For the corresponding ternary active layers, 5wt% of PC₇₁BM, ICMA or BisPCBM was added (dissolved in chlorobenzene with 20 mg mL⁻¹ concentration), resulting in a ratio of approximately 1:1:0.05. The ICMA solution was heated to 70°C to completely dissolve prior to mixing. At a time 30min before spin coating, v/v 0.5% DIO was added and then all active layers were dynamically spin coated with a two-step program, first 900 rpm for 5s followed by 4000rpm for 60s. For the binary devices with an ICMA interlayer a 20 mg mL⁻¹ ICMA solution at 70°C was dynamically spin coated (1000rpm for 60s) on top of ZnO, followed by an annealing at 120°C for 15min. Subsequently, the PBDB-TF:IT-4F layer was spin coated as explained before. For the PTB7-

3 Increasing Photostability of Inverted Nonfullerene Organic Solar Cells by Using Fullerene Derivative Additives

Th:IT-4F binary active layer a 1:1.5 weight ratio with a total concentration of 20 mg mL⁻¹ in chlorobenzene was prepared, and for the corresponding ternary active layer 5wt% of ICMA was added (20 mg mL⁻¹ in chlorobenzene). Also, v/v 0.5% DIO was added 30min before spin coating the active layer (1500rpm for 60s). For the PBDB-TF:BTP-4F binary active layer a 1:1.2 weight ratio with a total concentration of 16 mg mL⁻¹ in chloroform was prepared, and for the corresponding ternary active layer 5wt% of ICMA was added (16mg mL⁻¹ in chloroform). 30min before spin coating v/v 0.5% 1-chloronaphthalene was added and the mixture was spin coated with 3000rpm for 30s. Finally, on top of all devices 10nm of MoO_x and 100nm of Ag were evaporated through a mask.

Characterization Techniques. *JV*-measurements were performed using a Keithley 2401 source-measure unit and a Newport ABA solar simulator, which was calibrated to AM1.5G using a Fraunhofer silicon diode. UV-vis spectra of the thin films on glass substrates were recorded with a Perkin Elmer Lambda 1050 instrument, using an integrating sphere and an InGaAs detector. EQE measurements were performed with a home-built setup using a 150 W Xe short arc lamp (LOT Oriel) combined with a monochromator (Horiba microHR) and two Si-diodes (Hamamatsu) to calibrate the photon flux and compensate for light intensity fluctuations. For voltage-dependent EQE measurements a potentiostat (Metrohm Autolab) was used to apply voltage and simultaneously measure current. Light intensity dependent *JV*-curves were measured using a Keithley 2401 source-measure unit and a white light LED as light source. A Si-photodiode was used to control the light intensity. FTIR measurements were done with a modified Bruker Vertex 70 FTIR instrument by focusing light from a tungsten halogen lamp through a CaF₂ beam splitter with integrated gold mirrors to illuminate the devices under short-circuit conditions. The current from the devices was amplified with a FEMTO DHPA-100 current amplifier, passed through an analog-to-digital converter, and fed back to the FTIR instrument for Fourier transformation. Every measurement was averaged over 10000 scans for noise reduction and then scaled to the respective EQE signals, which were obtained separately. FT-Raman powder measurements were done with a RAM II extension of the Bruker Vertex 70 with a germanium detector at an excitation wavelength of 1064 nm and a laser power of 50mW. GIWAXS and GISAXS measurements were performed at the P03 beamline at DESY⁵⁵ (Hamburg, Germany) at an energy of 12.85 keV. For GIWAXS a Pilatus 300k detector (Dectris) was used and the data were obtained at an incident angle of 0.32° and a sample detector distance (SDD) of 287mm. 2D-GIWAXS data were corrected and evaluated with the software GIXSGUI.⁵⁶ For GISAXS a Lambda pixel detector (DESY) was used and the data were obtained at an incident angle of 0.32° and an SDD of 3554mm. Data evaluation was performed

3 Increasing Photostability of Inverted Nonfullerene Organic Solar Cells by Using Fullerene Derivative Additives

with the open source Python program DPDAK. Horizontal line cuts were made at the critical angle of PBDB-TF (0.1° for 12.85 keV).

Stability Testing. All device photostability tests were performed in a nitrogen filled glovebox with water and oxygen levels <1 ppm. The illumination with UV light or white light LED was performed through the glass substrate and a shadow mask with 6.25 mm^2 . The devices were aged under a 365nm UV LED (Thorlabs), which was calibrated with a Si-diode (Hamamatsu) to match the UV part of AM1.5G (300-400nm, corresponds to 4.6 mW cm^{-2}). For the *JV*-measurements a Keithley 2401 was used and the devices were illuminated with a white light LED, which was also calibrated to 1 sun with a Si-diode. For the air stability tests, devices were aged under dark condition in air at a constant temperature of 20°C .

3 Increasing Photostability of Inverted Nonfullerene Organic Solar Cells by Using Fullerene Derivative Additives

3.6 Supporting Information

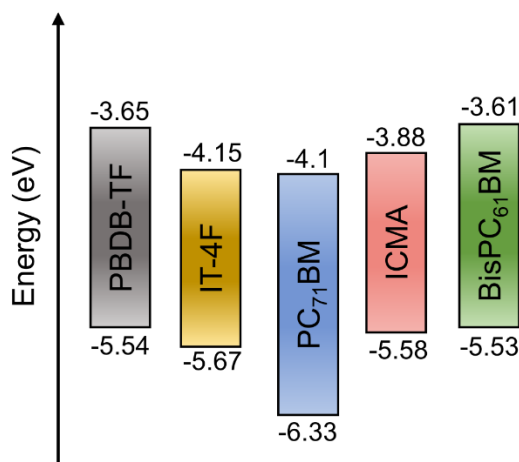


Figure S 3.1: HOMO and LUMO energy levels of the used active layer materials PBDB-TF and IT-4F, and of the fullerene derivatives PC71BM, ICMA and BisPCBM.

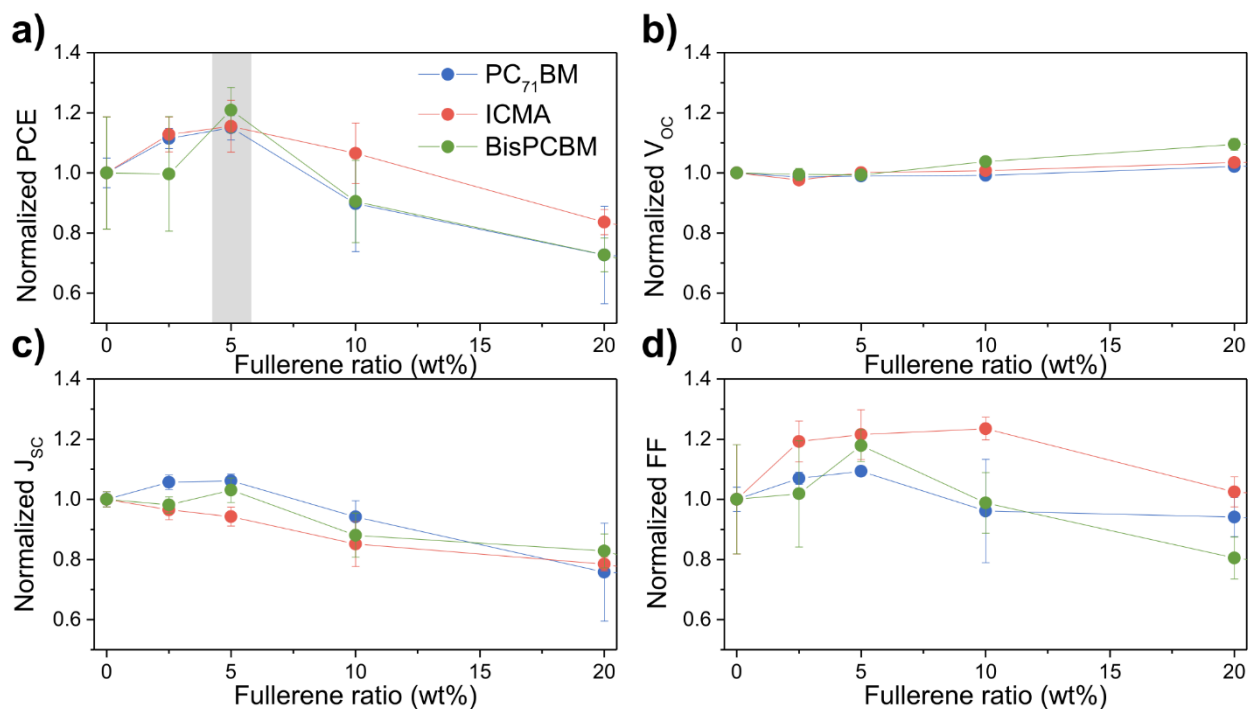


Figure S 3.2: Average a) PCE, b) VOC, c) JSC and d) FF (from at least seven individual cells) for ternary organic solar cells with varying concentrations of the three different fullerenes in the binary blend of PBDB-TF:IT-4F. The donor:acceptor ratio was kept at 1:1 and the fullerene:IT-4F ratio was changed.

3 Increasing Photostability of Inverted Nonfullerene Organic Solar Cells by Using Fullerene Derivative Additives

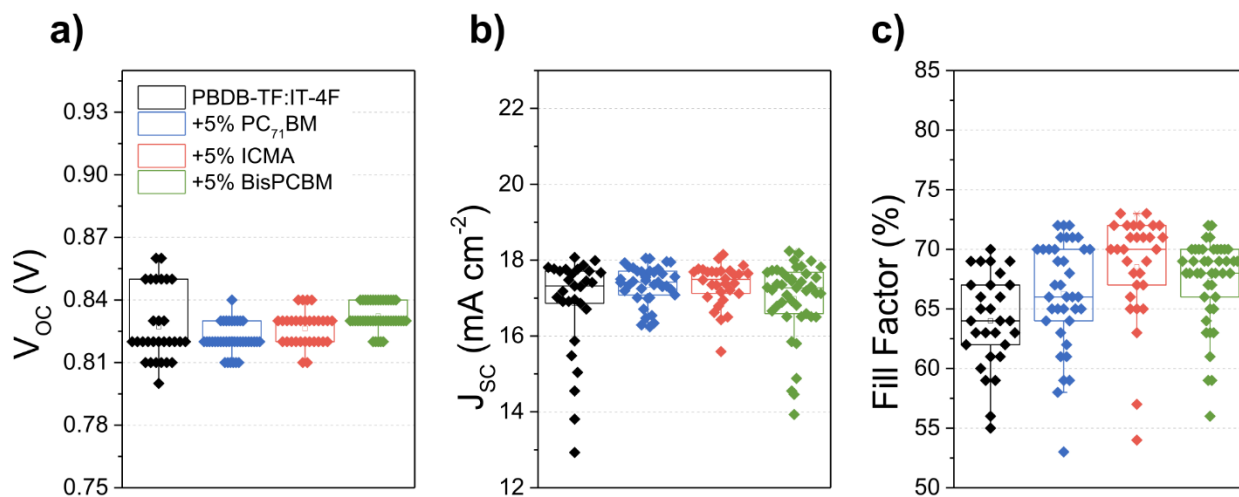


Figure S 3.3: Distribution of a) V_{OC} , b) J_{SC} and c) FF from 30 individual cells for the binary PBDB-TF:IT-4F cells and the three ternary OSCs with different added fullerene derivatives.

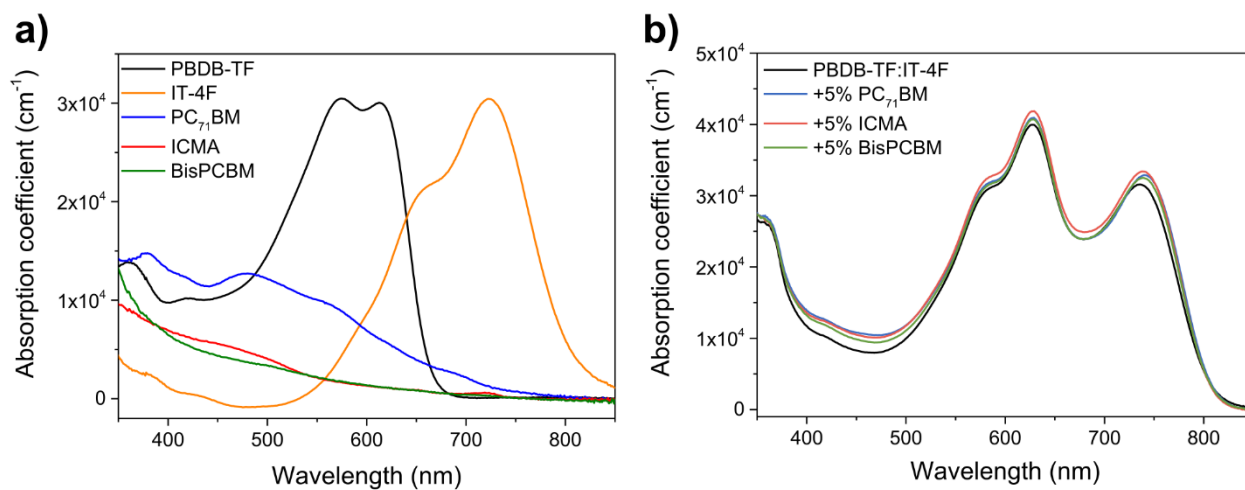


Figure S 3.4: Absorption coefficients of a) pristine materials on glass/ZnO, and of b) binary and ternary PBDB-TF:IT-4F blends on glass/ZnO.

3 Increasing Photostability of Inverted Nonfullerene Organic Solar Cells by Using Fullerene Derivative Additives

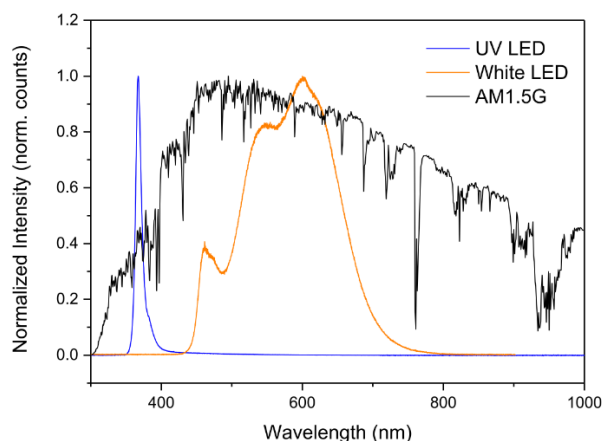


Figure S 3.5: Normalized spectra of the used 365nm UV LED and white light LED compared to the AM1.5G sun spectrum.

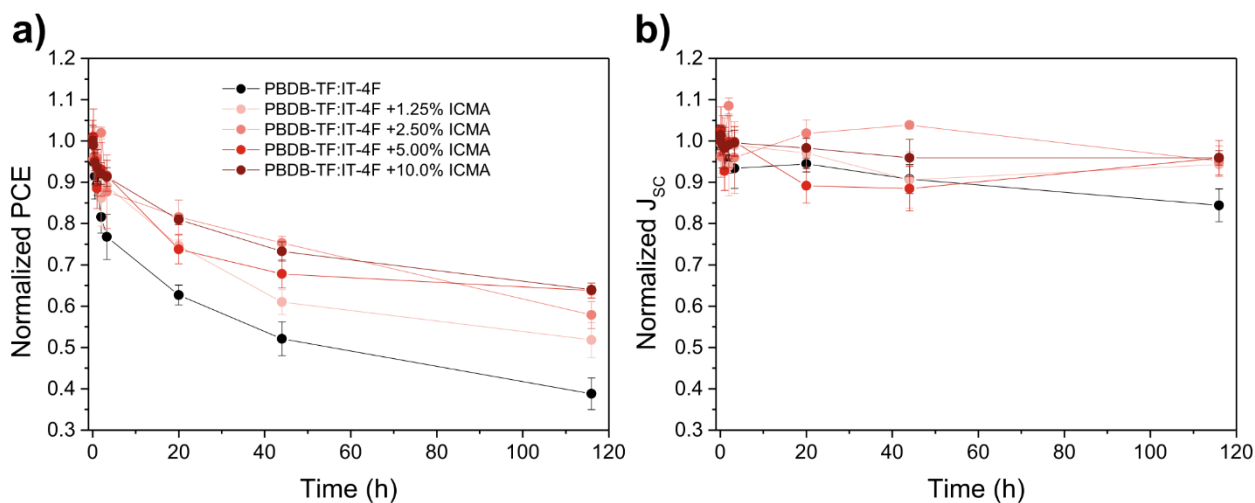


Figure S 3.6: UV stability of normalized a) PCE and b) J_{sc} as a function of time for binary and ternary PBDB-TF:IT-4F cells with different ratios of ICMA. Since the devices were removed from the sample holder between the individual measurements, the J_{sc} does not show a clear trend but small fluctuation, which originate from small differences in contacting and in the exact location of the illuminated area.

3 Increasing Photostability of Inverted Nonfullerene Organic Solar Cells by Using Fullerene Derivative Additives

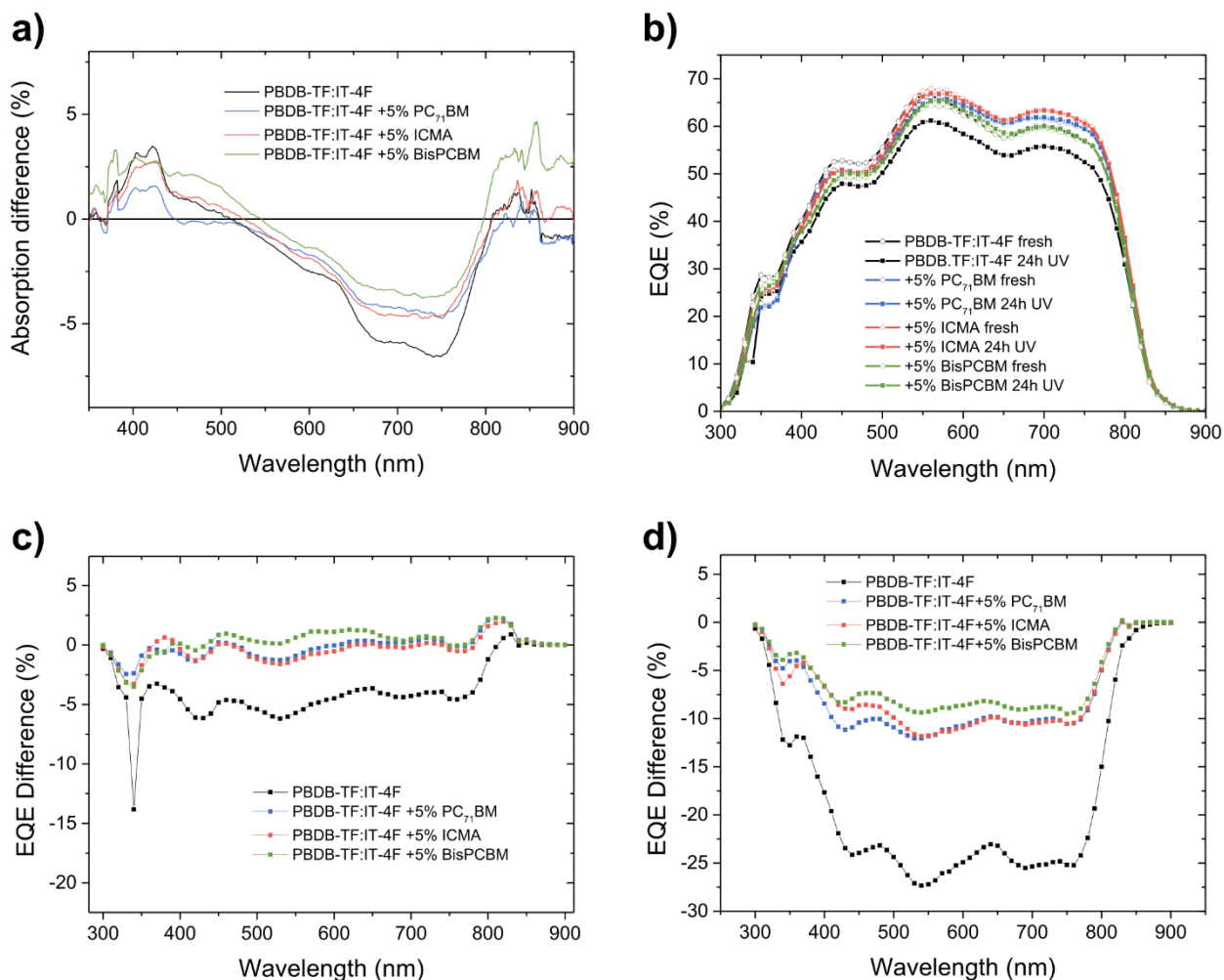


Figure S 3.7: a) Absorption difference of fresh and 24h UV aged binary and ternary cells related to the corresponding fresh device. b) EQE measurements of fresh and 24h UV aged binary and ternary cells and c) corresponding differences. d) EQE differences of fresh and 24h UV aged binary and ternary cells from voltage-dependent EQE measurements with a bias of 0.6V.

3 Increasing Photostability of Inverted Nonfullerene Organic Solar Cells by Using Fullerene Derivative Additives

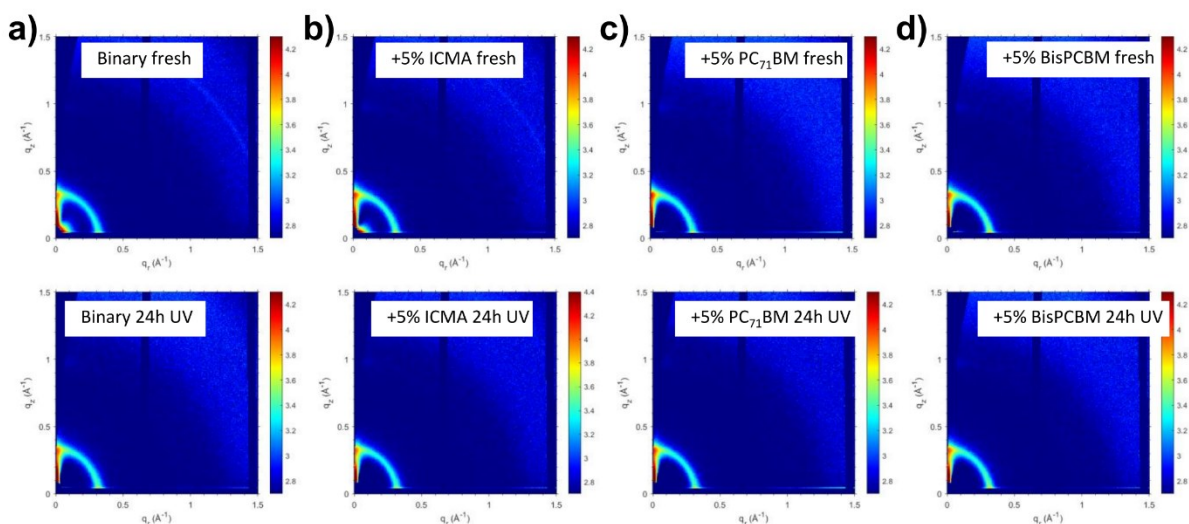


Figure S 3.8: 2D GIWAXS data of the fresh and 24h UV aged a) binary PBDB-TF:IT-4F blend and the PBDB-TF:IT-4F blends with addition of 5% b) ICMA, c) PC₇₁BM, and d) BisPCBM.

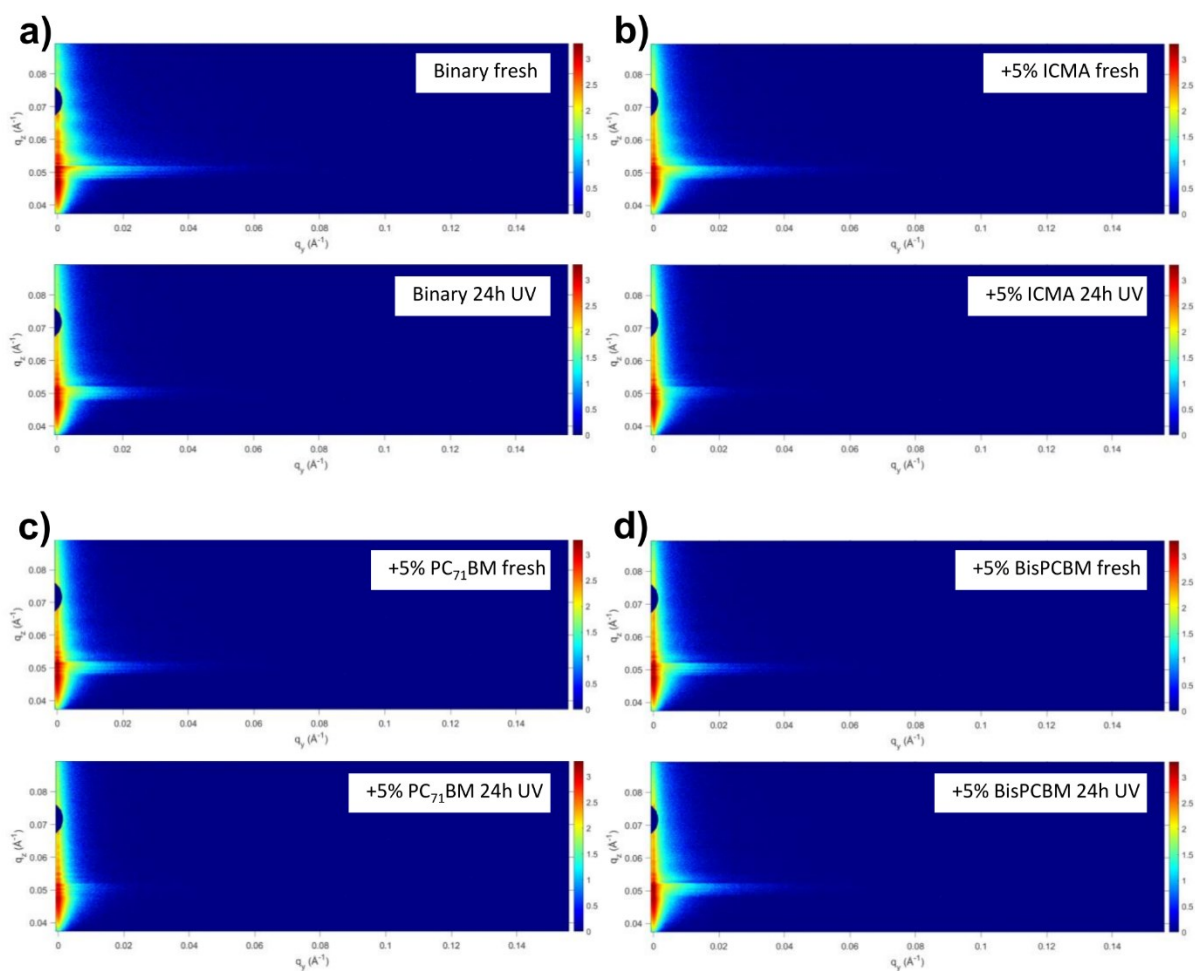


Figure S 3.9: 2D GISAXS data of the fresh and 24h UV aged a) binary PBDB-TF:IT-4F blend and ternary PBDB-TF:IT-4F blends with addition of 5% b) ICMA, c) PC₇₁BM, and d) BisPCBM.

3 Increasing Photostability of Inverted Nonfullerene Organic Solar Cells by Using Fullerene Derivative Additives

Table S 3.1: Fit parameters of the GISAXS data modeling of line cuts in the framework of the DWBA with three cylindrically shaped substructures. Radius and center-to-center domain distance (DC) for each of the modeled cylindrically-shaped substructures (large, medium, small) and their respective share in the fit of the total intensity.

Sample on glass/ITO	Radius large	Dc large	Radius medium	Dc medium	Radius small	Dc small	large	medium	small
	[nm]	[nm]	[nm]	[nm]	[nm]	[nm]	[%]	[%]	[%]
PBDB-TF:IT-4F fresh	99.5±3.0	200±15	44.7±3.0	102±10	12.1±1.5	63.9±7	2.3	9.0	88.7
PBDB-TF:IT-4F 24h UV	99.5±2.6	210±10	44.8±1.7	102±10	12.5±2.0	63.9±7	2.2	13.7	84.1
+5% ICMA fresh	100.1±3.0	215±15	44.5±2.0	102±10	12.5±1.3	62.8±9	2.4	8.7	88.9
+5% ICMA 24h UV	100.1±3.5	220±15	44.4±2.3	102±10	12.2±1.5	62.8±9	2.4	12.4	85.2
+5% PC₇₁BM fresh	99.0±2.5	210±15	44.5±1.9	99±13	12.0±1.3	62.5±10	2.5	9.5	88.0
+5% PC₇₁BM 24h UV	98.5±2.2	215±15	44.4±1.9	99±15	12.2±1.5	62.5±10	2.3	11.8	85.9
+5% BisPCBM fresh	101.6±3.0	212±10	44.0±2.5	100±15	12.3±1.3	62.8±15	2.5	8.9	88.6
+5% BisPCBM 24h UV	101.6±2.5	213±10	44.0±2.0	100±15	12.4±1.0	62.8±15	2.3	11.3	86.4

3 Increasing Photostability of Inverted Nonfullerene Organic Solar Cells by Using Fullerene Derivative Additives

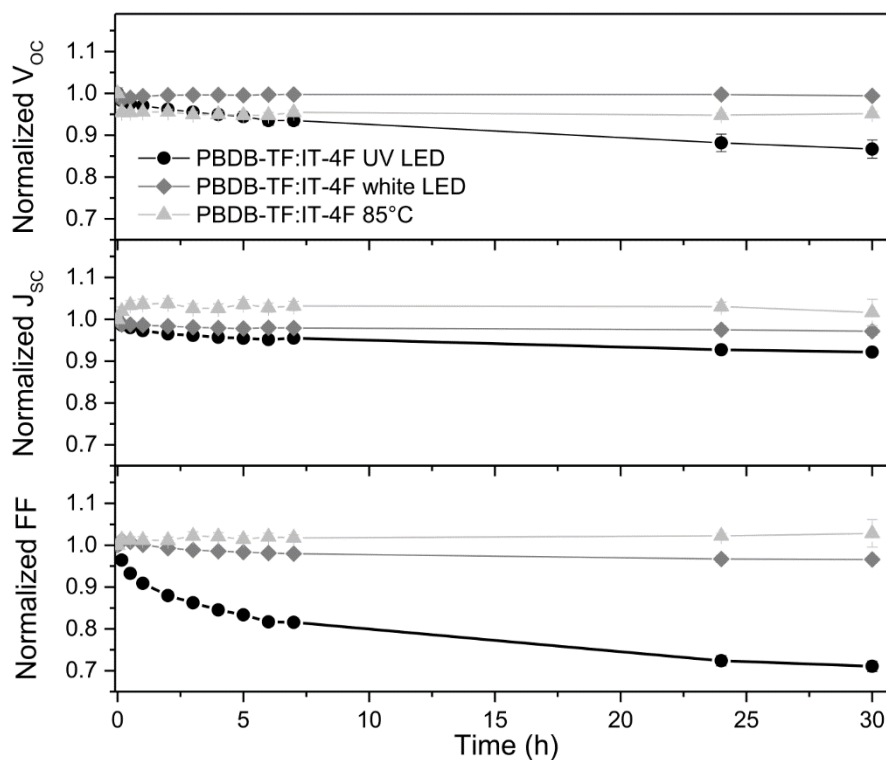


Figure S 3.10: Stability of V_{oc} , J_{sc} and FF as a function of time for binary PBDB-TF:IT-4F devices under different aging conditions. Devices were aged for 30 hours in nitrogen atmosphere either under a UV LED (black), a white light LED (grey) or in the dark on a hotplate at 85°C (light grey). For every aging condition, data of three individual devices were averaged and normalized to those of the fresh devices.

Table S 3.2: Record and average PCE, V_{oc} , J_{sc} and FF of binary PBDB-TF:IT-4F devices and ternary PBDB-TF:IT-4F:ICMA devices without DIO (from 14 individual cells processed in two batches).

	<i>PCE</i> (%)	<i>V_{oc}</i> (V)	<i>J_{sc}</i> (mA cm ⁻²)	<i>FF</i> (%)
PBDB-TF:IT-4F w/o DIO	8.4 (7.5±0.6)	0.90 (0.90±0.01)	15.2 (14.4±1.0)	61 (58±2)
PBDB-TF:IT-4F:ICMA w/o DIO	8.6 (7.8±1.0)	0.90 (0.90±0.01)	15.7 (14.8±0.6)	61 (58±6)

3 Increasing Photostability of Inverted Nonfullerene Organic Solar Cells by Using Fullerene Derivative Additives

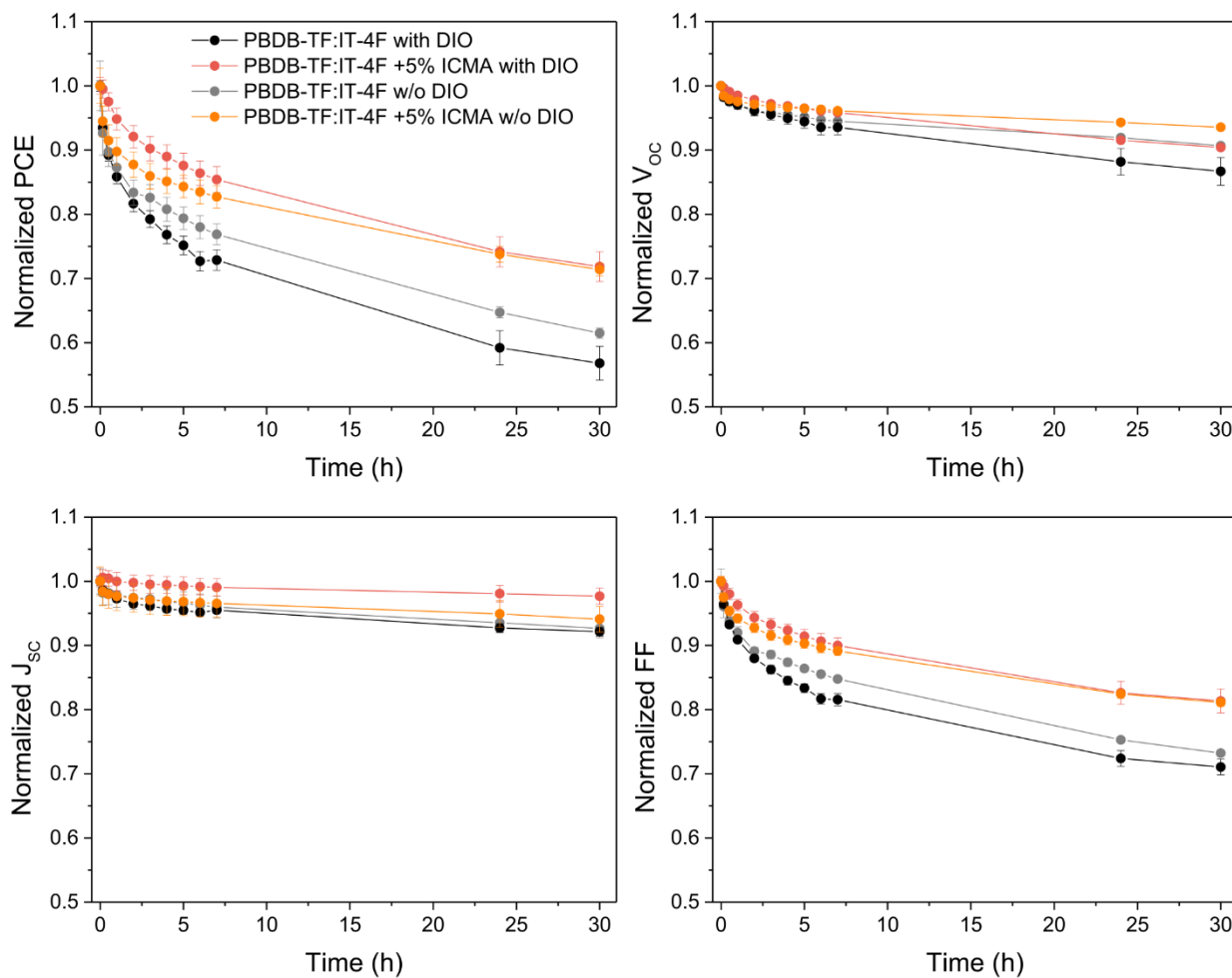


Figure S 3.11: UV stability of PCE, V_{oc} , J_{sc} and FF as a function of time for binary PBDB-TF:IT-4F and ternary PBDB-TF:IT-4F:ICMA devices with and without DIO.

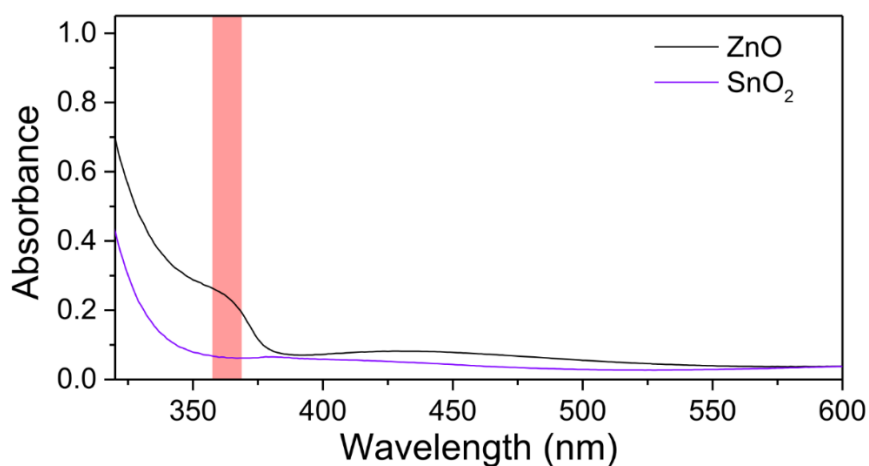


Figure S 3.12: UV-vis spectra of thin films of ZnO and SnO₂ on glass. The red bar marks the emission range of the used UV LED.

3 Increasing Photostability of Inverted Nonfullerene Organic Solar Cells by Using Fullerene Derivative Additives

Table S 3.3: Record and average PCE, V_{oc} , J_{sc} and FF of binary PBDB-TF:IT-4F devices with ZnO as ETL (from 30 individual cells) and from binary devices, with SnO₂ as ETL (from 26 individual cells).

	<i>PCE</i> (%)	<i>V_{oc}</i> (V)	<i>J_{sc}</i> (mA cm ⁻²)	<i>FF</i> (%)
PBDB-TF:IT-4F with ZnO	10.2 (8.8±1.0)	0.85 (0.83±0.02)	17.3 (16.9±1.3)	69 (64±4)
PBDB-TF:IT-4F with SnO ₂	8.4 (7.1±0.7)	0.84 (0.85±0.01)	16.4 (15.4±1.1)	61 (55±4)

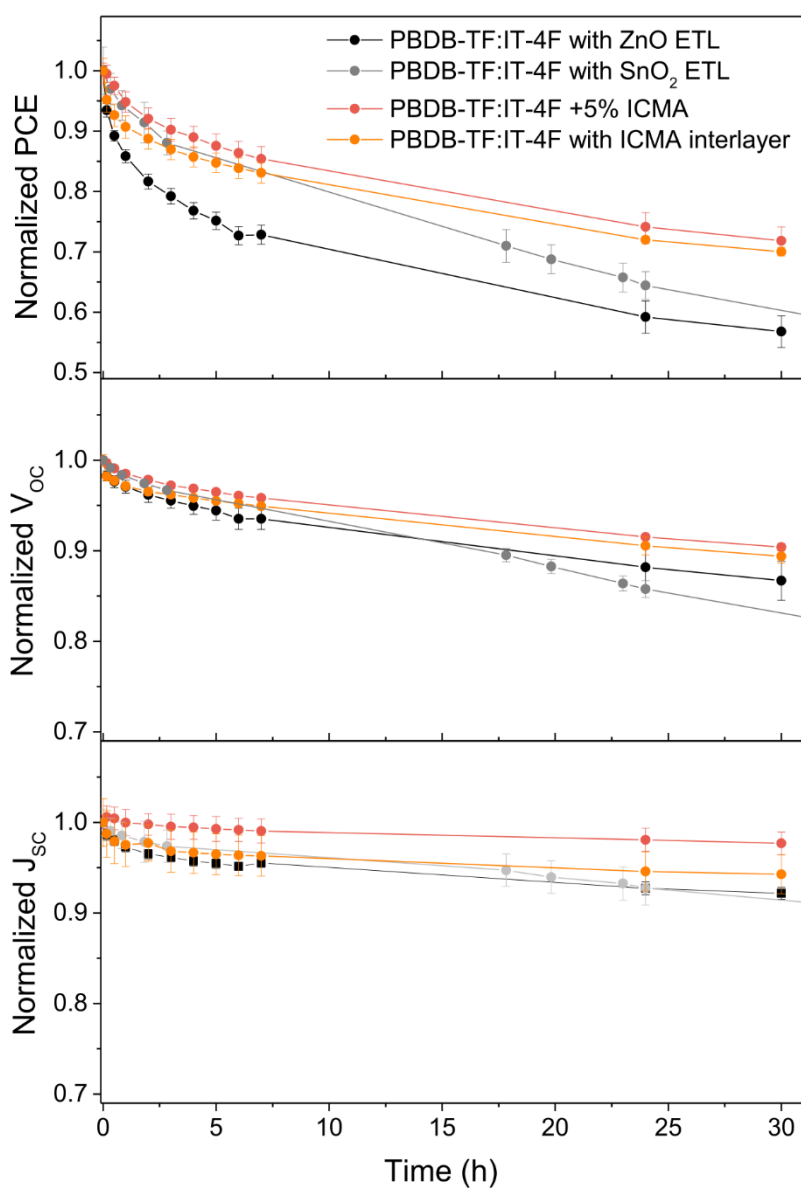


Figure S 3.13: UV stability of PCE, V_{oc} and J_{sc} as a function of time for binary PBDB-TF:IT-4F devices and the corresponding ternary devices with 5% ICMA added with a ZnO ETL, in comparison with PBDB-TF:IT-4F devices with a SnO₂ ETL and PBDB-TF:IT-4F devices with an ICMA interlayer on top of ZnO.

3 Increasing Photostability of Inverted Nonfullerene Organic Solar Cells by Using Fullerene Derivative Additives

Table S 3.4: Contact angles with water and glycerol on pristine films of the active layer materials and the resulting surface energies calculated according to the Wu model.

	Contact angle water (deg)	Contact angle glycerol (deg)	Surface energy (mN m ⁻¹)
PBDB-TF	103.0	97.1	18.0
IT-4F	98.6	84.9	24.5
PC ₇₁ BM	83.0	72.5	30.6
ICMA	70.1	80.1	40.3
BisPCBM	89.6	77.4	27.8

Table S 3.5: Average PCE, V_{OC} , J_{SC} and FF of binary PBDB-TF:BTP-4F and PTB7-Th:IT-4F devices and the corresponding ternary devices with 5 % ICMA added (from 15 individual cells processed).

	<i>PCE</i> (%)	V_{OC} (V)	J_{SC} (mA cm ⁻²)	<i>FF</i> (%)
PBDB-TF:BTP-4F	12.3 ± 0.5	0.85 ± 0.01	21.9 ± 0.2	67 ± 3
PBDB-TF:BTP-4F +5% ICMA	12.8 ± 0.8	0.86 ± 0.01	20.9 ± 0.8	71 ± 3
PTB7-Th:IT-4F	6.5 ± 0.6	0.66 ± 0.01	16.0 ± 0.3	62 ± 6
PTB7-Th:IT-4F +5% ICMA	7.4 ± 0.1	0.67 ± 0.01	16.2 ± 0.2	69 ± 1

3 Increasing Photostability of Inverted Nonfullerene Organic Solar Cells by Using Fullerene Derivative Additives

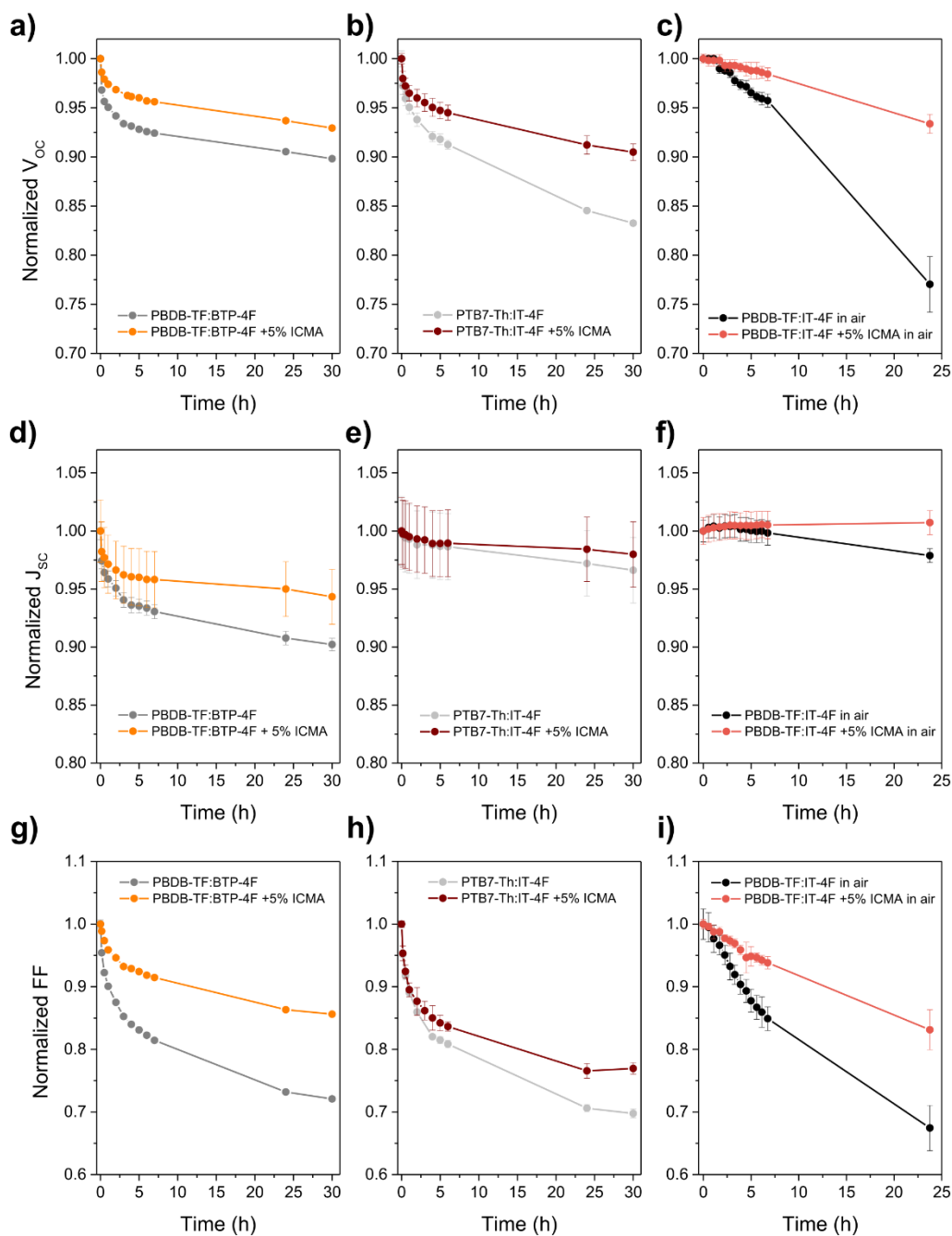


Figure S 3.14: UV stability of V_{OC} , J_{SC} and FF as a function of time for binary PBDB-TF:BTP-4F devices (a,d,g) and PTB7-Th:IT-4F devices (b,e,h) and the corresponding ternary devices where 5 % ICMA was added. Air stability in the dark of V_{OC} , J_{SC} and FF for binary PBDB-TF:IT-4F devices and corresponding ternary devices with 5 % ICMA added (g,h,i). In all cases, four individual devices were averaged and normalized to the value of the fresh device.

3.7 References

1. Lin, Y. *et al.* Self-Assembled Monolayer Enables Hole Transport Layer-Free Organic Solar Cells with 18% Efficiency and Improved Operational Stability. *ACS Energy Lett.* **5**, 2935–2944; 10.1021/acsenergylett.0c01421 (2020).
2. Liu, Q. *et al.* 18% Efficiency Organic Solar Cells. *Science Bulletin* **65**, 272–275; 10.1016/j.scib.2020.01.001 (2020).
3. Lin, Y. *et al.* A Simple n-Dopant Derived from Diquat Boosts the Efficiency of Organic Solar Cells to 18.3%. *ACS Energy Lett.* **5**, 3663–3671; 10.1021/acsenergylett.0c01949 (2020).
4. Mateker, W. R. & McGehee, M. D. Progress in Understanding Degradation Mechanisms and Improving Stability in Organic Photovoltaics. *Adv. Mater.* **29**; 10.1002/adma.201603940 (2017).
5. Chochos, C. L. *et al.* The Role of Chemical Structure in Indacenodithienothiophene- alt - benzothiadiazole Copolymers for High Performance Organic Solar Cells with Improved Photo-stability through Minimization of Burn-in Loss. *J. Mater. Chem. A* **5**, 25064–25076; 10.1039/C7TA09224E (2017).
6. Zhang, C. *et al.* Overcoming the Thermal Instability of Efficient Polymer Solar Cells by Employing Novel Fullerene-Based Acceptors. *Adv. Energy Mater.* **7**, 1601204; 10.1002/aenm.201601204 (2017).
7. Li, N. *et al.* Abnormal Strong Burn-in Degradation of Highly Efficient Polymer Solar Cells Caused by Spinodal Donor-Acceptor Demixing. *Nat Commun* **8**; 10.1038/ncomms14541 (2017).
8. Du, X. *et al.* Unraveling the Microstructure-Related Device Stability for Polymer Solar Cells Based on Nonfullerene Small-Molecular Acceptors. *Adv. Mater.* **32**; 10.1002/adma.201908305 (2020).
9. Schaffer, C. J. *et al.* A Direct Evidence of Morphological Degradation on a Nanometer Scale in Polymer Solar Cells. *Adv. Mater.* **25**, 6760–6764; 10.1002/adma.201302854 (2013).
10. Street, R. A., Northrup, J. E. & Krusor, B. S. Radiation Induced Recombination Centers in Organic Solar Cells. *Phys. Rev. B* **85**; 10.1103/PhysRevB.85.205211 (2012).

3 Increasing Photostability of Inverted Nonfullerene Organic Solar Cells by Using Fullerene Derivative Additives

11. Distler, A. *et al.* The Effect of PCBM Dimerization on the Performance of Bulk Heterojunction Solar Cells. *Adv. Energy Mater.* **4**, 1300693; 10.1002/aenm.201300693 (2014).
12. Heumueller, T. *et al.* Morphological and Electrical Control of Fullerene Dimerization Determines Organic Photovoltaic Stability. *Energy Environ. Sci.* **9**, 247–256; 10.1039/C5EE02912K (2016).
13. Jacobs, I. E. *et al.* Photoinduced Degradation from Trace 1,8-Diiodooctane in Organic Photovoltaics. *J. Mater. Chem. C* **6**, 219–225; 10.1039/C7TC04358A (2018).
14. Jiang, Y. *et al.* Photocatalytic Effect of ZnO on the Stability of Nonfullerene Acceptors and its Mitigation by SnO₂ for Nonfullerene Organic Solar Cells. *Mater. Horiz.* **6**, 1438–1443; 10.1039/C9MH00379G (2019).
15. Gevorgyan, S. A. *et al.* Lifetime of Organic Photovoltaics: Status and Predictions. *Adv. Energy Mater.* **6**; 10.1002/aenm.201501208 (2016).
16. Wang, W. *et al.* In Operando Morphology Investigation of Inverted Bulk Heterojunction Organic Solar Cells by GISAXS. *J. Mater. Chem. A* **3**, 8324–8331; 10.1039/C5TA01109D (2015).
17. Sorrentino, R., Kozma, E., Luzzati, S. & Po, R. Interlayers for Non-Fullerene Based Polymer Solar Cells: Distinctive Features and Challenges. *Energy Environ. Sci.* **375**; 10.1039/D0EE02503H (2021).
18. Youssef, Z. *et al.* Dye-Sensitized Nanoparticles for Heterogeneous Photocatalysis: Cases Studies with TiO₂, ZnO, Fullerene and Graphene for Water Purification. *Dyes and Pigments* **159**, 49–71; 10.1016/j.dyepig.2018.06.002 (2018).
19. Baruah, S., K. Pal, S. & Dutta, J. Nanostructured Zinc Oxide for Water Treatment. *Nanosci Nanotechnol.—Asia* **2**, 90–102; 10.2174/2210681211202020090 (2012).
20. Lam, S.-M., Sin, J.-C., Abdullah, A. Z. & Mohamed, A. R. Degradation of Wastewaters Containing Organic Dyes Photocatalysed by Zinc Oxide: a Review. *Desalin. Water Treat.* **41**, 131–169; 10.1080/19443994.2012.664698 (2012).
21. Park, S. & Son, H. J. Intrinsic Photo-Degradation and Mechanism of Polymer Solar Cells: the Crucial Role of Non-Fullerene Acceptors. *J. Mater. Chem. A* **7**, 25830–25837; 10.1039/C9TA07417A (2019).

- 3 Increasing Photostability of Inverted Nonfullerene Organic Solar Cells by Using Fullerene Derivative Additives
22. Soultati, A. *et al.* Suppressing the Photocatalytic Activity of Zinc Oxide Electron-Transport Layer in Nonfullerene Organic Solar Cells with a Pyrene-Bodipy Interlayer. *ACS Appl. Mater. Interfaces* **12**, 21961–21973; 10.1021/acsami.0c03147 (2020).
23. Wöll, C. The Chemistry and Physics of Zinc Oxide Surfaces. *Progress in Surface Science*, 55–120; 10.1016/J.PROGSURF.2006.12.002 (2007).
24. Noei, H. *et al.* The Identification of Hydroxyl Groups on ZnO Nanoparticles by Infrared Spectroscopy. *Phys. Chem. Chem. Phys.* **10**, 7092–7097; 10.1039/b811029h (2008).
25. Liu, B. *et al.* Visible Light-Induced Degradation of Inverted Polymer:Nonfullerene Acceptor Solar Cells: Initiated by the Light Absorption of ZnO Layer. *Sol. RRL* **35**; 10.1002/solr.202000638 (2020).
26. Liang, Z., Zhang, Q., Jiang, L. & Cao, G. ZnO Cathode Buffer Layers for Inverted Polymer Solar Cells. *Energy Environ. Sci.* **8**, 3442–3476; 10.1039/C5EE02510A (2015).
27. Wilken, S., Parisi, J. & Borchert, H. Role of Oxygen Adsorption in Nanocrystalline ZnO Interfacial Layers for Polymer–Fullerene Bulk Heterojunction Solar Cells. *J. Phys. Chem. C* **118**, 19672–19682; 10.1021/jp506641m (2014).
28. Polydorou, E. *et al.* Insights into the Passivation Effect of Atomic Layer Deposited Hafnium Oxide for Efficiency and Stability Enhancement in Organic Solar Cells. *J. Mater. Chem. C* **6**, 8051–8059; 10.1039/C8TC02243G (2018).
29. Sadeghianlemraski, M., Harding, C. R., Welch, G. C. & Aziz, H. Significant Photostability Enhancement of Inverted Organic Solar Cells by Inserting an N-Annulated Perylene Diimide (PDIN-H) between the ZnO Electron Extraction Layer and the Organic Active Layer. *ACS Appl. Energy Mater.* **3**; 10.1021/acsam.0c01587 (2020).
30. Bosi, S., Da Ros, T., Spalluto, G. & Prato, M. Fullerene Derivatives: an Attractive Tool for Biological Applications. *Eur. J. Med. Chem.* **38**, 913–923; 10.1016/j.ejmech.2003.09.005 (2003).
31. Zeynalov, E. B., Allen, N. S. & Salmanova, N. I. Radical Scavenging Efficiency of Different Fullerenes C₆₀–C₇₀ and Fullerene Soot. *Polym. Degrad. Stab.* **94**, 1183–1189; 10.1016/j.polymdegradstab.2009.04.027 (2009).
32. Ji, G. *et al.* 12.88% Efficiency in Doctor-Blade Coated Organic Solar Cells through Optimizing the Surface Morphology of a ZnO Cathode Buffer Layer. *J. Mater. Chem. A* **7**, 212–220; 10.1039/C8TA08873J (2019).

- 3 Increasing Photostability of Inverted Nonfullerene Organic Solar Cells by Using Fullerene Derivative Additives
33. Yu, R. *et al.* Improved Charge Transport and Reduced Nonradiative Energy Loss Enable Over 16% Efficiency in Ternary Polymer Solar Cells. *Adv. Mater.* **31**; 10.1002/adma.201902302 (2019).
34. Pan, M.-A. *et al.* 16.7%-Efficiency Ternary Blended Organic Photovoltaic Cells with PCBM as the Acceptor Additive to Increase the Open-Circuit Voltage and Phase Purity. *J. Mater. Chem. A* **7**, 20713–20722; 10.1039/C9TA06929A (2019).
35. Galli, D. *et al.* Suppressing the Surface Recombination and Tuning the Open-Circuit Voltage of Polymer/Fullerene Solar Cells by Implementing an Aggregative Ternary Compound. *ACS Appl. Mater. Interfaces* **10**, 28803–28811; 10.1021/acsami.8b09174 (2018).
36. Koster, L. J. A., Mihailetschi, V. D., Ramaker, R. & Blom, P. W. M. Light Intensity Dependence of Open-Circuit Voltage of Polymer:Fullerene Solar Cells. *Appl. Phys. Lett.* **86**, 123509; 10.1063/1.1889240 (2005).
37. Cowan, S. R., Roy, A. & Heeger, A. J. Recombination in Polymer-Fullerene Bulk Heterojunction Solar Cells. *Phys. Rev. B* **82**, 433; 10.1103/PhysRevB.82.245207 (2010).
38. Goris, L. *et al.* Optical Absorption by Defect States in Organic Solar Cells. *J. Non-Cryst. Solids* **352**, 1656–1659; 10.1016/j.jnoncrysol.2005.09.053 (2006).
39. Goris, L. *et al.* Observation of the Subgap Optical Absorption in Polymer-Fullerene Blend Solar Cells. *Appl. Phys. Lett.* **88**, 52113; 10.1063/1.2171492 (2006).
40. Zhang, M., Guo, X., Ma, W., Ade, H. & Hou, J. A Large-Bandgap Conjugated Polymer for Versatile Photovoltaic Applications with High Performance. *Adv. Mater.* **27**, 4655–4660; 10.1002/adma.201502110 (2015).
41. Stamm, M. Polymer Surface and Interface Characterization Techniques. In *Polymer Surfaces and Interfaces*, edited by M. Stamm (Springer Berlin Heidelberg, Berlin, Heidelberg, 2008), Vol. 100, pp. 1–16.
42. Schaffer, C. J. *et al.* Effect of Blend Composition and Additives on the Morphology of PCPDTBT:PC₇₁BM Thin Films for Organic Photovoltaics. *ACS Appl. Mater. Interfaces* **7**, 21347–21355; 10.1021/acsami.5b05939 (2015).
43. Wienhold, K. S. *et al.* Effect of Solvent Additives on the Morphology and Device Performance of Printed Nonfullerene Acceptor Based Organic Solar Cells. *ACS Appl. Mater. Interfaces* **11**, 42313–42321; 10.1021/acsami.9b16784 (2019).

- 3 Increasing Photostability of Inverted Nonfullerene Organic Solar Cells by Using Fullerene Derivative Additives
44. Wienhold, K. S. *et al.* Following in Operando the Structure Evolution-Induced Degradation in Printed Organic Solar Cells with Nonfullerene Small Molecule Acceptor. *Sol. RRL* **4**; 10.1002/solr.202000251 (2020).
45. Doumon, N. Y. *et al.* Improved Photostability in Ternary Blend Organic Solar Cells: the Role of [70]PCBM. *J. Mater. Chem. C* **5**, 13176; 10.1039/C8TC06621C (2019).
46. Zhu, Y. *et al.* Rational Strategy to Stabilize an Unstable High-Efficiency Binary Nonfullerene Organic Solar Cells with a Third Component. *Adv. Energy Mater.* **9**, 1900376; 10.1002/aenm.201900376 (2019).
47. Tremolet de Villers, B. J. *et al.* Removal of Residual Diiodooctane Improves Photostability of High-Performance Organic Solar Cell Polymers. *Chem. Mater.* **28**, 876–884; 10.1021/acs.chemmater.5b04346 (2016).
48. Doumon, N. Y. *et al.* 1,8-Diiodooctane Acts as a Photo-Acid in Organic Solar Cells. *Scientific reports* **9**, 4350; 10.1038/s41598-019-40948-1 (2019).
49. Classen, A. *et al.* Revealing Hidden UV Instabilities in Organic Solar Cells by Correlating Device and Material Stability. *Adv. Energy Mater.* **9**, 1902124; 10.1002/aenm.201902124 (2019).
50. Vandewal, K., Benduhn, J. & Nikolis, V. C. How to Determine Optical Gaps and Voltage Losses in Organic Photovoltaic Materials. *Sustainable Energy Fuels* **2**, 538–544; 10.1039/C7SE00601B (2018).
51. Xu, Z. C., Zhang, H. S., Li, Z., Yang, X. S. & Zhang, G. Theoretical Study on Electronic Structures and Spectroscopic Properties of Indene-C60 Monoadduct (ICMA). *AMR* **535-537**, 1287–1290; 10.4028/www.scientific.net/AMR.535-537.1287 (2012).
52. Souheng Wu. Calculation of Interfacial Tension in Polymer Systems. *J. Polymer. Sci.*, 19–30; 10.1002/polc.5070340105 (1971).
53. Xu, Z. *et al.* Vertical Phase Separation in Poly(3-hexylthiophene): Fullerene Derivative Blends and its Advantage for Inverted Structure Solar Cells. *Adv. Funct. Mater.* **19**, 1227–1234; 10.1002/adfm.200801286 (2009).
54. Venkatesan, S., Ngo, E., Khatiwada, D., Zhang, C. & Qiao, Q. Enhanced Lifetime of Polymer Solar Cells by Surface Passivation of Metal Oxide Buffer Layers. *ACS Appl. Mater. Interfaces* **7**, 16093–16100; 10.1021/acsami.5b04687 (2015).

3 Increasing Photostability of Inverted Nonfullerene Organic Solar Cells by Using Fullerene Derivative Additives

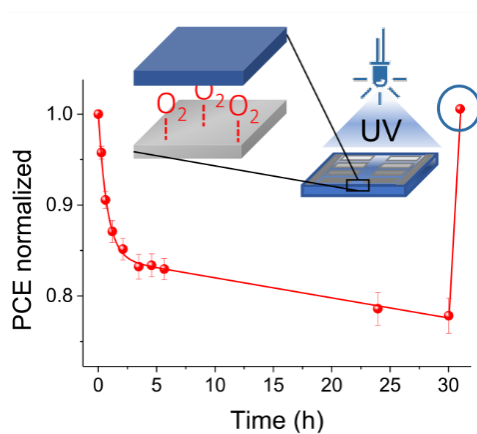
55. Buffet, A. *et al.* P03, the Microfocus and Nanofocus X-Ray Scattering (MiNaXS) Beamline of the PETRA III Storage Ring: the Microfocus Endstation. *J. Synchrotron Radiat.* **19**, 647–653; 10.1107/S0909049512016895 (2012).
56. Jiang, Z. GIXSGUI : a MATLAB Toolbox for Grazing-Incidence X-Ray Scattering Data Visualization and Reduction, and Indexing of Buried Three-Dimensional Periodic Nanostructured Films. *J Appl Crystallogr* **48**, 917–926; 10.1107/S1600576715004434 (2015).

4 The Neglected Influence of Zinc Oxide Light-Soaking on Stability Measurements of Inverted Organic Solar Cells

This chapter is based on the following publication:

Marcella Günther, Soroush Lotfi, Sergio Sánchez Rivas, Dominic Blätte, Jan P. Hofmann, Thomas Bein, Tayebbeh Ameri. The Neglected Influence of Zinc Oxide Light-Soaking on Stability Measurements of Inverted Organic Solar Cells

Manuscript under Revision



4.1 Abstract

Although zinc oxide (ZnO) is one of the most commonly used materials for electron transport layers in organic solar cells (OSCs), it also comes with disadvantages such as the so-called light-soaking issues, i.e. its need for an exposure to ultraviolet (UV) light to reach its full potential in OSCs. Here, the impact of ZnO light-soaking issues on stability measurements of OSCs is investigated. It is found that in the absence of UV light a reversible degradation occurs, which is independent of the used active layer material and accelerates at higher temperatures but can be undone with a short UV exposure. This reversible aging is attributed to the re-adsorption of oxygen, which for manufacturing reasons is trapped at the interface of ZnO, even in an oxygen-free environment. This oxygen can be removed with a UV-pretreatment of the ZnO, but at the expense of device efficiency and a production that has to take place in an oxygen-free environment. This work establishes that stability measurements of ZnO-containing OSCs must be performed exclusively with a light source including a UV-part, since the usage of a simple white light source – as often reported in the literature – can lead to erroneous results.

4.2 Introduction

Zinc oxide is one of the most popular and widely used electron transport materials in organic solar cells, owing to its many advantageous properties, such as high transparency, conductivity and stability, low cost and toxicity, and an easy solution-based processing.^[1,2] On the other hand, however, ZnO is also a complex material with a pronounced defect chemistry, whose electronic properties strongly depend on processing conditions and environment. One of its major problems is the so-called light-soaking issue.^[3] ZnO-containing solar cells need an exposure to light with an energy corresponding to the ZnO band gap – usually in the UV range – to reach their full potential.^[4,5] Without this light-soaking, the current-voltage characteristics show an s-shape with a reduced fill factor (FF) and an increased serial resistance, as schematically shown in **Figure 4.1** with the red curve. The necessary exposure time and wavelength of light depend on the exact properties of the used ZnO but are usually in the range of some seconds and between 360-380 nm, respectively. Importantly, the light-soaking issues are reversible, meaning that after some time without UV illumination, the cell performance can degrade again with the s-shape and reduced fill factor coming back. The cause of the light-soaking issues is attributed to oxygen being chemically adsorbed on the surface of zinc oxide, which traps negative charges at the surface of the ZnO and thus at the interface to the photoactive layer of the solar cell. This leads to an upward band bending towards the surface of the ZnO layer and consequently a hindered electron extraction, resulting in enhanced interface recombination and a decreased FF. UV irradiation generates electron-hole pairs in the ZnO, of which the holes can recombine with the trapped electrons, leading to a desorption of the oxygen and a reduced band bending. Consequently, the electron extraction issue at the interface of active layer and ZnO is resolved.^[5-7] However, the irradiation with UV can also result in the generation of oxygen radicals which can decompose the absorbing layer, which is why the duration of UV illumination is usually kept as short as possible.^[8-11]

Since oxygen is responsible for the light-soaking issues, they are especially pronounced in oxygen-containing atmospheres, where the FF is decreasing within several minutes without UV illumination due to oxygen diffusing through the active layer to the ZnO interface and adsorbing there.^[4] On the contrary, the light-soaking issues are strongly reduced in an oxygen-free environment (e.g., a glove box) and it can be reasonably assumed that in such an atmosphere one short initial UV exposure is enough to resolve the light-soaking issues long-term.

This assumption is particularly important when it comes to stability measurements of ZnO-containing solar cells. Thermal stability or photostability of OSCs is often investigated in an oxygen-free atmosphere using a light source without UV part to determine the performance of

4 The Neglected Influence of Zinc Oxide Light-Soaking on Stability Measurements of Inverted Organic Solar Cells

the cells over time.^[12–16] This is either done to distinguish UV-induced aging from other aging factors or it is for pragmatic or financial reasons, since it is by far easier and cheaper to do long-term aging with a white light LED, which has a stable intensity and only needs little cooling, in contrast to expensive xenon-lamp solar simulators.

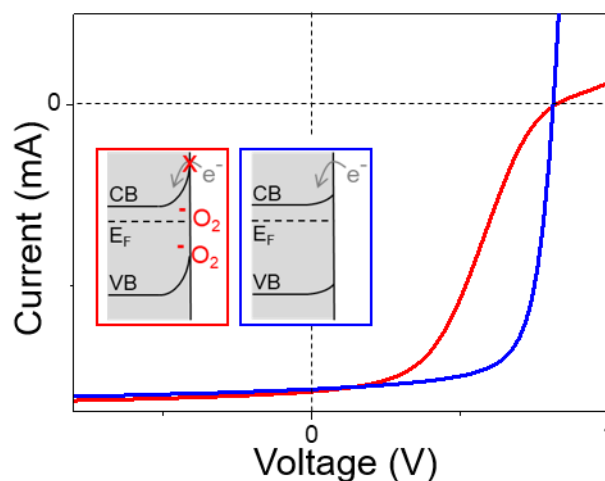


Figure 4.1: Schematic current-voltage curves for a ZnO-containing organic solar cell before (red) and after (blue) UV light-soaking. The insets show the valence band (VB), conduction band (CB) and Fermi-level (E_F) of the zinc oxide with adsorbed oxygen and upward band-bending (red), which hinders the electron injection from the active layer, and after the desorption of oxygen (blue) with decreased band-bending.

In this work, we show that the influence of ZnO light-soaking cannot be neglected even in an oxygen-free atmosphere and that, therefore, investigations on thermal or photostability can be misleading under such conditions. We demonstrate for several different active materials that stability measurements of ZnO-containing solar cells which are performed with a light source without UV-component in an oxygen-free atmosphere show a reversible degradation that can be recovered completely by a short UV treatment. This reversible degradation is amplified at elevated temperatures, which makes it prone to be mistaken for thermal degradation of the solar cell. Using XPS measurements, we show that the reversible degradation is caused by oxygen, which is unavoidably trapped at the interface between ZnO and the active layer, and which re-adsorbs on the ZnO thermally activated, resulting in a hindered electron extraction and a decreased fill factor.

4.3 Results and Discussion

In order to study the influence of ZnO light-soaking issues on thermal stability measurements, inverted organic solar cells with an architecture ITO|ZnO (30-40 nm)|active layer (80-100 nm)|MoO_x (10 nm)|Ag (100 nm) were built, containing the active layer materials PBDB-TF and IT-4F at a 1:1 weight ratio. The molecular structures and a scheme of the cell architecture can be found in **Figure S 4.1**. The commercially available ZnO nanoparticle dispersion (2.5 wt% in 2-propanol) was spin coated on ITO substrates, annealed at 120 °C for 10 min in air and subsequently transferred into a nitrogen containing glove box in which the spin coating of the active layer and the evaporation of MoO_x and Ag was carried out. The finished cells were then subjected to the measurement routine schematically depicted in **Figure 4.2**. All steps of this routine were performed in a nitrogen containing glove box, with the cells having no further contact with.

First, current density-voltage (J - V) curves were measured for the freshly prepared cells with a white light LED (step 1 in **Figure 4.2a**) at room temperature (= 19 °C). The used LED has a cut-off wavelength of 430 nm, thus containing no UV part, and was calibrated with a silicon photodiode to match the photocurrent under AM 1.5 (see **Figure S 4.2** for emission spectrum and experimental part for calibration details). The cells then were illuminated with a UV LED for 5 seconds to overcome the light-soaking issues and a second J - V curve was measured with the white light LED (step 2 in **Figure 4.2a**). The UV LED with a wavelength of 365 nm was calibrated with a silicon photodiode to match the UV part of AM 1.5G (= 4.6 mW/m²). The spectrum of the UV LED is also shown in **Figure S 4.2**. After those two initial J - V measurements, the cells were subjected to a thermal aging on a hotplate for 30 hours at 85 °C, being kept in the dark except for J - V measurements performed at regular intervals with the white light LED (step 3 in **Figure 4.2a**), which is in accordance with the typical procedure in the literature for thermal aging.^[17,18] To examine whether the absence of a UV component had an influence on the measurement results during the 30 h of thermal aging, the cells were then again illuminated with the UV LED for 5 seconds and a final J - V measurement was taken with the white light LED (step 4 in **Figure 4.2a**).

For better comparability, the performance data of all cells measured with this procedure and presented below are normalized to the respective cell's performance after the initial 5 s UV-soaking (step 2). All presented data points are averaged over six independently measured cells. The freshly prepared PBDB-TF:IT-4F cells in general showed the expected strong s-shape in step 1 due to the missing UV soaking, with a low fill factor of 46.0 ± 1.0 %, a low power conversion efficiency of 6.8 ± 0.4 %, an open-circuit voltage (V_{OC}) of 0.80 ± 0.05 V, and a

4 The Neglected Influence of Zinc Oxide Light-Soaking on Stability Measurements of Inverted Organic Solar Cells

short-circuit current density (J_{SC}) of $18.8 \pm 0.7 \text{ mA cm}^{-2}$ (average over all measured cells). After the initial 5 s UV-soaking in step 2, the performance improved to an average PCE of $11.8 \pm 0.3 \%$, a FF of $73.5 \pm 0.2 \%$, a V_{OC} of $0.84 \pm 0.01 \text{ V}$, and a J_{SC} of $18.7 \pm 0.4 \text{ mA cm}^{-2}$. These values are a bit lower than the 12-13 % PCE which are usually reported in the literature for inverted PBDB-TF:IT-4F cells,^[8,19] however, since the aim of this project was a deeper understanding of the stability behavior, the cells were not further optimized.

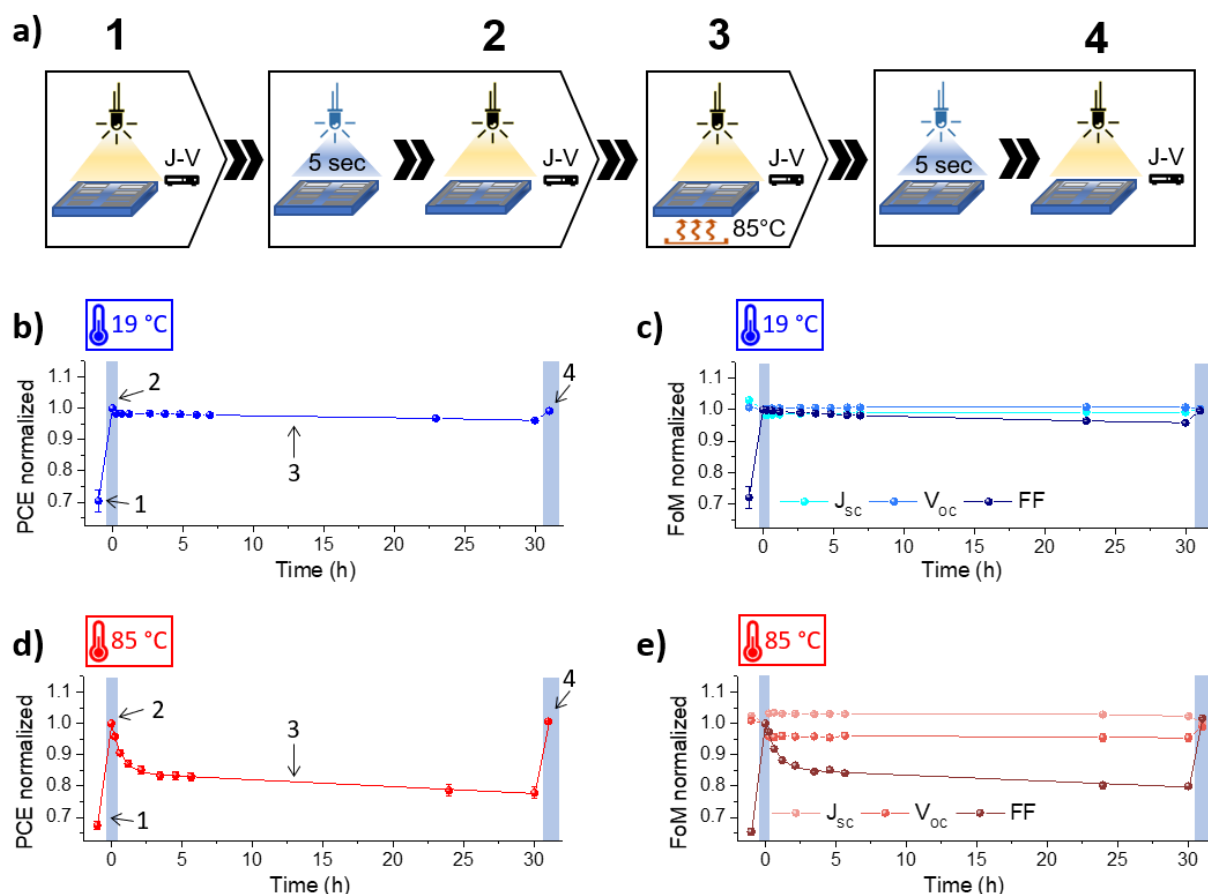


Figure 4.2: a) Scheme depicting the measurement procedure used. The whole procedure is performed in an oxygen-free environment and at 19°C if not otherwise stated. As a first step, a J - V curve is measured of the pristine cells with a white light LED, followed by a 5 s UV illumination (365 nm) and another J - V measurement with the white light LED (step 2). Then the cells are thermally aged for 30 hours at 85°C and measured at regular time intervals with the white light LED (step 3). As a last step, the cells are again illuminated with UV light for 5 s and measured. b, c) Normalized performance as a function of time for the different figures of merit (FoM) of PBDB-TF:IT-4F solar cells, which were measured according to the described procedure but as a were kept at 19°C in step 3 as a reference. The blue markings indicate the time of the UV treatments. d, e) Normalized performance as a function of time for PBDB-TF:IT-4F cells measured at 85°C according to the described procedure.

The results of the J - V measurements performed with the described routine for reference cells kept at room temperature (19°C) are shown in **Figure 4.2b, c**. After the initial UV soaking, the cells show a relatively constant PCE over time, however, after 30 hours, a small relative loss of

4 The Neglected Influence of Zinc Oxide Light-Soaking on Stability Measurements of Inverted Organic Solar Cells

about 4 % in PCE is apparent, which can be attributed to a decreasing FF, while J_{SC} and V_{OC} are stable over time. Notably, this small loss is fully recovered after the final 5 s of UV illumination, showing that it is not a real thermal aging effect. Thus, already the behavior at room temperature is an indication that the absence of UV illumination can produce erroneous stability results. Nevertheless, the influence is relatively small and can probably be justifiably neglected on the chosen timescale, especially if other aging influences are responsible for much larger losses.

However, the behavior over time changes drastically when the cells are thermally aged at a temperature of 85 °C (**Figure 4.2d, e**), which is the commonly used condition for thermal stability tests.^[17] After the initial UV soaking, the cells' performance shows a strong exponential decay, with a relative PCE loss of 15 % already after two hours. After approximately 20 hours, more than 20 % of the initial efficiency is lost, exceeding the cell's life time according to the T_{80} definition.^[18] The PCE loss is mainly attributed to the decreasing FF, while the J_{SC} and V_{OC} are constant over time with a small initial increase and decrease, respectively, which is due to the J - V measurement being performed at elevated cell temperature. Strikingly, here again the final UV soaking step recovers all of the losses and restores the initial cell performance, clearly proving that the cells did not thermally degrade during the measurement time. Instead, the usage of a white light source without a UV part for characterizing cells at elevated temperature resulted in a PCE loss, that could be wrongly attributed to thermal degradation, but is fully recoverable by UV illumination.

Hence, the main question is why the lack of a UV illumination component, especially at elevated temperatures, leads to a decrease in cell performance. Two causes would seem plausible: The behavior could originate from the active layer, for example, when thermal degradation is cured by UV illumination, although this would be rather unusual for organic solar cells. Or the behavior could be caused by the interfacial layers, in which case ZnO light-soaking issues would be an apparent possibility.

To investigate whether the active layer is responsible for this behavior, cells with two alternative active layers – one being PTB7-Th:PC₇₁BM and one being PBDB-TF:Y6 (systematic molecule names can be found in the experimental part; the structures are shown in **Figure S 4.3**) - were prepared with the otherwise same cell architecture and subjected to the same measurement procedure at 85 °C. The behavior of the FF over time for the different active layers is shown in **Figure 4.3**. Again, all values are normalized to the performance after the initial UV-soaking and averaged over six independently measured cells. The corresponding graphs for PCE, V_{OC} and J_{SC} can be found in **Figure S 4.4**. For all three different active layers,

4 The Neglected Influence of Zinc Oxide Light-Soaking on Stability Measurements of Inverted Organic Solar Cells

a clear degradation of the FF after the initial UV-soaking occurs, with a comparable, exponential decay in the first few hours. For PBDB-TF:IT-4F and PBDB-TF:Y6, the initial performance can be fully restored with the UV-soaking step after 30 hours. For PTB7-Th:PC₇₁BM, the performance is only partly restored. This can probably be explained by a real thermal aging of the active layer, as PBT7-Th:PC₇₁BM blends are known to phase-separate at elevated temperatures, resulting in a decreased FF and PCE.^[20]

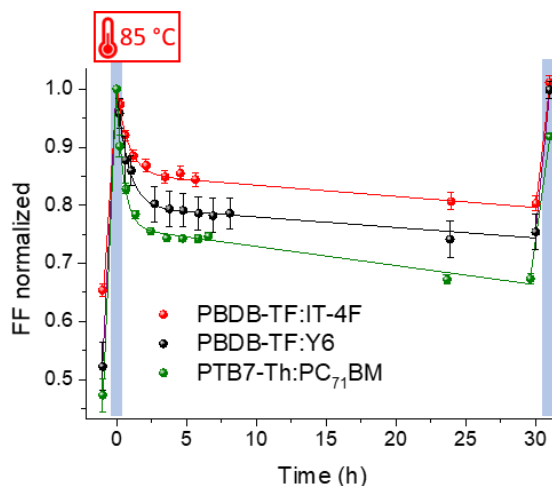


Figure 4.3: Normalized fill factor as a function of time for the three different active layers PBDB-TF:IT-4F (red), PBDB-TF:Y6 (black) and PTB7-Th:PC₇₁BM (green). The measurements were run according to the procedure described in FIG 2a, with the first data point being the pristine cells, the second data point (blue marking) being the UV-soaked cells, followed by a thermal aging at 85 °C, and the last data point representing the cells that were again soaked with UV-light (blue marking).

Since the used alternative active layers show a comparable behavior to the initial PBDB-TF:IT-4F system, although they exhibit both molecularly and morphologically major differences, it seems to be very unlikely that those materials are responsible for the observed behavior. Instead, it is much more likely that this reversible thermal degradation originates from the interface layers. And indeed, a very similar behavior originating from ZnO light-soaking is well-known in the literature:^[4,5] When ZnO-containing cells with a protective UV-filter are measured in air, their performance degrades within several minutes, with the $J-V$ curve developing a strong s-shape with reduced FF and increased serial resistance. When the UV-filter is removed, the performance can be fully recovered. This behavior is attributed to oxygen diffusing into the cell and adsorbing on the ZnO interface with the active layer, resulting in band bending and hindered electron extraction. Illuminating the cell with UV-light results in immediate desorption of oxygen and thus in a recovered performance.

In contrast to those literature reports, however, the measurements in this work were carried out under exclusion of oxygen and at elevated temperature. The question is therefore whether the

4 The Neglected Influence of Zinc Oxide Light-Soaking on Stability Measurements of Inverted Organic Solar Cells

observed behavior nevertheless can be explained by the adsorption of oxygen and where this oxygen comes from in an oxygen-free atmosphere.

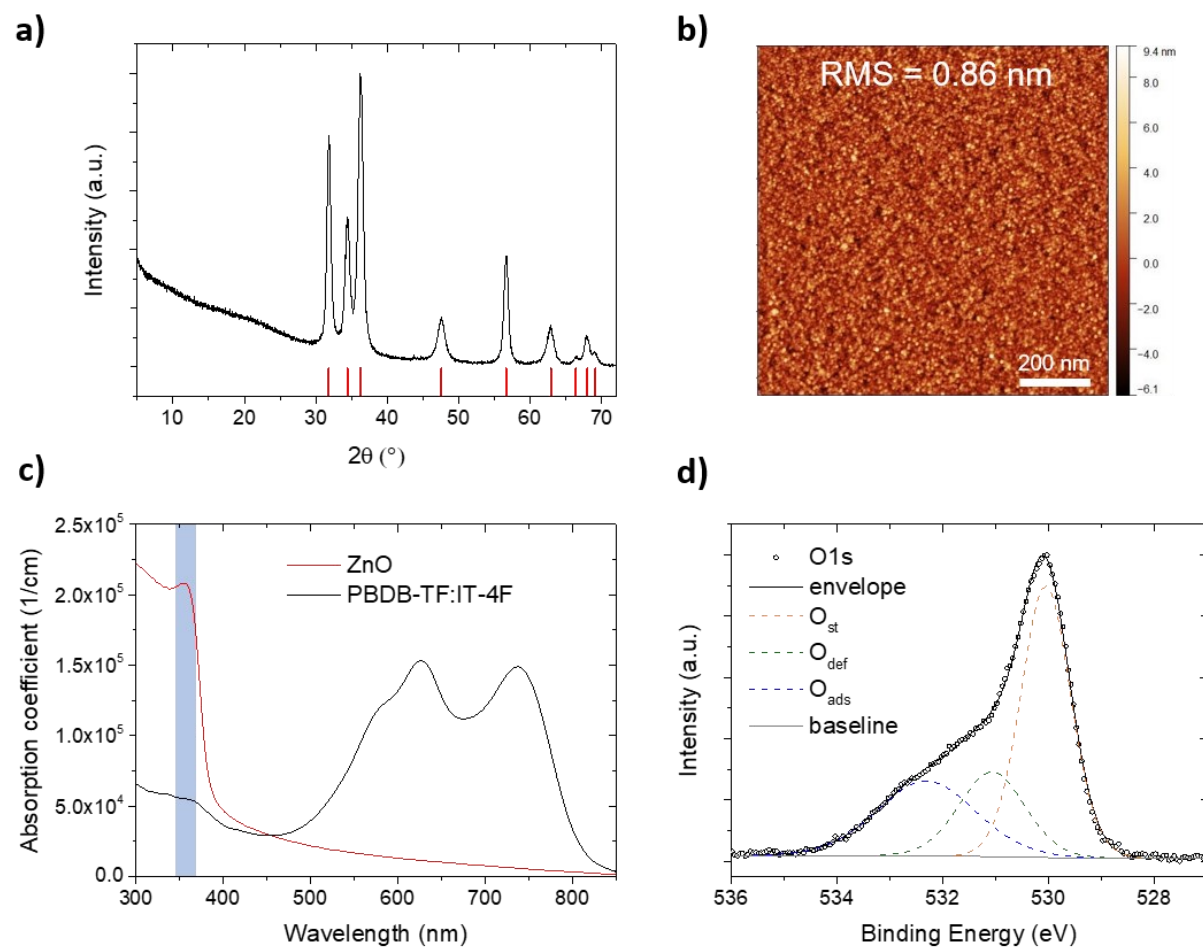


Figure 4.4: a) Powder X-ray diffractogram of the used ZnO (black line) with red bars indicating the diffraction lines of ZnO hexagonal wurtzite structure. b) Atomic force microscopy image of the ZnO layer surface, showing densely packed ZnO nanoparticles with a root mean square (RMS) roughness of 0.86 nm. c) UV-vis absorption spectra of a ZnO film (red line) and a PBDB-TF:IT-4F film (black line) on a quartz substrate, respectively, with the blue bar indicating the emission range of the used UV-LED. d) O 1s XPS spectrum of the ZnO layer, fitted with three components for stoichiometric oxygen (O_{st}) of bulk ZnO, oxygen in oxygen deficient regions (O_{def}), and adsorbed oxygen species (O_{ads}). The black line represents the envelope of the fitted components.

To answer this question, the used ZnO layer was examined in more detail. The layer consists of commercially available ZnO nanoparticles, which are highly crystalline with the typical Wurtzite crystal structure, as confirmed with the powder X-ray diffraction (XRD) pattern shown in **Figure 4.4a**. From the reflection line broadening an approximate particle size of 12 nm is calculated with the Scherrer equation. As apparent from the atomic force microscopy (AFM) image in **Figure 4.4b**, the spin coated and annealed ZnO films consist of closely packed nanoparticles with very good coverage, exhibiting a smooth surface with a low roughness of 0.86 nm root mean square. From the UV-vis spectra of the ZnO film and the active layer PBDB-

4 The Neglected Influence of Zinc Oxide Light-Soaking on Stability Measurements of Inverted Organic Solar Cells

TF:IT-4F shown in **Figure 4.4c** it is evident that the spectral range of the UV LED is mainly absorbed by the ZnO, while the active layer primarily absorbs in the visible range.

In order to obtain more information about the chemical speciation of possibly adsorbed oxygen on the surface, the ZnO layer was investigated with X-ray photoelectron spectroscopy (XPS). As expected, mainly the elements zinc and oxygen are visible in the survey spectrum, which is shown in **Figure S 4.5**. In addition, however, carbon is detectable, which indicates organic impurities, for example residues of spin coating the ZnO nanoparticles from 2-propanol or adventitious carbon species adsorbed from handling the samples in ambient conditions. In **Figure 4.4d** the high-resolution scan of the O 1s region is shown. According to literature, the spectrum was fitted with three components corresponding to stoichiometric O^{2-} ions in the wurtzite structure (O_{st} , 530.0 eV), O^{2-} ions in oxygen deficient regions of the wurtzite structure (O_{def} , 531.0 eV), and adsorbed oxygen species (O_{ads} , 532.2 eV).^[21–23] This may be atmospheric oxygen which is physisorbed or chemisorbed as oxygen atoms or molecules, depending on temperature and atmospheric composition.^[6,24] The details are a controversial topic in literature, but below 150°C and in an ambient atmosphere chemisorbed O_2^- seems to be the dominating species.^[24] Additional adsorbed oxygen species coming from sources other than atmospheric oxygen may also be involved, such as CO_x , -OH or H_2O . However, due to the close-lying O 1s binding energies of the different possible adsorbates in the 532–533 eV region it is not possible to unambiguously identify the molecular nature of the O-containing adsorbate. Notably, the adsorbed species is stably present and neither affected or desorbed by sample storage in a N_2 glove box nor by handling in ultra-high vacuum conditions during XPS analysis.^[21]

Based on the results presented so far, we hypothesize the following: The freshly prepared solar cells contain an adsorbed layer of oxygen species on top of the zinc oxide layer, which is unavoidable due to the necessary manufacturing of the ZnO layer in air, even if all other steps are performed in an oxygen-free atmosphere. The oxygen-containing adsorbates then are enclosed by the active layer spin coated on top and cause an upward band bending in the ZnO. The initial UV-treatment or the first illumination of the pristine cells with a UV containing AM 1.5G spectrum results in a desorption of those oxygen species and thus in a good cell performance. However, due to the active layer being on top of the ZnO, the desorbed oxygen species are confined at the interface and therefore are able to re-adsorb. The adsorption of oxygen onto ZnO is known to be an endothermic process, where the activation energy strongly depends on the exact ZnO layer properties and environmental conditions.^[25,26] Therefore, the elevated temperature of 85 °C accelerates the re-adsorption and thus also speeds up the

4 The Neglected Influence of Zinc Oxide Light-Soaking on Stability Measurements of Inverted Organic Solar Cells

performance loss, while at room temperature the re-adsorption and the resulting degradation are very slow.

To verify this hypothesis, thermal stability was measured at several temperatures for eight hours with the procedure described in Figure 2a. In case the hypothesis is correct, the thermal degradation should show a strong, consistent temperature dependence and it should be possible to determine an apparent activation energy from the temperature-dependent decay time constants. And indeed, as shown in **Figure 4.5a**, the fill factor follows an exponential decay over time for all tested temperatures, with the slope of this decay increasing with temperature. For all degradation temperatures, after eight hours, the FF could be fully restored by a 5 s UV illumination (measurement points at 8 h, blue marking in Figure 5a). Interestingly, the cells measured at 85 °C even show a small improvement of performance after the re-soaking compared to the freshly UV-soaked cells, which probably can be attributed to a beneficial annealing effect on the active layer morphology. To obtain the decay time constant τ , the measurement data of the fill factor over time $FF(t)$ for each temperature was fitted with an exponential decay with offset y_0 and scaling factor A according to equation (4.1):

$$FF(t) = y_0 + A \cdot \exp\left(-\frac{t}{\tau}\right) \quad (4.1)$$

The use of $FF(t)$ for this fit can be justified by the fact that the FF is the parameter that should be most sensitive to possible band bending at the ZnO interface and therefore should have a direct linear correlation to the amount of adsorbed oxygen species. The corresponding data for V_{oc} , J_{sc} , and PCE over time and the details for all fits can be found in **Figure S 4.6** and **Table S 4.1**. The obtained time constants then were plotted semi-logarithmically in an Arrhenius-type diagram vs. the inverse temperature, as shown in **Figure 4.5b**. The linear trend of the data points is clearly evident, indicating that the temperature-dependent behavior is indeed controlled by one process with a uniform activation energy. More importantly, from the slope of the linear fit, an apparent activation energy can be determined with a value of $E_A \approx 0.36$ eV. There are no literature values for the activation energy of oxygen adsorption on ZnO within a solar cell, however, there are values for this process on pure ZnO nanowires. Madel et al.^[25] investigated the persistent photoconductivity of ZnO nanowires and found an activation energy of 0.16 eV for oxygen adsorption in a pure oxygen atmosphere. For a lower atmospheric oxygen content, the activation energy was found to increase, with a value of 0.33 eV in an atmosphere with 1% oxygen in argon. In comparison, for the case investigated here, an activation energy of 0.36 eV seems to match this trend, considering that there is no atmospheric oxygen but only the oxygen trapped at the interface.

4 The Neglected Influence of Zinc Oxide Light-Soaking on Stability Measurements of Inverted Organic Solar Cells

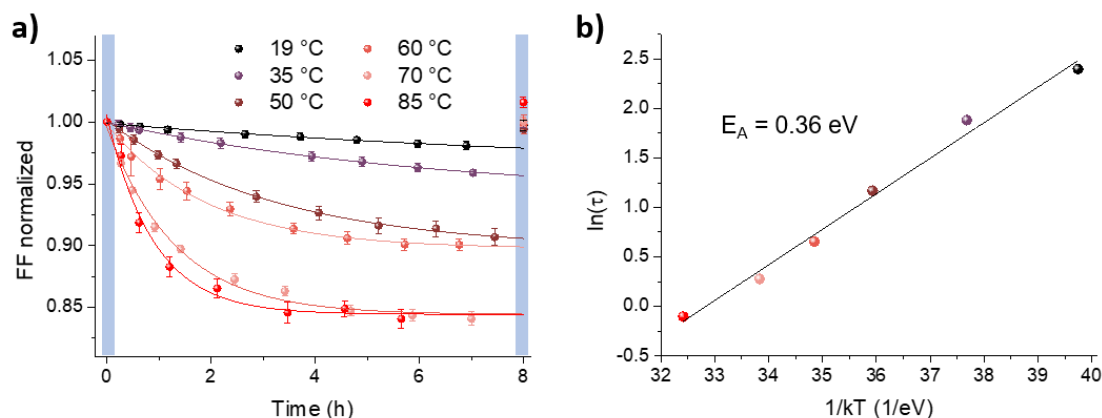


Figure 4.5: a) Development of the normalized fill factor as a function of time for PBDB-TF:IT-4F devices heated at different temperatures between 19 °C and 85 °C, with the data points being the average of five separately aged solar cells. All values are normalized to the initial performance after 5 s of UV illumination (time = 0, blue marking) and after 8 hours of thermal degradation the devices were exposed to a second UV illumination of 5 s (blue marking). The exponential fits of the respective data points according to equation 1 are shown as solid lines. b) Semi-logarithmic Arrhenius-type diagram of the time constants obtained from the exponential fits over the inverse temperature T multiplied with the Boltzmann constant k . The linear fit of the data is indicated with a solid black line, with the fit's slope corresponding to the activation energy $E_A = 0.36$ eV.

Provided that the presented hypothesis is correct, the problem of the thermal degradation should be solvable by removing the oxygen species adsorbed on the ZnO by UV illumination before the additional solar cell layers are deposited.

To this end, we transferred freshly prepared ZnO layers into a nitrogen-filled glove box and exposed them to UV illumination for different time periods before depositing the other layers and avoiding any further contact with oxygen, analogous to the approach described by Liu et al.^[27] which they used to reduce photocatalytic decomposition of active layer materials by oxygen adsorbed on ZnO. The cells pretreated in this way then were exposed to the same procedure as described in Figure 2 and heated at 85 °C for 30 hours. The resulting normalized PCE and FF over time for no pretreatment and pretreatments of 2 min, 10 min and 1h are shown in **Figure 4.6a** and **b**, the corresponding trends for J_{SC} and V_{OC} can be found in **Figure S 4.7**.

It is clearly visible that the FF loss is greatly reduced even for a ZnO pretreatment of two minutes compared to the untreated devices. A pretreatment of 10 min almost completely eliminates the degradation within this time frame, with a total loss in PCE of around 2 % after 30 hours. An even longer pretreatment time of up to one hour did not show any further improvement, which is why 10 min of UV treatment is assumed to be the optimum at the used UV light intensity.

4 The Neglected Influence of Zinc Oxide Light-Soaking on Stability Measurements of Inverted Organic Solar Cells

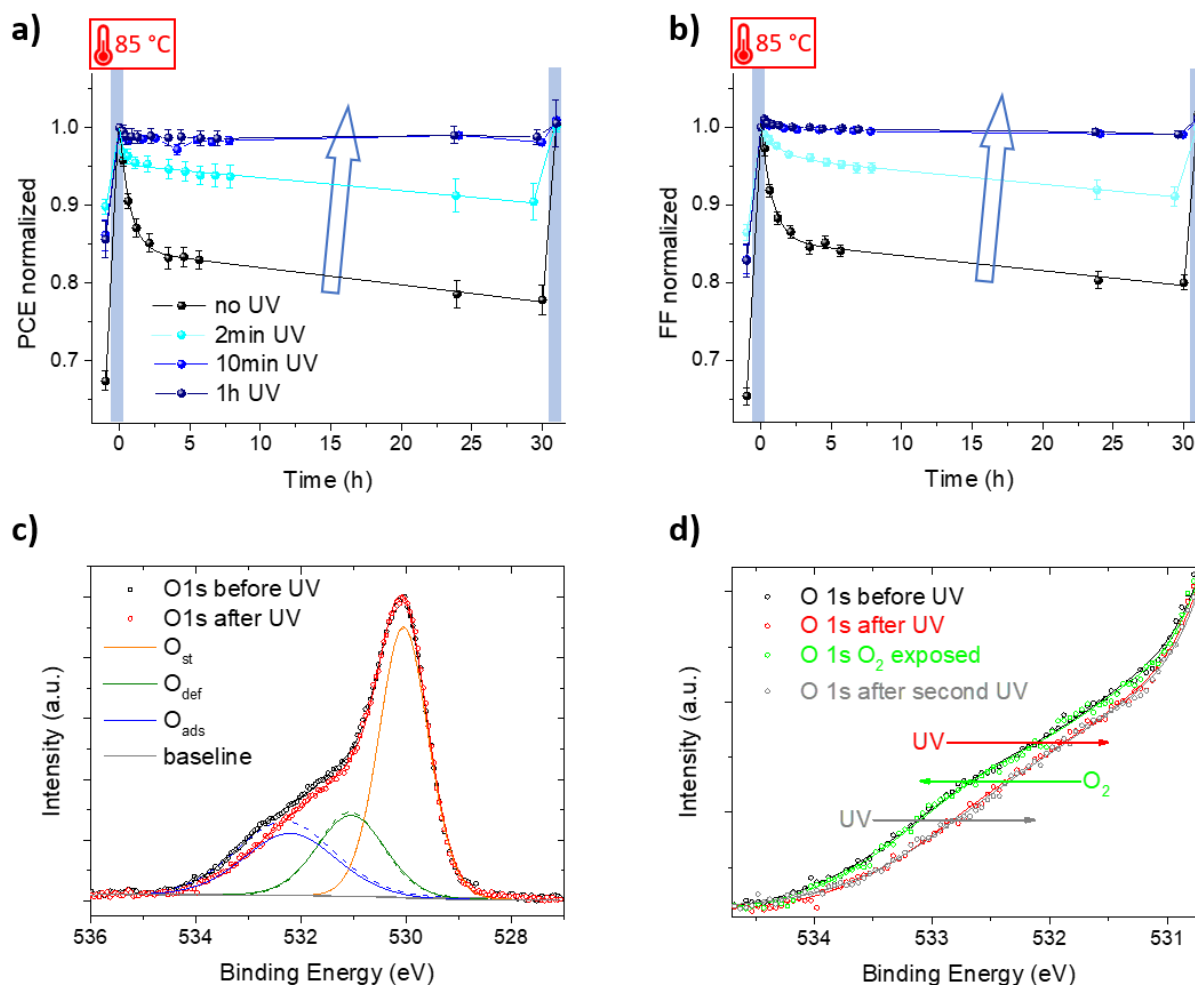


Figure 4.6: a) Normalized PCE and b) FF as a function of time for PBDB-TF:IT-4F solar cells, for which the ZnO was illuminated with UV light for different times as a pretreatment. The measurements were run according to the procedure described in FIG 2a, with the first data point being the pristine cells, the second data point being the UV-soaked cells (blue marking), followed by a thermal aging at 85 °C, and the last data point showing the cells that were again soaked with UV-light (blue marking). c) O 1s XPS spectra for a ZnO layer before (black) and after (red) UV illumination inside of the XPS chamber. The spectra were fitted with three components for the stoichiometric oxygen (O_{st}), the oxygen in oxygen deficient regions (O_{def}), and adsorbed oxygen species (O_{ads}), dashed lines and solid lines representing the fits for the spectrum before and after illumination, respectively. d) Enlarged high binding energy region of O 1s spectra for the ZnO layer before (black) and after (red) UV illumination and after oxygen exposure (green) and a second UV illumination (gray).

To understand how exactly the UV pretreatment affects the ZnO surface, a ZnO layer was illuminated with UV inside the XPS chamber and the O 1s spectrum was recorded before and after the illumination (technical details can be found in the experimental section). The corresponding min-max normalized O 1s spectra are shown in **Figure 4.6c**. As described above, both spectra were fitted with three components for stoichiometric oxygen (O_{st}), oxygen in oxygen deficient regions (O_{def}) and adsorbed oxygen species (O_{ads}). As to be expected, the O 1s spectrum shows no difference due to the UV treatment in the region of the stoichiometric oxygen

4 The Neglected Influence of Zinc Oxide Light-Soaking on Stability Measurements of Inverted Organic Solar Cells

signal. However, the illumination reduces the signal intensity in the region between 531-534 eV, which can be mainly assigned to a reduction of the adsorbed oxygen species, supporting the concept of a UV-induced desorption. To get an idea of which oxygen species are involved in the desorption and re-adsorption process, following the first UV illumination of the ZnO layer, the sample was exposed to an O₂ partial pressure of 0.1 mbar in the same vacuum system and a third O 1s spectrum was recorded. Afterwards, the ZnO layer was UV illuminated a second time and a final O 1s spectrum was obtained. A comparison of those four O 1s spectra in the relevant region between 531-534 eV is shown in **Figure 4.6d**.

It is clearly visible that the oxygen exposure again results in the same spectrum as for the ZnO layer before illumination, while the second illumination reproduces almost the same spectrum after the first illumination. We take this as a proof that the observed behavior of the corresponding solar cells is governed by the reversible desorption and re-adsorption of molecular oxygen, while the other adsorbed oxygen species do not interfere with the cell's performance. However, we note that when fitting the O1s spectra, the weighting between O_{ads} and O_{def} is not unambiguous. Another interpretation is also possible, where the observed changes could be partly attributed to a change of oxygen speciation in the oxygen deficient region. Nevertheless, we consider the simple, reversible desorption and re-adsorption of oxygen to be the chemically more plausible process and therefore chose the presented fitting.

Table 4.1: Averaged performance parameters for pristine PBDB-TF:IT-4F cells for different ZnO pretreatment times (J - V measurement performed after 5 s of UV soaking to achieve maximum performance).

ZnO treatment	J_{SC} [mA/cm ²]	V_{oc} [V]	FF [%]	PCE [%]
none	18.7 ± 0.4	0.84 ± 0.01	73.5 ± 0.2	11.8 ± 0.3
2min	18.3 ± 0.6	0.83 ± 0.01	73.5 ± 0.4	11.1 ± 0.5
10min	18.1 ± 0.6	0.82 ± 0.01	73.0 ± 0.1	10.8 ± 0.4
1h	18.1 ± 0.6	0.81 ± 0.01	73.0 ± 0.3	10.7 ± 0.3

To summarize, the UV pretreatment of the ZnO layer eliminates the problematic reversible degradation behavior, but it is not a flawless solution, since the pretreatment itself decreases the device efficiency. The performance parameters of the pristine cells after the initial 5 s UV-soaking are listed in **Table 4.1** for different ZnO pretreatment times. All figures of merit decrease with the duration of the ZnO pretreatment, with a drop of PCE from 11.8 % (untreated) to 10.8 % for the optimum time of 10 minutes pretreatment. The cause of this loss it not clearly attributable, but it seems reasonable that by changing the surface chemistry of ZnO through UV pretreatment (e.g., the dipole moment of the interface), the behavior of the devices is also

4 The Neglected Influence of Zinc Oxide Light-Soaking on Stability Measurements of Inverted Organic Solar Cells

affected. However, a small and time-independent loss in PCE after a ZnO pretreatment (around 8 % of relative PCE loss for 10 min UV pretreatment) is certainly preferable to a progressive thermal degradation, which means a loss of more than 20 % after only 30 h.

4.4 Conclusions

In conclusion, we have studied the influence of ZnO light-soaking on stability measurements of inverted organic solar cells. It was found that the inverted devices in the absence of UV illumination show a reversible degradation of performance, mainly governed by a loss of FF, which can be recovered by a short UV illumination. Such a behavior is principally known for OSCs with ZnO as ETL and is usually explained by the fact that atmospheric oxygen diffuses through the cells and adsorbs on the ZnO surface, resulting in an upward band bending in the ZnO, which hinders electron extraction and thus decreases FF and PCE. UV illumination helps desorbing the oxygen and thus recovers the performance. In this work, however, we show that this kind of reversible degradation unexpectedly also occurs in an oxygen-free environment and is amplified by higher temperatures. We hypothesize that instead of oxygen diffusing in from the atmosphere, the cause of the reversible degradation here is oxygen that is already adsorbed on the ZnO surface due to its production process. Although this oxygen can be desorbed with an initial UV treatment, it is then trapped at the interface between ZnO and active layer and can re-adsorb when no continuous UV illumination is applied. As evidence, we show that the reversible degradation is independent of the used active layer materials and that its temperature dependence can be attributed to the activation energy of oxygen re-adsorption. Finally, we demonstrate, supported by XPS measurements, that removing the oxygen from the ZnO surface by a UV pretreatment before building the solar cell solves the reversible degradation problem, however, at the price of a small loss of device efficiency.

This work establishes that stability measurements of ZnO-containing OSCs should be performed exclusively with light sources featuring a UV part and closely reproduce the AM 1.5G spectrum, otherwise there is a high risk of confusing real aging effects with ZnO light-soaking effects. Furthermore, there are additional implications for using ZnO in commercial OSCs: since the oxygen is typically adsorbed on the ZnO due to the manufacturing process, its presence cannot be avoided even by encapsulating the assembled cells. However, the oxygen present reduces the performance of the solar cells under operation, especially in the morning hours when the UV component in natural sunlight is not yet sufficient for complete oxygen desorption. This could only be avoided by pretreating the ZnO layer with UV and performing the whole manufacturing process under complete exclusion of oxygen. It is likely that such

4 The Neglected Influence of Zinc Oxide Light-Soaking on Stability Measurements of Inverted Organic Solar Cells

increased manufacturing cost and complexity could lead to a re-assessment of the utility of ZnO to serve as ETL in commercial OSCs.

4.5 Experimental Section

Materials. ITO substrates with a sheet resistance of $15 \Omega \text{ cm}^2$ were purchased from Kintec. The ZnO nanoparticle dispersion (N-10) was obtained from Avantama AG. Poly[(2,6-(4,8-bis(5-(2-ethylhexyl)thiophen-2-yl)-benzo[1,2-b:4,5-b']dithiophene))-alt-(5,5-(1',3'-di-2-thienyl-5',7'-bis(2-ethylhexyl)benzo[1',2'-c:4',5'-c']dithiophene-4,8-dione))] (PBDB-TF), 3,9-bis(2-methylene-((3-(1,1-dicyanomethylene)-6,7-difluoro)-indanone))-5,5,11,11-tetrakis(4-hexylphenyl)-dithieno[2,3-d:2',3'-d']-s-indaceno[1,2-b:5,6-b']dithiophene (IT-4F) and 2,2'-((2Z,2'Z)-((12,13-bis(2-ethylhexyl)-3,9-diundecyl-12,13-dihydro-[1,2,5]thiadiazolo[3,4-e]thieno[2'',3''':4',5']thieno[2',3':4,5]pyrrolo[3,2-g]thieno[2',3':4,5]thieno[3,2-b]indole-2,10-diyl)bis(methanylylidene))bis(5,6-difluoro-3-oxo-2,3-dihydro-1H-indene-2,1-diylidene))dimalononitrile (Y6) were purchased from Solarmer. Poly[4,8-bis(5-(2-ethylhexyl)thiophen-2-yl)benzo[1,2-b:4,5-b']dithiophene-2,6-diyl-alt-(4-(2-ethylhexyl)-3-fluorothieno[3,4-b]thiophene-)-2-carboxylate-2-6-diyl)] (PTB7-Th) was obtained from 1-Material.

[6,6]-Phenyl-C₇₁-butyric acid methyl ester (PC₇₁BM, 99.5%) was purchased from Solaris Chem. Chlorobenzene (anhydrous, 99.8%), chloroform (anhydrous, >99%, amylene stabilized), 1,8-diiodooctane (DIO) and MoO₃ powder (99.97% trace metals basis) were purchased from Merck. 1-chloronaphthalene was obtained from TCI.

Device Fabrication. The ITO substrates were cleaned with detergent and ultrasonicated in water, acetone and 2-propanol for 10 min. They were dried with a nitrogen flow and plasma-cleaned for 10 min. Subsequently, the ZnO nanoparticle dispersion was spin coated with 1400 rpm for 45 s and annealed for 10 min at 120 °C in air. The substrates then were transferred into a nitrogen glovebox (oxygen level <0.1 ppm) and all following steps and measurements were performed without any further contact with oxygen, if not otherwise stated. For the active layer solutions, the components were separately dissolved in the respective solvent, followed by mixing and stirring overnight. The respective additive was added 30 min before spin coating. PBDB-TF:IT-4F solutions were prepared with a 10:10 mg/ml weight ratio in chlorobenzene with 0.5 vol% DIO and dynamically spin coated at 900rpm for 5 s and 4000 rpm for 60 s. For PTB7-Th:PC₇₁BM, a ratio of 8:12 mg/ml in chlorobenzene with 3 vol% DIO was used and the solution was dynamically spin coated with 1500 rpm for 45 s. PBDB-TF:Y6 solutions were

4 The Neglected Influence of Zinc Oxide Light-Soaking on Stability Measurements of Inverted Organic Solar Cells

prepared with 7.25:8.75 mg/ml in chloroform with 0.5 vol% 1-chloronaphthalene and dynamically spin coated with 3000 rpm for 30 s. Finally, 10 nm of MoO_x and 100 nm of Ag were evaporated through a mask.

Characterization Techniques. *J-V* measurements were carried out in a nitrogen-filled glove box using a Keithley 2401 source-measure unit and a white light LED (Bridgelux), which was calibrated to 100 mW cm⁻² with a silicon diode (Hamamatsu S1227-66BQ). The cells were illuminated through a shadow mask with 6.25 mm² open area. Wide angle X-ray diffraction measurements were performed in transmission with a STOE STADI P diffractometer (Cu K_{α1}, λ = 1.5406 Å) and a Ge(111) single crystal monochromator equipped with a DECTRIS solid state strip detector MYTHEN 1K. For the sample preparation, the ZnO dispersion was drop-cast on a heating plate at 120 °C (same conditions as for the annealing of the spin coated films) and the emerging powder was used. The ZnO crystal structure was assigned using the ICSD database.^[28] AFM measurements were done with a NANOINK atomic force microscope in tapping mode. UV-vis spectra of thin films on quartz substrates were recorded in transmission with a PerkinElmer LAMBDA 1050 instrument with integrating sphere. XPS measurements were performed in the cluster tool Darmstadt Integrated System for Solar Cell research (DAISY-SOL) using a Thermo Fisher Scientific Escalab 250 system equipped with a monochromatized Al K_α X-ray source (1486.6 eV) operated at 200 W power and 650 μm spot size. The XPS spectra were collected at a take-off angle of 90° with respect to the sample surface. All XPS region scans (O 1s, Zn 2p) were acquired with a pass energy of 10 eV, a step size of 0.05 eV and a dwell time of 50 ms per measurement point. Survey spectra were obtained with a pass energy of 50 eV, step size of 0.5 eV and a dwell time of 50 ms. All spectra were binding energy calibrated to the main C 1s peak with a value of 285.0 eV. Measurements were carried out in ultra-high vacuum (UHV ≤ 1x10⁻⁹ mbar). For re-adsorption experiments, the sample was exposed to an oxygen partial pressure of 0.1 mbar inside a separate vacuum chamber with a base pressure of 1x10⁻⁸ mbar as a part of the cluster tool vacuum system, i.e., all transfer operations were done under UHV conditions (<1x10⁻⁹ mbar). Peak fitting was performed using a sum of Gaussian (70%) and Lorentzian (30%) lines, while the secondary electron background was subtracted utilizing the Shirley function using CasaXPS software version 2.3.25.^[29]

Stability testing. All stability tests were done in a nitrogen-filled glovebox with oxygen and water levels <1 ppm. For thermal stability measurements, all devices were first put into a home built metal sample holder and subjected to a *J-V* measurement at room temperature (19 °C). Then the devices in the sample holder were transferred to a temperature-controlled heating plate

4 The Neglected Influence of Zinc Oxide Light-Soaking on Stability Measurements of Inverted Organic Solar Cells

and J - V measurements were performed in regular intervals with the devices maintaining the chosen temperature. The UV soaking before and after the thermal stability measurements was performed with a 365 nm UV LED (Thorlabs Solis-365C) which was calibrated with a Si-diode (Hamamatsu) to match the UV part of AM 1.5G (4.6 mW cm^{-2}).

4 The Neglected Influence of Zinc Oxide Light-Soaking on Stability Measurements of Inverted Organic Solar Cells

4.6 Supporting Information

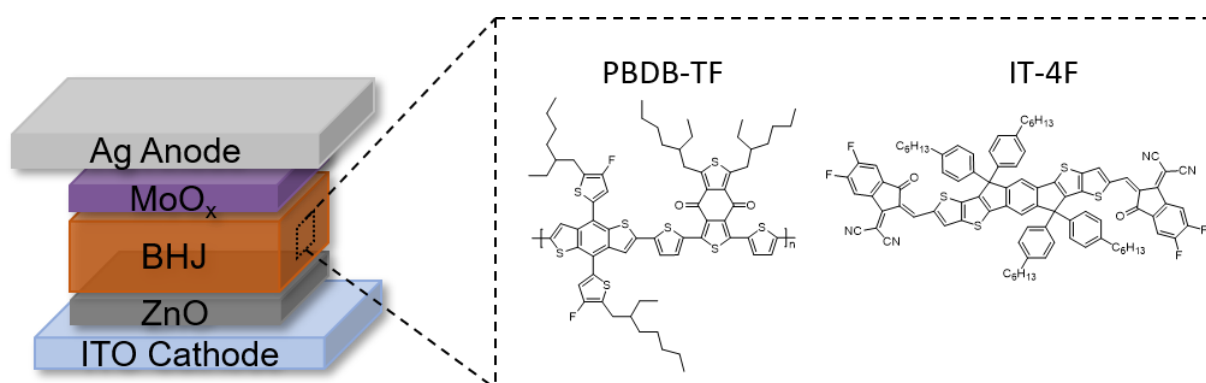


Figure S 4.1: Schematic architecture of the inverted organic solar cells and molecular structures of the used absorbing materials PBDB-TF and IT-4F.

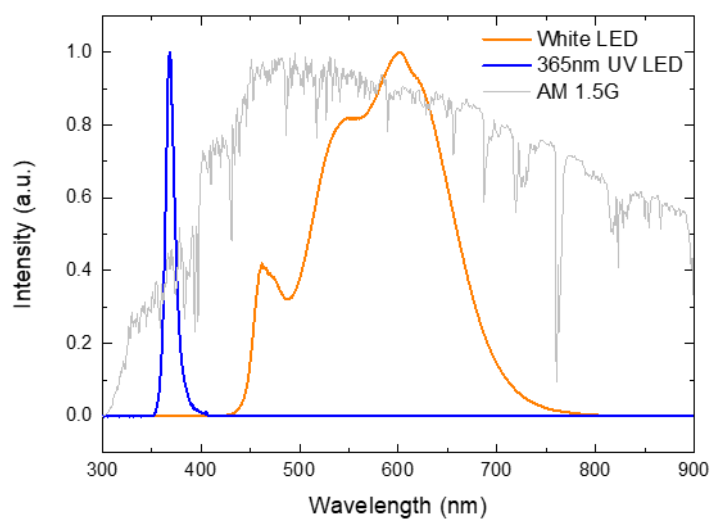


Figure S 4.2: Normalized spectra of the used white LED and UV LED compared to the normalized AM 1.5G spectrum.

4 The Neglected Influence of Zinc Oxide Light-Soaking on Stability Measurements of Inverted Organic Solar Cells

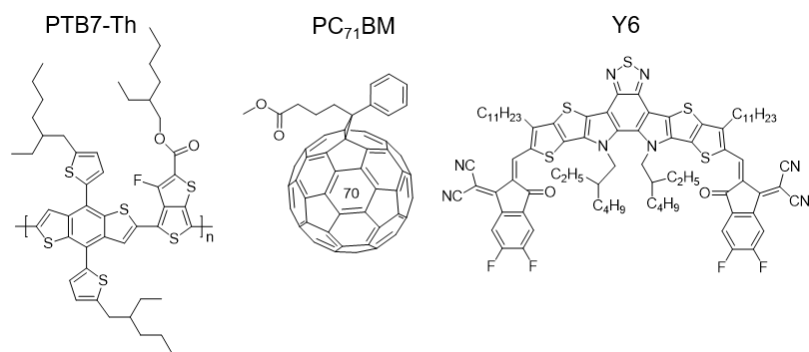


Figure S 4.3: Chemical structures of the molecules used for the alternative blends PBDB-TF:Y6 and PTB7-Th:PC₇₁BM.

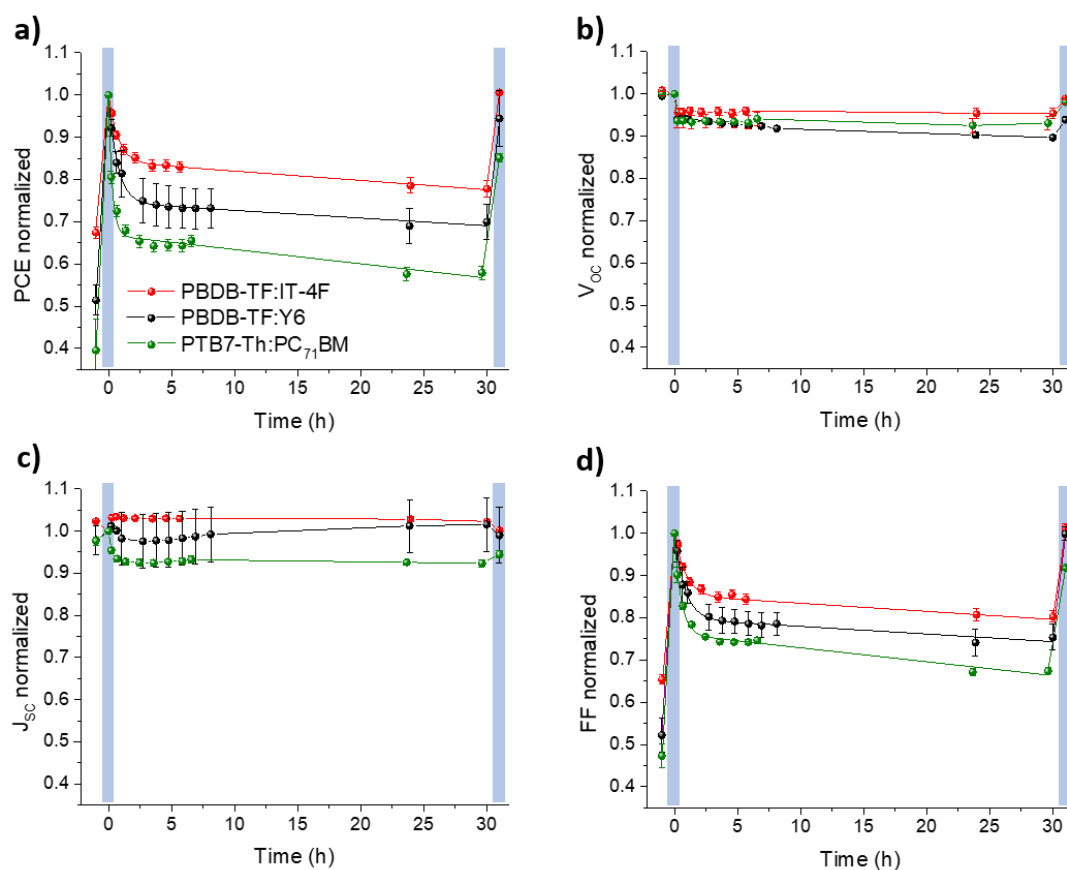


Figure S 4.4: Normalized **a)** PCE, **b)** V_{OC} , **c)** J_{SC} , and **d)** FF as a function of time for the three different active layers PBDB-TF:IT-4F (red), PBDB-TF:Y6 (black), and PTB7-Th:PC₇₁BM (green). The measurements were run according to the procedure described in FIG 2a of the main text, with the first data point being the pristine cells, the second data point (blue marking) being the UV-soaked cells, followed by a thermal aging at 85 °C, and the last data point representing the cells that were UV-soaked again (blue marking). All data points are averaged over 6 independently measured cells.

4 The Neglected Influence of Zinc Oxide Light-Soaking on Stability Measurements of Inverted Organic Solar Cells

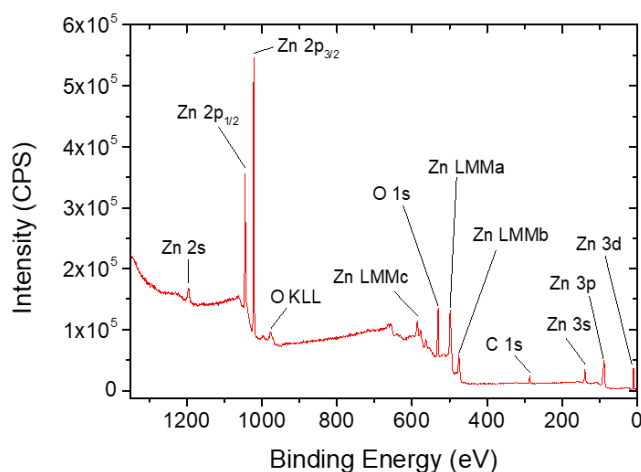


Figure S 4.5: XPS survey scan of the ZnO layer, showing emissions from the elements Zn, O, and C.

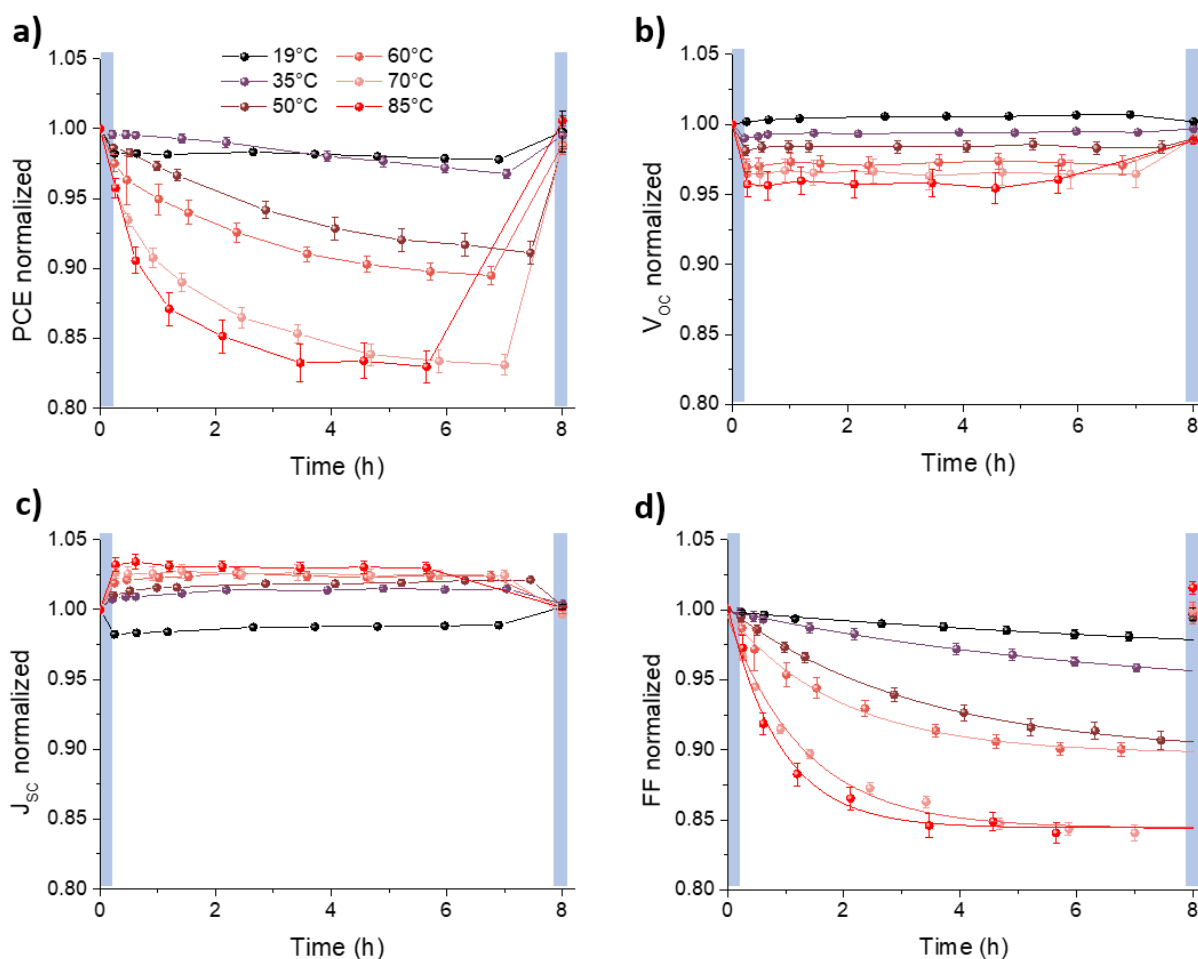


Figure S 4.6: Development of the normalized **a)** PCE, **b)** V_{oc} , **c)** J_{sc} , and **d)** FF as a function of time for PBDB-TF:IT-4F devices heated at different temperatures between 19 °C and 85 °C, with the data points being the average of five separately aged solar cells. All values are normalized to the initial performance after 5s of UV illumination (time = 0, blue marking) and after 8 hours of thermal degradation the devices were exposed to a second UV illumination of 5 s (blue marking).

4 The Neglected Influence of Zinc Oxide Light-Soaking on Stability Measurements of Inverted Organic Solar Cells

Table S 4.1: Fitting parameters for the exponential fit of the fill factor decay over time for different temperatures and adjusted R-square for each fit.

Temperature (°C)	τ (s ⁻¹)	A	y ₀	Adjusted R-square
85	0.9007	0.1595	0.8443	0.988
70	1.3202	0.1513	0.8442	0.992
60	1.9213	0.1005	0.8973	0.995
50	3.2166	0.1039	0.89771	0.999
35	6.5698	0.0611	0.9385	0.999
19	11.0092	0.0388	0.96	0.990

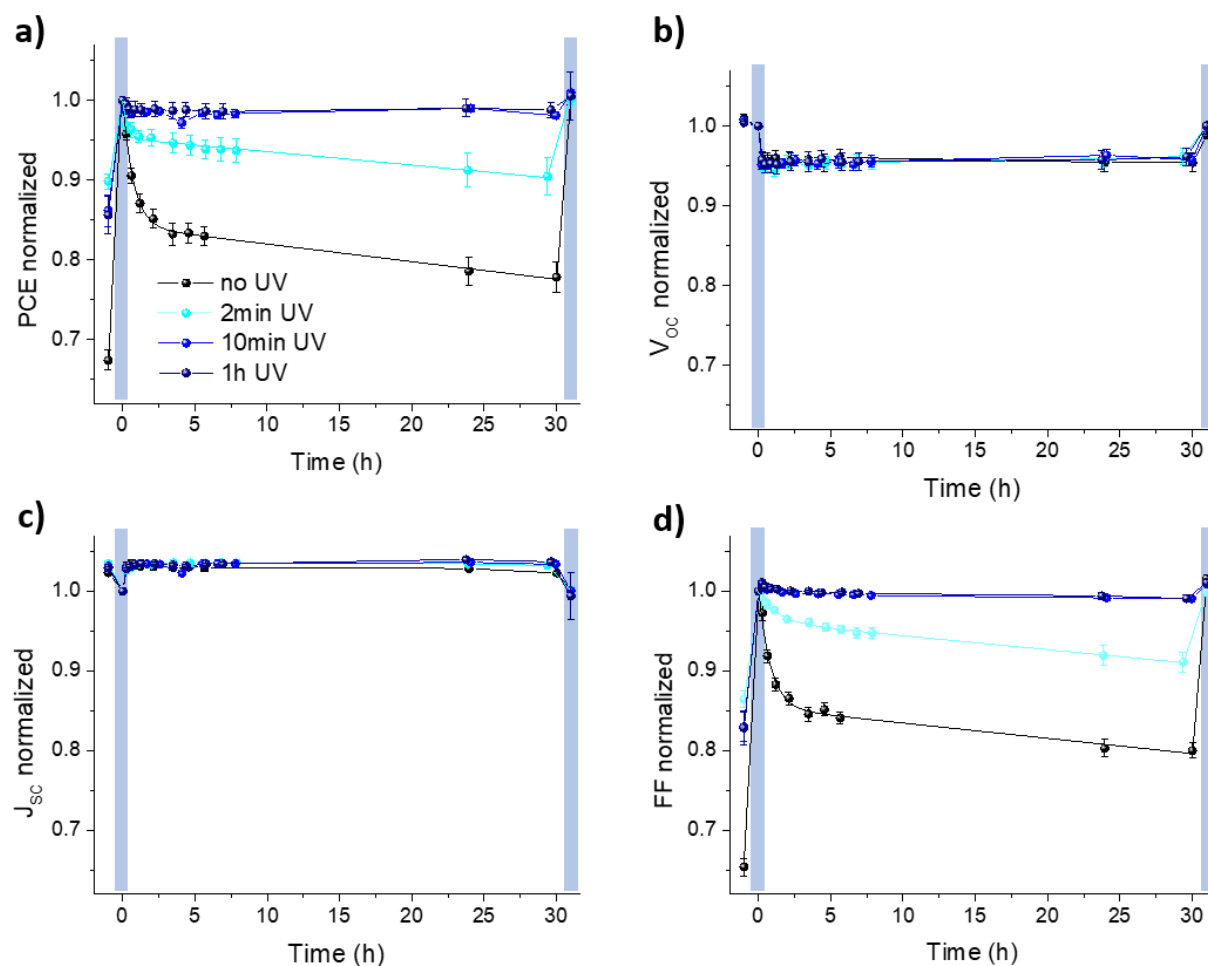


Figure S 4.7: Normalized **a)** PCE, **b)** V_{OC} , **c)** J_{SC} , and **d)** FF as a function of time for PBDB-TF:IT-4F cells, for which the ZnO was illuminated with UV light for different times as a pretreatment. The measurements were run according to the procedure described in FIG 2a in the main text, with the first data point being the pristine cells, the second data point being the UV-soaked cells (blue marking), followed by a thermal aging at 85 °C, and the last data point representing the cells that were UV-soaked again (blue marking).

4.7 References

- [1] R. M. Hewlett, M. A. McLachlan, *Adv. Mater.* **2016**, *28*, 3893.
- [2] C. Liu, C. Xiao, W. Li, *J. Mater. Chem. C* **2021**, *9*, 14093.
- [3] J. Kim, G. Kim, Y. Choi, J. Lee, S. Heum Park, K. Lee, *J. Appl. Phys.* **2012**, *111*, 114511.
- [4] M. R. Lilliedal, A. J. Medford, M. V. Madsen, K. Norrman, F. C. Krebs, *Solar Energy Materials and Solar Cells* **2010**, *94*, 2018.
- [5] S. Wilken, J. Parisi, H. Borchert, *J. Phys. Chem. C* **2014**, *118*, 19672.
- [6] D. A. Melnick, *The Journal of Chemical Physics* **1957**, *26*, 1136.
- [7] S.-W. Fan, A. K. Srivastava, V. P. Dravid, *Appl. Phys. Lett.* **2009**, *95*, 142106.
- [8] Y. Jiang, L. Sun, F. Jiang, C. Xie, L. Hu, X. Dong, F. Qin, T. Liu, L. Hu, X. Jiang, Y. Zhou, *Mater. Horiz.* **2019**, *6*, 1438.
- [9] S. Park, H. J. Son, *J. Mater. Chem. A* **2019**, *7*, 25830.
- [10] A. Soultati, A. Verykios, S. Panagiotakis, K.-K. Armadorou, M. I. Haider, A. Kaltzoglou, C. Drivas, A. Fakharuddin, X. Bao, C. Yang, A. R. B. M. Yusoff, E. K. Evangelou, I. Petsalakis, S. Kennou, P. Falaras, K. Yannakopoulou, G. Pistolis, P. Argitis, M. Vasilopoulou, *ACS Appl. Mater. Interfaces* **2020**, *12*, 21961.
- [11] M. Günther, D. Blätte, A. L. Oechsle, S. S. Rivas, A. A. Yousefi Amin, P. Müller-Buschbaum, T. Bein, T. Ameri, *ACS Appl. Mater. Interfaces* **2021**, *13*, 19072.
- [12] H. Cha, J. Wu, A. Wadsworth, J. Nagitta, S. Limbu, S. Pont, Z. Li, J. Searle, M. F. Wyatt, D. Baran, J.-S. Kim, I. McCulloch, J. R. Durrant, *Adv. Mater.* **2017**, *29*.
- [13] N. Li, J. D. Perea, T. Kassar, M. Richter, T. Heumueller, G. J. Matt, Y. Hou, N. S. Güldal, H. Chen, S. Chen, S. Langner, M. Berlinghof, T. Unruh, C. J. Brabec, *Nature communications* **2017**, *8*, 14541.
- [14] X. Du, T. Heumueller, W. Gruber, A. Classen, T. Unruh, N. Li, C. J. Brabec, *Joule* **2019**, *3*, 215.
- [15] X. Du, T. Heumueller, W. Gruber, O. Almora, A. Classen, J. Qu, F. He, T. Unruh, N. Li, C. J. Brabec, *Adv. Mater.* **2020**, *32*.
- [16] M. Chang, L. Meng, Y. Wang, X. Ke, Y.-Q.-Q. Yi, N. Zheng, W. Zheng, Z. Xie, M. Zhang, Y. Yi, H. Zhang, X. Wan, C. Li, Y. Chen, *Chem. Mater.* **2020**, *32*, 2593.

4 The Neglected Influence of Zinc Oxide Light-Soaking on Stability Measurements of Inverted Organic Solar Cells

- [17] Matthew O. Reese, Suren A. Gevorgyan, Mikkel Jørgensen, Eva Bundgaard, Sarah R. Kurtz, David S. Ginley, Dana C. Olson, Matthew T. Lloyd, Pasquale Morvillo, Eugene A. Katz, Andreas Elschner, Olivier Haillant, Travis R. Currier, Vishal Shrotriya, Martin Hermenau, Moritz Riede, Kiril R. Kirov, Gregor Trimmel, Thomas Rath, Olle Inganäs, Fengling Zhang, Mattias Andersson, Kristofer Tvingstedt, Monica Lira-Cantu, Darin Laird, Christine McGuinness, Srinivas (Jimmy) Gowrisanker, Michael Pannone, Min Xiao, Jens Hauch, Roland Steim, Dean M. DeLongchamp, Roland Rösch, Harald Hoppe, Nieves Espinosa, Antonio Urbina, Gülsah Yaman-Uzunoglu, Jörg-Bernd Bonekamp, Albert J.J.M. van Breemen, Claudio Girotto, Eszter Voroshazi, Frederik C. Krebs, *Solar Energy Materials and Solar Cells* **2011**, *95*, 1253.
- [18] W. R. Mateker, M. D. McGehee, *Adv. Mater.* **2017**, *29*.
- [19] G. Ji, W. Zhao, J. Wei, L. Yan, Y. Han, Q. Luo, S. Yang, J. Hou, C.-Q. Ma, *J. Mater. Chem. A* **2019**, *7*, 212.
- [20] L. Krishnan Jagadamma, M. T. Sajjad, V. Savikhin, M. F. Toney, I. D. W. Samuel, *J. Mater. Chem. A* **2017**, *5*, 14646.
- [21] M. Chen, X. Wang, Y. Yu, Z. Pei, X. Bai, C. Sun, R. Huang, L. Wen, *Applied Surface Science* **2000**, *158*, 134.
- [22] C. Lennon, R. B. Tapia, R. Kodama, Y. Chang, S. Sivananthan, M. Deshpande, *Journal of Electronic Materials* **2009**, *38*, 1568.
- [23] J. d. O. Primo, C. Bittencourt, S. Acosta, A. Sierra-Castillo, J.-F. Colomer, S. Jaeger, V. C. Teixeira, F. J. Anaissi, *Frontiers in chemistry* **2020**, *8*, 571790.
- [24] M. Takata, D. Tsubone, H. Yanagida, *J American Ceramic Society* **1976**, *59*, 4.
- [25] M. Madel, F. Huber, R. Mueller, B. Amann, M. Dickel, Y. Xie, K. Thonke, *Journal of Applied Physics* **2017**, *121*, 124301.
- [26] J. Lagowski, E. S. Sproles, H. C. Gatos, *Journal of Applied Physics* **1977**, *48*, 3566.
- [27] Q. Liu, P. Mantilla-Perez, M. Montes Bajo, P. Romero-Gomez, J. Martorell, *ACS Appl. Mater. Interfaces* **2016**, *8*, 28750.
- [28] S. C. Abrahams, J. L. Bernstein, *Acta Crystallogr B Struct Sci* **1969**, *25*, 1233.
- [29] N. Fairley, V. Fernandez, M. Richard-Plouet, C. Guillot-Deudon, J. Walton, E. Smith, D. Flahaut, M. Greiner, M. Biesinger, S. Tougaard, D. Morgan, J. Baltrusaitis, *Applied Surface Science Advances* **2021**, *5*, 100112.

5 Elucidating the Origin of Open-Circuit Voltage in Ternary Organic Solar Cells Comprising a Nonfullerene and a Fullerene Acceptor

This chapter is based on the following manuscript:

Marcella Günther, Dominic Blätte, Andreas Weis, Lucie Quincke, Miguel Angel Torre Cachafeiro, Wolfgang Tress, Jose Dario Perea, Salvador Leon Cabanillas, Thomas Bein and Tayebbeh Ameri. Elucidating the Origin of Open-Circuit Voltage in Ternary Organic Solar Cells Comprising a Nonfullerene and a Fullerene Acceptor

To be submitted

5.1 Introduction

In retrospect, the development of organic solar cells (OSC) to date can be divided into two major eras based on the main acceptor type used: the era of the fullerene acceptors (FA) and the era of the nonfullerene acceptors (NFA). Since the invention of the bulk heterojunction (BHJ) OSC in 1995, C₆₀ and its derivatives and relatives have been the dominating acceptors, and the most popular representatives PC₆₁BM and PC₇₁BM have been able to support impressive power conversion efficiencies (PCEs) of 11-12 % in combination with various donor (D) molecules.^{1,2} But fullerene derivatives have a very limited optical absorption capability and their energy levels cannot be tuned freely, limiting performance enhancement of OSCs with fullerene acceptors to higher values. However, from 2015 onwards, novel NFA molecules were increasingly developed, that showed high absorption and flexibly tunable electrical properties. When in 2016 NFA-based systems for the first time exceeded the performance of comparable fullerene-based systems,^{3,4} a new era emerged, leading to an efficiency record of 19 % to date.⁵ Nevertheless, fullerenes are still widely used, but usually no longer as stand-alone acceptors, but in combination with an NFA in ternary solar cells. It has been demonstrated numerous times for many different material combinations that the efficiency of binary D:NFA cells can be significantly increased by the addition of a small amount of a fullerene.⁶⁻¹⁰ Intriguingly, while this seems to be almost a universal principle, there is still disagreement about the reasons for the positive effect of fullerenes and especially about the working mechanisms in such ternary systems.

5 Elucidating the Origin of Open-Circuit Voltage in Ternary Organic Solar Cells Comprising a Nonfullerene and a Fullerene Acceptor

A commonly reported effect of fullerenes as a third component is an improved morphology of the ternary blend by, for example, decreasing aggregation of the NFA.^{6,11} In addition, it is often observed that the incorporation of fullerenes improves the transport properties in the blend, with higher electron mobility, improved charge extraction, and consequently less recombination.^{7,11,12} While such enhancements are frequently cited, how exactly the fullerenes interact electronically with the other components in the process is rarely investigated. The few studies that focus more on mechanistic details of individual systems yield contradictory results. Zhou et al.¹² used an NFA to sensitize a binary D:FA host system, thus creating a cascade-type ternary system. They attributed the overall improved efficiency to the synergistic effect of the NFA improving the blend absorption and the fullerene acting as charge percolating network with high electron mobility. They found that the D:NFA interface is mainly responsible for the charge generation, but the generated electrons then are transferred to the FA for the transport to the electrode. Laquai and co-workers,¹³ on the other hand, observed for several D:NFA systems that the addition of the fullerene PC₇₁BM results in an energy transfer from the FA to the smaller band gap NFA which increases the quantum efficiency of the ternary device. While these two examples with their charge and energy transfer dominated behavior, respectively, should theoretically lead to a V_{OC} that is relatively independent of the mixing ratio of the two acceptors, other groups observed a tunability of the V_{OC} which depends on the FA:NFA ratio.¹⁴ For the explanation of such a composition-dependent V_{OC} in a ternary OSC, currently three major theories exist: the alloy model, the parallel-like model, and the chemical environment approach. The alloy model assumes that the two acceptors (or two donors, respectively) form an intimate mixture with common, averaged electronic properties, resulting in a delocalized composition-dependent charge transfer state, determining the V_{OC} .^{15,16} The parallel-like model, on the other hand, proposes the existence of two morphologically separated D:A networks (D:A₁ and D:A₂ or D₁:A and D₂:A) with two distinct CT states, whose weighted average determines the V_{OC} .^{17,18} Finally, the chemical environment approach assumes that the electronic properties of the blend are determined by the majority components (D:A₁ or D₁:A) but that their energy levels in turn are influenced by their chemical environment which depends on the blend composition and the amount of the second acceptor (or second donor).^{19,20}

So, in summary, there are several different and apparently incompatible approaches explaining the working principles of D:NFA:FA systems. It is, of course, quite possible that all these explanations are correct and that the individual D:NFA:FA systems are simply fundamentally different, due to molecular, morphological and energetic details. However, it can be assumed that at least a few common basic principles exist and that similar systems behave in a

5 Elucidating the Origin of Open-Circuit Voltage in Ternary Organic Solar Cells Comprising a Nonfullerene and a Fullerene Acceptor

mechanistically similar way. For this reason, we have taken a concise approach in this work and aim to study the mechanisms in ternary D:NFA:FA systems by systematically varying the components and their ratio while monitoring the results on performance and mechanisms.

In this work, we consider eight different D:NFA:FA systems with two different donor polymers and four different fullerenes with systematically varying LUMO levels and compare them with two separate D:NFA:NFA systems. For all systems, we find a composition-dependent performance with a linearly tunable V_{OC} that directly relates to the LUMO of the respective second acceptor. We study the voltage losses in detail and find them to be independent of the third component's nature. Finally, we use a combination of different measurements to demonstrate that the considered D:NFA:FA systems follow an alloy-like mechanism with a CT state being delocalized over both acceptors.

5 Elucidating the Origin of Open-Circuit Voltage in Ternary Organic Solar Cells Comprising a Nonfullerene and a Fullerene Acceptor

5.2 Results and Discussion

5.2.1 Properties of the Employed Materials

We studied ternary systems based on one of two different polymer donors PTB7-Th and PBDB-TF in combination with the nonfullerene acceptor IT-4F, providing two different binary donor:acceptor (D:A) host systems. The molecular structures of all used materials are shown in **Figure 5.1a**, their systematic names can be found in the experimental part. As third components, acting as second acceptor, the four different fullerene derivatives ICMA, PCBM, BisPCBM, and TrisPCBM were deployed, resulting in eight different ternary D:NFA:FA systems. Additionally, ITIC was used as a third component to have two D:NFA:NFA systems for comparison.

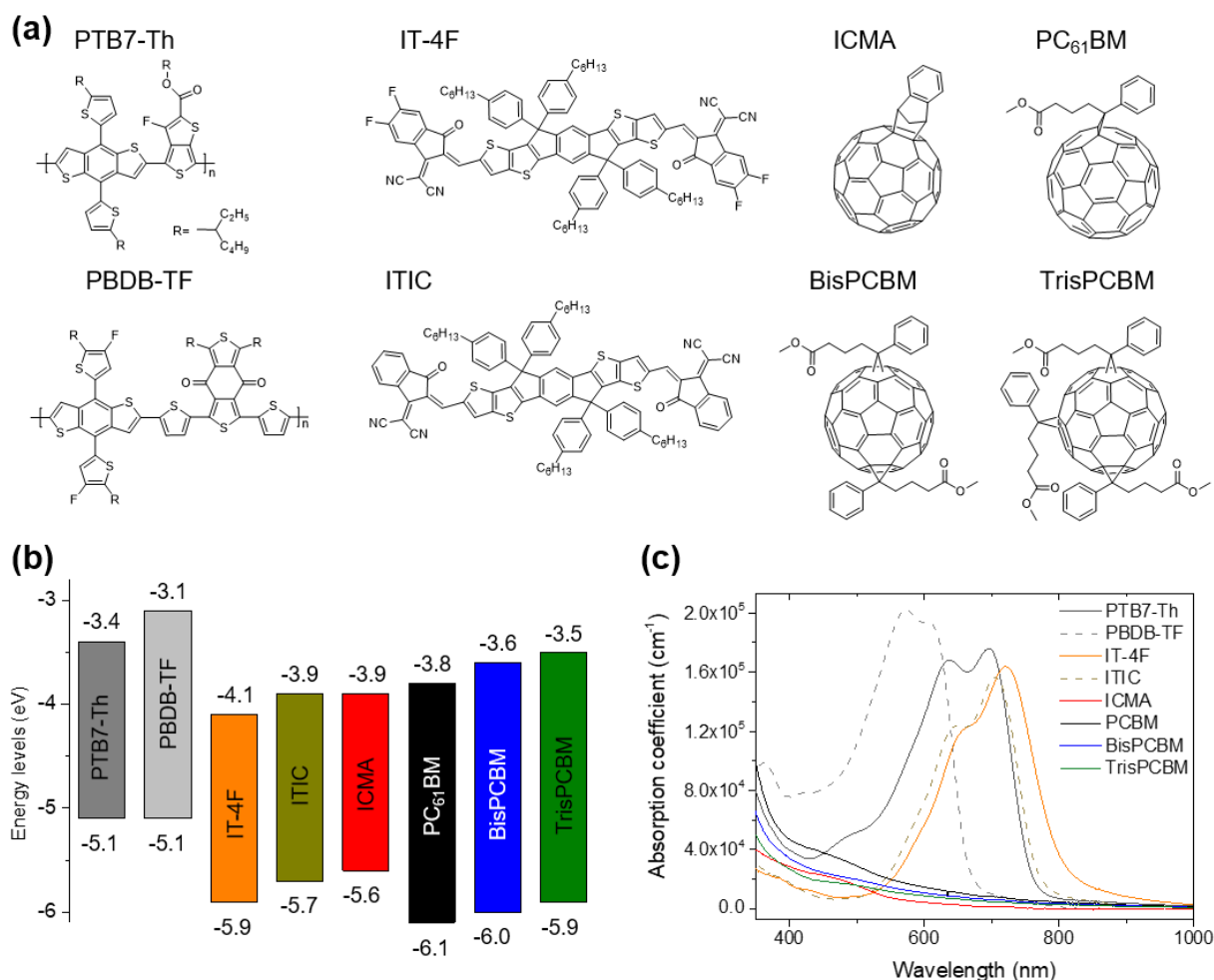


Figure 5.1: a) Molecular structures b) energy levels and c) absorption coefficients of the employed donor polymers PTB7-Th and PBDB-TF, the nonfullerene acceptors IT-4F and ITIC, and the fullerene derivatives ICMA, PCBM, BisPCBM and TrisPCBM.

For this type of systematic study, the exact values of the frontier molecular energy levels are crucial, but their precise experimental determination has been proven difficult and controversial

5 Elucidating the Origin of Open-Circuit Voltage in Ternary Organic Solar Cells Comprising a Nonfullerene and a Fullerene Acceptor

in the past years.^{21–23} Only recently it was shown that different measurement methods can lead to very different results for the ionization energy (IE) and the electron affinity (EA) and that therefore values from different publications are only poorly comparable.²³ To circumvent this problem for our work, we have specifically selected the fullerene derivatives so that they exhibit a clear trend of energy levels based on their molecular structure due to the increasing number of electron-donating substituents on the C₆₀ framework. In this way, we can be sure that the EA of the fullerene derivatives increases continuously in the series ICMA<PCBM<BisPCBM<TrisPCBM, regardless of possibly erroneously analytically determined values. For better clarity, we nevertheless show in **Figure 5.1b** measured literature values for IP and EA of all components used, whereby all values were obtained with photoelectron spectroscopy of the solid materials.^{23–26}

In **Figure 5.1c**, the absorption spectra of all used components are shown. It is clearly evident that the absorption in the respective ternary blends is mainly dominated by the ‘host’ components, while the fullerenes with their small absorption coefficient make only a minor contribution. **Table 5.1** lists the surface energies of the individual components that we determined according to the Wu model²⁷ from the contact angles of water and glycerol on films of the pristine materials.

Table 5.1: Contact angles of films of pristine materials measured with water and with glycerol, and the calculated surface energies according to the Wu model.

Material	Contact angle water [°]	contact angle glycerol [°]	Surface energy Wu model [mN/m]
PTB7-Th	101.0	95.8	18.8
PBDB-TF	103.0	97.1	18.0
IT-4F	98.6	84.9	24.5
ITIC	89.1	82.1	25.6
ICMA	70.1	80.1	40.3
PCBM	84.3	71.4	31.2
BisPCBM	89.6	77.4	27.8
TrisPCBM	92.2	80.5	26.1

The host donors PTB7-Th and PBDB-TF have a very similar surface energy, close to that of the host acceptor IT-4F. The materials chosen as third components show an increasing surface

5 Elucidating the Origin of Open-Circuit Voltage in Ternary Organic Solar Cells Comprising a Nonfullerene and a Fullerene Acceptor

energy in the sequence ITIC<TrisPCBM<BisPCBM<PCBM<ICMA. It is commonly assumed that a similar surface energy results in a good miscibility while very different values indicate an unfavorable miscibility. From these results we infer that the third components (the second acceptors) possibly show a decreasing miscibility with the host blend with increasing surface energy.

5.2.2 Photovoltaic Performance of the Ternary Devices

Based on the components above, ternary organic solar cells were made from the 10 different systems (PTB7-Th:IT-4F+ICMA/PCBM/BisPCBM/TrisPCBM and PBDB-TF:IT-4F+ICMA/PCBM/BisPCBM/TrisPCBM being the eight D:NFA:FA systems and PTB7-Th:IT-4F:ITIC and PBDB-TF:IT-4F:ITIC being the two D:NFA:NFA systems for comparison). All cells were built in an inverted architecture ITO | ZnO | Active Layer | MoO_x | Ag and the overall D:A weight ratio was kept constant (1:1.5 for PTB7-Th based cells, 1:1 for PBDB-TF based cells). Further manufacturing details can be found in the experimental section. For the ternary blends the host acceptor IT-4F was progressively replaced by the respective second acceptor component (FA or NFA). The most promising approaches discussed in literature for improving the PCE are usually based on the addition of smaller amounts of fullerenes to a D:NFA host system. Therefore, for our D:NFA:FA systems, we will focus in the following on compositions that are still dominated by a nonfullerene acceptor, i.e. where the fullerene fraction is less than 50 wt% of the acceptor phase. Yet, for the sake of completeness – and to better visualize trends – we show here compositions with 0 %, 10 %, 30 %, 50 % and 70 % fullerene fraction for each ternary system. Analogously, for the two D:NFA:NFA systems we show compositions up to an ITIC ratio of 70 %. We would like to note that the goal of this study is not record efficiencies, which is why the individual compositions were not optimized separately and fall behind in terms of efficiency compared to some other literature values. However, in this way, a better comparability of the cells with each other has been achieved, making trends due to the composition of the ternary blend more apparent. In **Figure 5.2a** and **b** the PCEs for all ternary cells based on PTB7-Th and PBDB-TF, respectively, are shown. The values were averaged over 15 individual cells each, but for clarity the error bars are not shown here. The detailed performance data of all ternary systems including error bars can be found in the supporting information (**Figure S 5.1** and **Figure S 5.2**). The PTB7-Th:IT-4F binary cells on average have an efficiency of 6.5 %. As the IT-4F is gradually replaced by one of the four different fullerene derivatives, the PCE is slightly increasing, mainly driven by an increasing fill factor, with the best performance being achieved for 30 % fullerene ratio.

5 Elucidating the Origin of Open-Circuit Voltage in Ternary Organic Solar Cells Comprising a Nonfullerene and a Fullerene Acceptor

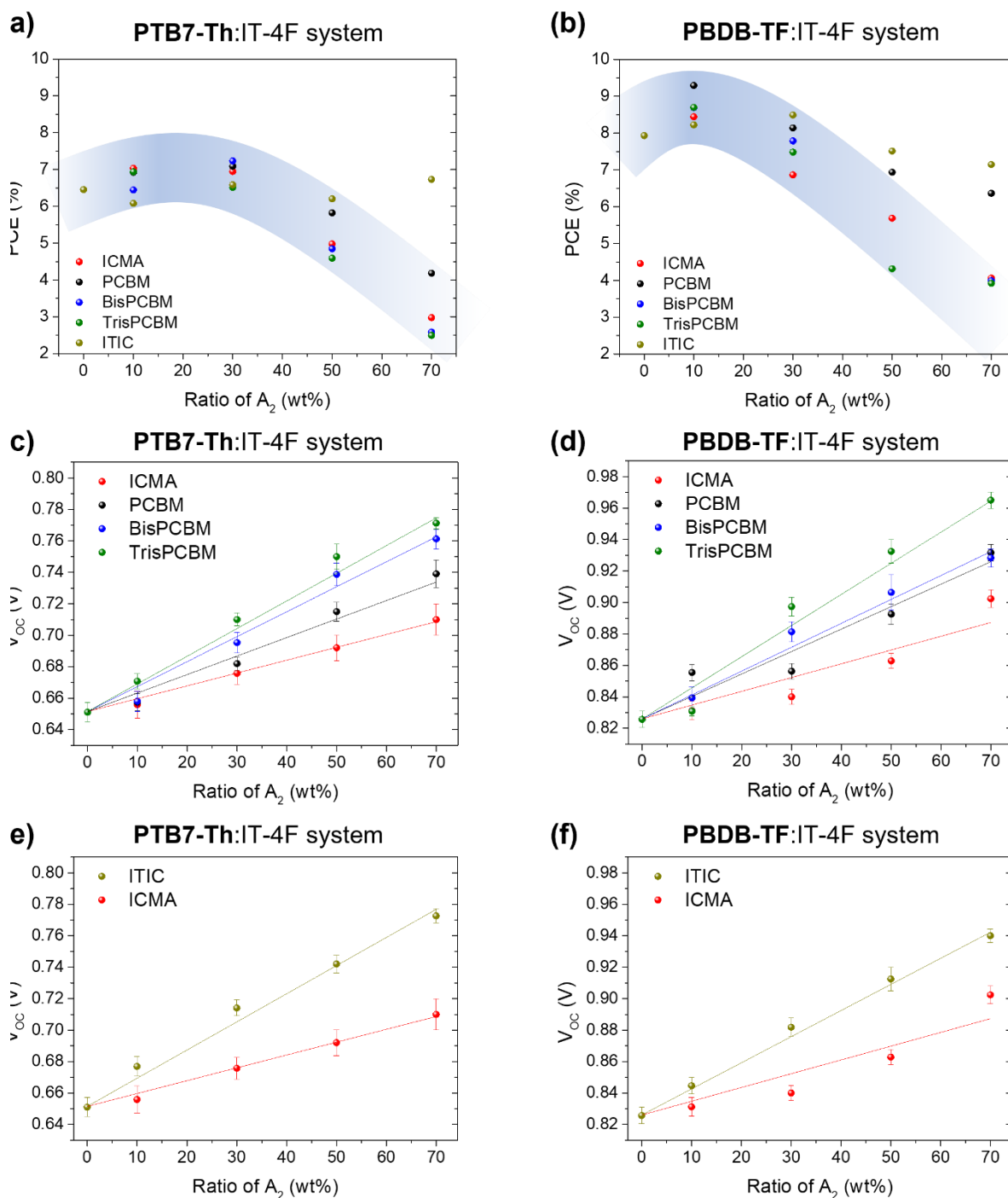


Figure 5.2. Averaged power conversion efficiency (PCE) of ternary systems based on the a) PTB7-Th:IT-4F and the b) PBDB-TF:IT-4F host system with the fullerene acceptors ICMA, PCBM, BisPCBM and TrisPCBM and the nonfullerene acceptor ITIC as third components. Open-circuit voltage trends for the c) PTB7-Th:IT-4F and the d) PBDB-TF:IT-4F host system with the fullerenes as third component. Open-circuit voltage trends for the e) PTB7-Th:IT-4F and the f) PBDB-TF:IT-4F host system with the nonfullerene acceptor ITIC as third component in comparison with the ICMA ternary system.

For higher ratios, the PCE is decreasing again (the overall trends of the PTB7-Th:IT-4F:FA systems are indicated in **Figure 5.2a** with the blue marking). In contrast to this, the PTB7-

5 Elucidating the Origin of Open-Circuit Voltage in Ternary Organic Solar Cells Comprising a Nonfullerene and a Fullerene Acceptor

Th:IT-4F:ITIC system shows a relatively constant PCE independent of the proportion of the third component ITIC. The PBDB-TF:IT-4F binary cells have an average PCE of 7.9 % and the corresponding ternary systems (**Figure 5.2b**) show a behavior comparable to the PTB7-Th based systems for both D:NFA:FA and D:NFA:NFA, although the efficiency improvement is greatest for a 10 % fullerene fraction. Notably, the PBDB-TF:IT-4F:PCBM ternary system shows the largest PCE improvement compared to the binary system and has the smallest losses for higher fullerene fractions. Overall, the PCE trends of all D:NFA:FA systems are very similar across the composition, regardless of the fullerene derivative used. More striking trends become apparent when we take a closer look on the V_{OC} . As shown in **Figure 5.2c** and **d**, all ternary systems show a relatively linearly increasing V_{OC} with growing fullerene ratio, clearly placing them in the group of ternary systems with composition-tunable V_{OC} . The most interesting observation, however, is that the slope of the increasing V_{OC} clearly differs between the different ternary systems. In both PTB7-Th based systems and PBDB-TF based systems, the ternary cells with TrisPCBM show the largest slope, followed by BisPCBM, PCBM, and ICMA with the smallest slope. This trend therefore follows exactly the trend of the decreasing LUMO levels of the fullerenes. As a reference, **Figure 5.2e** and **f** show the V_{OC} trends of the respective D:NFA:NFA systems, which also depict a clear linear composition-dependency. Interestingly, in comparison to the ternary systems with ICMA, the ITIC ternary systems have a significantly greater slope, although ICMA and ITIC should have a similar LUMO energy according to literature values.

5.2.3 CT Energies and Loss Analysis

In order to investigate the observed V_{OC} trends in more detail, the CT state energies were determined with Fourier-transform photocurrent spectroscopy (FTPS). To focus, all following analytics were only done for the binary host system PTB7-Th:IT-4F with the fullerenes ICMA, PCBM, and BisPCBM, and with the nonfullerene ITIC. For the cells based on the PBDB-TF:IT-4F host system a determination of the CT state energies via FTPS is not possible, since the energetically relatively high CT state absorption is overlapped by the absorption of IT-4F. In **Figure 5.3a-d** the determined CT state energy E_{CT} and the V_{OC} (times the elemental charge q) of the corresponding cells for the different compositions of the four ternary systems are shown. The FTPS data with the corresponding Marcus fits can be found in **Figure S 5.3**.

It is clearly evident that for all four ternary systems, the CT state energy increases linearly with the third component fraction, following the trends of the V_{OC} . However, in all cases E_{CT} shows a somewhat flatter increase than the V_{OC} , indicating that there are changes in the recombination

5 Elucidating the Origin of Open-Circuit Voltage in Ternary Organic Solar Cells Comprising a Nonfullerene and a Fullerene Acceptor

behavior. In an energetic state picture, as schematically illustrated in **Figure 5.3e**, the difference between E_{CT} and V_{OC} corresponds to the sum of the radiative and nonradiative voltage losses ΔV_{OC}^{rad} and ΔV_{OC}^{nr} . With the radiative limit of the open-circuit voltage qV_{OC}^{rad} the losses then can be calculated separately. We therefore determined qV_{OC}^{rad} following Rau's reciprocity theorem according to **equation (5.1)**:²⁸

$$V_{OC}^{rad} = \frac{k_B T}{q} \ln \left(\frac{J_{sc}}{J_0^{rad}} \right) \quad (5.1)$$

where $k_B T$ is the thermal energy at room temperature, q is the elemental charge, J_{sc} is the short-circuit current density and J_0^{rad} is the radiative saturation current density which can be calculated from the external quantum efficiency spectrum (EQE) and the blackbody spectrum Φ_{bb} with **equation (5.2)**:²⁹

$$J_0^{rad} = q \int_0^{\infty} EQE \cdot \Phi_{bb} dE \quad (5.2)$$

The respective EQE spectra of all ternary cells can be found in **Figure S 5.4**. As established by Vandewal and co-workers with the so-called power gap law, non-radiative voltage losses in binary OSCs decrease with increasing E_{CT} since the wavefunction overlap of the CT state and higher vibrational modes of its ground state is decreased.³⁰ We assume that the same principle also applies to ternary blends and therefore show the results of the voltage loss analysis in **Figure 5.3f** as a plot versus the respective CT state energy to compare the different ternary systems. On the contrary, the plot of the voltage losses versus the ratio of the third component leads to misleading trends due to the differences in E_{CT} for the different systems, as shown in **Figure S 5.5**. Notably, the plot of the voltage losses versus E_{CT} depicts very similar voltage losses and trends over composition for all ternary systems, independent of the third component's nature. For all systems, the radiative losses increase with the ratio of the second acceptor while the nonradiative losses decrease, resulting in a slight reduction of overall losses with increasing CT state energy. This very similar behavior, related only to the energy of the CT state and showing no differences for chemically different components, suggests that the observed trends for the ternary systems can be explained by the power gap law. Thus, in all cases, the third component has a positive effect on the recombination behavior only insofar as it shifts the CT state energy upward. In the literature, the positive effect of fullerenes on efficiency in ternary systems is often attributed to reduced nonradiative recombination. We cannot confirm this reasoning for the systems we considered, because although the nonradiative recombination does indeed decrease with increasing fullerene content, the radiative recombination increases at the same time, so that the overall recombination is only marginally

5 Elucidating the Origin of Open-Circuit Voltage in Ternary Organic Solar Cells Comprising a Nonfullerene and a Fullerene Acceptor

reduced. Moreover, the decreasing non-radiative recombination is not caused by the special properties of fullerenes themselves but would be achievable with any other third component with higher LUMO that shifts the CT state energy upward.

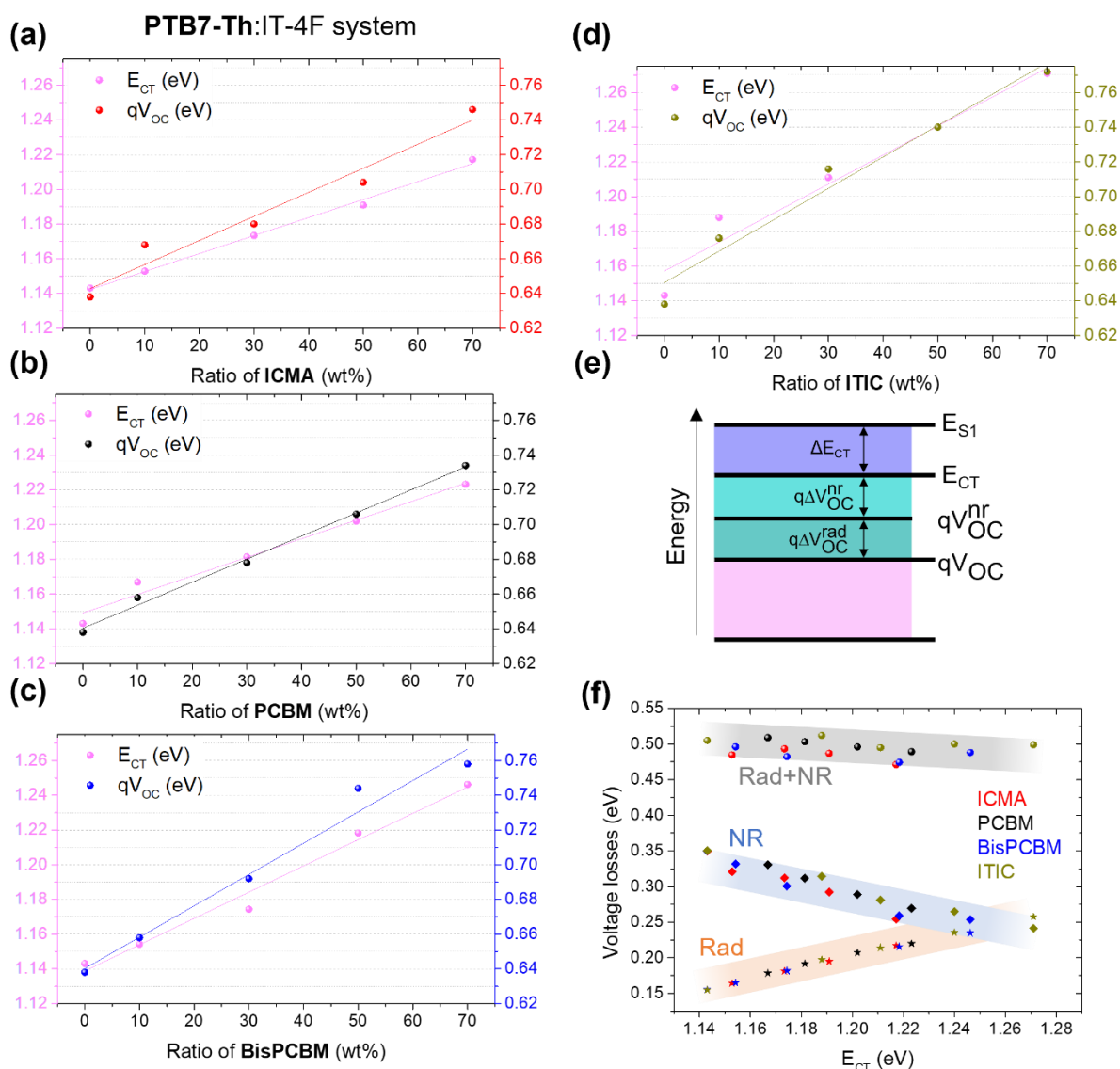
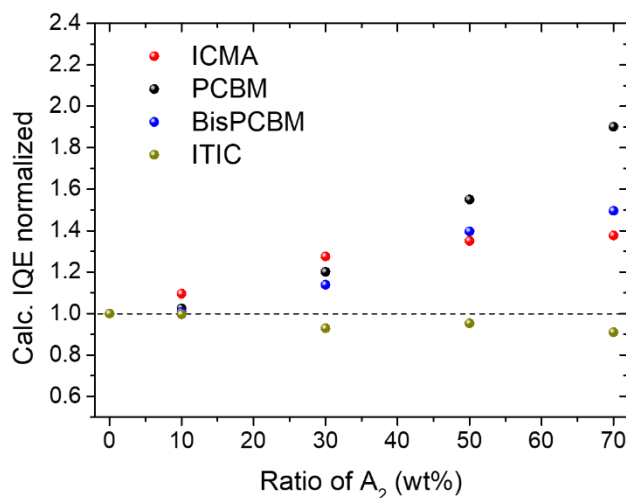


Figure 5.3. Charge transfer state energy (E_{CT}) determined by Marcus fitting of FTPS measurements and corresponding open-circuit voltage times the elemental charge q for ternary cells with varying ratios of the second acceptor a) ICMA, b) PCBM, c) BisPCBM, and d) ITIC. e) Energetic state picture of an organic solar cell showing the energetic position of the excited singlet state E_{S1} , the charge transfer state E_{CT} , the open-circuit voltage in the radiative limit qV_{OC}^{rad} , and the open-circuit voltage qV_{OC} . Additionally, the voltage losses due to the formation of the CT state (ΔE_{CT}), due to radiative recombination ($q\Delta V_{OC}^{rad}$), and due to nonradiative recombination ($q\Delta V_{OC}^{NR}$) are depicted. f) Calculated voltage losses for the four different ternary systems in dependence of the CT state energy of the respective composition, divided by radiative and nonradiative losses.

5.2.4 Internal Quantum Efficiency

Although recombination behavior does not appear to differ much between cells with different second acceptors, there is still a striking difference between the optical properties of cells with fullerenes or an NFA as a third component. When the host acceptor IT-4F is gradually replaced by a fullerene to form a ternary blend, the total absorption of the blend decreases due to the smaller absorption coefficient of the third component. This is not the case for ITIC replacing IT-4F since they both have a comparable absorption coefficient. However, despite the decrease in total absorption, the efficiency of the ternary cells initially increases with increasing fullerene content up to 30 % and also the EQE spectra do not reflect the decreasing absorption, which is a strong hint towards changes in the internal quantum efficiency (IQE). In principle the IQE for organic solar cells has to be determined by optically modeling the whole device stack via transfer matrix modeling to account for interference effects in the different layers.³¹ However, this approach also bears inaccuracies, especially when determining the IQE for a range of systematically varied active layer compositions, since the optical constants would have to be determined individually for each layer. Consequently, we decided for a simpler approach with the reasoning that all ternary cells were built in the same architecture with the same interlayers and a comparable active layer thickness in a range of ± 10 nm, thus having a comparable internal reflection in all ternary devices. This assumption allows for a simplified calculation of a pseudo-IQE from the quotient of the EQE and the absorption coefficient at the wavelength of maximum absorption (= 714 nm). The absorption coefficient spectra for all ternary blends can be found in **Figure S 5.6**. These quotients, normalized to the quotient of the binary PTB7-Th:IT-4F cell, are shown in **Figure 5.4** for the different ternary systems.



5 Elucidating the Origin of Open-Circuit Voltage in Ternary Organic Solar Cells Comprising a Nonfullerene and a Fullerene Acceptor

Figure 5.4. Calculated internal quantum efficiency (IQE) by dividing the EQE by the absorption coefficient at the absorption maximum (714 nm). The values for the different ternary blends were normalized to the quotient of the binary PTB7-Th:IT-4F.

Here, the difference between the ternary systems with a FA and with a NFA as the third component becomes very clear. The FA ternary systems all show an increasing IQE with increasing fullerene ratio, while for the NFA ternary system the IQE remains nearly constant for all compositions. Basically, the IQE is composed of three contributions: the efficiency of exciton dissociation $\eta_{d,ex}$, the efficiency of CT state dissociation $\eta_{d,CT}$, and the efficiency of charge collection η_{coll} .³² Under the now established assumption that any recombination of free charge carriers proceeds via the reformation of a CT state,^{33–35} major changes in the efficiency of CT state dissociation and charge collection should also manifest themselves in a change in recombination behavior. However, as shown in the previous discussion and in **Figure 5.3f**, there are no differences in recombination behavior between FA and NFA ternary systems that could explain the differences in IQE. We therefore hypothesize that the fullerenes used here will allow for a more efficient exciton dissociation compared to the NFA ITIC. This difference could possibly be explained by the findings of Laquai and co-workers,²⁶ who demonstrated that for D:NFA the main mechanism for the CT state formation is a hole transfer from the NFA to the donor, while in D:FA systems, the dominating mechanism is an electron transfer from the donor to the FA. It may well be that these two mechanisms operate with different efficiencies, which would explain the change in the IQE when a NFA is replaced by a FA.

5.2.5 Assignment to a Model

In summary, the preceding discussion has shown that for all ternary systems presented, there is a linear increase in V_{OC} with the ratio of the third component. Furthermore, it has been shown that this increase is directly due to an increase in the respective CT state energy. As outlined in the introduction, such a composition-dependent V_{OC} tunability can be explained with three different approaches: the alloy model, the parallel-like model and the influence of the chemical environment. We would like to rule out the influence of the chemical environment as the main contributor to the observed increase in E_{CT}/V_{OC} for several reasons: First of all, the slope of the composition-dependent V_{OC} for the different fullerenes increases in the row ICMA<PCBM<BisPCBM<TrisPCBM and thus directly correlates with their increasing LUMO level, suggesting an electronic involvement of the third components in the CT state. Moreover, all the third components used form functional binary solar cells with the employed donors, therefore being capable of forming a charge transfer state with the donor. There is no

5 Elucidating the Origin of Open-Circuit Voltage in Ternary Organic Solar Cells Comprising a Nonfullerene and a Fullerene Acceptor

reason why they should not do so in a ternary blend and instead only passively influence the host components. And finally, the employed third components have very different dielectric properties and if their presence in the environment of the host molecules indeed was influencing the CT state energy, it would result in opposing trends. For example, the permittivity of ITIC with $\epsilon \approx 3.0$ is smaller than the one of IT-4F ($\epsilon \approx 3.4$), while the permittivity of PCBM ($\epsilon \approx 4.6$) is much higher, but nevertheless both ITIC and PCBM as third components cause an up-shifting E_{CT} .^{36,37}

From all this we conclude that while the presence of the third components may well have some minor effect on the energetic situation of the host components, the observed bigger picture of the V_{OC} trends is not due to such effects but originate from an electronic involvement of the third component in the CT state formation.

To obtain a clearer picture of the working principle of the D:NFA:FA systems we under study, we chose the ternary PTB7-Th:IT-4F:PCBM as representative for some further measurements. An important hint can be found when looking at the optical behavior of the binary IT-4F:PCBM acceptor blend. In **Figure 5.5**, the normalized absorption and photoluminescence spectra of pristine IT-4F and blends of IT-4F and PCBM with varying ratios are shown. The absorption spectrum is dominated by IT-4F since PCBM only has a small absorption coefficient above 600 nm (see **Figure 5.1c**). For increasing PCBM ratios, the absorption of IT-4F is slightly red-shifted which most probably is due to the induced disorder upon mixing. It would be expected that the PL for the same reason also shows a small red-shift, however, as visible in **Figure 5.4b** it instead exhibits a strong blue-shift, which increases linearly with the PCBM ratio up to the PL of pristine PCBM. Notably, the width of the PL peaks remains nearly constant, and no broadening is observed for the mixed blends. A very similar behavior is also found for the corresponding electroluminescence measurements of the respective acceptor blends, as shown in **Figure S 5.7**. These observations suggest that while the absorption happens via the generation of a local exciton in the IT-4F molecules, the emission occurs from an excited state which is delocalized between IT-4F and PCBM, thus clearly following an alloy-like behavior as proposed by Street et al.¹⁵

5 Elucidating the Origin of Open-Circuit Voltage in Ternary Organic Solar Cells Comprising a Nonfullerene and a Fullerene Acceptor

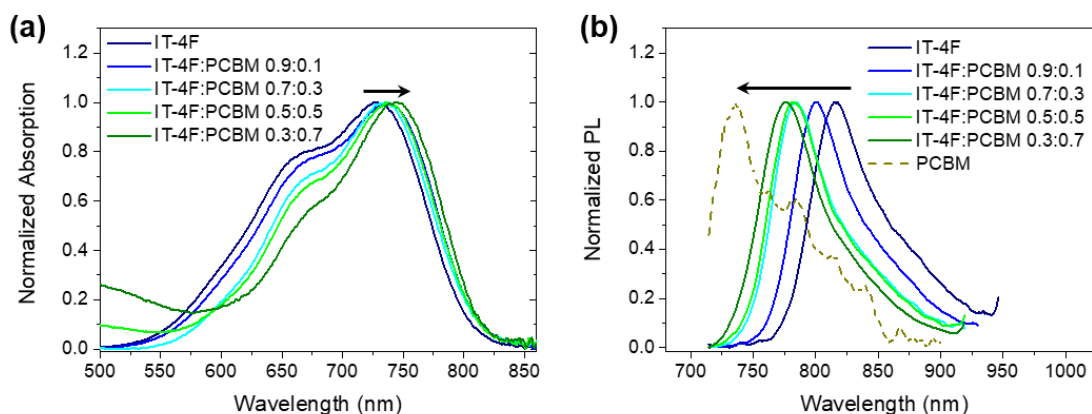


Figure 5.5. a) Normalized absorption spectra and b) photoluminescence spectra of binary acceptor blends with varying weight ratios of IT-4F and PCBM.

To further investigate this in the complete ternary blend also containing the polymer donor, we performed an experiment suggested by Savoie et al.³⁸ to distinguish between an alloy-like and parallel-like behavior. We performed JV -measurements on the ternary PTB7-Th:IT-4F:PCBM devices using a 785 nm laser diode that exclusively excites the IT-4F. In case of a parallel-like mechanism, this should result in a V_{OC} that is independent of the ternary composition, since IT-4F and PCBM do not interact electronically and the V_{OC} is only determined by the CT state between donor and IT-4F. As a comparison, we used a white light LED which was calibrated to 100 mW cm^{-2} and adjusted the laser diode intensity for each device in a way that the same short-circuit current was achieved as with the LED. The absorption spectra of the three components and the emission spectra of the used light sources are shown in the **Figure 5.6a**. In **Figure 5.6b**, the obtained V_{OC} values of the ternary devices with increasing PCBM ratio are presented for the LED and the laser diode being used as light source. The full JV -curves can be found in **Figure S 5.8**. It is evident that in both cases the V_{OC} values are very similar for each ternary device and that the linear increase of the V_{OC} with the PCBM ratio is the same, thus ruling out the idea of a parallel-like mechanism and further supporting the idea of alloyed CT states.

5 Elucidating the Origin of Open-Circuit Voltage in Ternary Organic Solar Cells Comprising a Nonfullerene and a Fullerene Acceptor

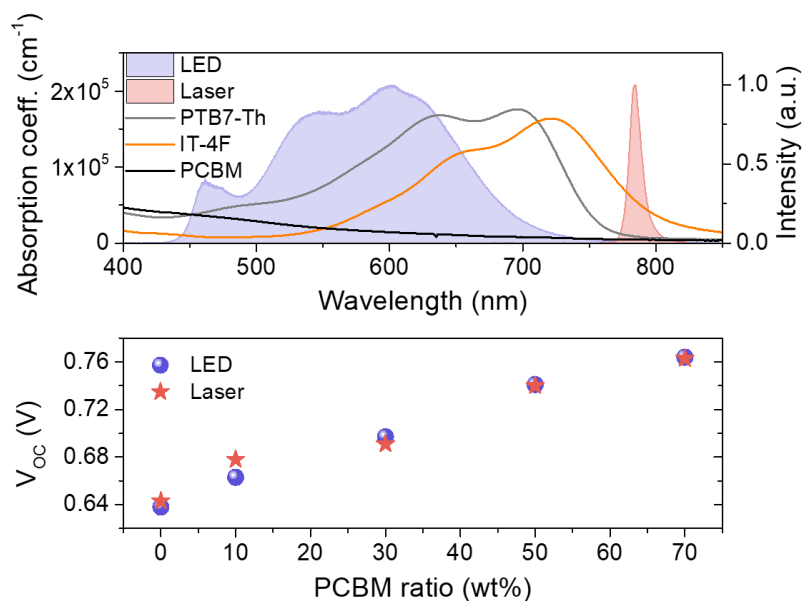


Figure 5.6. a) Absorption coefficient spectra of the pristine materials PTB7-Th, IT-4F, and PCBM and their overlap with the emission of a white light LED (blue) and of a 785 nm laser diode (red). b) Open-circuit voltage from *IV*-measurements that were performed with the white light LED (blue) and with the laser diode (red) as a source of illumination.

To further examine the question of whether these are indeed newly formed states and not a mere superposition of the states of the individual materials, we compared our observed V_{OC} trends with the model of Kemerink et al. that was developed to describe the composition-dependence of the V_{OC} in ternary blends analytically.³⁹ This model is based on a state-filling approach in which the states in the ternary blend are described via a joint, disorder broadened gaussian density of states (DOS), corresponding to the superpositioned DOS of the single components. By filling the effective DOS according to a Fermi-Dirac distribution and assuming a constant occupation over all compositions, the quasi-Fermi levels of holes and electrons can be calculated and from their difference the V_{OC} is obtained. In **Figure S 5.9**, the corresponding formulas and the logic of the modeling script used are shortly summarized, for more details we refer to the work of Kemerink et al. In **Figure S 5.10**, the measured V_{OC} trends of the PTB7-TH:IT-4F based systems with ICMA, PCBM, BisPCBM and TrisPCBM are compared with the correspondingly modeled V_{OC} trends. While the experimental and modeled values for the ternary ICMA system still agree very well, the modeled values for the other systems deviate further and further downward from the experimental values as the LUMO of the third component increases. This indicates that when state-filling a joint DOS, the energetically higher DOS of the third component is not adequately weighted and that the description via a superposition is not applicable for the ternary systems under consideration here. Instead, the

5 Elucidating the Origin of Open-Circuit Voltage in Ternary Organic Solar Cells Comprising a Nonfullerene and a Fullerene Acceptor

experimental V_{OC} trends only can be explained with the assumption of newly formed states due to a delocalization.

5.3 Conclusion and Outlook

In summary, we conducted an extensive study to understand the working principles and the origin of V_{OC} in ternary systems consisting of a polymer donor, a nonfullerene acceptor and a fullerene acceptor. We considered eight different D:NFA:FA systems based on two different donor polymers and four different fullerenes and additionally two D:NFA:NFA systems as a comparison. For all of the investigated ternary systems, the third component worked as second acceptor having an energetically higher LUMO than the host acceptor. We found a composition-tunable V_{OC} for all ternary systems, with the extent of tunability directly related to the third component's LUMO position. We studied the voltage losses in dependence of the ternary composition and showed that for all systems the nonradiative recombination decreases with increasing third component fraction, however, this beneficial effect is almost completely cancelled by increasing radiative recombination. Overall, the recombination behavior is independent of the nature of the third component and is exclusively related to the CT state energy, confirming that the power gap law established by Vandewal and co-workers also applies to ternary systems. We suggest that the positive effect of small amounts of fullerenes in ternary organic solar cells instead comes from the fact that exciton splitting proceeds more efficiently with fullerenes than with NFAs. However, to prove this hypothesis additional transient absorption measurements will be necessary to compare the exciton lifetime of the donor in the presence of nonfullerene or fullerene acceptors.

Eventually, by a judicious combination of different measurements we are able to demonstrate that the considered D:NFA:FA systems follow an alloy model and that the CT state indeed must be delocalized over both acceptors, thus shining light on the mechanisms in a promising class of ternary organic solar cells.

5.4 Experimental Section

Materials: ITO substrates with $15 \Omega \text{ cm}^2$ were obtained from Kintec. A ZnO nanoparticle dispersion in 2-propanol (Avantama N-10) was purchased from Avantama AG. Poly[4,8-bis(5-(2-ethylhexyl)thiophen-2-yl)benzo[1,2-b;4,5-b']dithiophene-2,6-diyl-alt-(4-(2-ethylhexyl)-3-fluorothieno[3,4-b]thiophene-)-2-carboxylate-2,6-diyl)] (PTB7-Th) has been received from 1-Material. Poly[(2,6-(4,8-bis(5-(2-ethylhexyl)thiophen-2-yl)-benzo[1,2-b;4,5-b']dithiophene))-alt-(5,5-(1',3'-di-2-thienyl-5',7'-bis(2-ethylhexyl)benzo[1',2'-c;4',5'-c']dithiophene-4,8-dione))] (PBDB-TF) and 3,9-bis(2-methylene-((3-(1,1-dicyanomethylene)-6,7-difluoro)-indanone))-5,5,11,11-tetrakis(4-hexylphenyl)-dithieno[2,3-d:2',3'-d']-s-indaceno[1,2-b:5,6-b']dithiophene (IT-4F) were obtained from Solarmer. 3,9-bis(2-methylene-(3-(1,1-dicyanomethylene)-indanone))-5,5,11,11-tetrakis(4-hexylphenyl)-dithieno[2,3-d:2',3'-d']-s-indaceno[1,2-b:5,6-b']dithiophene (ITIC) was provided by Ossila. Indene-C₆₀ monoadduct (ICMA), [6,6]-Phenyl-C61-butyric acid methyl ester (PCBM), bis(1-[3-(methoxycarbonyl)propyl]-1-phenyl)-[6,6]C₆₂ (BisPCBM), and tris(1-[3-(methoxycarbonyl)propyl]-1-phenyl)-[6,6]C₆₃ (TrisPCBM), were obtained from Solenne BV. Chlorobenzene, 1,8-diiodooctane (DIO), and MoO₃ powder (99.97 % trace metals basis) were purchased from Merck.

Device Fabrication: ITO patterned substrates were cleaned with detergent and ultrasonicated successively in water, acetone, and 2-propanol. They were dried under an air flow and plasma-cleaned. Then a 40-50 nm ZnO layer was spin coated with 1400 rpm for 60 s and annealed for 10 min at 120 °C in air. The substrates were then moved into a nitrogen filled glove box, where all further processing steps were performed. All photoactive layer solutions were prepared one day prior to spin coating and stirred overnight. For the PTB7-Th:IT-4F based cells, a fixed D:A ratio of 8:12 mg/ml in chlorobenzene was chosen, for the PBDB-TF:IT-4F based cells, the D:A ratio was kept at 10:10 mg/ml in chlorobenzene. For the respective ternary cells, the nonfullerene acceptor was successively replaced by the respective fullerene acceptor (in weight %) while maintaining the D:A weight ratio. To all active layer solutions 0.5 vol% DIO was added 30 min prior to spin coating. The PTB7-Th:IT-4F based binary and ternary active layer solutions were dynamically spin coated with 1500 rpm for 45s, while the PBDB-TF:IT-4F based active layers were dynamically spin coated at 900 rpm for 5 s and at 4000 rpm for 60 s. Finally, 10 nm of MoO_x and 100 nm Ag were evaporated through a mask on top of the substrates.

UV-vis spectra: All spectra were recorded from thin films on glass substrates in transmission mode with a PerkinElmer LAMBDA 1050 instrument with integrating sphere.

5 Elucidating the Origin of Open-Circuit Voltage in Ternary Organic Solar Cells Comprising a Nonfullerene and a Fullerene Acceptor

Contact angle measurements: Contact angle measurements were performed with an optical tensiometer (nanoScience instruments) by dripping water or glycerol on thin films of the pristine materials. The photographs were evaluated with the One Attension software package in the Young-Laplace analysis method. The surface energies were calculated from the contact angles with water and glycerol following the Wu model.²⁷

Solar Cell Characterization: *JV*-measurements were performed using a Keithley 2401 source-measure unit and a Newport ABA solar simulator, which was calibrated to AM1.5G using a Fraunhofer silicon diode. The cells were illuminated through a shadow mask with an area of 0.0831 cm². For wavelength-dependent *JV*-measurements, a white light LED, calibrated to 100 mW cm⁻², was used. For the monochromatic excitation of IT-4F, a 785 nm laser diode was employed, which was defocused to illuminate the whole cell area and whose intensity was chosen in a way that the resulting cell photocurrent corresponded to the photocurrent generated by the calibrated LED. The cells were illuminated through a shadow mask with an area of 0.0625 cm².

Fourier-Transform Photocurrent Spectroscopy: FTPS measurements were done with a modified Bruker Vertex 70 FTIR instrument by focusing light from a tungsten halogen lamp through a CaF₂ beam splitter with integrated gold mirrors to illuminate the devices under short-circuit conditions. The current from the devices was amplified with a FEMTO DHPA-100 current amplifier, passed through an analog-to-digital converter, and fed back to the FTIR instrument for Fourier transformation. Every measurement was averaged over 10000 scans for noise reduction.

External Quantum Efficiency: EQE measurements were performed with a home-built setup using a 150 W Xe short arc lamp (LOT Oriel) combined with a monochromator (Horiba microHR) and two Si-diodes (Hamamatsu) to calibrate the photon flux and compensate for light intensity fluctuations.

5 Elucidating the Origin of Open-Circuit Voltage in Ternary Organic Solar Cells Comprising a Nonfullerene and a Fullerene Acceptor

5.5 Supporting Information

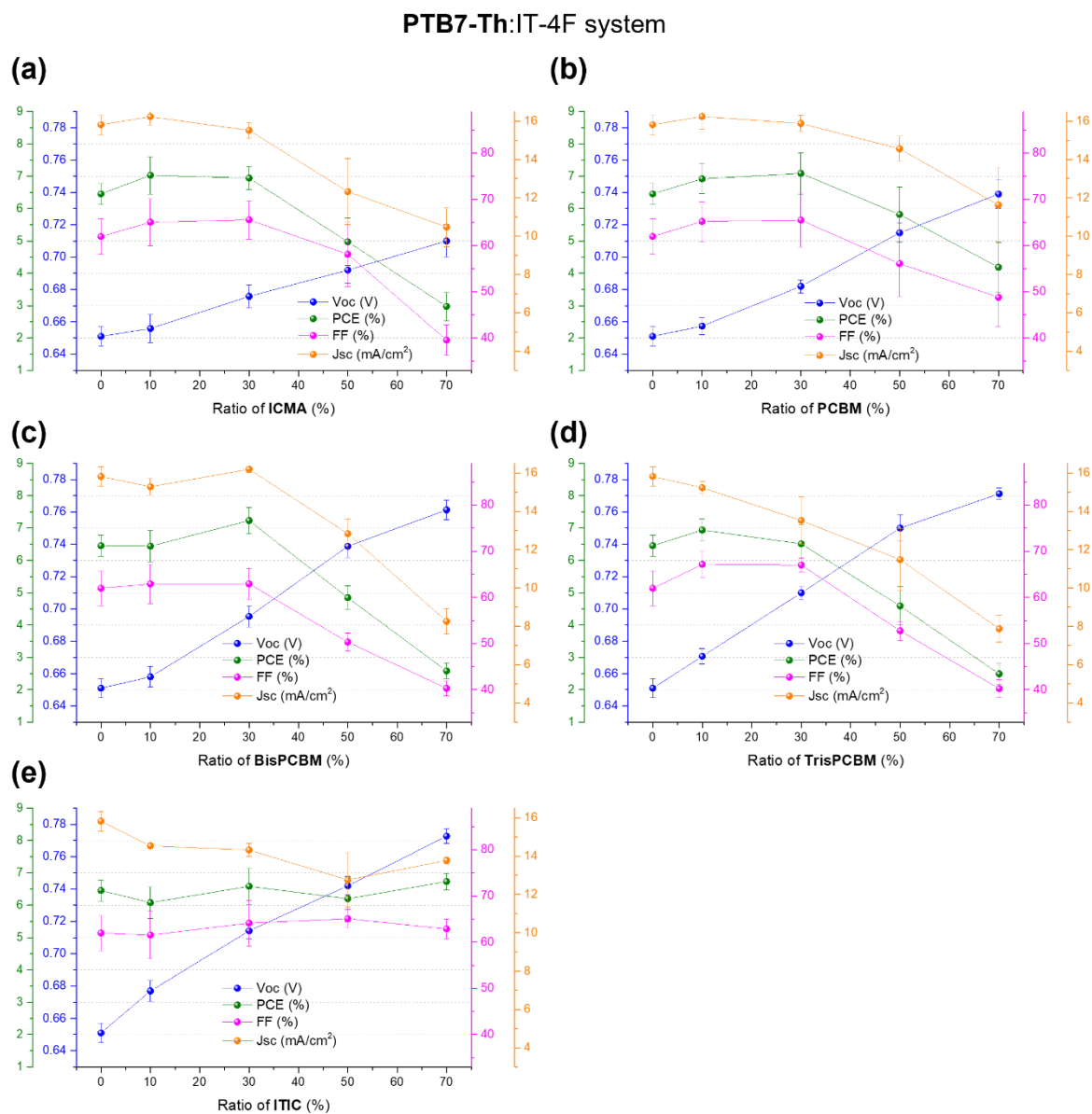


Figure S 5.1: Detailed performance parameters for the ternary cells based on the PTB7-Th:IT-4F host system with varying ratios of the third component a) ICMA, b) PCBM, c) BisPCBM, d) TrisPCBM, and e) ITIC. All values are averaged over 15 individual cells.

5 Elucidating the Origin of Open-Circuit Voltage in Ternary Organic Solar Cells Comprising a Nonfullerene and a Fullerene Acceptor

PBDB-TF:IT-4F system

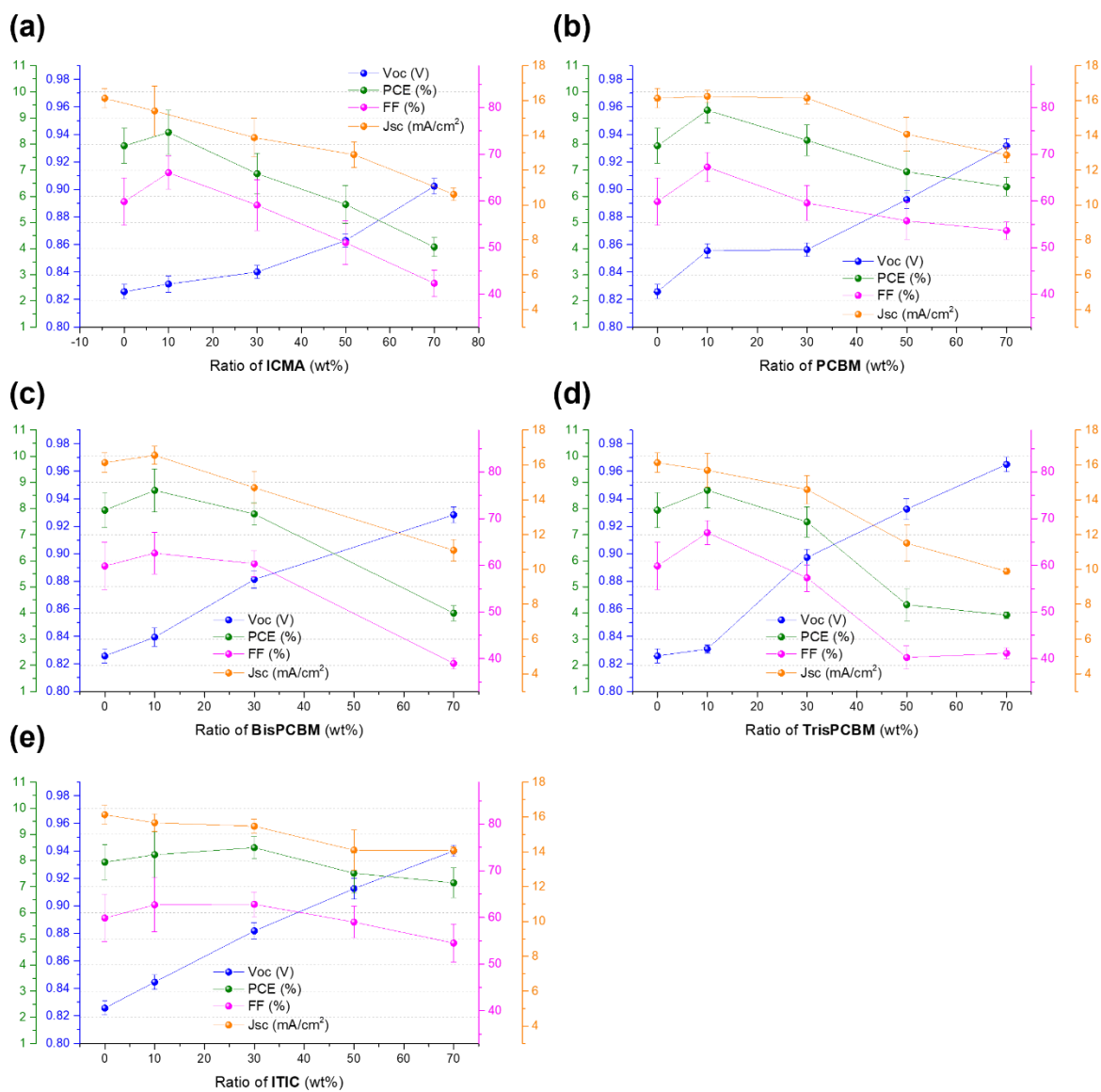


Figure S 5.2: Detailed performance parameters for the ternary cells based on the PBDB-TF:IT-4F host system with varying ratios of the third component a) ICMA, b) PCBM, c) BisPCBM, d) TrisPCBM, and e) ITIC. All values are averaged over 15 individual cells.

5 Elucidating the Origin of Open-Circuit Voltage in Ternary Organic Solar Cells Comprising a Nonfullerene and a Fullerene Acceptor

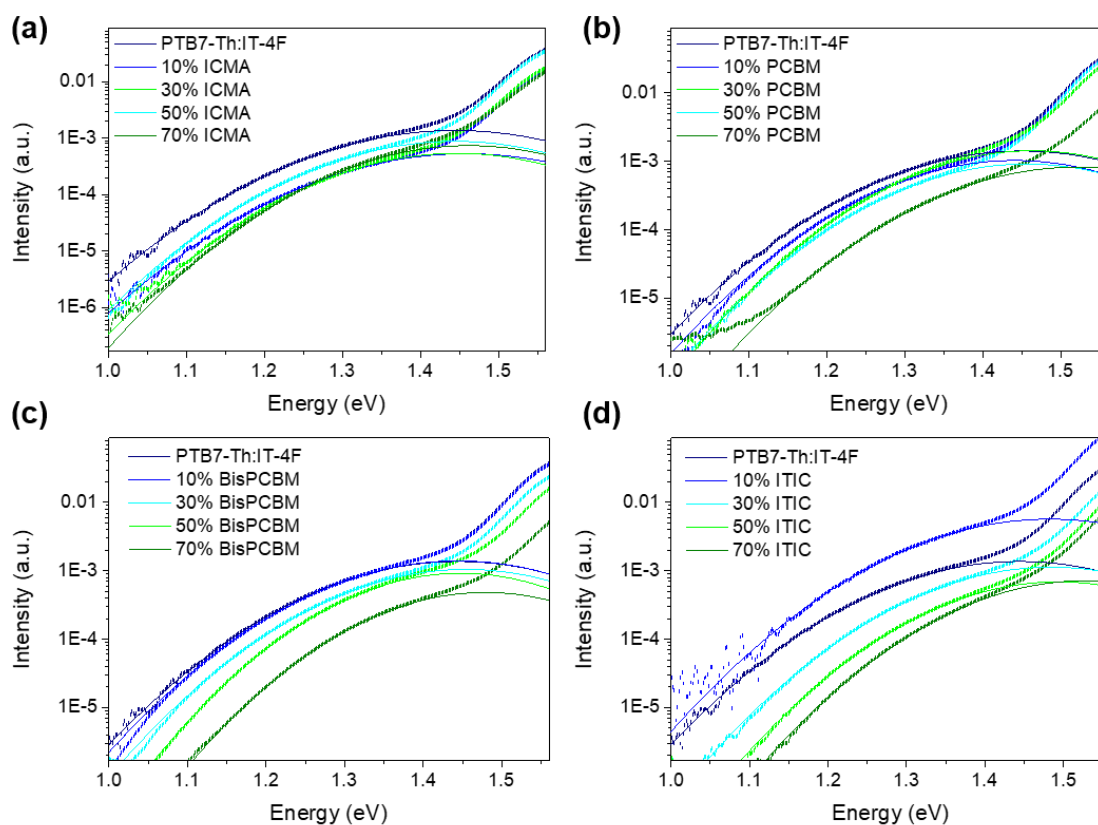


Figure S 5.3: FTPS data and corresponding Marcus Fits for ternary cells based on the PTB7-Th:IT-4F host system with a) ICMA, b) PCBM, c) BisPCBM, and d) ITIC as third component.

5 Elucidating the Origin of Open-Circuit Voltage in Ternary Organic Solar Cells Comprising a Nonfullerene and a Fullerene Acceptor

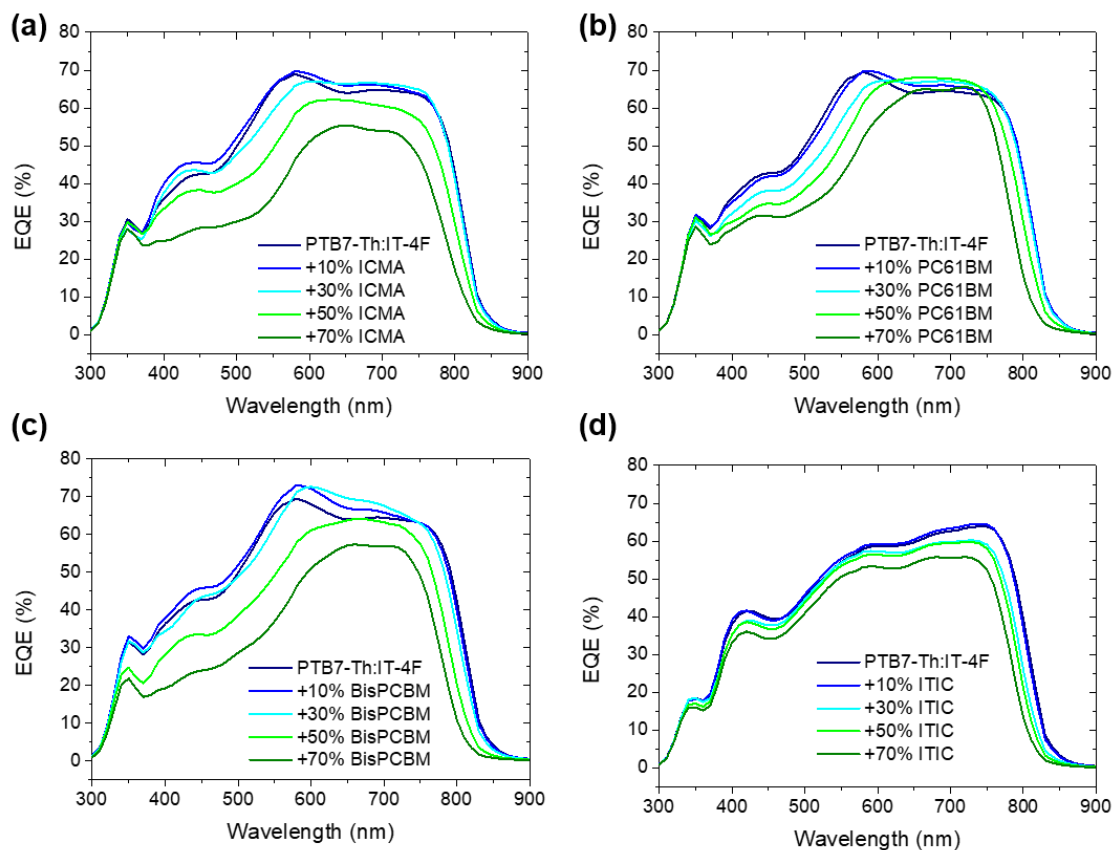


Figure S 5.4: External quantum efficiency spectra of ternary cells based on the PTB7-Th:IT-4F host system with varying ratios of the third component a) ICMA b) PCBM c) BisPCBM and d) ITIC.

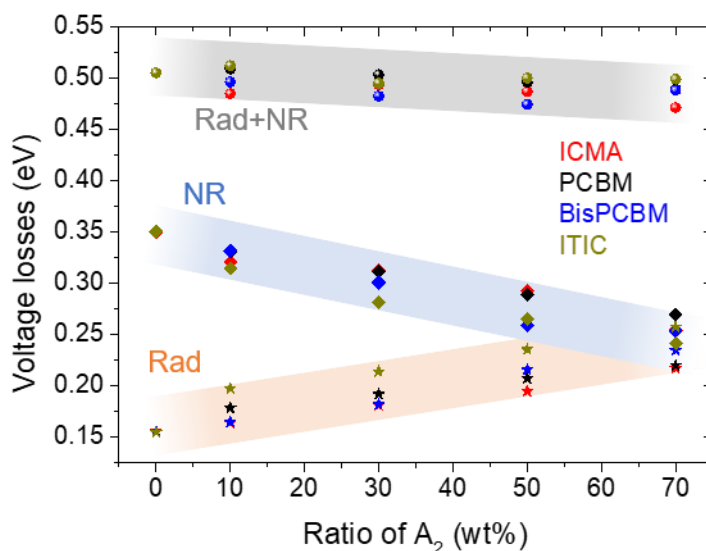


Figure S 5.5: Voltage loss analysis for different compositions of ternary cells based on the PTB7-Th:IT-4F host system with ICMA, PCBM, BisPCBM and ITIC as third component. Shown are the radiative losses (Rad), the nonradiative losses (NR) and the sum of both (Rad+NR).

5 Elucidating the Origin of Open-Circuit Voltage in Ternary Organic Solar Cells Comprising a Nonfullerene and a Fullerene Acceptor

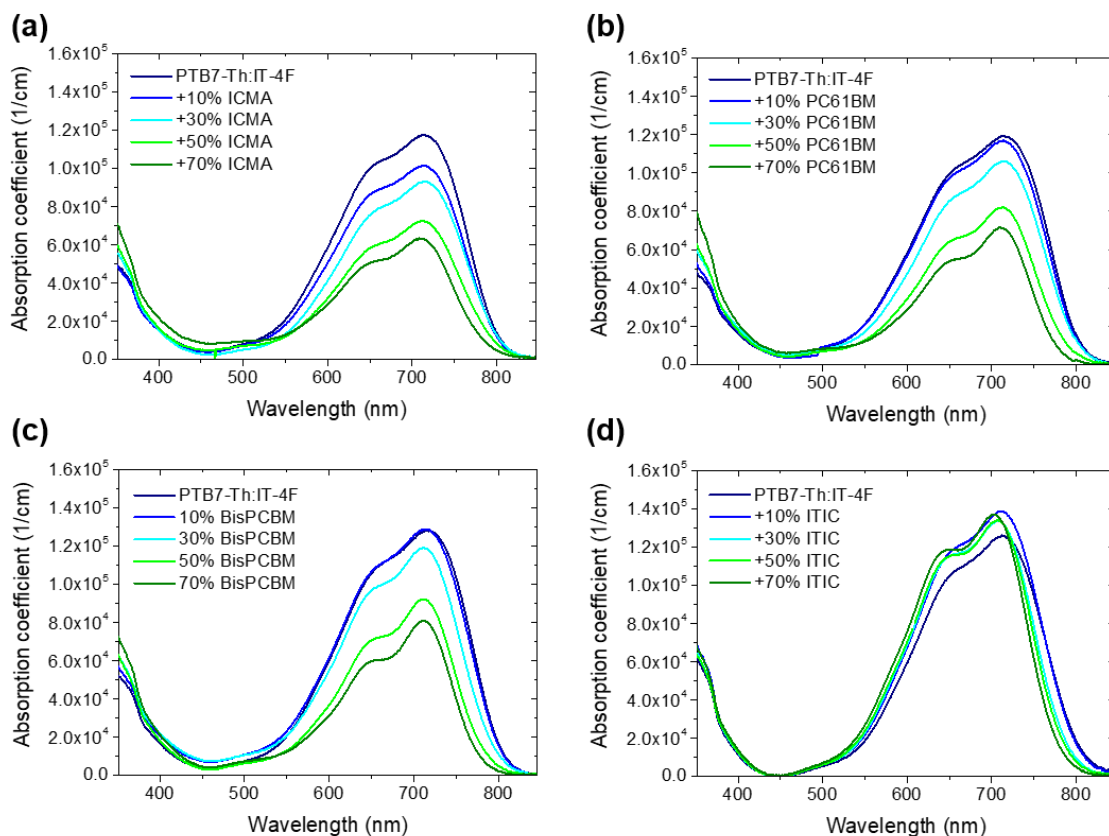


Figure S 5.6: Absorption coefficients of ternary blends based on the PTB7-Th:IT-4F host system with varying ratios of the third component a) ICMA b) PCBM c) BisPCBM and d) ITIC.

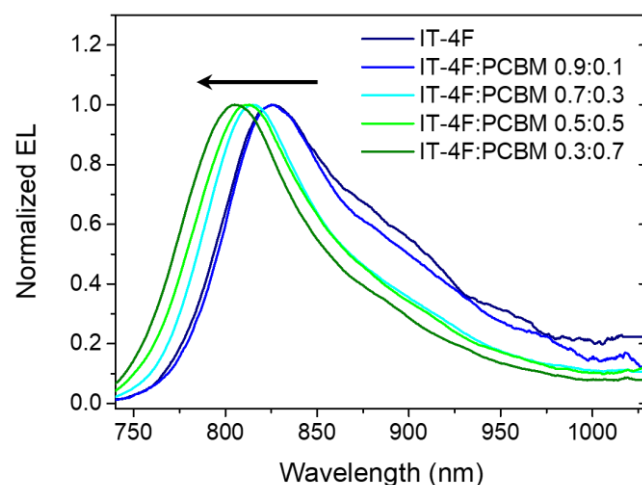


Figure S 5.7: Normalized electroluminescence spectra of binary acceptor blends with varying weight ratios of IT-4F and PCBM.

5 Elucidating the Origin of Open-Circuit Voltage in Ternary Organic Solar Cells Comprising a Nonfullerene and a Fullerene Acceptor

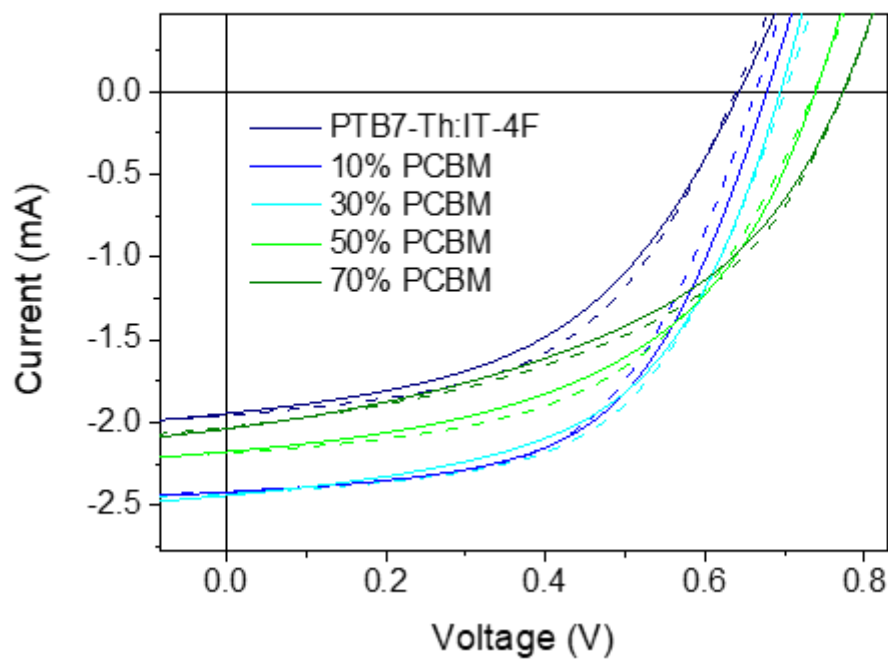


Figure S 5.8: IV-curves of ternary blends based on the PTB7-Th:IT-4F host system with varying ratios of the second acceptor PCBM. The solid lines show the measurements where a 785nm laser diode was used, while the dotted lines indicate the measurements with a white light LED for illumination.

5 Elucidating the Origin of Open-Circuit Voltage in Ternary Organic Solar Cells Comprising a Nonfullerene and a Fullerene Acceptor

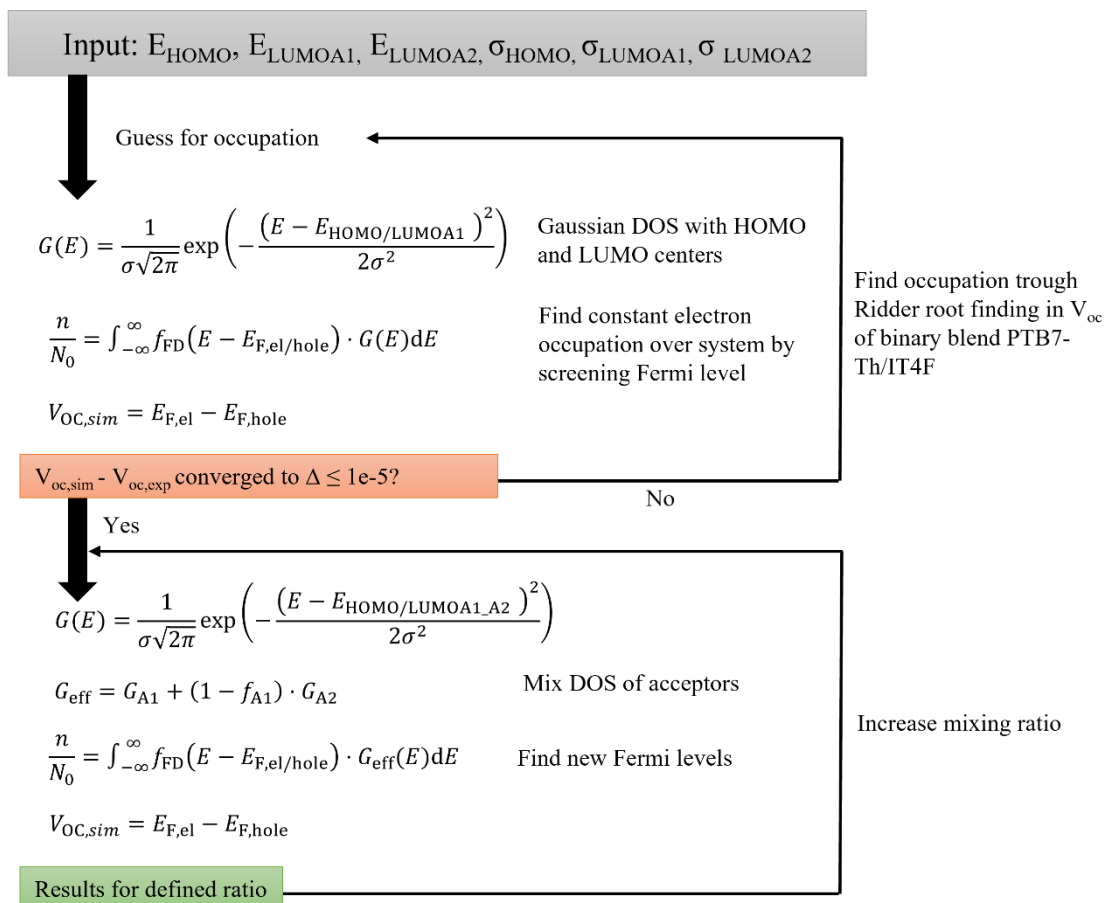


Figure S 5.9: Schematic describing the script used to model the open-circuit voltage of ternary blends. The model is based on the state-filling approach of Kemerink et al.³⁹

5 Elucidating the Origin of Open-Circuit Voltage in Ternary Organic Solar Cells Comprising a Nonfullerene and a Fullerene Acceptor

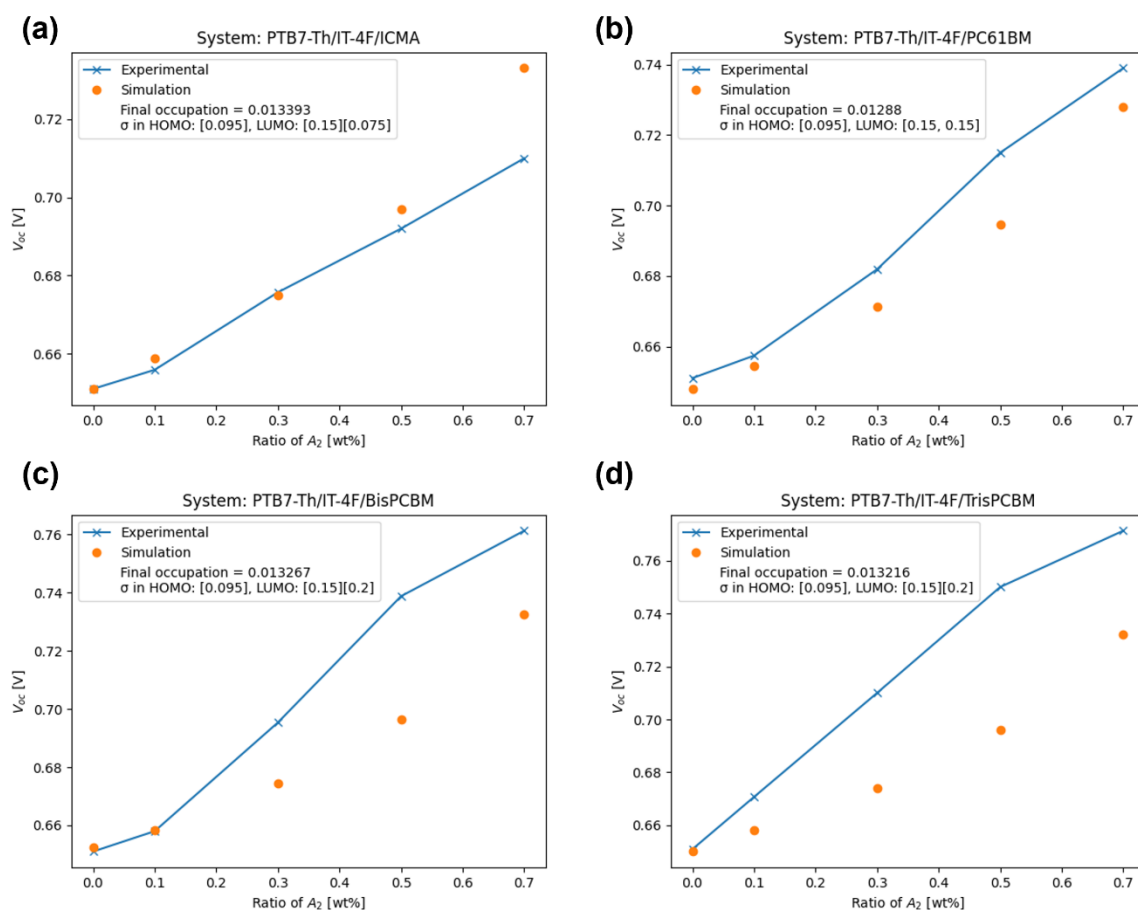


Figure S 5.10: Comparison of the experimentally obtained open-circuit voltage (blue curve) and the simulated values (orange) according to the state-filling model of Kemerink et al.³⁹ for ternary blends based on the PTB7-Th:IT-4F host system with the second acceptor a) ICMA, b) PCBM, c) BisPCBM, and d) TrisPCBM.

5 Elucidating the Origin of Open-Circuit Voltage in Ternary Organic Solar Cells Comprising a Nonfullerene and a Fullerene Acceptor

5.6 References

1. Zhao, J. *et al.* Efficient organic solar cells processed from hydrocarbon solvents. *Nat Energy* **1** (2016).
2. Deng, D. *et al.* Fluorination-enabled optimal morphology leads to over 11% efficiency for inverted small-molecule organic solar cells. *Nature communications* **7**, 13740 (2016).
3. Li, S. *et al.* Energy-Level Modulation of Small-Molecule Electron Acceptors to Achieve over 12% Efficiency in Polymer Solar Cells. *Advanced materials (Deerfield Beach, Fla.)* **28**, 9423–9429 (2016).
4. Zhao, W. *et al.* Molecular Optimization Enables over 13% Efficiency in Organic Solar Cells. *Journal of the American Chemical Society* **139**, 7148–7151 (2017).
5. Wei, Y. *et al.* Binary Organic Solar Cells Breaking 19% via Manipulating the Vertical Component Distribution. *Adv. Mater.* **34**, e2204718 (2022).
6. Li, X. *et al.* Roles of Acceptor Guests in Tuning the Organic Solar Cell Property Based on an Efficient Binary Material System with a Nearly Zero Hole-Transfer Driving Force. *Chem. Mater.* **32**, 5182–5191 (2020).
7. Qiu, B. *et al.* Understanding the Effect of the Third Component PC 71 BM on Nanoscale Morphology and Photovoltaic Properties of Ternary Organic Solar Cells. *Sol. RRL* **4**, 1900540 (2020).
8. Jiang, K. *et al.* Alkyl Chain Tuning of Small Molecule Acceptors for Efficient Organic Solar Cells. *Joule* **3**, 3020–3033 (2019).
9. Ma, L. *et al.* A ternary organic solar cell with 300 nm thick active layer shows over 14% efficiency. *Sci. China Chem.* **63**, 21–27 (2020).
10. Zhang, K.-N. *et al.* High-Performance Ternary Organic Solar Cells with Morphology-Modulated Hole Transfer and Improved Ultraviolet Photostability. *Sol. RRL* **4**, 2000165 (2020).
11. Lu, H. *et al.* Ternary-Blend Polymer Solar Cells Combining Fullerene and Nonfullerene Acceptors to Synergistically Boost the Photovoltaic Performance. *Adv. Mater.* **28**, 9559–9566 (2016).

- 5 Elucidating the Origin of Open-Circuit Voltage in Ternary Organic Solar Cells Comprising a Nonfullerene and a Fullerene Acceptor
12. Zhou, Z. *et al.* High-efficiency small-molecule ternary solar cells with a hierarchical morphology enabled by synergizing fullerene and non-fullerene acceptors. *Nat Energy* **3**, 952–959 (2018).
13. Karuthedath, S. *et al.* Impact of Fullerene on the Photophysics of Ternary Small Molecule Organic Solar Cells. *Adv. Energy Mater.* **9**, 1901443 (2019).
14. Privado, M. *et al.* Fullerene/Non-fullerene Alloy for High-Performance All-Small-Molecule Organic Solar Cells. *ACS Appl. Mater. Interfaces* **13**, 6461–6469 (2021).
15. Street, R. A., Davies, D., Khlyabich, P. P., Burkhart, B. & Thompson, B. C. Origin of the tunable open-circuit voltage in ternary blend bulk heterojunction organic solar cells. *JACS* **135**, 986–989 (2013).
16. Khlyabich, P. P., Rudenko, A. E., Thompson, B. C. & Loo, Y.-L. Structural Origins for Tunable Open-Circuit Voltage in Ternary-Blend Organic Solar Cells. *Adv. Funct. Mater.* **25**, 5557–5563 (2015).
17. Yang, L., Zhou, H., Price, S. C. & You, W. Parallel-like bulk heterojunction polymer solar cells. *JACS* **134**, 5432–5435 (2012).
18. Hadmojo, W. T. *et al.* Performance Optimization of Parallel-Like Ternary Organic Solar Cells through Simultaneous Improvement in Charge Generation and Transport. *Adv. Funct. Mater.* **27**, 1808731 (2019).
19. Mollinger, S. A., Vandewal, K. & Salleo, A. Microstructural and Electronic Origins of Open-Circuit Voltage Tuning in Organic Solar Cells Based on Ternary Blends. *Adv. Energy Mater.* **5**, 1501335 (2015).
20. Schwarze, M. *et al.* Band structure engineering in organic semiconductors. *Science* **352**, 1446–1449 (2016).
21. Davis, R. J. *et al.* Determination of energy level alignment at interfaces of hybrid and organic solar cells under ambient environment. *J. Mater. Chem.* **21**, 1721–1729 (2011).
22. Sworakowski, J., Lipiński, J. & Janus, K. On the reliability of determination of energies of HOMO and LUMO levels in organic semiconductors from electrochemical measurements. A simple picture based on the electrostatic model. *Organic Electronics* **33**, 300–310 (2016).
23. Bertrandie, J. *et al.* The Energy Level Conundrum of Organic Semiconductors in Solar Cells. *Adv. Mater.*, e2202575 (2022).

- 5 Elucidating the Origin of Open-Circuit Voltage in Ternary Organic Solar Cells Comprising a Nonfullerene and a Fullerene Acceptor
24. Ball, J. M. *et al.* Soluble fullerene derivatives: The effect of electronic structure on transistor performance and air stability. *Journal of Applied Physics* **110**, 14506 (2011).
25. Bao, Q. *et al.* Trap-Assisted Recombination via Integer Charge Transfer States in Organic Bulk Heterojunction Photovoltaics. *Adv Funct Materials* **24**, 6309–6316 (2014).
26. Karuthedath, S. *et al.* Intrinsic efficiency limits in low-bandgap non-fullerene acceptor organic solar cells. *Nat Mater* **20**, 378–384 (2021).
27. Wu, S. Calculation of Interfacial Tension in Polymer Systems. *J. Polymer. Sci.* **34**, 19–30 (1971).
28. Rau, U. Reciprocity relation between photovoltaic quantum efficiency and electroluminescent emission of solar cells. *Phys. Rev. B* **76** (2007).
29. Jungbluth, A., Kaienburg, P. & Riede, M. Charge transfer state characterization and voltage losses of organic solar cells. *J. Phys. Mater.* **5**, 24002 (2022).
30. Benduhn, J. *et al.* Intrinsic non-radiative voltage losses in fullerene-based organic solar cells. *Nat. Energy* **2**, 17053 (2017).
31. Burkhard, G. F., Hoke, E. T. & McGehee, M. D. Accounting for interference, scattering, and electrode absorption to make accurate internal quantum efficiency measurements in organic and other thin solar cells. *Advanced materials (Deerfield Beach, Fla.)* **22**, 3293–3297 (2010).
32. Armin, A. *et al.* A History and Perspective of Non-Fullerene Electron Acceptors for Organic Solar Cells. *Adv. Energy Mater.* **11**, 2003570 (2021).
33. Hinrichsen, T. F. *et al.* Long-lived and disorder-free charge transfer states enable endothermic charge separation in efficient non-fullerene organic solar cells. *Nat. Commun.* **11**, 5617 (2020).
34. Armin, A., Durrant, J. R. & Shoaee, S. Interplay Between Triplet-, Singlet-Charge Transfer States and Free Charge Carriers Defining Bimolecular Recombination Rate Constant of Organic Solar Cells. *J. Phys. Chem. C* **121**, 13969–13976 (2017).
35. Burke, T. M., Sweetnam, S., Vandewal, K. & McGehee, M. D. Beyond Langevin Recombination: How Equilibrium Between Free Carriers and Charge Transfer States Determines the Open-Circuit Voltage of Organic Solar Cells. *Adv. Energy Mater.* **5**, 1500123 (2015).

5 Elucidating the Origin of Open-Circuit Voltage in Ternary Organic Solar Cells Comprising a Nonfullerene and a Fullerene Acceptor

36. Hughes, M. P. *et al.* Determining the Dielectric Constants of Organic Photovoltaic Materials Using Impedance Spectroscopy. *Adv Funct Materials* **28**, 1801542 (2018).
37. Zhang, X. *et al.* Fluorination with an enlarged dielectric constant prompts charge separation and reduces bimolecular recombination in non-fullerene organic solar cells with a high fill factor and efficiency > 13%. *Nano Energy* **56**, 494–501 (2019).
38. Savoie, B. M., Dunaisky, S., Marks, T. J. & Ratner, M. A. The Scope and Limitations of Ternary Blend Organic Photovoltaics. *Adv. Energy Mater.* **5**, 1400891 (2015).
39. Felekidis, N., Wang, E. & Kemerink, M. Open circuit voltage and efficiency in ternary organic photovoltaic blends. *Energy Environ. Sci.* **9**, 257–266 (2016).

6 Conclusions and Outlook

This work focused on a subset of organic solar cells consisting of a polymer donor with a nonfullerene acceptor and investigated how their stability and performance are affected by the addition of fullerene derivatives in a ternary approach.

In the first chapter, we successfully demonstrated that the efficiency and UV photostability of several D:NFA based OSCs can be significantly enhanced by the incorporation of fullerene derivatives. The best working fullerene ICMA achieved a fivefold increased lifetime under UV illumination at a ratio as low as 5 wt%. The binary D:NFA cells under UV illumination showed a rapidly decreasing fill factor and an increasing monomolecular recombination behavior, which was shown to be due to the literature-known photocatalytic decomposition of IT-4F on the ZnO surface causing the formation of trap states. Since this decomposition occurs via radicals that are formed upon UV illumination from oxygen species adsorbed on the ZnO, the fullerene derivatives were added with the intention of acting as radical scavengers. With light-intensity dependent V_{OC} and FTPS results, we demonstrated that the added fullerenes indeed suppress the emergence of trap states. Absorption measurements of UV aged IT-4F films on ZnO with and without fullerenes furthermore confirmed that the decomposition of IT-4F is reduced in the presence of fullerenes. We therefore proposed that the fullerenes act as a sacrificial agent when attacked by the radical species, since due to their large electronic system they are able to delocalize the radical and do not form a trap state. Our work highlights that adding fullerenes in a ternary approach, compared to the addition of protective interlayers, provides a simple, low-cost, and transferable method to increase the photostability of ZnO-containing OSCs.

Prompted by those findings, in the second chapter we addressed more generally the influence of ZnO and its peculiar properties on stability studies of OSCs, focusing in particular on the light-soaking issues emanating from ZnO. These light-soaking issues normally occur in an ambient atmosphere when oxygen species from the environment penetrate the OSC and adsorb at the ZnO surface, resulting in a charge accumulation at the interface and a hindered electron extraction. To avoid those issues, a permanent illumination with UV light is necessary, which excites the ZnO and thus helps desorbing the oxygen species. In a protective atmosphere, no light-soaking issues are normally assumed to occur, which is why JV -measurements are often performed with white light LEDs without UV part. However, we found that even in a protective

6 Conclusions and Outlook

atmosphere the light-soaking issues cannot be ignored and that ZnO-containing OSCs in the absence of UV illumination show a significant degradation of performance over time, which can be recovered with a short UV exposure. This degradation was found to be independent of the used active layer material and to accelerate at elevated temperatures. At 85°C, which is the standard temperature for thermal stability measurements, a PCE loss of more than 20 % was observed after only 24 hours, which was fully recoverable by UV illumination. We explained this behavior with oxygen species – which are unavoidably contained in the ZnO through the production process in air – thermally activated adsorbing on the ZnO over time, thus resulting in a reversible loss of performance. With XPS measurements of the ZnO layers we proved that indeed oxygen species are adsorbed on the ZnO surface, and that they cannot be desorbed even under ultra-high vacuum. With in-situ UV illumination and oxygen flushing we furthermore demonstrated that it is molecular oxygen which is desorbed under illumination and re-adsorbs again in the dark. Finally, we showed that a UV pre-treatment of the pristine ZnO layers and a completely oxygen-free manufacturing of the solar cells can resolve the light-soaking issues, however at the price of a small loss of device efficiency. Our work underlined that stability measurements of ZnO-containing OSCs have to be performed thoroughly and exclusively with an accurate light source to avoid misleading results due to light-soaking issues. We also pointed out that when ZnO is used in commercial, encapsulated OSCs, the production must actually be completely oxygen-free, since otherwise the re-adsorption of the contained oxygen residues would lead to a loss of efficiency over time.

In the last chapter, the goal was to broaden the understanding of mechanisms and performance improvement in D:NFA:FA ternary solar cells, because although this type of system continuously provides excellent results reported in the literature regarding efficiency, its operating principles are still controversial. For this reason, a comprehensive study was conducted with systematically varied components and compositions to examine the influence of the components' properties on the device performance. Eight different D:NFA:FA systems based on two different polymer donors and four different fullerene derivatives were considered and the dependence of the performance on the acceptor ratio was screened. It was found that for all systems the open-circuit voltage increases linearly with the ratio of the fullerene and that this trend is directly related to the LUMO position of the fullerene. Furthermore, for all ternary systems compared to the binary D:NFA system the PCE was improved for smaller fullerene ratios added (10-30 %).

Using a combination of different optoelectronic measurements, it could be demonstrated that the ternary blends can be described by an alloy-like model with a CT state that is delocalized between the nonfullerene and the fullerene acceptor, resulting in a composition-averaged V_{OC} . To understand why the addition of small fullerene amounts leads to an improved efficiency, the recombination behavior in dependence of the composition was studied. Although we found that the nonradiative recombination decreases with higher fullerene ratios, radiative recombination increases at the same time, almost completely canceling the positive effect. Most importantly, by also investigating a D:NFA:NFA ternary system, we found the recombination behavior to be independent of the third component's nature and instead being exclusively related to the CT state energy of the ternary system, thus confirming the applicability of the power gap law, established for binary OSCs, also for ternary OSCs. Since changes in recombination behavior therefore could not explain the positive effect of fullerenes on efficiency, we examined the internal quantum efficiency of D:NFA:FA systems compared to D:NFA:NFA systems, which show no similar PCE improvement. We observed that the IQE increases for increasing fullerene ratios but is independent of the composition for the D:NFA:NFA system. We therefore hypothesized that the splitting of the donor exciton into a CT state proceeds more efficiently with fullerenes being the acceptor than with nonfullerenes, which could be due to differences in the process of CT state formation.

In summary, this thesis illustrates that the addition of fullerenes as third components to polymer:nonfullerene OSCs can have a beneficial effect on both stability and efficiency by combining the advantages of the two acceptor types. However, there are still many unanswered questions about how exactly this interaction works. In this thesis, the functional principles were elucidated for a specific subgroup of possible materials, but comparable studies for other materials with different structure or energy level situation are missing. With further research focusing on even more optimal use of the synergies between fullerene and nonfullerene acceptors, D:NFA:FA ternary systems could pave the way for organic solar cells exceeding 20 % efficiency.

7 List of Abbreviations

AFM	atomic force microscopy
BHJ	bulk heterojunction
CS	charge separated
CT	charge transfer
D	donor
DFT	density functional theory
DOOS	density of occupied states
DOS	density of states
DSC	differential scanning calorimetry
EA	electron affinity
EL	electroluminescence
EQE	external quantum efficiency
ETL	electron transport layer
FA	fullerene acceptor
FF	fill factor
FTO	fluorine doped tin oxide
FTPS	fourier-transform photocurrent spectroscopy
FWHM	full width at half maximum
GISAXS	grazing incidence small angle X-ray scattering
GIWAXS	grazing incidence wide angle X-ray scattering
GIXRD	grazing incidence X-ray diffraction
HOMO	highest occupied molecular orbital
HTL	hole transport layer
IP	ionization potential
IPES	inverse photoemission spectroscopy
IQE	internal quantum efficiency
ITO	indium doped tin oxide
J_{sc}	short-circuit current density
LED	light emitting diode
LUMO	lowest unoccupied molecular orbital
NFA	nonfullerene acceptor

7 List of Abbreviations

OPV	organic photovoltaic
OSC	organic solar cell
PCE	power conversion efficiency
PL	photoluminescence
PSR	photocurrent spectral response
RSoXS	resonant soft X-ray scattering
TOSC	ternary organic solar cell
UPS	ultraviolet photoelectron spectroscopy
UV	ultraviolet
Vis	visible
V_{oc}	open-circuit voltage
XPS	X-ray photoelectron spectroscopy
XRD	X-ray diffraction

8 Publications

- 1. Elucidating the Origin of Open-Circuit Voltage in Ternary Organic Solar Cells Comprising a Nonfullerene and a Fullerene Acceptor**
Marcella Günther, Dominic Blätte, Andreas Weis, Lucie Quincke, Miguel Angel Torre Cachafeiro, Wolfgang Tress, Jose Dario Perea, Salvador Leon Cabanillas, Thomas Bein, Tayebbeh Ameri, *to be submitted*
- 2. Models and Mechanisms of Ternary Organic Solar Cells**
Marcella Günther, Negar Kazerouni, Dominic Blätte, Jose Dario Perea, Barry C. Thompson, Tayebbeh Ameri, *under review at Nature Materials Reviews*.
- 3. The Neglected Influence of Zinc Oxide Light-Soaking on Stability Measurements of Inverted Organic Solar Cells**
Marcella Günther, Soroush Lotfi, Sergio Sánchez Rivas, Dominic Blätte, Jan P. Hofmann, Thomas Bein and Tayebbeh Ameri, *under review at Adv. Funct. Mater.*
- 4. Ultra-Thin Protective Coatings for Sustained Photoelectrochemical Water Oxidation with Mo:BiVO₄**
Michael Beetz, Sebastian Häringer, Patrick Elsässer, Jonathan Kampmann, Lena Sauerland, Florian Wolf, Marcella Günther, Anna Fischer, Thomas Bein, *Adv. Funct. Mater.* **2021**, 31, 45, 2011210
- 5. 1,10-Phenanthroline as an Efficient Bifunctional Passivating Agent for MAPbI₃ Perovskite Solar Cells**
Ali Buyruk, Dominic Blätte, Marcella Günther, Manuel A. Scheel, Nicolai F. Hartmann, Markus Döblinger, Andreas Weis, Achim Hartschuh, Peter Müller-Buschbaum, Thomas Bein, Tayebbeh Ameri, *Appl. Mater. Interfaces* **2021**, 13, 28, 32894-32905

6. Increasing Photostability of Inverted Nonfullerene Organic Solar Cells by Using Fullerene Derivative Additives

Marcella Günther, Dominic Blätte, Anna Lena Oechsle, Sergio Sánchez Rivas, Amir Abbas Yousefi Amin, Peter Müller-Buschbaum, Thomas Bein, Tayebah Ameri, *ACS Appl. Mater. Interfaces* **2021**, 13, 16, 19072-19084

7. Ternary Sensitization of Organic Solar Cells: A Multifunctional Concept to Boost Power Conversion Efficiency

Negar Kazerouni[#], Marcella Günther[#], Barry C. Thompson, Tayebah Ameri, *Emerging Photovoltaic Technologies*, Jenny Stanford Publishing, **2020**